Before there was light

Excited state dynamics in luminescent (nano)materials

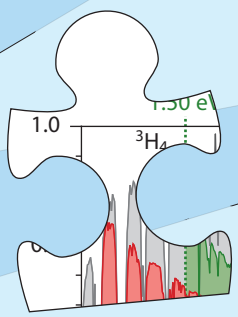

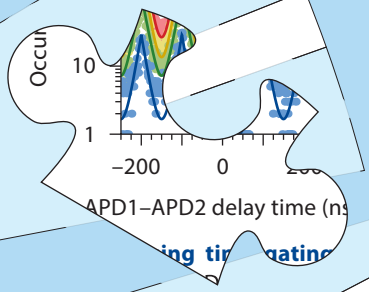

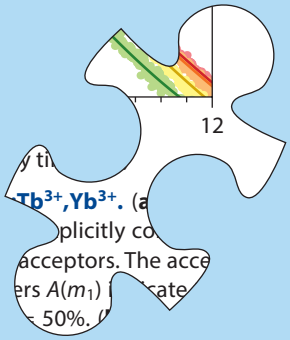

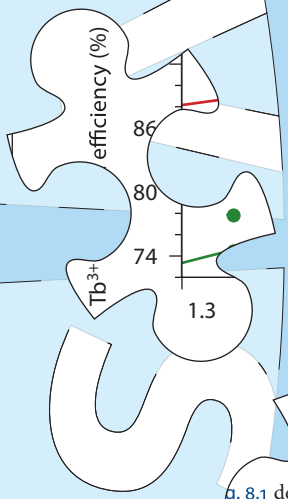

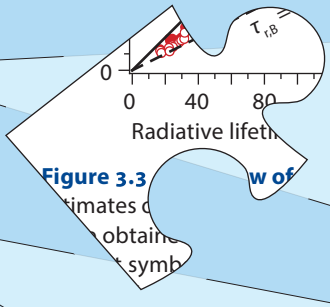

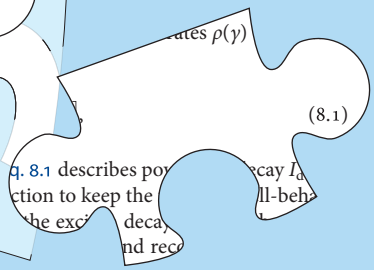

Freddy Rabouw

Before there was light

Excited state dynamics in luminescent (nano)materials

PhD thesis, Universiteit Utrecht
Before there was light: excited state dynamics in luminescent (nano)materials
Freddy Rabouw, September 2015

ISBN 978-90-39363-97-3
Printed by Uitgeverij BOXPress || Proefschriftmaken.nl

Before there was light

Excited state dynamics in luminescent (nano)materials

Voor er licht was

De dynamica van de aangeslagen toestand in luminescente (nano)materialen

(met een samenvatting in het Nederlands)

Proefschrift

ter verkrijging van de graad van doctor aan de Universiteit Utrecht op gezag van de rector magnificus, prof.dr. G.J. van der Zwaan, ingevolge het besluit van het college voor promoties in het openbaar te verdedigen

op maandag 28 september 2015

des middags te 2.30 uur

door

Frederik Teunis Rabouw

geboren op 5 augustus 1988 te Gouda

Promotoren:

Prof. dr. D.A.M. Vanmaekelbergh
Prof. dr. A. Meijerink

Dit proefschrift maakt deel uit van het onderzoekprogramma 'Light management in new photovoltaic materials' van de Stichting voor Fundamenteel Onderzoek der Materie (FOM), die wordt gefinancierd door de Nederlandse Organisatie voor Wetenschappelijk Onderzoek (NWO)

Contents

List of publications

2015

22. **Near-infrared emitting $CuInSe_2/CuInS_2$ dot core/rod shell heteronanorods by sequential cation exchange**
Van der Stam, W., Bladt, E., Rabouw, F.T., Bals, S. & De Mello Donegá, C.
Submitted

21. **Dynamics of intraband and interband Auger processes in colloidal core–shell quantum dots**
Rabouw, F.T., Vaxenburg, R., Bakulin, A.A., Van Dijk-Moes, R.J.A., Bakker, H.J., Rodina, A., Lifshitz, E., Efros, Al.L., Koenderink, A.F. & Vanmaekelbergh, D.
Submitted

20. **Delayed exciton emission and its relation to blinking in CdSe quantum dots**
Rabouw, F.T., Kamp, M., Van Dijk-Moes, R.J.A., Gamelin, D.R., Koenderink, A.F., Meijerink, A. & Vanmaekelbergh, D.
Submitted

19. **Quantum confinement regimes in CdTe nanocrystals probed by single dot spectroscopy: from strong confinement to the bulk limit**
Tilchin, J., Rabouw, F.T., Isarov, M., Vaxenburg, R., Van Dijk-Moes, R.J.A., Lifshitz, E. & Vanmaekelbergh, D.
ACS Nano, ASAP doi:10.1021/acsnano.5b02597

18. **Multi-photon quantum cutting in $Gd_2O_2S:Tm^{3+}$ to enhance the photo-response of solar cells**
Yu, D.C., Martín-Rodríguez, R., Zhang, Q.Y., Meijerink, A. & Rabouw, F.T.
Light Sci. Appl. **4**, e344 (2015)

17. **Resolving the ambiguity in the relation between Stokes shift and Huang-Rhys parameter**
De Jong, M., Seijo, L., Meijerink, A. & Rabouw, F.T.
Phys. Chem. Chem. Phys. **17**, 16959–16969 (2015)

16. **Shape-dependent multi-exciton emission and whispering gallery modes in supraparticles of CdSe/multi-shell quantum dots**
Vanmaekelbergh, D., Van Vugt, L.K., Bakker, H.E., Rabouw, F.T., De Nijs, B., Van Dijk-Moes, R.J.A., Van Huis, M.A., Baesjou, P. & Van Blaaderen, A.
ACS Nano **9**, 3942–3950 (2015)

15. **Upconversion dynamics in Er^{3+}-doped Gd_2O_2S: influence of excitation power, Er^{3+} concentration, and defects**
Martín-Rodríguez, R., Rabouw, F.T., Trevisani, M., Bettinelli, M. & Meijerink, A.
Adv. Optical Mater. **3**, 558–567 (2015)

14. **Modeling the cooperative energy transfer dynamics of quantum cutting for solar cells**
Rabouw, F.T. & Meijerink, A.
J. Phys. Chem. C **119**, 2364–2370 (2015)

13. **Photonic effects on the radiative decay rate and luminescence quantum yield of doped nanocrystals**
Senden, T., Rabouw, F.T. & Meijerink, A.
ACS Nano **9**, 1801–1808 (2015)

12. **Luminescent $CuInS_2$ quantum dots by partial cation exchange in $Cu_{2-x}S$ nanocrystals**
Van der Stam, W., Berends, A.C., Rabouw, F.T., Willhammar, T., Ke, X., Meeldijk, J.D., Bals, S. & De Mello Donegá, C.
Chem. Mater. **27**, 621–628 (2015)

2014

11. **Lanthanide-doped CaS and SrS luminescent nanocrystals: a single-source precursor approach for doping**
Zhao, Y., Rabouw, F.T., Van Puffelen, T., Van Walree, C.A., Gamelin, D.R., De Mello Donegá, C. & Meijerink, A.
J. Am. Chem. Soc. **136**, 16533–16543 (2014)

10. **Insights into the energy transfer mechanism in Ce^{3+}–Yb^{3+} codoped YAG phosphors**
Yu, D.C., Rabouw, F.T., Boon, W.Q., Kieboom, T., Ye, S., Zhang, Q.Y. & Meijerink, A.
Phys. Rev. B **90**, 165126 (2014)

9. **Self-assembled CdSe/CdS nanorod sheets studied in the bulk suspension by magnetic alignment**
Pietra, F., Rabouw, F.T., Van Rhee, P.G., Van Rijssel, J., Petukhov, A.V., Erné, B.H., Christianen, P.C.M., De Mello Donegá, C. & Vanmaekelbergh, D.
ACS Nano **8**, 10486–10495 (2014)

8. **Long-range orientation and atomic attachment of nanocrystals in 2D honeycomb superlattices**
Boneschanscher, M., Evers, W.H., Geuchies, J.J., Altantzis, T., Goris, B., Rabouw, F.T., Van Rossum, S.A.P., Van der Zant, H.S.J., Siebbeles, L.D.A., Van Tendeloo, G., Swart, I., Hilhorst, J., Petukhov, A.V., Bals, S. & Vanmaekelbergh, D.
Science **244**, 1377–1380 (2014)

7. **Photonic effects on the Förster resonance energy transfer efficiency**
Rabouw, F.T., Den Hartog, S.A., Senden, T. & Meijerink, A.
Nat. Commun. **5**, 3601 (2014)

6. **On the efficient luminescence of β-$Na(La_{1-x}Pr_x)F_4$**
Herden, B., Meijerink, A., Rabouw, F.T., Haase, M. & Jüstel, T.
J. Lumin. **146**, 302–306 (2014)

2013

5. **Reduced Auger recombination in single CdSe/CdS nanorods by one-dimensional electron delocalization**
Rabouw, F.T., Lunnemann, P., Van Dijk-Moes, R.J.A., Frimmer, M., Pietra, F., Koenderink, A.F. & Vanmaekelbergh, D.
Nano Lett. **13**, 4884–4892 (2013)

4. **Calibrating and controlling the quantum efficiency distribution of inhomogeneously broadened quantum rods by using a mirror ball**
Lunnemann, P., Rabouw, F.T., Van Dijk-Moes, R.J.A., Pietra, F., Vanmaekelbergh, D. & Koenderink, A.F.
ACS Nano **7**, 5984–5992 (2013)

3. **Nanoscale lithographic positioning of fluorescing quantum dot nanocrystals on planar samples**
Rabouw, F.T., Frimmer, M., Mohtashami, A. & Koenderink, A.F.
Opt. Mater. **35**, 1342–1347 (2013)

2012

2. **Semiconductor nanorod self-assembly at the liquid/air interface studied by in situ GISAXS and ex situ TEM**
Pietra, F., Rabouw, F.T., Evers, W.H., Byelov, D.V., Petukhov, A.V., De Mello Donegá, C. & Vanmaekelbergh, D.
Nano Lett. **12**, 5515–5523 (2012)

1. **Single-source precursor synthesis of colloidal CaS and SrS nanocrystals**
Zhao, Y., Rabouw, F.T., De Mello Donegá, C., Meijerink, A. & Van Walree, C.A.
Mater. Lett. **80**, 75–77 (2012)

List of presentations

2015

Sep 2015 **Delayed exciton emission and its relation to blinking in CdSe quantum dots** (oral)
at the Nanogé conference FQDots15 in Santiago de Compostela, Spain

Sep 2015 **Multi-photon quantum cutting in $Gd_2O_2S:Tm^{3+}$** (oral)
at the International Conference on Optical Materials in Budva, Montenegro

July 2015 **Excited state dynamics of luminescent nanoparticles dispersed in a solvent** (oral)
in the group of Prof. David Norris at ETH Zürich, Switzerland

June 2015 **Delayed emission following charge carrier storage in spherical quantum dots and nanoplatelets** (oral)
in the group of Prof. Benoît Dubertret at ESPCI, Paris, France

2014

July 2014 **Photonic effects on the Förster resonance energy transfer efficiency in doped nanocrystals** (oral)
at the International Conference on Luminescence in Wrocław, Poland

May 2014 **Decay dynamics and energy transfer in co-doped nanocrystals** (poster)
at the 30 Years of Quantum Dots conference in Paris, France
prize for best poster, awarded by Nature Nanotechnology (1-year subscription)

May 2014 **Reduced Auger recombination in single CdSe/CdS nanorods** (poster)
at the 30 Years of Quantum Dots conference in Paris, France

May 2014 **Photonic effects on the Förster resonance energy transfer efficiency in doped nanocrystals** (oral)
at the Nanax6 conference in Bad Hofgastein, Austria

Mar 2014 **Colloidal nanorods with reduced Auger recombination** (oral)
Debye Lunch Lecture at Utrecht University, The Netherlands

Jan 2014 **Colloidal nanorods with reduced Auger recombination** (oral)
at the FOM@Physics conference in Veldhoven, The Netherlands

2013

Nov 2013 **Excited state dynamics in $LaPO_4$ nanocrystals: the local density of optical states** (oral)
at the Max Planck Institute for Chemical Energy Conversion, Mülheim an der Ruhr, Germany

June 2013 **Colloidal nanorods: single emitter spectroscopy** (oral)
at the workshop on Micro- and Nano-Scale Quantum Optics in Eindhoven, The Netherlands

Mar 2013 **Reduced Auger recombination in single CdSe/CdS nanorods by one-dimensional electron delocalization** (oral)
at the Nanogé conference on Single Quantum Dots in Mallorca, Spain
prize for best oral presentation, awarded by Europhysics Letters (€ 300)

Feb 2013 **Luminescence of lanthanide doped nanocrystals: local field effects** (poster)
at the NWO Chemistry meeting in Veldhoven, The Netherlands

2012

Nov 2012 **Single nanorod spectroscopy: intensity, lifetime, and wavelength blinking** (oral)
in the group of Prof. Manfred Bayer at the Technical University Dortmund, Germany

2011

Mar 2011 **Lanthanide doped CaS nanocrystals: towards single ion luminescence** (poster)
at the PAC symposium in Utrecht, The Netherlands
prize for second best poster, awarded by the Royal Netherlands Chemical Society (€ 250)

CHAPTER 1

Introduction

ABSTRACT • Our everyday lives rely heavily on artificial light sources. Life can continue after sun-down only because our environment is lit by billions of fluorescent lamps and light emitting diodes (LEDs), while even during day times we communicate with each other via the LED screens of our electronic devices. At the same time, harvesting the natural light from the sun becomes increasingly important to meet the global energy demand in the future. There is an ongoing search for materials to efficiently generate artifical light, or to efficiently harvest the energy of natural light from the sun. In this thesis we contribute to this search. We devote particular attention to luminescent nanomaterials. As light sources or light absorbers, nanomaterials can have advantages over macroscopic materials in terms of cheaper and easier production, more tunability, and the possibility to form transparent dispersions. In addition, nanoscale luminescent materials are promising for applications such as tracking biomolecules in medical imaging.

1.1 • The basics and applications of luminescent materials

Light from the sun contains many different colors. Most of the solar power is contained in the visible part of the electromagnetic spectrum, i.e. in the form of red, orange, yellow, green, blue, or purple light. The majority of the materials on earth, namely all but those completely white, absorb at least some of the visible light. However, the absorbed energy of the light is lost as heat in most cases, and cannot be used to generate other useful types of energy such as electricity. Moreover, most materials do not emit visible light (except for thermal radiation which contains a significant visible component only above temperatures of ~600°C).

Special types of materials are needed to efficiently generate artificial light, or to efficiently harvest the energy of natural light from the sun. Typically, such materials have an energy gap, i.e. a range of energies that the electrons in the material cannot possibly attain, between the electronic ground state and electronic excited states (Fig. 1.1a) with a width comparable to the energy of a photon of visible light. The material is excited over the energy gap for example by absorption of light, or by charge injection. It can then relax to a lower-energy state by the emission of a photon (yielding artificial light; Fig 1.1b) or by ejecting charge carriers (yielding electricity, or promoting chemical reactions; Fig. 1.1c).

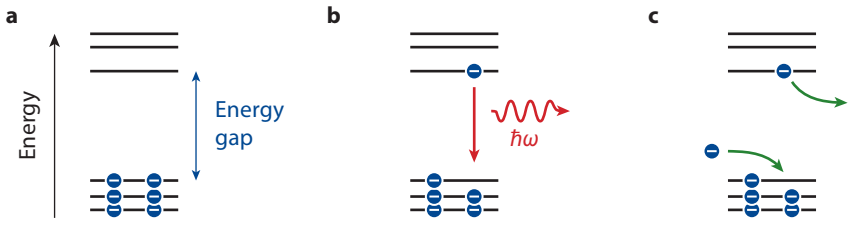

Figure 1.1 • The electronic structure of luminescent materials. (**a**) The electronic structure of luminescent materials is often described as a set of "orbitals", the allowed states of the electrons in the material, depicted by the horizontal lines. The material is the lowest-energy electronic state (i.e. the ground state) if the electrons are in the lowest possible configuration with at most two electrons per orbital. (**b**,**c**) The material is in an excited state if one (or more) of the electrons occupy a higher-energy orbital. This material can relax to the ground state (**b**) under the emission of a photon carrying the excess energy, or (**c**) by ejecting the excited electron and restoring charge neutrality via an external circuit.

In this thesis we investigate two types of luminescent materials. The first are colloidal nanocrystals of semiconductor material, also known as colloidal quantum dots (QDs; Chs. 3,4,8). What makes QDs special, is that the electronic structure and therefore the optical properties do not only depend on the chemical composition, but also on the size and shape (see also Fig. 2.1).[151] The emission of QDs can be tuned to any wavelength over a very wide range from the mid-infrared to the ultraviolet, for example with different sizes of the II-IV chalcogenides of Hg (mid-infrared),[209] Pb (near-infrared),[179] Cd (visible),[18] and Zn (blue and ultraviolet).[63] In addition to II-IV QDs, there are other types such as III-V QDs (e.g. InP)[91] and ternary QDs (e.g. $CuInS_2$).[196,246] QDs are typically synthesized using wet chemical techniques, from an organic solution containing cation and anion precursor molecules.[18] The size and shape of the nanocrystals formed are determined by for example the reaction temperature, affecting the nucleation and growth rates of QDs, or by the presence of organic surfactant molecules.

The second type of luminescent materials investigated in this thesis are insulator (nano)crystals doped with lanthanide ions. Owing to the chemical similarity of the luminescent lanthanide ions with other non-luminescent rare earth elements like Y or La, (nano)crystals with a wide range of doping concentrations can rather easily be synthesized, for example by co-precipitation.[19,54] Absorption and emission of infrared, visible, and ultraviolet light is due to transitions between electronic states localized on the lanthanide dopants. Each of the lanthanide elements support their own characteristic transitions. When different types of lanthanides are combined (i.e. co-doped) in the same crystal, there is a variety of energy transfer processes possible (see Chs. 5–7).

Fig. 1.2 shows a simple schematic of the concepts used in lighting or lasers (Fig. 1.2a), and photovoltaics (Fig. 1.2b). Nanocrystal QDs are potentially useful in all roles in the schematics. They can be the active electroluminescent material in LEDs,[218] a phosphor material to optimize the color output of a LED[127] or to concentrate sunlight onto a solar cell in luminescent solar concentrators,[233] or the gain material in a QD laser.[230] They can even be the active absorber material in solar cells.[185] Furthermore, they can be used as biolabels owing to the small size and tunable surface chemistry. Important challenges in the research field of QDs are for example (1) to gain more control over the large-scale structures formed when QDs are assembled for device appli-

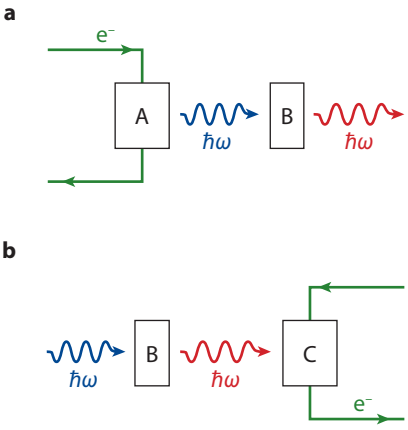

Figure 1.2 • Conversion of light to electricity and vice versa. (**a**) The concept typically used in artificial lighting: an electroluminescent material (A) directly and efficiently converts electricity (green) to light (blue arrow). An optional phosphor (B) then absorbs this light (partially) and converts it to another color, to achieve the desired color output (red arrow). The same concept can be used to achieve lasing, under strong excitation and with optical feedback. (**b**) The reverse concept usable to generate electricity from light. A photovoltaic material (C) can convert light into electricity. An optional phosphor material (B) is placed in front to first (partially) absorb the incident light and emit it as another color. This phosphor layer can be useful to redirect and concentrate the light, or to reduce the spectral mismatch with the band gap of the photovoltaic material (see Ch. 5).

cations,[182,225,238] and (2) to improve the efficiency and stability of QDs, especially under strong excitation when Auger processes lead to non-radiative losses (see Chs. 2–4,8).

Luminescent lanthanide ions doped in insulator crystals find extensive use as phosphor or laser gain materials (B in Fig. 1.2).[5] Because of the wide variety of energies of electronic transitions, and the possibility to co-dope different types of lanthanides into the same crystal, lanthanide-doped crystals are excellent spectral converters.[205] They are currently used in virtually all fluorescent lamps, converting ultraviolet from the mercury discharge into visible light. A new challenge is to optimize the conversion of the blue light from the InGaN LED to a desirable warm color of white.[67] Particularly interesting is the possibility of upconversion (converting two low-energy photons into one higher-energy photon) and downconversion (converting one high-energy photons into two lower-energy photon; Chs. 5,6) processes due to energy transfer between lanthanide ions.[205] These processes have the potential to reduce spectral mismatch losses in solar cells. In addition, upconversion nanocrystals are promising for low-background bio-imaging.[224]

1.2 • Outline of this thesis

This thesis is organized as follows:

Chapter 2 provides a theoretical background, and introduces the most important concepts and terminology needed to understand the rest of the thesis. There is a description of the electronic structure of colloidal QDs and lanthanide ions. There is also an overview of the decay processes occurring in luminescent materials, the processes that take place when the material is excited.

In Chapter 3 we investigate luminescent nanorods with a spherical CdSe core and a rod-shaped CdS shell. We perform experiments on single nanorods under strong excitation. Intermittent charging leads to blinking, i.e. periods when the decay accelerates and the luminescence is partially quenched because of Auger processes, while at the same time the emission spectrum is different.

Chapter 4 discusses nonradiative Auger(-like) processes in CdSe/CdS core–shell QDs. Auger recombination of the biexciton state is slower in QDs with a thicker shell. Cooling of the electron from the excited P-state to the lowest S-state, which is also believed to be an Auger process, is however unaffected by shell growth. We compare the results to theoretical calculations, and discuss the factors governing the rates of the two types of Auger processes.

Chapter 5 introduces Gd_2O_2S doped with Tm^{3+} as a new downconversion material that, depending on the excitation wavelength, can emit up to four photons per absorption event. We identify the energy transfer processes between Tm^{3+} ions that cut the energy of the absorbed photon into up to four smaller quanta, and quantify the rates and efficiencies as a function of Tm^{3+} concentration.

Chapter 6 explains how in downconversion crystals doped with lanthanide ions, measurements of the excited state dynamics can be used to determine and quantify the energy transfer processes. We introduce a simple analytical model for the energy transfer dynamics in doped crystals, and compare it to Monte Carlo simulations.

In Chapter 7 we measure the effect of the photonic environment on the excited state dynamics of $LaPO_4$ nanocrystals doped with Ce^{3+} and Tb^{3+}. The local density of optical states experienced by the lanthanides changes when the nanocrystals are dispersed in a medium with different refractive index. This affects the radiative decay rates, the efficiency of energy transfer from Ce^{3+} to Tb^{3+} within the nanocrystal, and the photoluminescence quantum efficiency of Tb^{3+}.

In Chapter 8 we focus on the delayed emission on the timescale of microseconds from core–shell QDs with a CdSe core. We combine single-QD and ensemble measurements, and investigate the effect of the photonic environment. A new model is developed to explain the connection between delayed emission and blinking.

In Chapter 9 we give a short summary of the main results of this thesis. An outlook is given on possible future research directions and applications, including some preliminary results.

CHAPTER 2

Theoretical background

With contributions based on

Calibrating and controlling the quantum efficiency distribution of inhomogeneously broadened quantum rods by using a mirror ball
Lunnemann, P., Rabouw, F.T., Van Dijk-Moes, R.J.A., Pietra, F., Vanmaekelbergh, D. & Koenderink, A.F.
ACS Nano **7**, 5984–5992 (2013)

Resolving the ambiguity in the relation between Stokes shift and Huang-Rhys parameter
De Jong, M., Seijo, L., Meijerink, A. & Rabouw, F.T.
Phys. Chem. Chem. Phys. **17**, 16959–16969 (2015)

ABSTRACT • Photoluminescence (PL) is the emission of light by a luminescent species (or: emitter), following absorption of light. The PL investigated in this thesis originates from two types of emitters: colloidal semiconductor nanocrystals, and lanthanide ions. This chapter introduces the optical and electronic properties of these emitters, and the terminology used in later chapters. In particular, we discuss the process of photo-emission and a variety of other pathways through which a photoexcited emitter can decay back to its ground state.

2.1 • Colloidal quantum dots

Colloidal quantum dots (QDs) are nanocrystals (NCs) of semiconductor material which are so small that the optical and electronic properties are size and shape dependent. The dependence is due to *quantum confinement effects*: electronic wavefunctions are confined to smaller volumes than they would occupy in the bulk material. One of the most notable consequences of quantum confinement in colloidal QDs is visible in Fig. 2.1. It shows the tunability of the photoluminescence (PL) emission wavelength across the visible spectrum, by changing the diameter of colloidal CdSe QDs from 2 nm (left; blue) to 6 nm (right; red). This tunability, as well as good photostability, cheap wet-chemical synthesis procedures, and large excitation cross-sections, make colloidal QDs promising for many applications.

In the following explanation of quantum confinement of the electronic states in a QD, we specifically discuss QDs of CdSe (being the most studied colloidal QD material). However, very similar reasonings are valid for QDs of other II-VI or III-V direct band gap semiconductors.

The particle-in-a-box model for one-particle states. Because of quantum confinement the electronic states in a QD are different from the corresponding bulk crystal. Indeed, while bulk CdSe would emit near-infrared light, QDs of CdSe emit at visible wavelengths (Fig. 2.1). An intuitive model to understand this difference as well as the effect of the QD size (Fig. 2.1) is the *effective mass approximation* (EMA).

The EMA starts from the electronic band structure of the bulk crystal, presented in Fig. 2.2 for CdSe. Near the band gap, CdSe has one conduction band (CB) and three valence bands (VBs), which arise from Cd 5s and Se 4p atomic orbitals, respectively. Every point on the lines (i.e. the bands) in a band structure diagram as Fig. 2.2 is a single-particle state, which has a well-defined energy and wavevector. These states extend over the whole volume of the bulk crystal, which is (modeled as) infinitely large. Obviously, such infinitely extended states cannot exist in a NC because electrons are confined to a small volume. In its simplest form, the EMA treats the effect of

Figure 2.1 • The effect of quantum confinement on the photoluminescence of CdSe quantum dots. The vials contain colloidal dispersions of CdSe QDs with diameters ranging from 2 nm on the left to 6 nm on the right. Upon UV illumination the emission wavelength of the QDs strongly depends on their size. The colors emitted range from blue (480 nm) for the smallest QDs to red (630 nm) for the largest QDs. Photograph taken by Mark Vis.

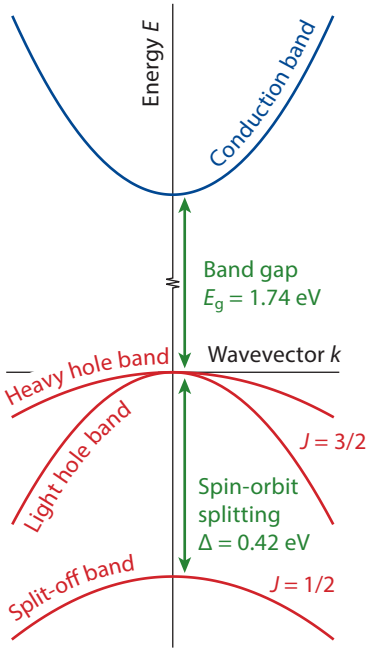

Figure 2.2 • The electronic band structure of bulk CdSe near the band gap. CdSe is a direct band gap semiconductor with a band gap at the Γ point (k = 0) of E_g = 1.74 eV. There is a single conduction band at high energy with Cd 5s character and with an effective mass of $m_e = 0.11m_0$. The structure of the valence band at low energy is more complex, because it arises from three sets of Se 4p atomic orbitals. Spin–orbit coupling splits the valence band into three subbands. In order of increasingly negative energy these are the heavy hole band (hh; total angular momentum J = 3/2; projection $J_z = \pm 3/2$), the light hole band (lh; J = 3/2; $J_z = \pm 1/2$), and the split-off band (so; J = 1/2). Alternatively, the hh, lh, and so bands are sometimes labeled the A, B, and C subbands. The effective masses are $m_{hh} = 1.14m_0$, $m_{lh} = 0.31m_0$, and $m_{so} = 0.49m_0$, respectively.[28] The splitting between hh and lh bands at high energy, and the so band at lower energy is Δ = 0.42 eV in CdSe. The heavy and light hole bands are nearly degenerate at the Γ point in zinc blende (cubic) CdSe, whereas in wurtzite (hexagonal) CdSe there is a small crystal field splitting of Δ_{cr} = 25 meV.

quantum confinement on each electronic band individually. More sophisticated theories include the effect of band mixing due to spatial confinement, resulting in quantum confined electronic states that contain contributions from several bands.[38]

The single-particle states in a NC can be written as

$$\psi(\mathbf{r}) = \phi(\mathbf{r})u(\mathbf{r}). \tag{2.1}$$

Here $u(\mathbf{r})$ is a function with the periodicity of the crystal lattice (e.g. a regular lattice of 5s-like atomic orbitals for the CB states). $\phi(\mathbf{r})$ is an envelope function which describes the contribution of atomic orbitals centered on atoms at different locations in the crystal. The envelope function has the form of a plane wave [$\phi(\mathbf{r}) = e^{i\mathbf{k}\cdot\mathbf{r}}$] for an infinitely extended Bloch wavefunction in a bulk crystal. In case of a NC, on the other hand, it describes the finite extension (by having zero amplitude outside the NC) and the symmetry (s, p, etc.) of the electronic states.

The EMA assumes that the electronic bands are isotropic, and parabolic. This ensures that a single parameter, namely the effective mass, describes how high-wavevector components in the envelope function contribute to the kinetic energy of a state. Calculation of the (confinement) energies E and wavefunctions in a NC then reduces to solving a simple particle-in-a-box problem *for the envelope function*:[28,61]

$$\left[\frac{-\hbar^2}{2m^*}\nabla^2 + V(\mathbf{r})\right]\phi(\mathbf{r}) = E\phi(\mathbf{r}), \tag{2.2}$$

where m^* is the effective mass of the band under consideration. The potential energy term $V(\mathbf{r})$ describes the physical size and shape of the QD. In the most simple case of a spherical QD and assuming infinite potential barriers to the outside one can write:

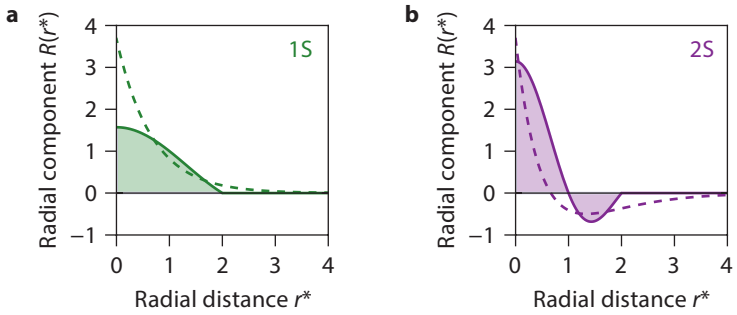

Figure 2.3 • The envelope wavefunctions of electronic states in a spherical quantum dot. We compare the radial component of (**a**) the 1S, and (**b**) 2S envelope wavefunctions of a spherical QD (solid lines) to the corresponding hydrogen orbitals (dashed lines). For a fair comparison we normalize the radial coordinate for the two systems to its expectation value $\langle r \rangle$ in the 1S state. $\langle r \rangle = \frac{1}{2}a$ for the spherical QD, so that the surface of the QD lies at $r^* = 2$. $\langle r \rangle = \frac{3}{2}a_0$ (a_0 = Bohr radius) for the hydrogen atom. The qualitative difference between the plots arises because in a hydrogen atom the spherically symmetric potential $V(r)$ is due to a point charge at $r = 0$, while in a QD there is a particle-in-a-box potential with an abrupt step at $r = a$.

$$V(r) = \begin{cases} 0 & ; \quad r \leq a \\ \infty & ; \quad r > a \end{cases}, \tag{2.3}$$

where a is the radius of the QD. Alternatively, $V(\mathbf{r})$ can describe more complex geometries such as non-spherical or core–shell QDs. Any composition and shape (e.g. the heteronanorods of Ch. 3) can be accounted for by taking the appropriate position dependent potential energy $V(\mathbf{r})$ and effective mass $m^*(\mathbf{r})$.

For a spherical QD (Eq. 2.3) the electronic states (i.e. the solutions to Eq. 2.2) are very similar to those of the hydrogen atom: discrete energies, and eigenfunctions with s, p, d, ... symmetries. Consequently, colloidal QDs are sometimes referred to as *artificial atoms*. Different from the hydrogen atom, however, the azimuthal quantum number l is not restricted, so that states such as 1P and 1D do exist in a QD.† The energies are

$$E_{nl} = \frac{\hbar^2 \chi_{nl}^2}{2m^* a^2}, \tag{2.4}$$

with n the principal quantum number, and χ_{nl} the nth root of the spherical Bessel function $j_l(x)$.‡

As for the hydrogen wavefunctions, the envelope functions in a QD can be separated into a radial and an angular part:

$$\phi(\mathbf{r}) = R_{nl}(r) Y_l^m(\theta, \varphi). \tag{2.5}$$

$Y_l^m(\theta, \phi)$ are spherical harmonics, identical to those encountered in the hydrogen atom. They determine the symmetry of the wavefunction, e.g. s-symmetry for $l = 0$, p-symmetry for $l = 1$, etc. The radial components

$$R_{nl}(r) = N j_l(\chi_{nl} r/a), \tag{2.6}$$

† The electronic states in a QD are commonly labeled with capital letters for the symmetry, although they are single-particle states.

‡ Some relevant values of χ_{nl} are $\chi_{ns} = n\pi$, $\chi_{1p} = 4.493$, and $\chi_{1d} = 5.763$.

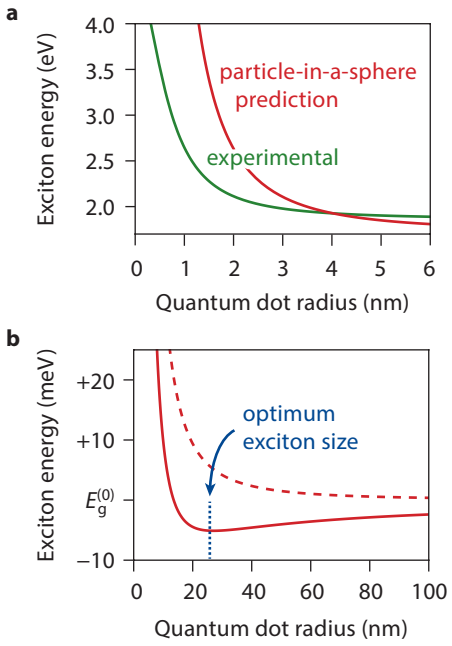

Figure 2.4 • The energy of the first exciton state as a function of the CdSe quantum dot size. (**a**) In the strong quantum confinement regime (i.e. small QD sizes) the particle-in-a-sphere model (red line) predicts significantly stronger quantum confinement than observed experimentally (green line). For the theoretical curve we use $E_g^{(0)} = 1.74$ eV and $\varepsilon = 9.3$. The experimental curve is a trend line through data points as given in Ref. 106. (**b**) We can extrapolate the theoretical exciton energy to large QDs of up to 100 nm radius (solid line; neglecting Coulomb attraction yields the dashed line). A minimum in the exciton energy appears for a QD radius of 27 nm. This reflects the presence of a finite natural exciton size, set by the balance between Coulomb energy (scaling as $1/a$) and confinement energy (scaling as $1/a^2$). In QDs of a few nm radius the exciton is squeezed into a smaller volume than this natural size, resulting in an increased energy. Despite the simplications of the model and the assumption of strong confinement, this approach gives a reasonable estimate of the exciton Bohr radius of $a_X = 5$ nm, and the exciton binding energy of 15 meV in bulk CdSe.

with N a normalization constant, are different from those of hydrogen orbitals. The difference is illustrated in Fig. 2.3, showing the radial components of the 1S and 2S envelope functions in a spherical QD, as well as the corresponding hydrogen orbitals.

Exciton states. Throughout this thesis the main characterization technique will be optical spectroscopy. Hence, we are mainly interested in the properties of *excitons*, i.e. electron–hole pairs which are created (annihilated) when the QD absorbs (emits) light. The simplest approach to determine exciton energies and wavefunctions is to assume *strong confinement*, i.e. by treating electron–hole interactions as a small perturbation to the confinement imposed by the finite NC size.

The exciton wavefunction can then be written as the product of electron and hole single-particle states as calculated above:

$$\Psi_X(\mathbf{r}_e, \mathbf{r}_h) = \psi_e(\mathbf{r}_e)\psi_h(\mathbf{r}_h) \tag{2.7}$$

while electron–hole Coulomb interaction is accounted for as a first order energy correction to the exciton energy. The resulting expression for the exciton energy is the sum of the bulk band gap energy, the (single-particle) confinement energies of electron and hole, and the electron–hole Coulomb interaction. For the lowest-energy exciton, with both electron and hole in a 1S particle-in-a-sphere state the energy is

$$E_X(a) = E_g^{(0)} + \frac{\hbar^2\pi^2}{2m_e^* a^2} + \frac{\hbar^2\pi^2}{2m_h^* a^2} - 1.79\frac{e^2}{4\pi\varepsilon\varepsilon_0 a}\,, \tag{2.8}$$

where $E_g^{(0)}$ and ε are the bulk band gap and the bulk static dielectric constant of the QD material. The number 1.79 results from an integration of the Coulomb interaction over the position of electron and hole as given by the 1S single-particle envelope functions (Eq. 2.5). Eq. 2.8 could be extended with terms describing (Coulomb) charging energies due to the dielectric mismatch

between QD and environment. In practice, these terms can be neglected because the interaction of the carriers with their own image is cancelled by the interaction with the image of the other carrier.[39]

In Fig. 2.4a we compare the theoretical exciton energy from the particle-in-a-sphere model (Eq. 2.8) to the experimental exciton energies[106] (which give rise to the many different emission colors of Fig. 2.1). We see that the simple EMA gives a reasonable qualitative picture of quantum confinement, although it overestimates the confinement energy.

In Fig. 2.4b we plot the theoretical exciton energy for QD sizes of up to 100 nm, although the assumption of strong confinement is no longer valid for such large QDs (moreover, high-quality QDs in this size range are not available experimentally). This plot is insightful since it explains the existence of a finite exciton Bohr radius a_X: the balance between Coulomb attraction and confinement energy results in an optimum electron–hole separation. This is an estimate for the exciton Bohr radius a_X, i.e. the finite separation that electron and hole would naturally assume in a bulk crystal. For large NCs ($a \gg a_X$) there are no quantum confinement effects, since the exciton assumes its optimum size and lowest-energy state irrespective of the exact crystal size. For small NCs ($a < a_X$), on the other hand, the finite crystal size determines the extension and energy of excitons, hence the pronounced quantum confinement effects.

Beyond the particle-in-a-box model. Although the single-band EMA provides an insightful qual-

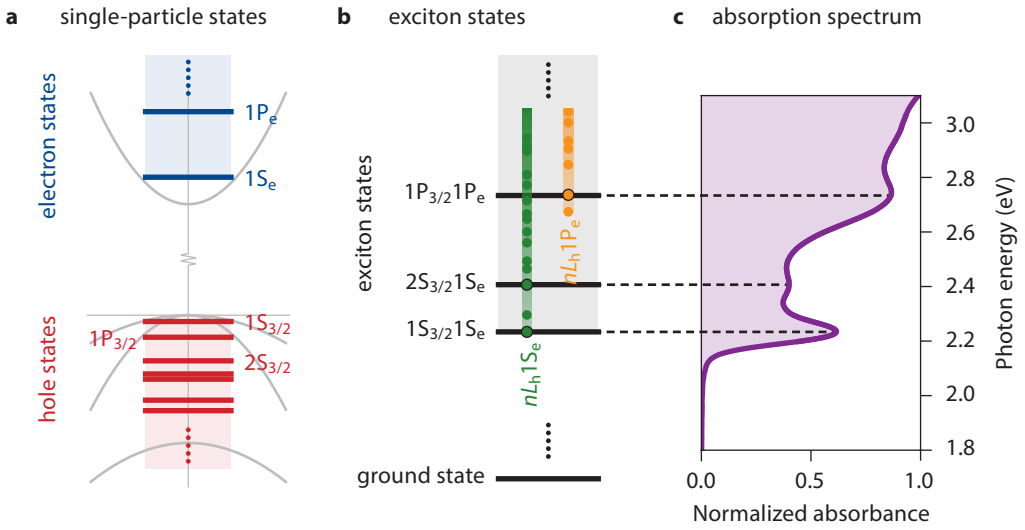

Figure 2.5 • Assignment of the absorption spectrum of spherical quantum dots. (**a**) Single-particle states in a spherical CdSe QD near the band gap show a higher density of hole states than electron states. The difference arises because hole states originate from three nearly degenerate VBs, and because the CB has a low effective mass resulting in high electron confinement energies. (**b**) In the strong confinement limit, exciton states can be described as a combination of electron and hole single-particle states. (**c**) The absorption spectrum of a QD shows the energies of transitions between the ground state and the different exciton states. The three distinct peaks in the absorption spectrum (indicated by dashed lines) can be assigned, in order of increasing energy, to transitions to the $1S_{3/2}1S_e$, $2S_{3/2}1S_e$, and $1P_{3/2}1P_e$ exciton states. There are more exciton states in the QD which, however, do not appear (distinctly) in the absorption spectrum because of optical selection rules.

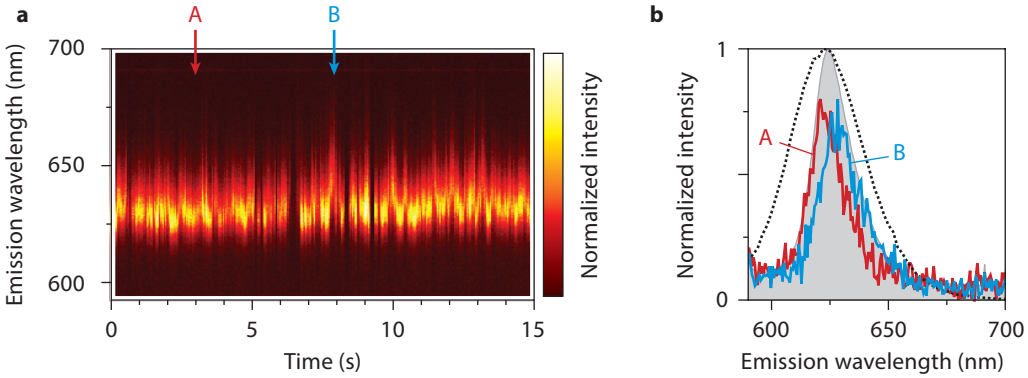

Figure 2.6 • Spectral diffusion in the emission from a single quantum dot. (**a**) The room-temperature emission from a single CdSe/CdS/CdZnS/ZnS QD fluctuates in time, and sometimes completely turns off. Even when the QD is bright, the spectrum is not constant but shifts back and forth over a few nm seemingly randomly. Integration time per spectrum = 50 ms. (**b**) The emission spectrum of this QD integrated over 25 s (gray area) is roughly twice narrower than the ensemble emission spectrum (dashed black line) of the batch. Spectra A (red) and B (blue) are "instantaneous" emission spectra from the trace in **a** (highlighted by arrows), integrated over 50 ms. These are again narrower than the time-averaged spectrum. The core–multi-shell QDs were synthesized by Relinde van Dijk-Moes.

itative description of the quantum confinement effect (see above), more sophisticated models have been developed to explain experimental results in greater detail. Depending on the level of detail desired different models can be used.[30,61]

An important early work is by Norris and Bawendi,[28] who assigned the absorption spectrum of CdSe QDs. Like in the simple particle-in-a-box-model, they start from the bulk band structure (Fig. 2.2) to calculate CB (electron) and VB (hole) states independently. However, they go beyond the particle-in-a-box-model by considering coupling between the three VBs. This results in complicated hole states containing contributions from all three VBs. The states are labeled as nL_M, with M the total angular momentum, L the lowest envelope angular momentum contained, and n an index. Fig. 2.5 shows how transitions appearing in the absorption spectrum of a CdSe QD are commonly labeled following this formalism.

Whatever theoretical model is used to explain or predict the electronic structure of QDs (e.g. the EMA, multi-band models[38] such as the one of Norris and Bawendi,[28] or atomistic models such as tight binding[61]), difficulties arise because in practice the exact atomic structure of a QD is not known and cannot be precisely controlled. Unless in the extremely small size limit of magic size clusters,[177] a batch of nominally identical QDs exhibits wide variations in atomic composition. QDs vary in size, surface termination, ligand coverage, crystal strain and defects, etc. Fig. 2.6 illustrates that as a result, the emission spectrum of a batch of nominally identical QDs is inhomogeneously broadened (Fig. 2.6b). Perhaps more surprisingly, even the emission from a single QD varies on the time scale of milliseconds (Fig. 2.6a). This effect is called *spectral diffusion*, and believed to be caused by small and slow fluctuations in the structure and surroundings of the QD, for example a reorganization of (charged) surface ligands.

2.2 • Lanthanide ions

Lanthanides are the elements with atomic numbers 57 through 71, usually displayed as a separate row at the bottom of the periodic table. The most common oxidation state of lanthanides is 3+. As a trivalent cation the lanthanides have the electronic configuration $[Ln^{3+}] = [Xe]\ 4f^n$, where n increases across the series from 0 for La^{3+} to 14 for Lu^{3+}. Many lanthanides can absorb and emit photons in the UV, visible and/or NIR part of the spectrum. The transitions involved are usually intraconfigurational f-f transitions, i.e. the electrons redistribute themselves over the 4f-orbitals while the configuration $4f^n$ remains the same. In addition, some lanthanide ions exhibit f–d transitions in the visible or UV part of the spectrum. These are transitions from the $4f^n$ ground state to a $4f^{n-1}5d^1$ excited state (or vice versa).

The trivalent ions from the lanthanide series, as well as those of the other 'rare earth' elements Sc and Y, are chemically very similar. As a result, natural rare earth ores always contain mixtures of many rare earth elements, and are hard to purify. A convenient consequence of the chemical similarity is that rare earth doped crystalline materials can relatively easily be tuned to any desired chemical composition. Usually, phosphor and laser materials based on lanthanide luminescence consist of a host crystal with non-luminescent rare earth ions such as Y^{3+} (e.g. YAG: $Y_3Al_5O_{12}$) or La^{3+} (e.g. $LaPO_4$), with a few percent of the cation sites substituted with luminescent dopants such as Nd^{3+} or Tb^{3+}.

The effect of the host material. The f–f transitions in lanthanide ions are special because the host material in which the ion is embedded, affects the energies only weakly. The 4f-orbitals are 'shielded' from influences of the environment by electrons in the more extended 5s- and 5p-orbitals. Owing to this shielding effect it has been possible to construct the Dieke diagram (see Fig. 2.8) of the $4f^n$ energy levels in lanthanide ions. This diagram is accurate irrespective of the host material in which the ions are embedded, and therefore very valuable for understanding and predicting the optical properties of lanthanide doped materials. Depending on the host material the energies of the levels can shift slightly or split in the crystal field, to a small extent typically within the width of the horizontal bars in the Dieke diagram.

The energies of f–d transitions, on the other hand, depend strongly on the host material because 5d-orbitals are much more extended than 4f-orbitals. For example, in Ce^{3+} the expectation values for the radial distance from the nucleus are $\langle r \rangle = 0.540$ Å for a 4f-electron and $\langle r \rangle = 1.199$ Å for a 5d-electron.[75] The energy of the $4f^{n-1}5d^1$ excited state is therefore affected by the host material, in two ways. First, the 5d energy is lowered with respect to the lanthanide ion in vacuum by (partial) chemical binding to orbitals on the ligands surrounding the ion: the *nephelauxetic effect*. Second, a crystal field can lift the degeneracy of the 5d-orbitals, and split the $4f^{n-1}5d^1$ state into several crystal field components. The resulting energy of the lowest-energy f–d transition can, depending on the host material, be up to 34000 cm^{-1} (= 4.2 eV) lower than in the free ion.[37] Of the trivalent lanthanides, only Ce^{3+} can (depending on the host material) have its lowest-energy f–d transition in the visible while for other Ln^{3+} ions it always lies in the UV.[37]

The presence of a host material further enables that transitions on luminescent centers couple to vibrations. The result is that absorption and emission bands broaden, and that a *Stokes shift* appears (i.e. the maxima of absorption and emission bands are separated). Also in terms of the extent of vibrational coupling, f–f transition and f–d transitions are very different.

The situation leading to vibrational coupling is illustrated in Fig. 2.7. A luminescent cation in a solid is surrounded by coordinating anions. There is an equilibrium geometry (Fig. 2.7b) in which the system is at its lowest possible energy. Deviations from this equilibrium towards either

shorter (Fig. 2.7a) or longer (Fig. 2.7c) bond lengths lead to a higher energy of the system. Because any deviation from the equilibrium increases the energy, the associated energy potential is in a first-order approximation harmonic (Fig. 2.7d). A quantum mechanical description of the energy potential of the central ion with surrounding ligands yields vibrational states with energy levels $\left(n + \frac{1}{2}\right)\hbar\omega$, where n is the vibrational quantum number, and $\hbar\omega$ the energy of the vibrational mode. Electronic transitions couple to vibrations because the nuclear coordinates do not change *during* an electronic transition, while the equilibrium geometry is different in the electronic excited state compared to the ground state. Fig. 2.7e shows how an electronic transition on the central ion can be accompanied by a change in the vibrational state, making a variety of combined electronic and vibrational (vibronic) transitions possible.

At cryogenic temperatures the resulting spectrum can exhibit fine structure consisting of lines corresponding to the different vibronic transitions. The line corresponding to the transition from vibrational level 0 to vibrational level 0 (red in Fig. 2.7e) is called the zero-phonon line, while the rest are phonon replicas. At increasing temperatures the lines broaden and start to overlap, until the fine structure disappears. The result is a broad absorption and a broad emission band. The energy separation between the maxima of the absorption and emission bands is called the *Stokes*

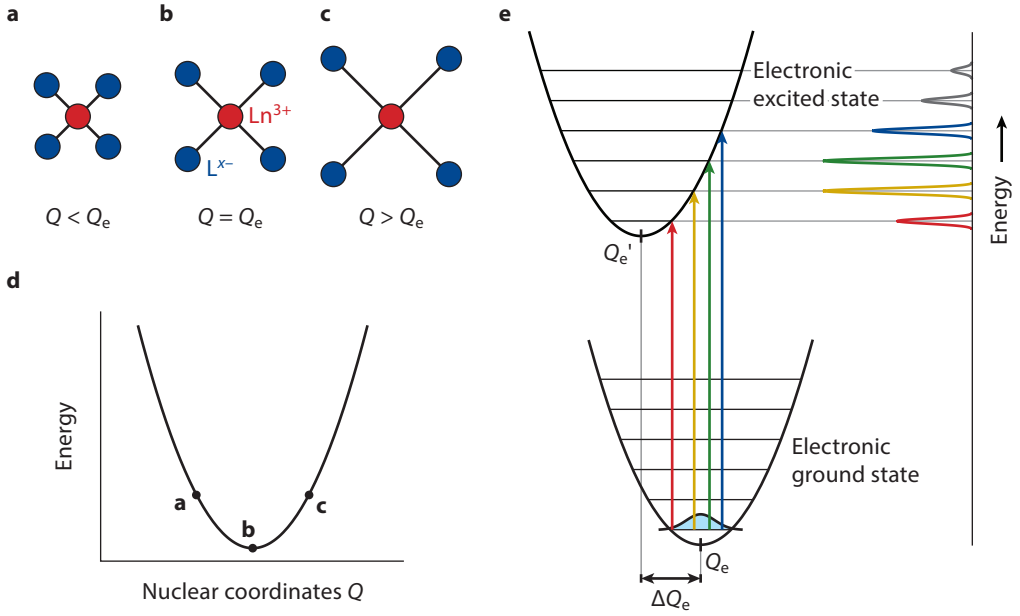

Figure 2.7 • Coupling of electronic transitions to vibrations. (**a**, **b**, **c**) We consider the breathing mode of a luminescent ion (red) symmetrically coordinated by anion ligands (blue). The potential energy is a function of the ion–ligand separation. (**d**) As a first-order approximation the energy of the vibration is harmonic, i.e. the energy is a function of the square of the deviation from the equilibrium distance at **b**. (**e**) A configuration coordinate diagram of an f–d transition. Indicated are the potential energy curves in the electronic ground and excited states, as well as the corresponding equilibrium geometries Q_e and Q_e'. Multiple transitions are possible in the absorption process (upward arrows) and the emission process (not shown), giving rise to a structured absorption (graph on the right) and emission (not shown) band at cryogenic temperature or broad bands at room temperature.

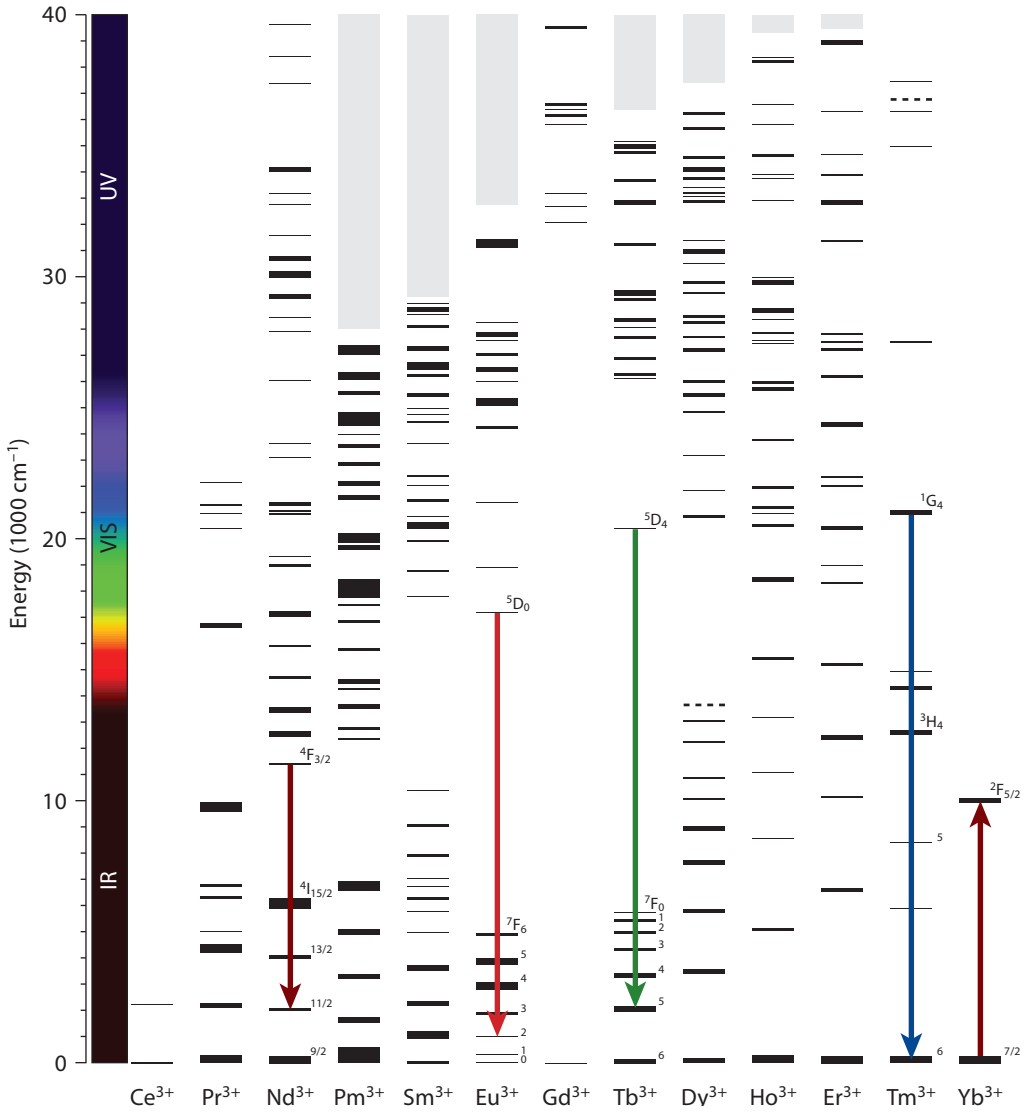

Figure 2.8 • The classic Dieke diagram of energy levels of the trivalent lanthanides. The energy levels of the $4f^n$ configuration of Ln^{3+} ions are depicted, with *n* increasing from left to right from 1 in Ce^{3+} to 13 in Yb^{3+}. The width of the horizontal lines represents the extent to which the corresponding level can be split in a crystal field. Gray areas contain energy levels which in the classic Dieke diagram are not depicted. Some examples of relevant transitions are highlighted. The $^4F_{3/2} \rightarrow {}^4I_{11/2}$ transition at 1064 nm (dark red downward arrow) is the lasing transition in the widely used YAG:Nd^{3+} laser. The red light from most fluorescent lamps originates from the $^5D_0 \rightarrow {}^7F_2$ transition in Y_2O_3:Eu^{3+} at 610 nm (red downward arrow). The $^5D_4 \rightarrow {}^7F_5$ transition of Tb^{3+} at 540 nm (green downward arrow) is the strongest emission of the green phosphor $LaPO_4$:Ce^{3+},Tb^{3+} commonly used in fluorescent lamps and examined in Ch. 7. The $^1G_4 \rightarrow {}^3H_6$ transition of Tm^{3+} at 480 nm (blue downward arrow) gives the blue upconversion emission of β-$NaYF_4$:Yb^{3+},Tm^{3+} upon pumping in the $^2F_{7/2} \rightarrow {}^2F_{5/2}$ transition of Yb^{3+} (980 nm; dark red upward arrow). Adapted from the work of Mathijs de Jong.

shift, resulting from the fact that phonon replicas in absorption and emission are at the high- and at the low-energy side of the zero-phonon line, respectively. The width of the bands and the magnitude of the Stokes shift depend on the displacement ΔQ_e (see Fig. 2.7e) between the equilibrium geometries of ground and excited state. The existence of such a displacement, in turn, is caused by the change in bonding between central ion and ligands upon the electronic transition.

As mentioned above, the 4f-orbitals of trivalent lanthanides are shielded from the environment by 5s- and 5p-electrons. As a result, intraconfigurational f–f transitions have hardly any influence on the strength of chemical bonding between the lanthanide ion and surrounding ligands. In other words, the displacement ΔQ_e is small, much smaller than depicted in the configuration coordinate diagram of Fig. 2.7e. Narrow absorption and emission lines and negligible Stokes shifts are therefore characteristics of f–f transitions. Note that the Stokes shift is a parameter defined as the distance between the maxima of absorption and emission for the *same* electronic transition. Despite the negligible Stokes shift of f–f transitions, photoluminescence from a lanthanide ion can be at much longer wavelength than the excitation if the absorbing and emitting transitions are different.

Typical f–d transitions, on the other hand, give rise to broad bands and exhibit a large Stokes shift. In the $4f^{n-1}5d^1$ excited state one electron occupies a 5d-orbital. The 5d-orbitals are extended and overlap with ligand orbitals (see above). Consequently, the chemical bonding between central ion and ligands changes upon the $4f^n \rightarrow 4f^{n-1}5d^1$ transition. In fact, the equilibrium distance between the Ln^{3+} ion and the ligands can become shorter,[52,75] as depicted in Fig. 2.7e. The large value for ΔQ_e results in broad bands and a large Stokes shift.

Energy levels within the $4f^n$ configuration. We have already introduced the Dieke diagram of the $4f^n$ energy levels of trivalent lanthanides. The diagram as depicted in Fig. 2.8 contains only the $4f^n$ states up to 30000–40000 cm^{-1} above the ground state. For most Ln^{3+} ions there are (many) more states at higher energies. The very highest state, a $^1S_0$ state in Tb^{3+}, is calculated to be at 193000 cm^{-1} (24 eV).[70] It is important to realize that the states depicted in the Dieke diagram are multi-electron states. As such, each of the energy levels corresponds to a complete configuration of the lanthanide ion. This is in contrast to molecular-orbital diagrams commonly used for e.g. organic molecules (see also Fig. 1.1), where the molecular orbitals are one-electron states of which several are simultaneously occupied by electrons.

There are in total 14 4f-orbitals, taking into account that each spatial orbital can be occupied by two electrons of opposite spin. For an ion with n 4f-electrons, there are $\binom{14}{n}$ ways in which they can be distributed over the available orbitals. To understand how these different distributions lead

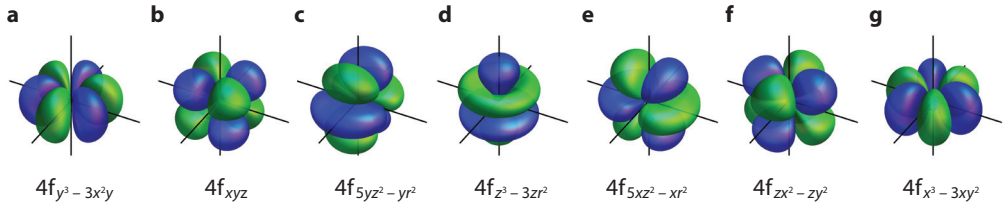

Figure 2.9 • The 4f-orbitals. The real-valued 4f-orbitals as commonly depicted. The angular components are composed of the complex-valued spherical harmonics as (**a**) $= Y_3^3 - Y_3^{-3}$, (**b**) $= Y_3^2 - Y_3^{-2}$, (**c**) $= Y_3^1 - Y_3^{-1}$, (**d**) $= Y_3^0$, (**e**) $= i\left(Y_3^1 + Y_3^{-1}\right)$, (**f**) $= i\left(Y_3^2 + Y_3^{-2}\right)$, (**g**) $= i\left(Y_3^3 + Y_3^{-3}\right)$.

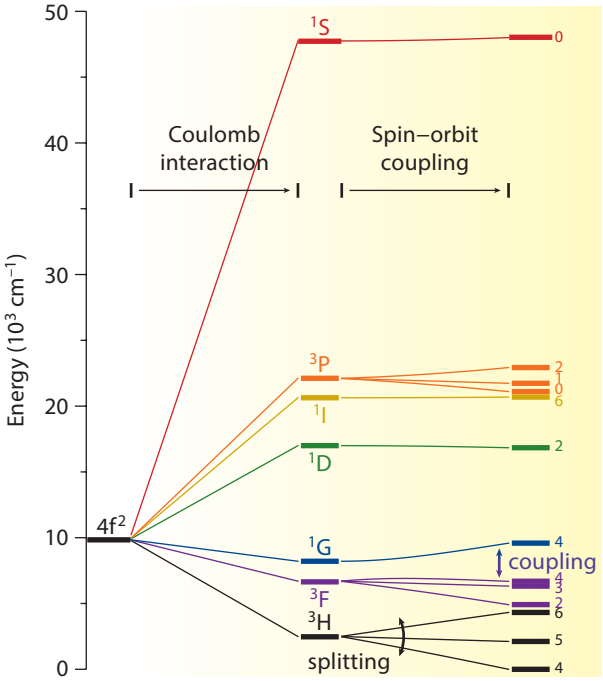

Figure 2.10 • 4f^n energy levels. The 4f^2-configuration of Pr^{3+} gives rise to 13 different energy levels under the influence of Coulomb interaction and spin-orbit coupling. To zeroth order the 4f^2-state is 91-fold degenerate. Coulomb interaction splits the 91 states in 7 *LS*-terms. Note that this splitting is as large as almost 50000 cm^{-1}, and can be even larger in the heavier lanthanides with more 4f-electrons. Degeneracies are further lifted by spin–orbit coupling. The *LS*-terms (except the singlet terms) split into different spin–orbit terms as linear combinations are made of the constituent states. For example, the ^{3}H term splits into $^3H_4$, $^3H_5$ and $^3H_6$. In addition, there is coupling between different *LS*-terms as constituent wavefunctions mix. For example, the $^3F_4$ term has contributions from ^{1}G and ^{3}H in addition to the dominant contribution from ^{3}F.

to the energy levels in the Dieke diagram (Fig. 2.8), we start with the 4f-orbitals. Fig. 2.9 shows the seven different spatial 4f-orbitals as they are customarily depicted. We consider the case of Pr^{3+} with electron configuration [Xe]4f^2, the simplest trivalent lanthanide with electron–electron interactions within the 4f-shell. The two 4f-electrons of Pr^{3+} have $\binom{14}{2} = 91$ possible distributions over the 4f-orbitals. The two-electron states can be written as anti-symmetric combinations of the one-electron orbitals:

$$\psi_i^{(0)}(\mathbf{r}_1, \mathbf{r}_2) = \phi_j(\mathbf{r}_1)\phi_k(\mathbf{r}_2) - \phi_k(\mathbf{r}_1)\phi_j(\mathbf{r}_2), \tag{2.9}$$

where 1 and 2 label the two electrons, the two-electron states $\psi^{(0)}$ are indexed by $i = 1, \ldots, 91$, and the one-electron orbitals ϕ are indexed by $j, k = 1, \ldots, 14$. If we only consider the kinetic energy of 4f-electrons and interactions with the nucleus and the 54 core electrons, then all 4f^2-states $\psi^{(0)}$ have the same energy. Additional energy terms are responsible for the many and widely separated energy levels of the Dieke diagram (Fig. 2.8). The most important ones are Coulomb interaction V_C between 4f-electrons, and spin–orbit coupling V_{so}.

The Coulomb interaction term accounts for repulsion between two negatively charged electrons:

$$V_C = \frac{e^2}{4\pi\varepsilon_0 r_{12}}, \tag{2.10}$$

where r_{12} is the separation between the two electrons. A quick estimate using $r_{12} \approx 1$ Å (the size of a 4f-orbital) yields that the Coulomb repulsion energy $V_C \approx 14$ eV. Hence, electron–electron repulsion can indeed have a large effect on the energies of 4f^2-states. Adding the effect of Coulomb interaction causes that the two-electron states are now linear combinations of the old 4f^2-states

$\psi^{(0)}$ of Eq. 2.9. More precisely, they form linear combinations that have a well-defined total orbital angular momentum L as well as a well-defined total spin angular momentum S. This gives rise to splitting into LS-terms as depicted in Fig. 2.10. L (or S) is maximum if the orbital (or spin) angular momenta of the individual electrons are parallel, or minimum if they are anti-parallel. In the $4f^2$-configuration, L can range from $3 - 3 = 0$ (yielding the S term) to $3 + 3 = 6$ (yielding the I term), and S can be $½ - ½ = 0$ (yielding the singlet terms) or $½ + ½ = 1$ (yielding the triplet terms). Note that each of the terms (except ^{1}S) is degenerate, hence contains several two-electron states.

Further splitting occurs when the effect of spin–orbit coupling is taken into consideration. This is the interaction of the spin angular momentum of an electron with its orbital angular momentum. In the corresponding classical picture, the electron tends to align its intrinsic magnetic moment (from the spin) with the magnetic field that it experiences because of its rotational motion around the charged nucleus. The spin–orbit interaction is written as

$$V_{\mathrm{so}} = \zeta \sum_i \mathbf{l}_i \cdot \mathbf{s}_i \,, \tag{2.11}$$

where ζ is the spin–orbit coupling strength (scaling with the fourth power of the nuclear charge), and the summation runs over the individual electrons with orbital angular momentum $\mathbf{l}$ and spin angular momentum $\mathbf{s}$. Inclusion of spin–orbit coupling causes that the two-electron states are yet other linear combinations of wavefunctions $\psi^{(0)}$ of Eq. 2.9. The new states have a well-defined value of the total angular momentum $J = L + S$. Each is $(2J + 1)$-fold degenerate before taking into account other effects such as a crystal field.

The resulting energy levels after taking into account Coulomb interaction and spin–orbit coupling are depicted in the last column of Fig. 2.10. They closely resemble the experimental energy levels as known from the Dieke diagram (Fig. 2.8). With further corrections beyond Coulomb and spin–orbit interaction, it is possible to get an even better agreement.

2.3 • Excited state dynamics

Experimental methods. Emitters such as colloidal quantum dots, organic dye molecules, or lanthanide ions can undergo transitions between energy levels. Valuable information on the positions of the energy levels and about the processes underlying transitions between them can be obtained using spectroscopy. Most straightforwardly, absorption, emission and excitation spectra (Fig. 2.11) reveal the energy difference between the levels involved. More important in this thesis are *photoluminescence (PL) decay measurements*. We bring emitters in the excited state with a short laser pulse, and record the time until emitted photons are detected. We thus obtain information about the lifetime of the excited state, which depends not only on the process of photon emission itself, but also on the other decay processes.

Decay processes are commonly expressed in terms of *rate constants*. We consider an emitter of which the excited state can decay via two pathways, A and B. The rate constants γ_A and γ_B give the probability dp_i that a particular decay process i (= A, B) occurs on the time interval between t and $t + dt$:

$$dp_i = \gamma_i N(t) dt, \tag{2.12}$$

where $N(t)$ is the probability that the emitter is in its excited state at time t after the laser pulse. Or alternatively, in a real experiment we either examine a huge ensemble of emitters, or excite the same emitter very many times. Then $N(t)$ can be interpreted as the number of emitters excited (or the number of times the single emitter is still excited) at delay time t after the laser pulse. dp_i is then the expected number of occurrences of process i on the interval $[t, t + dt]$. Following the laser pulse, the excited state can decay via either process A or B:

$$dN = -\Gamma N(t) dt, \tag{2.13}$$

where $\Gamma = \gamma_A + \gamma_B$ is the total decay rate of the excited state. The solution to this equation is exponential decay of the excited state:

$$N(t) = N(0) e^{-\Gamma t}. \tag{2.14}$$

For the excited state dynamics to be measurable, at least one of the processes A or B must be radiative, i.e. involving the emission of a photon. Suppose that process A is the radiative decay

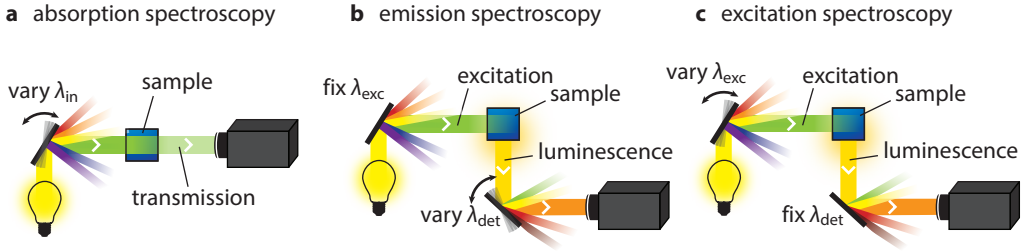

Figure 2.11 • The setup for absorption, emission, and excitation spectroscopy. (**a**) Absorption spectra are recorded by measuring the transmission through the sample of light of varying incident wavelength λ_{in}. (**b**) In emission spectroscopy one excites the sample with light of a fixed excitation wavelength λ_{exc}, and measures the luminescence intensity as a function of detection wavelength λ_{det}. (**c**) In excitation spectropy one measures the luminescence intensity of the sample at a fixed detection wavelength λ_{det}, while varying the excitation wavelength λ_{exc}.

process. Then the photon emission rate $\phi(t)$ (i.e. the number of photons emitted per unit of time) is

$$\phi(t) = \frac{\mathrm{d}p_\mathrm{A}}{\mathrm{d}t} = \gamma_\mathrm{A} N(t) = \gamma_\mathrm{A} N(0) \mathrm{e}^{-\Gamma t}. \tag{2.15}$$

From a fit of the experimental PL decay to this equation we can obtain the total decay rate Γ of the excited state. Hence, although we detect only photons emitted through process A, the experiment yields information about the total decay rate $\Gamma = \gamma_\mathrm{A} + \gamma_\mathrm{B}$, which depends also on process B. This can be either an advantage or a disadvantage. For example, it is possible to quantify the rate of energy transfer from one emitter (= the donor) to another (= the acceptor) by measuring the emission of photons by donors, and comparing the results to a reference measurement on isolated donors (see Chs. 5–7). On the other hand, it is hard to determine the purely radiative decay rate of excited energy levels if other relaxation processes contribute significantly.

Integrating Eq. 2.15 yields the total number of photons emitted through process A:

$$\int_0^\infty \phi(t)\, \mathrm{d}t = \frac{\gamma_\mathrm{A}}{\Gamma} N(0). \tag{2.16}$$

This number is proportional the ratio of the rate γ_A to the total decay rate Γ, expressing the probability that decay occurs via pathway A. If the competing process B is non-radiative (i.e. no photon is emitted), then the ratio $\eta_\mathrm{A} = \gamma_\mathrm{A}/\Gamma$ is called the *quantum efficiency* of the emitter. If, on the other hand, both processes A and B are radiative (for example radiative transitions to two different lower-energy levels), then the ratio $\beta_\mathrm{A} = \gamma_\mathrm{A}/\Gamma$ is called the *branching ratio* of transition A (see Ch. 5).

Often difficulties arise when the different emitters in the ensemble have unequal decay rates Γ. Suppose there are two populations of emitters, with decay rates Γ_1 and Γ_2. After the excitation pulse, both populations decay exponentially as in Eq. 2.14, but with their own respective rates. Unless the two populations can be distinguished based on emission wavelength, the experimental PL decay curve is biexponential:

$$I(t) \propto \phi_1(t) + \phi_2(t) = \gamma_{\mathrm{rad},1} N_1(0) \mathrm{e}^{-\Gamma_1 t} + \gamma_{\mathrm{rad},2} N_2(0) \mathrm{e}^{-\Gamma_2 t}, \tag{2.17}$$

where $I(t)$ is the photon detection rate, $\phi_i(t)$ is the photon emission rate from population i, and $\gamma_{\mathrm{rad},i}$ is the radiative decay rate of population i. In principle, it is still possible to fit experimental data to Eq. 2.17 and obtain the two rates Γ_1 and Γ_2.

In general, however, there are not two well-defined populations in the sample. Instead, there is a distribution of decay rates $\rho(\Gamma)$. For example, an ensemble of colloidal QDs is often assumed to have a log-normal distribution of radiative decay rates, because of subtle variations in size and structure (see also Fig. 2.14c). The resulting signal is multi-exponential. Fig. 2.12 illustrates how fit results on such multi-exponential PL decay curves are difficult to interpret, and that the choice of a particular fit procedure can lead to misinterpretations.

In analogy with the ensemble experiments, a PL decay curve recorded on a single QD can also be multi-exponential. This might seem surprising as multi-exponential decay usually indicates multiple sub-populations in an ensemble, which are obviously not present when examining a single QD. A multi-exponential PL decay trace from a single QD is proof that the QD does not always decay at the same rate. The decay rate might vary in time as non-radiative pathways (such as Auger decay; see Chs. 3,4,8) open and close and/or the radiative decay rate changes, for example because the QD can become charged. In addition, subtle fluctuations in the local environment of the QD (such as charges on the surface) change electronic states, and are hence responsible for

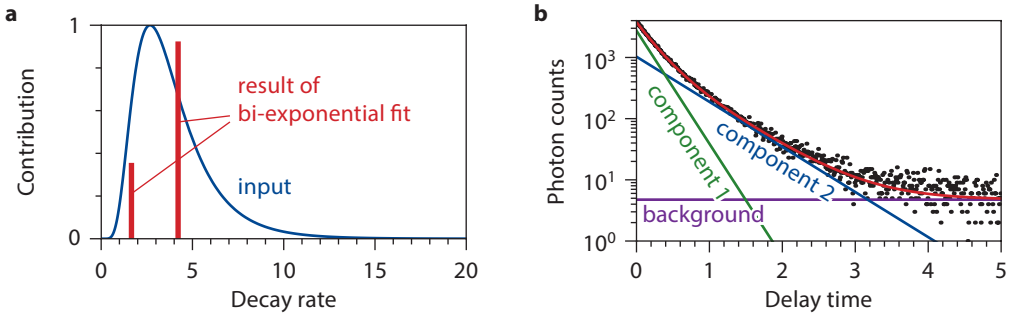

Figure 2.12 • Extracting information from multi-exponential photoluminescence decay curves. (**a**) A log-normal distribution of decay rates (blue solid line) is often assumed for an ensemble of colloidal quantum dots. (**b**) We use this distribution to simulate a photoluminescence decay curve (black dots) with background. Note that the plot is on semi-log scale, so that single exponential decay would yield a straight line. In red we show that it is possible with a bi-exponential model to get a good fit to the simulated data. However, the interpretation of the two components (red bars in **a**; green and blue lines in **b**) is not straightforward, since the actual distribution of decay rates is wide and monomodal (blue line in **a**).

spectral diffusion (see Fig. 2.6) but also affect the decay rate. Random changes in decay rate are often occompanied by a change in quantum efficiency, resulting in *blinking* as a characteristic of the emission intensity trace of a single QD: the brightness of the QD randomly fluctuates between different levels (see Chs. 3,8).

Radiative decay. Radiative decay is the process by which an excited luminescent center emits a photon to relax to the ground state (or another lower-energy state). Lasers make use of stimulated emission, radiative decay promoted by an existing high-intensity light field. The more common type of radiative decay, investigated throughout this thesis, is *spontaneous emission* of a photon by a luminescent center in its excited state. The rate of spontaneous emission follows Fermi's golden rule:

$$\gamma_{\mathrm{rad}} = \frac{2\pi}{\hbar} |V|^2 \rho. \tag{2.18}$$

Here V is the matrix element describing the interaction with the electromagnetic field, and gives rise to the *selection rules* that determine the strengths of electronic transitions. ρ is the local density of optical states (LDOS) which reflects the number of photon states (with the right energy and polarization) into which the excited emitter can emit.

The value of V reflects how strongly a transition couples to the electromagnetic field, and is set by the electronic structure of the emitter. As illustrated in Fig. 2.13 the strongest transitions are those that couple efficiently to a homogeneous (but rapidly oscillating) electric field, such as one-electron transitions between atomic orbitals with s- and p-symmetry. These are called electric dipole transitions, with typical radiative decay rates between ns^{-1} (organic dye molecules) and $\mu\mathrm{s}^{-1}$ (lead chalcogenide quantum dots). An important class of electric dipole forbidden transitions are the intraconfigurational f–f transitions of Ln^{3+} ions (between energy levels of the Dieke diagram of Fig. 2.8). The f–f transition strengths are small but nevertheless finite. For magnetic dipole transitions, such as the $^5D_0 \rightarrow {}^7F_1$ transition of Eu^{3+}, the finite transition strength is due to coupling to the magnetic field of light. Alternatively, most f–f transitions are forced electric dipole transitions, which gain strength as the crystal field surrounding the Ln^{3+} ion admixes slight

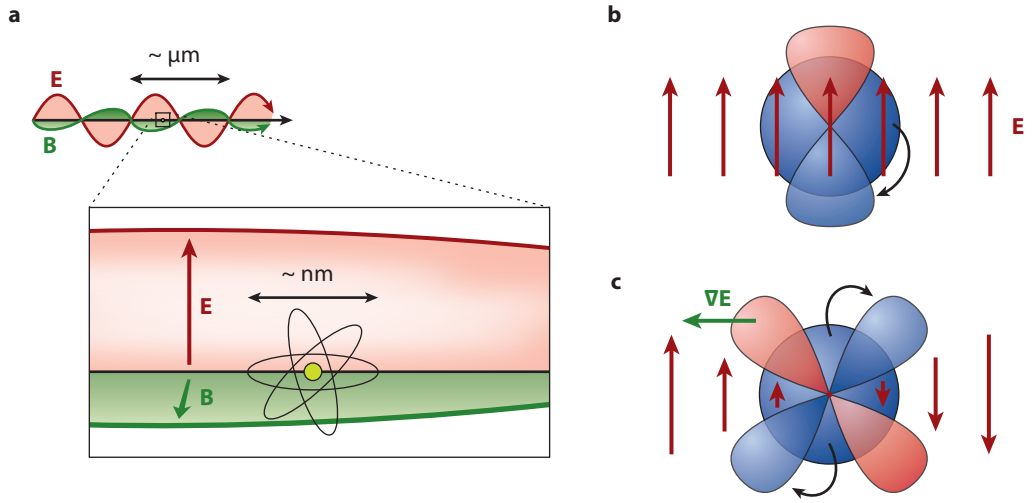

Figure 2.13 • Interaction of an emitter with the electromagnetic field. (**a**) For electronic transitions in the visible the photon states are very large, with wavelengths of several hundreds of nanometers. In contrast, the extension of the active electrons of the emitter itself is only a few ångströms (Ln^{3+} ions) to a few nanometers (quantum dots). Consequently, the emitter experiences the photon state as nearly homogeneous electric and magnetic fields with only a small gradient. (**b**) *Electric dipole transitions*, which can couple to the homogeneous component of the electric field of a photon state, (e.g. one-electron transitions from s to p atomic orbitals) are therefore the strongest transitions. (**c**) Electric quadrupole transitions couple to the field gradient, and include s to d.

5d-character into the 4f-orbitals. Typical radiative decay rates are of the order of ms^{-1}.

The LDOS ρ depends on the *photonic environment* of the emitter, i.e. the nearby refractive index and spatial variations of it. Most notably, the very insightful Drexhage experiment[8] of 1970 demonstrated how the proximity of a mirror within a few wavelengths of the emitter affects the LDOS and hence the radiative decay rate. Since then, control over spontaneous emission by LDOS tuning has become a field of intense research exploiting specially designed photonic structures such as photonic crystals, plasmonic nanostructures, or dielectric cavities with the aim to optimize the efficiency, directionality and polarization of luminescence.[86,131,156,160] Conversely, as demonstrated in Fig. 2.14 and Ch. 7, it is possible to specifically determine the radiative decay rate (rather than the sum of all decay rates) of a luminescent species by measuring decay dynamics as a function of LDOS.

As an example, Fig. 2.14 illustrates a Drexhage experiment on CdSe/CdS nanorods, as those examined in Ch. 3. The nanorods are spin-coated on a glass cover slip on which a Ag coated ball of 4.0 mm diameter is positioned, which acts as a mirror (Fig. 2.14a). By raster scanning the focus of a confocal microscope over the surface of the cover slip, we can measure the distribution of PL lifetimes for on average a single nanorod per pixel at varying distance from the Ag mirror. Figs. 2.14b,c show that the PL lifetimes of the nanorods oscillate with increasing radial distance from the point where the Ag coated ball rests on the cover slip (i.e. with increasing emitter–mirror separation). This is a direct visualization that the LDOS varies with distance from a mirror.[8] The distribution of PL decay rates (Figs. 2.14c,d) is related to intrinsic variations in nanorod size and shape affecting

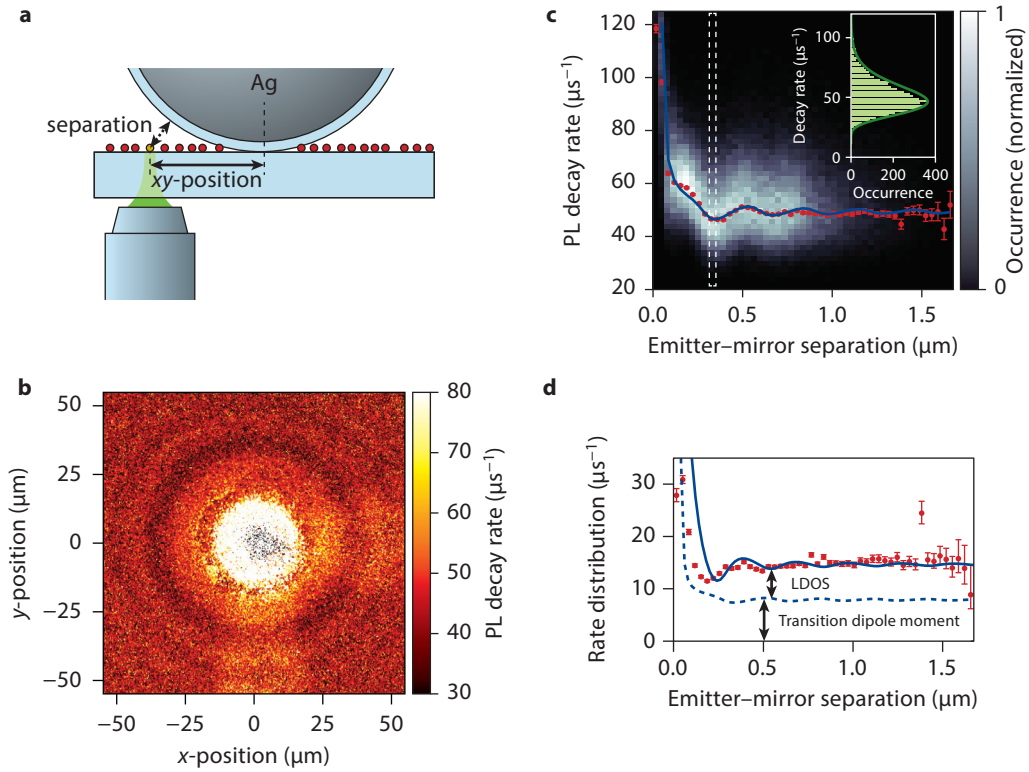

Figure 2.14 • A Drexhage experiment on CdSe/CdS nanorods. (**a**) CdSe/CdS nanorods are spin-coated on a glass cover slip, after which a silver coated ball with 4 mm diameter is positioned on top. There are nanorods at different *xy*-positions from the point where the ball touches the cover slip, hence with different distances from the reflecting silver surface. (**b**) An *xy*-scan over the surface of the cover slip, where at each position the PL lifetime of the nanorods present is measured. The PL lifetime oscillates with increasing radial distance from the point where the ball touches the cover slip [at (0,0)]. (**c**) A histogram of the PL decay rates as a function of emitter–mirror separation. Red data points are the average PL decay rates for each separation. The blue solid line is a fit to the sum of an LDOS-dependent radiative component and a constant non-radiative component, from which we extract that the PL quantum yield is 87% in a homogeneous environment of glass. The inset illustrates, for an emitter–mirror separation of 0.32 μm, that the decay rates of these nanorods are approximately log-normal distributed. (**d**) The width of the rate distributions (red data points) also oscillates with increasing emitter–mirror separation. The trend can be reproduced if we assume that (1) there is a distribution in the transition dipole moments (V in Eq. 2.18; dashed line) because the size and shape of the nanorods is not homogeneous, and (2) there is a distribution of LDOS experienced (ρ in Eq. 2.18; adding up to the solid line) because the emission of nanorods is polarized along the long axis.

the transition dipole moment (V in Eq. 2.18) and because the nanorods emit with a preferential polarization along the long axis leading to variations in the LDOS experienced (ρ in Eq. 2.18).

Auger decay. Auger decay results from scattering between two electrons in an excited emitter: one electron relaxes to a lower-lying energy level, while the other is excited to a higher level. Auger processes are particularly efficient in colloidal QDs (unless they are specially designed to have re-

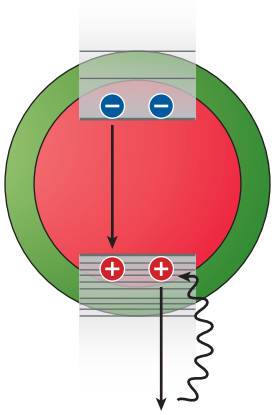

Figure 2.15 • Auger decay of biexcitons in colloidal quantum dots. A biexciton state in a colloidal QD comprises two electrons in the conduction band plus two holes in the valence band, resulting from the absorption of two photons (or alternatively, from multi-exciton generation). In principle there could be two successive photon emission events when the two electron–hole pairs recombine. Usually, however, (unless the QD structure is specially designed) the first electron–hole pair has a high probability to recombine via an Auger process (straight arrows). The recombination energy is then transferred to one of the remaining charge carriers rather than being emitted as a photon. The *positive trion pathway* (where the remaining hole accepts the recombination energy; as depicted) is usually faster than the *negative trion pathway* (where the remaining electron is the acceptor).[226] This difference is mainly due to the higher density of electronic states in the valence band than in the conduction band (see Figs. 2.2 and 2.5). Following Auger decay, the excited hole relaxes back to the top of the valence band (wavy arrow), so that the QD ends up in the single exciton state.

duced Auger rates). Basically all excited states of a conventional QD suffer from rapid Auger decay, except the lowest-energy single exciton. For example, if a QD is strongly illuminated it sometimes absorbs two photons in rapid succession. The QD is then in a biexciton state, with two electrons in the conduction band and two holes in the valence band. The biexciton state could in principle relax back to the ground state of the QD by a cascade of two sequential photon emission events. However, the first relaxation step, from the biexciton state to the single-exciton state, is often a fast Auger process as illustrated in Fig. 2.15. Consequently, the lifetime of the biexciton state is very short (< ns) and relaxation to the ground state yields only one fluorescent photon rather than two.

We make use of this fact in Chs. 3,8 to prove that we are investigating single emitters rather than a cluster: we always check that a presumably single emitter emits no more than one photon per laser pulse. Indeed, if a single emitter is in the focus of the confocal microscope, the detectors can never observe two fluorescent photons following a single laser pulse (see Fig. 3.1a), irrespective of whether one or many photons are absorbed from the pulse. In Ch. 4 we investigate QDs with a thick shell, which have relatively slow biexciton Auger decay. Consequently, radiative decay can compete with Auger decay, and the biexciton state has a significant probability to decay to the ground state via cascade emission of two photons. It is then nevertheless possible to prove the observation of a single QD, by using the time gating analysis explained in Fig. 4.4.

Auger decay of the biexciton state (Fig. 2.15) is useful if one wants the QD to act as a single-photon emitter. For many other applications, on the other hand, Auger processes are undesired loss pathways. For example, achieving gain in QD lasers is difficult because the lifetime of the biexciton state is so short. Moreover, QDs randomly charge under intense illumination, and may neutralize only milliseconds to seconds later (see Chs. 3,8), giving rise to blinking. When charged the QD can have a low PL quantum efficiency, because the trion state (= charged exciton) suffers from Auger decay. Depending on the sign of the charge,[226] and the size and composition of the QD, the brightness of the charged state ranges from completely dark[235] to on par with the neutral state.[180]

Energy transfer. An excited emitter can act as an energy donor. Another nearby species can act as the energy acceptor, if its energy level structure is appropriate. For energy transfer to occur the emission spectrum of the donor must (partially) overlap with the absorption spectrum of the ac-

ceptor. The stronger the transitions involved, the faster is the rate of energy transfer. As discussed above, the strongest transitions are usually electric dipole transitions. Energy transfer is therefore usually of the Förster type: an electric dipole transition of the donor couples an electric dipole transition of the acceptor, resulting in a tranfer rate proportional to the inverse sixth power of the donor–acceptor separation.

A convenient parameter to describe the strength of energy transfer for a particular donor-acceptor couple is the critical Förster radius R_0. It is defined as the donor–acceptor separation at which energy transfer has the same rate as intrinsic decay of the donor, e.g. by photon emission. At this separation the energy transfer efficiency is therefore 50% by definition. Typical values of R_0 are a few nanometers for couples of organic dye molecules, or a few ångströms for couples of lanthanide ions. Because energy transfer depends so strongly on the donor–acceptor separation (with the inverse sixth power), it is very efficient at separations smaller than R_0 but rapidly becomes neglible as the separation increases.

As discussed above, lanthanide ions have a rich energy level structure. Most ions even have several long-living energy levels. Consequently, many different types of energy transfer processes can occur between lanthanide ions, as depicted in Fig. 2.16. These can lead to interesting phenomena such as upconversion (the generation of one high-energy photon from two low-energy excitations; Fig. 2.16b) and downconversion (the generation of two low-energy photons from one high-energy excitation; Fig. 2.16c,d and see Chs. 5,6). For some couples of lanthanide ions, such as Tm^{3+}–Yb^{3+}, the energy level structure enables that each of the four processes of Fig. 2.16 can be encountered depending on excitation wavelength, excitation power, and donor–acceptor separation.

An important class of materials in which energy transfer between lanthanide ions is exploited is doped crystals. Energy transfer between dopant ions allows that the absorption and emission of the crystal are independently tuned. For example, $LaPO_4$ doped with Ce^{3+} and Tb^{3+}, investigated

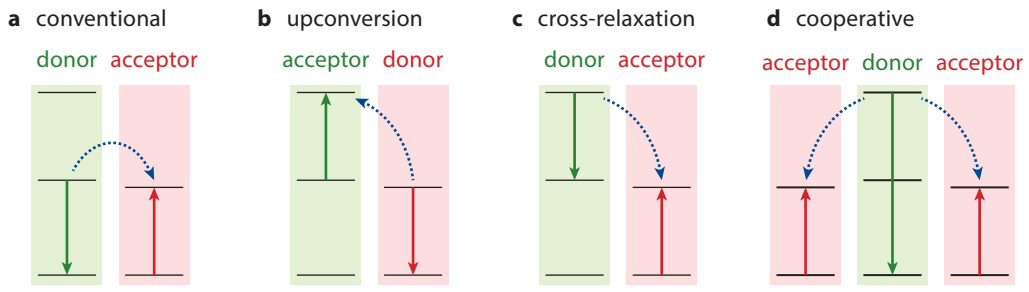

Figure 2.16 • Different types of energy transfer processes. (**a**) Most commonly, the acceptor is initially in its ground state while in the process the donor returns to its ground state. (**b**) Energy transfer upconversion occurs when the acceptor was initially in a metastable intermediate state. The result is that two quanta of energy, initially distributed over two luminescent centres, are collected on a single one (namely the acceptor). If the excited final state of the acceptor is emissive, the process yields a high-energy *upconverted* photon from two low-energy excitations. (**c**) Cross-relaxation is the process where the donor does not decay to its ground state, but instead to an intermediate energy level. The excitation energy of the donor is only partially transferred. (**d**) Cooperative energy transfer is distribution of the donor energy over two acceptor centres, by simultaneous transfer. If both final states of cross-relaxation (**c**) or cooperative energy transfer (**d**) are emissive, these processes create two low-energy *downconverted* photons from a single high-energy excitation.

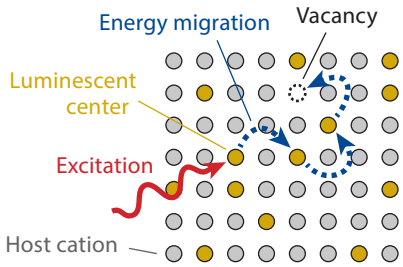

Figure 2.17 • Concentration quenching in doped crystals. If luminescent centers (yellow) are close together, an excitation can migrate through the crystal (blue dotted arrows). Eventually it may reach a quenching site such as a vacancy (dashed circle) and be lost as heat. Although this specific illustration depicts luminescent dopant ions in a crystal, concentration quenching occurs more generally whenever luminescent species are in close proximity.

in nanocrystalline form in Ch. 7, is used in fluorescent lamps. Ce^{3+} strongly absorbs the UV radiation from the mercury discharge, and then transfers its energy to Tb^{3+} which efficiently emits in the green. In Chs. 5–7 we describe how to model, fit, and predict the dynamics and the efficiency of energy transfer in doped crystals.

Although energy transfer can be a desired process for spectral conversion, it can also lead to undesired effects. Most importantly, energy transfer among like species results in *concentration quenching*, as illustrated in Fig. 2.17. If the average distance between luminescent centers is smaller than the Förster radius R_0, energy can efficiently migrate from one center to another until it reaches a quenching site. For the case of a crystal with luminescent dopant ions this can be a vacancy or impurity in the host crystal. In a quantum dot solid this can be a dark quantum dot in the ensemble (for example, a species with defective surface passivation). Concentration quenching manifests as a drop in PL quantum yield as luminescent centers are brought close together.

A special type of energy transfer is coupling to vibrations. Any composite material supports vibrations: the solid host crystals of luminescent ions, the semiconductor material of colloidal quantum dots, and the surface ligands and organic solvent molecules surrounding nanocrystals. Emitters can transfer their energy to such vibrational modes. Visible luminescence is due to electronic transitions over energy gaps of more than 14000 cm^{-1} (= 1.7 eV). Bridging such large gaps requires *multi-phonon relaxation*, i.e. the creation of multiple quanta of vibrational energy, which have energies of at most 3000 cm^{-1} (= 0.4 eV).

According to the energy-gap law[22] the rate of (multi-)phonon relaxation depends exponentially on the number of phonons required to bridge an energy gap. An excited emitter can therefore rapidly relax down a ladder of electronic excited states, until the next following relaxation step is larger than a few phonons. Consequently, a QD typically emits from the lowest excitonic state (Fig. 2.5b), and a Tb^{3+} ion from the $^5D_4$ state (Fig. 2.8). For the emitting state, multi-phonon relaxation can reduce the quantum efficiency and shorten the lifetime. For example, the quantum yield of PbSe and PbS quantum dots is lower if the exciton emission is resonant with an overtone of the oleic acid surface ligands.[140] Similarly, we show in Ch. 7 that the PL quantum efficiency of the $^5D_4$ state of Tb^{3+}-doped nanocrystals is lower when the Tb^{3+} ions are in close proximity to surface ligands, which support high-energy vibrations.

CHAPTER 3

Reduced Auger recombination in single CdSe/CdS nanorods by one-dimensional electron delocalization

Based on

Reduced Auger recombination in single CdSe/CdS nanorods by one-dimensional electron delocalization
Rabouw, F.T., Lunnemann, P., Van Dijk-Moes, R.J.A., Frimmer, M., Pietra, F., Koenderink, A.F. & Vanmaekelbergh, D.
Nano Lett. **13**, 4884–4892 (2013)

ABSTRACT • Progress to reduce non-radiative Auger decay in colloidal nanocrystals has recently been made by growing thick shells. However, the physics of Auger suppression is not yet fully understood. Here, we examine the dynamics and spectral characteristics of single CdSe-dot-in-CdS-rod nanocrystals. These exhibit blinking due to charging/discharging. We show that one-dimensional electron delocalization into the rod-shaped shell can be as effective as a thick spherical shell at reducing Auger recombination of the negative trion state.

3.1 • Introduction

Random switching, or 'blinking', between bright and dark states is a phenomenon generally observed in fluorescent colloidal nanocrystal quantum dots (QDs) when examined at the single emitter level.[27,96] The presence of dark states drastically reduces the efficiency of colloidal QDs for example in LEDs, lasers, and solar cells, in bio-imaging, or as reliable single-photon sources. Blinking is commonly understood in terms of the charging/discharging model.[29] According to this model a dark period is initiated if one charge carrier of a photo-excited exciton is trapped at the QD surface or ejected into the surrounding matrix. The remaining carrier quenches photoemission of subsequent excitons by opening a non-radiative Auger recombination pathway, in which it accepts the exciton recombination energy. Many recent experimental findings have been explained in terms of the charging/discharging model.[99,107,109,122,126,158,180,184,207] However, there are experimental results that pose a challenge to this model.[139,146,150] Galland *et al.*[154] have proposed that in addition to charging/discharging, there may be a second blinking mechanism related to surface traps.

Recently, a potential solution to the problem of blinking was presented with the introduction of colloidal QDs of CdSe with a thick CdS shell.[95,99] In this system lower-intensity periods are no longer completely dark, but still have approximately 20–30% brightness compared to high-intensity periods. The unusual brightness of lower-intensity periods has been ascribed to suppression of non-radiative Auger recombination in the trion (charged exciton) state. In addition, relatively high biexciton quantum efficiencies[192,214] have been found in these core–shell QDs, also ascribed to slow Auger rates. However, the physical origin of Auger suppression has not yet been clearly identified,[204] mainly because in thick-shell QDs several potentially important properties are combined: a smooth carrier confinement potential due to core–shell interface alloying,[130,155,197] electron delocalization into the CdS shell, and increased spatial separation between the emitting core and the nanocrystal surface.[207] The latter property combined with a temperature-dependent band offset has been invoked[207] to explain the observation of slow Auger rates at cryogenic temperatures.[107,135,178,207] Moreover, different authors do not even agree on the sign of the charge of the unusually bright trion state.[107,109,122,154,178,180,184] Clearly, blinking and Auger suppression are not yet entirely understood.

Here, we investigate single CdSe/CdS dot-in-rod structures, nanorods (NRs) of CdS with a spherical CdSe core. These NRs are presently of high interest because of the easy synthesis procedure, and their high brightness and photostability. Moreover, they have recently been identified as promising single-photon emitters,[215] which can exhibit efficient negative trion emission.[221] They have a peculiar shape and band structure, such that holes are tightly confined to the core, while electrons can delocalize along the long direction of the CdS rod.[57,83,88,98,119,120,144,163,208] We show that partial electron delocalization in the long direction of the CdS rod can be as effective as the more 'conventional' thick spherical CdS shell[95,99] for the suppression of Auger decay.

We perform detailed studies on single NRs using a combination of photoluminescence (PL) decay and time-resolved spectral measurements under ambient conditions. We quantify the rate constants and binding energies of the different states of the NRs. From a comparison of the experimental results with quantum-mechanical effective-mass calculations, we specifically identify lower-intensity periods with the negative trion state, in accordance with Tenne *et al.*[221] Remarkably, we find that our NRs are comparable to the thick-shell (10–12 monolayers) QDs in terms of quantum efficiency of the trion state, although the CdSe core is only covered by a very thin shell of CdS (3 monolayers) in the short direction of the NR. We conclude that electron delocalization in just one dimension (i.e. along the length of the NR) is sufficient to achieve efficient suppression of non-radiative Auger recombination. More precisely, we measure an average Auger lifetime of 11 ns over 18 single NRs, which is an order of magnitude longer than the lifetime of the negative trion state in spherical thin-shell CdSe/CdS QDs.[112] Our observations illustrate that Auger losses in colloidal nanocrystals can effectively be reduced by wavefunction engineering in specifically designed heterostructures.

3.2 • Characterization of bright and gray states

We investigate single colloidal NRs with a CdSe dot core of 3.2 nm diameter, and a CdS rod shell of 5.6 nm diameter and 21 nm length (with 10% size polydispersity; see also Fig. 3.4a). The characterization of a single NR consists of two parts (see Methods for technical details). First, we do time-correlated single-photon counting (TCSPC) for 200 s in a Hanbury Brown-Twiss setup, allowing for the simultaneous acquisition of an intensity trace over time scales of seconds to minutes, the photon–photon correlation function $g^{(2)}$, and PL decay curves. We divide the total measurement time into time bins of 10 ms. For each time bin we extract the number of photon counts, and the PL lifetime by fitting a single-exponential decay function to the histogram (165 ps binning) of delay times between pump pulse and arrival of a fluorescence photon, using a maximum-likelihood routine.[27] Subsequently, we flip a mirror in the detection arm of our setup and record a series of 2000 emission spectra each with an integration time of 20 ms. We fit each 20 ms emission frame to a single Gaussian and extract (1) the integrated emission intensity, and (2) the peak emission wavelength.

We have examined a total of 18 single NRs. Fig. 3.1a shows the results of TCSPC measurements on one of them: the intensity and extracted PL lifetime traces, and the corresponding histograms. The vanishing photon–photon correlation at zero time delay (inset) proves that we are examining a single emitter, and that biexciton emission does not obscure our measurements.[159,†] We see that the NR exhibits both intensity blinking and PL lifetime blinking, i.e. random switching between well-defined values for these parameters. Nevertheless, the emission intensity never approaches the background value of 0.1 cts/10 ms so the NR always remains emissive. Furthermore, the blinking behavior does not change over the measurement time of 200 s, hence the NR does not degrade. In the intensity histogram (Fig. 3.1a, top right) we distinguish three states: a bright state with mean emission intensities of M_A = 179 cts/10 ms that we label 'A', and two lower-intensity 'gray' states (M_B = 63 cts/10 ms, M_C = 41 cts/10 ms) that we label 'B' and 'C'. The good correspondence to a Poissonian intensity distribution (red line) for each of the three peaks in the histogram indicates that three well-defined states are involved. In order to examine the correlation between intensity and PL lifetime we combine the two traces and obtain the fluorescence-lifetime-intensity-distri-

† From photon–photon correlation $g^{(2)}$ plots (Fig. 3.1a inset) one can determine the quantum efficiency of the biexciton state X_2. Nair *et al.*[159] have shown that, in the limit of low excitation rates, the height of the zero-delay peak in a normalized $g^{(2)}$ plot is equal to ratio of X_2 quantum efficiency to X^0 quantum efficiency. For our NRs a zero-delay peak cannot be distinguished, hence X_2 emission is completely quenched.

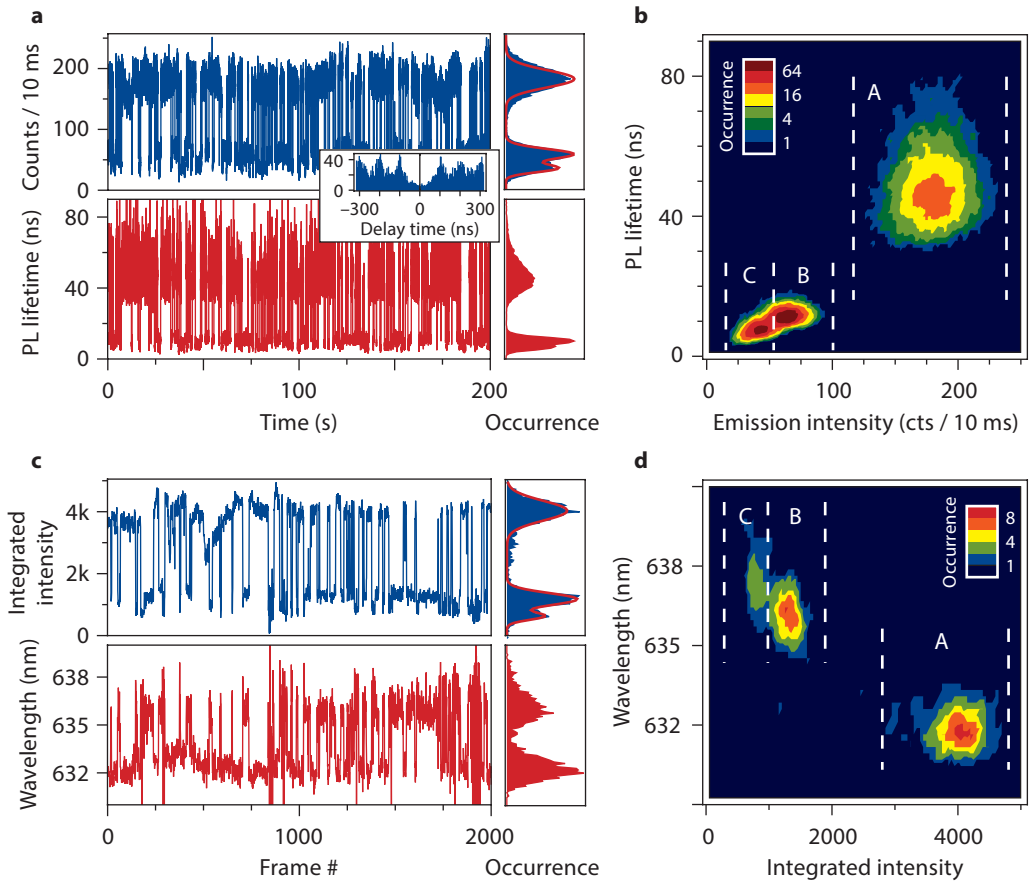

Figure 3.1 • Photoluminescence intensity, lifetime, and emission wavelength fluctuations. (**a**) The intensity trace (top) and PL lifetime trace (bottom) of a single CdSe/CdS NR measured over 200 s using TCSPC, and corresponding histograms (right). We used a time binning of 10 ms. The background counts are less than 0.1 cts/10 ms. Inset: the absence of a zero-delay peak in the photon–photon correlation proves that we are looking at a single NR. (**b**) The fluorescence-lifetime-intensity-distribution (FLID) constructed from the data in **a**, indicating in logarithmic color scale the frequency of occurrence for a combination of emission intensity and PL lifetime. The three distinct states A, B, and C are highlighted by dashed lines. (**c**) The intensity trace (top) and emission wavelength trace (bottom) of the same single NR measured on the spectrometer, and corresponding histograms (right). Each spectral frame is obtained by integration over 20 ms. (**d**) The emission-wavelength-intensity-distribution (EWID) constructed from the data in **c**, indicating in color scale the frequency of occurrence for a combination of integrated intensity and emission wavelength. Again, states A, B, and C are highlighted by dashed lines.

bution (FLID)[82] of the NR, as presented in Fig. 3.1b. The logarithmic color scale quantifies the frequency of occurrence for a combination of emission intensity and PL lifetime. We notice from the FLID that the bright state A has a long PL lifetime, while the two distinct gray states B and C have shorter PL lifetimes.

Continuing, we focus on the spectral measurements performed on the same NR and at the

same laser power. Fig. 3.1c shows the integrated intensity and emission wavelength traces, and the corresponding histograms. Still, no degradation of the NR occurs. Intensity and emission wavelength blinking are clearly visible. Again, three peaks appear in the intensity histogram (Fig. 3.1c, top right). These peaks have the same relative mean intensities and weights (obtained from a fit to three Gaussians; red line) as those in the intensity histogram constructed from the TCSPC data (Fig. 3.1a). Clearly, in the spectral measurements we resolve and identify the same three states A, B, and C as in the TCSPC measurements. Combination of the intensity and emission wavelength traces yields the emission-wavelength-intensity-distribution (EWID; Fig. 3.1d). We see that the emission wavelengths of states B and C are very close. In fact, state B and C are indistinguishable based on the wavelength histogram alone (Fig. 3.1c) because of fit uncertainties and the fact that each of the states may exhibit spectral diffusion[25,41] comparable to the separation between B and C. Still, the EWID (Fig. 3.1d) unambiguously shows the presence of two distinct states B and C, that differ slightly in terms of emission wavelength.

In the following we aim to identify the different states from their PL decay and spectral characteristics. Therefore, we assign each time bin from the TCSPC series (Fig. 3.1a) and each spectral frame from the spectral series (Fig. 3.1c) to state A, B, or C, based on the clear definition of the three states in the FLID (Fig. 3.1b) and EWID (Fig. 3.1d). We obtain the state-averaged PL decay curves and emission spectra, as presented in Fig. 3.2. PL decay curves (Fig. 3.2a) are excellently fitted with a single-exponential decay. The spectra (Fig. 3.2b) are asymmetrically broadened towards the low-energy side, and are fitted to a series of phonon replicas with a fixed spacing of 26 meV (see the Methods section for details). Table 3.1 summarizes the best-fit values for PL lifetime, PL decay amplitude, and emission wavelength (i.e. zero-phonon peak energy E_0), as well as the photon count rates obtained from the fit to the intensity histogram (Fig. 3.1a; see above).

Next, we wish to determine the quantum efficiency, η, of the gray states, and quantify the competition between radiative and non-radiative recombination that leads to the unusually high brightness. To this end, we use our fit results from Table 3.1, and inspired by previous works[122,180] we employ two different methods to estimate radiative and non-radiative contributions to the total decay. In both methods one assumes that the quantum efficiency of the bright state A $\eta_A = 1$[60,115,122,181] (it is at least 87%;[211] see Fig. 2.14) and that the excitation rate of the emitter is the

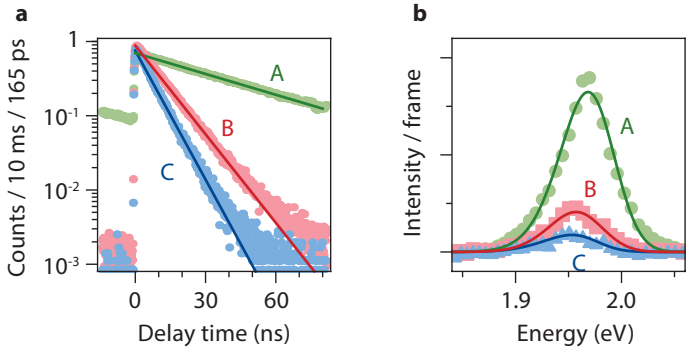

Figure 3.2 • State resolved PL decay curves and emission spectra. (**a**) PL decay curves (semi-log scale) of the states A (green), B (red), and C (blue). Solid lines are single exponential fits. (**b**) Emission spectra of the states A (green circles), B (red squares), and C (blue triangles). Solid lines are fits to a series of phonon replicas with a fixed spacing of 26 meV. See the Methods section for details of the fitting procedure.

	State A	State B	State C
Fit results			
Photon count rate M (cts / 10 ms)	179.5 ± 0.9	62.6 ± 0.8	40.8 ± 0.9
PL lifetime τ (ns)	46.4 ± 0.3	11.19 ± 0.08	7.04 ± 0.07
PL decay amplitude A (cts / 10 ms / 165 ps)	0.632 ± 0.003	0.939 ± 0.009	0.730 ± 0.010
Emission energy E_0 (meV)	1974 ± 3	1961 ± 5	1960 ± 11
Parameter estimates			
Quantum efficiency η (%)	100* 100*	34.9 ± 0.5 35.9 ± 0.5	22.7 ± 0.5 17.5 ± 0.3
Radiative lifetime τ_r (ns)	46.4 ± 0.3 46.4 ± 0.3	32.1 ± 0.5 31.2 ± 0.4	31.0 ± 0.8 40.1 ± 0.6
Non-radiative lifetime τ_{nr} (ns)	∞ ∞	17.19 ± 0.23 17.45 ± 0.23	9.11 ± 0.13 8.54 ± 0.11
Assignment			
	X^0	X^-	X^-

Table 3.1 • Characteristics of the three distinct states A, B, and C. Fit results were obtained from fits to the experimental TCSPC and spectral data. Estimates of quantum efficiency, radiative and non-radiative lifetimes are made using two methods, which are described in the text and specified in parentheses in the first column. Error margins represent 95% confidence intervals as obtained from the fitting errors. Additional uncertainty of a few percent stems from the choice of thresholds for the assignment of time slices to a state. * = by assumption.

same in each state. In the first method[122] one retrieves the quantum efficiency of gray state i from the photon count rate M: $\eta_i/\eta_A = M_i/M_A$. In the second method[180] one obtains the radiative decay rate $\tau_{r,i}^{-1}$ of state i from the PL decay amplitude: $\tau_{r,i}^{-1}/\tau_{r,A}^{-1} = A_i/A_A$. Table 3.1 shows the estimates of quantum efficiency, and radiative and non-radiative decay rates, obtained using the two different methods. Strikingly, the quantum efficiencies of the gray states (B and C) for this NR are very high, even comparable to those encountered in thick-shell CdSe/CdS QDs.[122,158]

To test whether the results are reproducible we examined 17 more single NRs. All NRs exhibit a clear gray state B similar to the NR discussed in detail above. The characteristics of the lowest-intensity state, however, are much less uniform. Four NRs do not show a third state at all, but only two states A and B. In the other NRs, the lowest-intensity states can be divided into two groups: five NRs have one bright (A) and two gray states (B and C) as encountered for the NR discussed above (Fig. 1). On the other hand, nine NRs show a bright (A) and a gray (B) state in addition to a lowest-intensity state which is almost dark (<3 cts/10 ms). First, we will focus on characterization and identification of the omnipresent gray state B. Later, we tentatively assign the different lowest-intensity states observed.

Fig. 3.3 summarizes the characteristics of gray state B of the 18 single NRs examined. Fig. 3.3a presents the correlation between the radiative lifetimes of states A and B, estimated using method 1 (via the photon count rate; open circles), and method 2 (via the PL decay amplitude; closed disks).

We see that the radiative lifetime is shorter in the gray state B than in the bright state A by a factor of 1.51 ± 0.21 (mean ± standard deviation). Fig. 3.3b shows the emission energies of states A and B. We see that the emission of the gray state B is consistently lower in energy than the emission of the bright state A, by 10 ± 7 meV. In Fig. 3.3c we plot the radiative and non-radiative lifetimes of state B [indicating the two methods for parameter estimation with open circles (method 1) and closed disks (method 2), as in Fig. 3.3a]. We see that in all NRs the radiative decay of state B is competitive with non-radiative decay, resulting in quantum efficiencies as high as 25 ± 10 %.

The increased radiative decay rate of the gray state compared to the bright state (Fig. 3.3a) is a strong indication in favor of the charging/discharging model. Radiative decay rates increase with the number of charge carriers in the system.[154,180] Alternative models, which invoke the presence of trap-related non-radiative decay channels during low-intensity periods,[66,108] cannot account for an increase in radiative decay rate. Hence, we conclude that bright periods (state A) correspond to the neutral state of the emitter, where emission originates from the uncharged exciton X^0. During gray periods (state B) the emitter is charged, and emission originates from a trion, i.e. a charged exciton.

3.3 • The effect of electron delocalization

In previous studies there has been disagreement on the sign of the trion charge associated with the observed gray states.[109,122,154,180,184] Here, by comparison of the experimental results to quantum mechanical effective-mass calculations we will show that the gray state B in our NRs is the negative trion state. To this end, we calculate radiative decay rates and transition energies of the neutral exciton X^0, negative trion X^-, and positive trion X^+. Details of the calculation method can be found in the Methods section. Briefly, we model the NR as the three-dimensional system de-

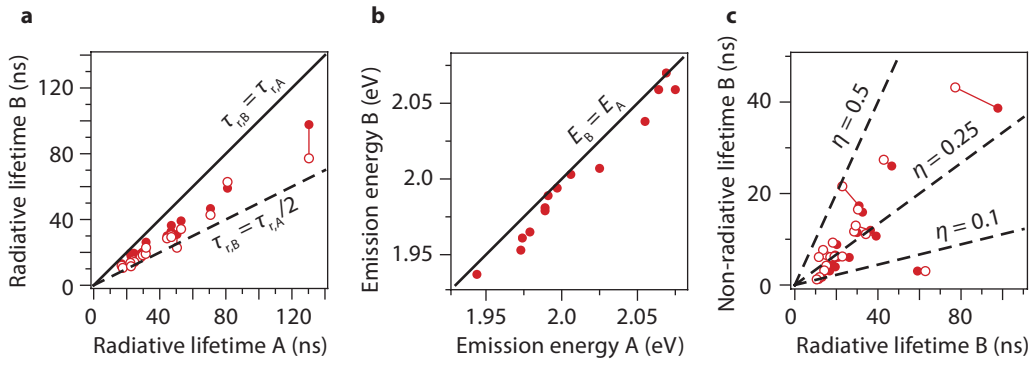

Figure 3.3 • Overview of the characteristics of the bright state A and gray state B for 18 single NRs. Estimates obtained by method 1 (via the photon count rate; see text for details) are given in open circles, those obtained by method 2 (via the PL decay amplitude; see text for details) in closed disks. Solid lines connect symbols that belong to the same NR, i.e. the results of method 1 and 2. Error margins are typically <1% (see Table 3.1) and within the size of the symbols. (**a**) The correlation between the radiative lifetimes of the bright state A (the neutral exciton X^0) and the gray state B (the negative trion X^-). Radiative decay is faster in the gray state than in the bright state by a factor 1.51 ± 0.21 (mean ± standard deviation). (**b**) The correlation between the emission energies of the bright and the gray state. Emission from the gray state is lower in energy by 10 ± 7 meV. (**c**) The correlation between the radiative and non-radiative lifetimes of the gray state. The resulting quantum efficiency of the gray state is 25 ± 10 %.

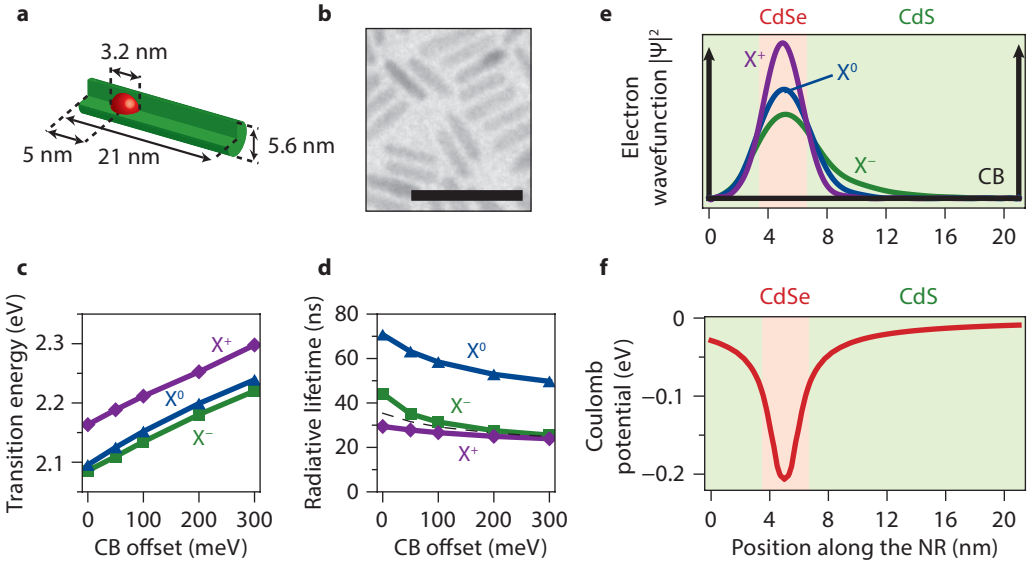

Figure 3.4 • Characteristics of the exciton, positive and negative trion states calculated using the effective mass approximation. (**a**) The dimensions of the model NR used for the effective-mass calculation. The spherical CdSe core of 3.2 nm diameter is embedded in a cylindrical CdS rod of 5.6 nm diameter and 21 nm length, and positioned with its center at 5 nm from one end of the rod. (**b**) A transmission electron microscopy image of the NRs. Scale bar is 40 nm. (**c**) The transition energy and (**d**) radiative lifetime of X^-, X^0 and X^+, calculated for different values of CB offset. The dashed line in **d** represents radiative decay which is exactly twice faster than in X^0. (**e**) The normalized electron wavefunctions $|\Psi|^2$ in the different states, showing the variable extent of electron localization (calculated for a CB offset of 0 meV). The thick black line represents the CB potential experienced by the electron (not including Coulomb interactions), with the infinite potential outside the NR. (**f**) The soft potential well experienced by the electron due to electron–hole Coulomb attraction. See the Methods section for details of the calculation method.

picted in Fig. 3.4a [the actual NRs examined (Fig. 3.4b) exhibit 10% size polydispersity]. The CdSe core is assumed to act as an infinite potential well for the hole.[186] The electron, on the other hand, is free to find the optimal extent of (de)localization under the influence of Coulomb attraction of the hole, a small conduction band (CB) offset, the different effective masses in CdS and CdSe, and (for the case of the two electrons in X^-) Coulomb repulsion of the other electron.

Figs. 3.4c,d present the results of our effective-mass calculations: the transition energies (Fig. 3.4c) and the radiative lifetimes (Fig. 3.4d) of the neutral exciton X^0, the negative trion X^- and the positive trion X^+. On the *x*-axis we varied the CB offset between 0 meV[68] and 300 meV[104] (with the CdSe core having the lower CB minimum), since its value is not well established in literature and is assumed to depend for example on strain in the nanocrystal.[136] The sensitivity of the CB offset may also partially explain the wide spread in radiative lifetimes that we find in our system experimentally, and has been found for single thick-shell CdSe/CdS QDs.[180] The calculated binding energies of X^- and X^+ are consistent with previous assignments of emission spectra of ensembles of charged QDs,[80,217] as well as single QDs at cryogenic temperatures.[107,135] The experimental transition energy difference between state B and state A is 10 meV (Fig. 3.3b), in

close agreement with the calculated 10–19 meV difference (Fig 3.4c; depending on the value of the CB offset) between X^- and X^0. Furthermore, the experimental ratio of radiative lifetimes $\tau_{r,A}/\tau_{r,B}$ is 1.51 (Fig. 3.3a), in fair agreement with the calculated ratio of $\tau_{r,X^0}/\tau_{r,X^-}$ = 1.60–1.95 (Fig. 3.4d). For the positive trion X^+, on the other hand, the calculations predict characteristics that are totally inconsistent with gray state B: approximately 60 meV *higher* transition energy (rather than lower), and a shorter radiative lifetime by a factor 2.1–2.4 compared to X^0. Accordingly, we identify the bright state A and the gray state B as the neutral exciton X^0 and the negative trion X^-, respectively.

Remarkably, we find, experimentally and theoretically, that the negative trion has a slower radiative decay rate than predicted by statistical scaling relations which are often used for rate estimates.[112,154,180] Scaling of the radiative rate with the number of recombination pathways would lead to a radiative rate of X^- that is twice faster than for X^0, since the hole has twice as many electrons with which to recombine.[180] However, the electron–hole overlap integrals in X^- and X^0 are different. Fig. 3.4d shows the electron wavefunctions in the X^+, X^0 and X^- states calculated for a CB offset of 0 meV. Clearly, the extent of electron localization varies significantly between the states. More precisely, electron–electron Coulomb repulsion enhances delocalization in X^- compared to X^0. Because of a smaller electron–hole overlap integral, radiative recombination via either pathway in X^- is slower than in X^0. As a result, the radiative decay for X^- is faster by a factor smaller than two (see Fig. 3.4d). Indeed, we have measured that $\tau_{r,A}/\tau_{r,B}$ = 1.51, which is 25% off the value of $\tau_{r,X^0}/\tau_{r,X^-}$ = 2 that one would expect from statistical scaling.[180] The 25% deviation is a direct manifestation of electron delocalization.

3.4 • Analysis of the lowest-intensity state

Next, we focus on the lowest-intensity states, which are intrinsically hard to characterize because of the low signal. We can divide the 18 NRs examined into two groups. Group 1 shows only bright ↔ gray blinking, i.e. the brightness does not fall below 20% of the brightest state. In five of these there are two distinct gray states B and C (as in Fig. 3.1), while the other four appear to have only one gray state B. Group 2, on the other hand, contains NRs showing bright ↔ gray blinking in addition to a 'dark state' with emission intensity <3 cts/10 ms. This dark state, that we label 'D', is very different from the gray states B and C as we will show below. Figs. 3.5a,b present the intensity histograms of two NRs, representative for group 1 (Fig. 3.5a) and group 2 (Fig. 3.5b). We have labeled the different states A, B, C and D according to their emission intensities. We clearly see that only the NR on the right exhibits a dark state D with <3 cts/10 ms. Figs. 3.5c,d show the blinking statistics of these two NRs. We plot the bright/dim duration probability distributions,[44,149] using the threshold intensities indicated by the dashed lines in Figs. 3.5a,b. The two NRs have qualitatively different duration probability distributions, which are representative for the other NRs of the respective groups. NRs *without* a dark state (group 1; Fig. 3.5a,c) show exponential distributions, while those *with* a dark state (group 2; Fig. 3.5b,d) show power-law distributions. Based on the bright/dim statistics, and on the PL decay and spectral properties, we will now make assignments, first for the gray state C (Fig. 3.5a) and then for the dark state D (Fig. 3.5b).

The characteristics of gray state C (Table 3.1) differ only slightly from the X^- state B: roughly 30% lower emission intensity, 30% shorter PL lifetime, and equal emission energy. Furthermore, the exponential statistics associated with a state C (Fig. 3.5a) indicate that A ↔ C blinking involves an Auger-assisted charging mechanism following the occasional creation of a biexciton and with a well-defined rate constant.[118] In fact, exponential statistics have been found for X^0 ↔ X^- blinking in thick-shell CdSe/CdS QDs.[154,180] We propose that gray state C is a negative trion X^- that differs from the X^0 state B by *the location where the ejected hole resides*.[82] Indeed, the charging/discharg-

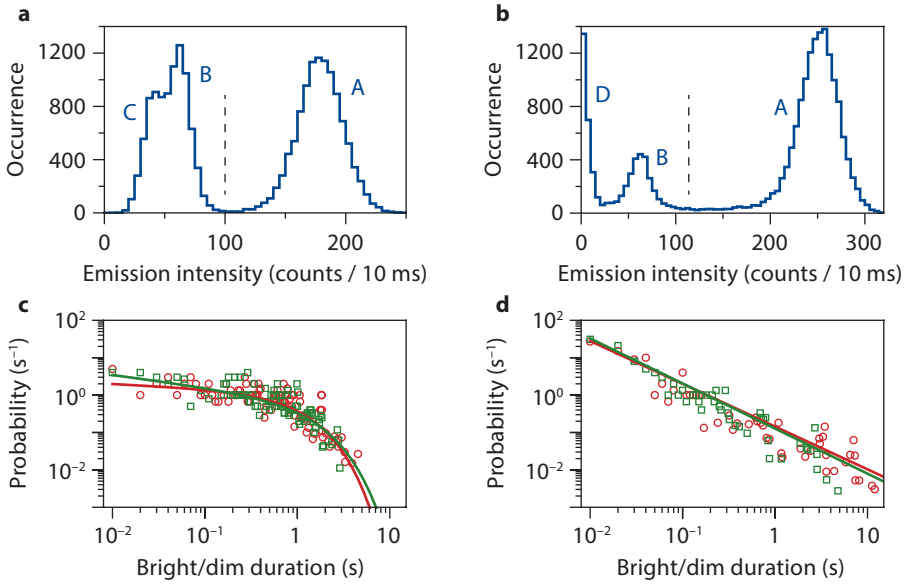

Figure 3.5 • Two types of duration probability distributions. Intensity histograms (**a**) of a NR from the first group (with a gray state C) and (**b**) of a NR from the second group (with a dark state D; right). Binning: 5 counts/10 ms. (**c**,**d**) The corresponding probability duration distributions of the bright periods (state A; red circles), and dim periods (states B + C/D; green squares) for (**c**) the NR from group 1, and (**d**) the NR from group 2 (right). The intensity thresholds used are depicted by dashed lines in **a**,**b**.

ing model for blinking involves ejection of a charge (here, the hole) that resides on the surface or in the environment of the NR for some time before returning. Because of the anisotropic shape of the NRs, there may be two possible types of locations for the ejected hole to reside, giving rise to two negative trion states X^- with similar but slightly different characteristics.

We can model the effect of the ejected hole by a single positive point charge on the NR surface in our effective-mass model. We put a point charge at the tip or at the side (nearest to the core) of the NR, 1 nm from the surface. We can then compare the resulting transition energy and radiative lifetime of the X^- state to the above calculations in which we neglected the ejected hole. Using a conduction band offset of −100 meV the changes are −3 meV and −1.6 ns for the charge at the tip, and −5 meV and −1.6 ns for the charge at the side. Hence, the ejected hole may indeed be responsible for the small distinction between the B and C states. However, the effects are so small that we cannot make statements about exactly where the ejected hole resides in the experiment.

The different statistics (Fig. 3.5c,d) imply that two completely different mechanisms underlie A ↔ D blinking and A ↔ B,C blinking. Moreover, state D (NRs from group 2; Fig. 3.5b) has very different properties from states B and C: very low emission intensity (<3% compared to the X^0 state) and very short PL lifetime (1–2 ns). In fact, state D has characteristics consistent with the dark state most commonly encountered in blinking QDs, and which we link in Ch. 8 to delayed emission at μs–ms timescales. We assign this type of blinking to trapping and release of the electron, leaving the NR (or the QDs in Ch. 8) with an excess positive charge. Hence, for roughly 50% of the NRs in the ensemble blinking is dominated by Auger-assisted ejection of the hole (leaving them negatively charged), while the rest exhibits trapping and release of the electron

(leaving them positively charged). Our results seem to comfirm those of Galland *et al.*[154] and Tenne *et al.*[221] who found that blinking can be due to combination of blinking mechanisms, but that they can be distinct in terms of the blinking statistics.‡

3.5 • Suppression of Auger recombination

We now return to the main focus of this chapter which is the properties of the negatively charged state B. We recognize the non-radiative lifetimes of state B (Fig. 3.3c) as Auger lifetimes of X^-. Auger recombination is slow enough that radiative decay can compete with it, resulting in X^- quantum efficiencies in our NRs (25%) as high as those observed in thick-shell CdSe/CdS QDs with 12 monolayer (5 nm) thick shells.[122,158] This finding is consistent with the recent observations of reduced blinking[215] and efficient negative trion emission[221] in CdSe/CdS NRs. However, it is remarkable if we consider that in our system the CdSe core is covered by a cylindrical CdS shell that is only 3 monolayers thin in the direction perpendicular to the long NR axis. The average Auger lifetime of 11 ns (distributed from 1.2 ns to 40.9 ns) is still an order of magnitude longer than observed in spherical thin-shell (2–3 monolayers) CdSe/CdS QDs.[112] Apparently, merely one-dimensional electron delocalization results in efficient Auger suppression in the negative trion state.

Our NRs are different from thick-shell QDs in terms of two important properties that have previously been argued to be responsible for a suppression of Auger recombination. First, the NRs have only a small separation between the emitting core and the outer surface. Apparently, charge carriers reaching the outer surface of a nanocrystal do not necessarily lead to efficient Auger decay. This finding seems to contrast with the model of Javaux *et al.*[207] who attribute the suppression of Auger recombination in core–shell QDs at cryogenic temperatures to surface-assisted Auger decay combined with temperature-dependent band offsets. Second, (unintentional) interfacial alloying[126,155,197] is most likely absent in our NRs, as evidenced by the low biexciton quantum efficiency (see Fig. 3.1a) and the short reaction time during synthesis (a few minutes[83] versus many hours for the thick-shell QDs[95]). We conclude that interfacial alloying is also no strict requirement to achieve suppression of Auger decay. We must, however, point out that we cannot exclude other subtle differences between our NRs and thick-shell QDs in terms of strain fields[100,121,136,164] or stacking faults.[206] More in-depth experimental[171] and theoretical work will have to be performed to quantify these differences and their potential effect on charge carrier dynamics.

We can qualitatively explain the occurrence of suppressed Auger decay in our NRs in terms of the simple theoretical model of Cragg and Efros.[130] They argued that the Auger recombination rate roughly scales with high spatial frequency components of the charge carrier wavefunctions, and that those high-frequency components are reduced in amplitude if the confinement potential experienced by the excess carrier is smoothened or 'softened'.[130,173] Based on this argumentation, Auger suppression has been linked to soft confinement potentials due to core–shell interface alloying.[126,155,197] Interestingly, in our NRs the confinement potential experienced by the electron is also soft, but for another reason. The extent of electron localization is namely dictated by long-range Coulomb attraction of the hole, which is tightly confined to the core. The softness of the Coulomb confinement potential is evident from Fig. 3.4f. Soft confinement leads to partial electron delocalization that allows for substantial radiative recombination (which does require electron–hole overlap), while restraining high-frequency components in the electron wavefunction (limiting Auger decay). As a consequence, in our NRs the negative trion has a high quantum effi-

‡ In the original paper on which this chapter is based [*Nano Lett.* **13**, 4884–4892 (2013)], the dark state D was tentatively assigned to the availability of trap states opening non-radiative decay channels. Following the detailed investigation of power-law dynamics of Ch. 8, we now assign it to a positively charged state.

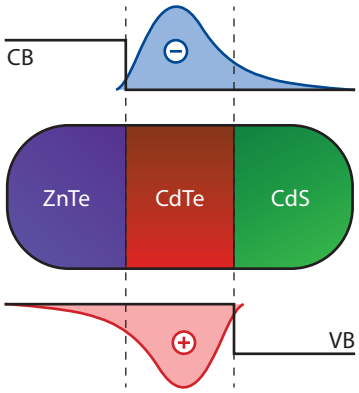

Figure 3.6 • The design of new colloidal systems with reduced Auger losses. A colloidal ZnTe/CdTe/CdS NR with a central CdTe region, and the two opposite tips composed of ZnTe and CdS promises to possess suppressed Auger recombination in all excitonic states (X^-, X^+, and X_2). The band alignment (black solid lines) is such[151] that Coulomb attraction results in electron–hole overlap in the central CdTe part, hence efficient radiative recombination. At the same time, partial delocalization of both electron (into the CdS tip) and hole (into the ZnTe tip) leads to suppressed Auger recombination in all excitonic states. In addition, as for our NRs, partial delocalization will also lead to slower radiative rates than predicted by statistical scaling relations. Moreover, the biexciton will be repulsive, which is good for lasing applications.

ciency. In fact, Auger suppression in thick-shell CdSe/CdS QDs may also in large part be enabled by the softness of the electron–hole Coulomb attraction. Indeed, also in the thick-shell systems the extent of electron delocalization is set by the Coulomb potential of the core-confined hole. However, this effect has so far mostly been overlooked in favor of the interface alloying model.[130]

Our findings point towards a new design rule for nanocrystals with reduced Auger recombination. As an alternative method to core–shell interface alloying,[126,155,197] a soft confinement potential can also result from electron delocalization and long-range electron–hole Coulomb interaction (Fig. 3.4f). Generalizing, we suggest that Auger recombination in nanostructures may be suppressed if the extent of confinement of the excess carrier is mainly set by Coulomb attraction of opposite charges rather than spatial confinement (as in conventional or thin-shell QDs). Indeed, relatively slow biexciton Auger decay has recently been found in spherical 'type-II' InP/CdS QDs,[175] where Coulomb interaction is an important factor determining the shape of charge carrier wavefunctions. Moreover, Auger decay is slow in bulk semiconductors,[26,40] where Coulomb interaction is the only interaction that binds electron–hole pairs.

We must emphasize that while our NRs are an excellent model system to study the effect of delocalization on Auger recombination, only Auger decay of the negative trion X^- is suppressed. Auger decay of excitonic states with an excess hole (biexcitons X_2 and positive trions X^+) is still efficient, because holes experience hard confinement by the large CdSe/CdS valence band offset. New nanostructure designs, aimed at increasing the importance of Coulomb interactions for the extent of confinement of both electrons and holes, may lead to suppression of Auger losses for all excitonic states. Wavefunction engineering promises to be a good strategy to achieve this goal, facilitated by the tremendous progress made in recent years in controlling the shape and composition of colloidal heterosystems.[151] As an example, in Fig. 3.6 we propose a colloidal nanostructure in which both electrons and holes can partially delocalize, and which promises to have suppressed Auger recombination in all excitonic states but efficient radiative recombination because of the presence of direct electron–hole overlap.

3.6 • Conclusion

To summarize, we have identified the negative trion state in blinking CdSe/CdS NRs based on its PL decay and spectral characteristics (i.e. faster radiative decay by a factor 1.51 and a lower transition energy by 10 meV compared to the neutral exciton). These characteristics are a direct

consequence of the shape and band alignment of our heterostructure. Furthermore, we have explained the blinking behavior involving multiple states as encountered in many of the NRs. Most importantly, we have quantified the suppression of non-radiative Auger recombination in the negative trion state, which leads to the quantum efficiency as high as 25%. Strikingly, this value is comparable to those reported for thick-shell CdSe/CdS QDs.[122,158] We attribute Auger suppression to the fact that the extension of the electron wavefunction is mainly dictated by a soft Coulomb confinement potential. We envision that our work will lead to new strategies for the minimization of non-radiative Auger losses that currently form a major obstacle for the application of colloidal nanocrystals in devices.

3.7 • Methods

Experimental details. The NRs examined in this study were synthesized following the method of Carbone *et al.*,[83] and then coated with a thin layer of silica following Ref. 97. The NRs have an ensemble quantum yield of 74%, measured using an integrating sphere. The silica layer serves as protection against photo bleaching.[62] Furthermore, we found that silica coated NRs cluster less than bare ones. We deposited the NRs on a glass slide from a dilute dispersion in ethanol. We used the microscope setup depicted and described in Ref. 153. All measurements were performed in ambient conditions. Single NRs were excited with 10 ps, 10 MHz, 532 nm linearly polarized pulses generated by a frequency doubled Nd:YVO_4 laser, through an oil immersion objective with a magnification of 100 and numerical aperture (NA) 1.4. We used a laser power of 200 nW focused to a diffraction-limited spot. From the count rate of the high-intensity state of single NRs (approximately 20 kHz), the estimated collection efficiency of our microscope setup (10%) and detection efficiency of our detectors (10%), we estimate that at this laser intensity we create $\langle N\rangle = 0.2$ excitons per laser pulse. This corresponds well to the value of $\langle N\rangle = 0.1$ excitons estimated from the absorption cross-section of the NRs ($\sigma_{abs} = 10^{-15}$ cm^2 at 532 nm).[46,88] Fluorescence light was collected through the same objective used for excitation, and separated from laser reflections using a long-pass filter with a cut-off at 590 nm. For timing and photon–photon correlation measurements we used a Hanbury Brown-Twiss setup with two ID Quantique id100-20 ULN avalanche photodiodes (APDs; dark counts <10 Hz) connected to a timing card (DPC 230, Becker & Hickl GmbH) with 165 ps time resolution. Spectral measurements were done with an Acton Research SpectraPro 2300i spectrograph equipped with a Pixis:100B back-illuminated Si CCD array by Princeton Instruments. We remark that the CCD camera used for spectral measurements required a few ms read-out time between successive frames.

Fitting procedures. We used single exponential decay functions to fit the state-resolved PL decay curves (Fig. 3.2a):

$$I(t) = A\,\exp(-t/\tau), \tag{3.1}$$

where the fit parameters A and τ are the PL decay amplitude and PL lifetime, respectively. We used a maximum-likelihood routine for the fits,[27] assuming Poissonian statistics. A flat background was not included since the dark-count rate of our detectors is <10 cts/s. For PL decay curves with a longer lifetime tail, we fitted only to the single exponential early-time signal. The values of the PL decay amplitudes A given (Table 3.1) are corrected for the relatively short laser repetition period ($T = 100$ ns) of our setup compared to the PL lifetimes ($\tau = 5$–50 ns):

$$A \rightarrow A/[1 + \exp(-T/\tau)]. \tag{3.2}$$

A correction is needed because the tail of a PL decay curve with $t > T$ is counted towards the early-time signal ($t \rightarrow t - T$), as clearly visible in the PL decay curve of state A (Fig. 3.2a): the signal at negative delay is the tail of the PL decay that extends over longer than 100 ns.

State-averaged emission spectra (Fig. 3.2b) are asymmetrically broadened towards the red side because of exciton–phonon coupling. They were fitted to a series of phonon replicas at fixed energy intervals of $\varepsilon_{LO} = 26$ meV (the longitudinal optical phonon energy in CdSe) using a non-linear least-squares method:

$$I(E) = I_0 \sum_{n=0}^{5} \frac{S^n}{n!} \exp\left[-\frac{1}{2}\left(\frac{E - E_0 + n\varepsilon_{LO}}{\sigma}\right)^2\right]. \tag{3.3}$$

Here the fit parameters I_0, E_0, and S are the peak amplitude, zero-phonon peak energy, peak width and Huang-Rhys factor, respectively. We obtained typical values for the Huang-Rhys factor of $S = 0.3$–1.2. The choice for a Gaussian lineshape for each phonon replica is set by broadening due to coupling to lower-energy phonon modes. We find typical values for the peak width of $\sigma = 30$–40 meV.

The effective mass calculation method. We performed quantum-mechanical effective-mass calculations[61] to obtain es-

timates for the transition energies and radiative decay rates of the neutral exciton, and positive and negative trions in our NRs. Schrödinger's equation was solved using the finite element routine of Comsol Multiphysics v4.1. We modeled a NR as a spherical CdSe core of 3.2 nm diameter, embedded in a cylindrical CdS rod of 5.6 nm diameter and 21 nm length with the center of the core at 5 nm from one end of the rod (Fig. 3.4a). We calculated five different states of the NR: (A) the 1h-state, (B) the 1e-state, (C) the 1e1h-state (= exciton X^0), (D) the 1e2h-state (= positive trion X^+), and (E) the 2e1h-state (= negative trion X^-).

(A) The 1h-state. Because of the strong confinement and large VB offset between CdS and CdSe, we always modeled the hole as a particle-in-a-spherical-box with infinite potential walls:

$$\left[-\frac{\hbar^2}{2m_h^*}\nabla^2 + V_{vb}(\mathbf{r})\right]\psi_h(\mathbf{r}) = E_h\psi_h(\mathbf{r}), \tag{3.4}$$

where we took $m_h^* = 0.45m_0$ (Ref. 148) for the hole effective mass in CdSe, and approximated the top of the VB as an infinite potential well:

$$V_{vb}(\mathbf{r}) = \begin{cases} 0 & ; \ \mathbf{r} \in \text{CdSe} \\ \infty & ; \ \mathbf{r} \in \text{elsewhere} \end{cases} \tag{3.5}$$

The ground state ψ_h and corresponding energy E_h are directly the solutions for the 1h-state of the NR. In a next step we calculated the Coulomb potential $\phi_h(\mathbf{r})$ due to the hole ground state ψ_h by solving Poisson's equation

$$\nabla^2\phi_h(\mathbf{r}) = \frac{e\left|\psi_h(\mathbf{r})\right|^2}{\varepsilon\varepsilon_0}, \tag{3.6}$$

where we took a dielectric constant of $\varepsilon = 10$ in all space. To ensure that ϕ_h approaches zero at infinity, we imposed a boundary condition on a spherical surface far from the nanorod:

$$\phi_h(|\mathbf{r} - \mathbf{r}_0| = 250\,\text{nm}) = \frac{e}{4\pi\varepsilon\varepsilon_0} \times \frac{1}{250\,\text{nm}} = 0.576\,\text{mV}, \tag{3.7}$$

with $\mathbf{r}_0$ the center of the CdSe core.

(B) The 1e-state. The electron wavefunctions and energies for the 1e-state are calculated by solving

$$\left[\frac{-\hbar^2}{2m_e^*(\mathbf{r})}\nabla^2 + V_{cb}(\mathbf{r})\right]\psi_e(\mathbf{r}) = E_e\psi_e(\mathbf{r}), \tag{3.8}$$

where the electron effective mass[148]

$$m_e^*(\mathbf{r}) = \begin{cases} 0.13m_0 & ; \ \mathbf{r} \in \text{CdSe} \\ 0.21m_0 & ; \ \mathbf{r} \in \text{elsewhere} \end{cases} \tag{3.9}$$

and the bottom of the conduction band

$$V_{cb}(\mathbf{r}) = \begin{cases} -V_{cbo} & ; \ \mathbf{r} \in \text{CdSe} \\ 0 & ; \ \mathbf{r} \in \text{CdS} \\ \infty & ; \ \mathbf{r} \in \text{elsewhere} \end{cases} \tag{3.10}$$

Here we assumed an infinite potential outside the rod. The CB offset between CdSe and CdS is not well known. Different values between 0 meV and 300 meV are given in literature.[68,104,136] Therefore, we performed our calculations for a range of values for the CB offset of $V_{cbo} = \{0, 50, 100, 200, 300\}$ meV.

(C) The 1e1h-state. The exciton (1e1h) wavefunction is written as

$$\Psi_{X^0}(\mathbf{r}_e, \mathbf{r}_h) = \psi_{e,X^0}(\mathbf{r}_e)\psi_h(\mathbf{r}_h). \tag{3.11}$$

Here we assume that the hole part ψ_h is equal to the wavefunction of the 1h-state, since the shape is determined by strong confinement. On the other hand, we allow the electron part ψ_{e,X^0} to adjust (compared to the 1e-state ψ_e) under the influence of Coulomb attraction from the hole. We solve

$$\left[\frac{-\hbar^2}{2m_e^*(\mathbf{r})}\nabla^2 + V_{cb}(\mathbf{r}) - e\phi_h(\mathbf{r})\right]\psi_{e,X^0}(\mathbf{r}) = E_{e,X^0}\psi_{e,X^0}(\mathbf{r}). \tag{3.12}$$

The total energy of the exciton is then given by

$$E_{X^0} = E_{e,X^0} + E_h. \tag{3.13}$$

(D) The 1e2h-state (= positive trion X^+). The positive trion (1e2h) ground state is written as

$$\Psi_{X^+}(\mathbf{r}_e, \mathbf{r}_{h1}, \mathbf{r}_{h2}) = \frac{1}{\sqrt{2}}\psi_{e,X^+}(\mathbf{r}_e)\left[\psi_h(\mathbf{r}_{h1})\overline{\psi_h}(\mathbf{r}_{h2}) - \overline{\psi_h}(\mathbf{r}_{h1})\psi_h(\mathbf{r}_{h2})\right], \tag{3.14}$$

where ψ_h and $\overline{\psi_h}$ denote two different hole spin projections. Again, we assume the hole part ψ_h equal to the wavefunction of the 1h-state, and allow the electron part ψ_{e,X^+} to adjust under the influence of Coulomb attraction from the two holes. We solve

$$\left[\frac{-\hbar^2}{2m_e^*(\mathbf{r})}\nabla^2 + V_{cb}(\mathbf{r}) - 2e\phi_h(\mathbf{r})\right]\psi_{e,X^+}(\mathbf{r}) = E_{e,X^+}\psi_{e,X^+}(\mathbf{r}). \tag{3.15}$$

The total energy of the positive trion is then given by

$$E_{X^+} = E_{e,X^+} + 2E_h + J_{hh}, \tag{3.16}$$

where

$$J_{hh} = \int \psi_h(\mathbf{r})e\phi_h(\mathbf{r})\psi_h(\mathbf{r})\,\mathrm{d}^3\mathbf{r} \tag{3.17}$$

is the hole–hole Coulomb repulsion energy. The value for J_{hh} = 160.682 meV obtained from the Comsol calculations lies within 0.05% of the value of the analytical Coulomb integral $J_{hh} = \int |\psi(\mathbf{r})|^2 \frac{e^2}{4\pi\varepsilon\varepsilon_0|\mathbf{r}-\mathbf{r}'|}|\psi(\mathbf{r}')|^2\,\mathrm{d}^3\mathbf{r}\,\mathrm{d}^3\mathbf{r}'$ evaluated in Wolfram Mathematica using the analytical particle-in-a-spherical-box ground state for the hole wavefunction $\psi(\mathbf{r})$.

(E) The 2e1h-state (= negative trion X^-). The negative trion (2e1h) ground state (with paired electron spins) is written as

$$\Psi_{X^-}(\mathbf{r}_{e1}, \mathbf{r}_{e2}, \mathbf{r}_h) = \frac{1}{\sqrt{2}}\left[\psi_{e,X^-}(\mathbf{r}_{e1})\overline{\psi_{e,X^-}}(\mathbf{r}_{e2}) - \overline{\psi_{e,X^-}}(\mathbf{r}_{e1})\psi_{e,X^-}(\mathbf{r}_{e2})\right]\psi_h(\mathbf{r}_h). \tag{3.18}$$

Again, we assume the hole part ψ_h equal to the wavefunction of the 1h-state, and allow the wavefunction ψ_{e,X^-} of the two electrons to adjust under the influence of Coulomb attraction from the hole and mutual Coulomb repulsion. We solve for ψ_{e,X^-} using an iterative procedure. We use the electron wavefunction ψ^i_{e,X^-} from iteration step i to obtain the Coulomb potential $\phi^i_e(\mathbf{r})$ using the Poisson equation:

$$\nabla^2\phi^i_e(\mathbf{r}) = \frac{e\left|\psi^i_e(\mathbf{r})\right|^2}{\varepsilon\varepsilon_0}, \tag{3.19}$$

with the dielectric constant and the boundary condition as before for ϕ_h. Then we solve the electron wavefunction ψ^{i+1}_{e,X^-} of the next iterative step from the Schrödinger equation

$$\left[\frac{-\hbar^2}{2m_e^*(\mathbf{r})}\nabla^2 + V_{cb}(\mathbf{r}) - e\phi_h(\mathbf{r}) + e\phi^i_e(\mathbf{r})\right]\psi^{i+1}_{e,X^-}(\mathbf{r}) = E^{i+1}_{e,X^-}\psi^{i+1}_{e,X^-}(\mathbf{r}). \tag{3.20}$$

This procedure is repeated until we obtain a self-consistent electron wavefunction and energy. Typically after less than 10 iterative steps the energy E_{e,X^-} has converged to within 1 meV. For the initial guess of the electron wavefunction we use the electron wavefunction of the neutral exciton state $\psi^1_{e,X^-} = \psi_{e,X^0}$. The energy of the negative trion is given by

$$E_{X^-} = 2E_{e,X^-} + E_h - J_{ee}, \tag{3.21}$$

where the term

$$J_{ee} = \int \psi_{e,X^-}(\mathbf{r})e\phi_{e,X^-}(\mathbf{r})\psi_{e,X^-}(\mathbf{r})\,\mathrm{d}^3\mathbf{r} \tag{3.22}$$

is subtracted to avoid double counting of the electron–electron repulsion.

(F) Radiative transition rates. Radiative transition rates can now be obtained from the electron–hole overlap integrals[186]

$$\begin{aligned}\tau^{-1}_{r,X^0} &= \frac{1}{2}C\left|\int \psi_{e,X^0}(\mathbf{r})\psi_h(\mathbf{r})\,\mathrm{d}^3\mathbf{r}\right|^2 \\ \tau^{-1}_{r,X^\pm} &= C\left|\int \psi_{e,X^\pm}(\mathbf{r})\psi_h(\mathbf{r})\,\mathrm{d}^3\mathbf{r}\right|^2\end{aligned} \tag{3.23}$$

The factor ½ in the expression for τ^{-1}_{r,X^0} accounts for the fact that only one spin-projection of the electron allows recombination with the hole (or equivalently, there is 50% thermal population of dark exciton states[24,186]). The prefactor $C = \frac{4e^2\omega n P^2 |\chi|^2}{9\times 4\pi\varepsilon_0 m_0^2 c^3 \hbar} = 1/(8.7\,\mathrm{ns})$ where n is the refractive index of the environment ($n = 1.5$ for glass), P is the Kane interband matrix element ($2P^2/m_0 = 19.0$ eV for CdSe),[186] and χ is a local field factor accounting for the local density of optical states on the position of the NR. We take $\chi = \frac{3n^2}{2n^2+n^2_{CdSe}} = 0.685$, ignoring the asymmetric shape of the NR, and the presence of air above the sample. The approximate value for χ only affects the absolute values obtained for the radiative decay rates, and do not lead to different ratios of the rates of X^0, X^- and X^+.

(G) Transition energies. The transition energies of X^0, X^- and X^+ can now be determined from the energies of the states calculated above, and the band gap energy. In the calculations we took the bottom of the CB in CdS as $E = 0$ for the electrons, and the top of the VB in CdSe as $E = 0$ for the holes. Then the transition energies are given by

$$\begin{aligned} \Delta E_{X^0} &= E_{X^0} + E_g + V_{cbo} \\ \Delta E_{X^+} &= E_{X^+} - E_h + E_g + V_{cbo} \\ \Delta E_{X^-} &= E_{X^-} - \left[\sum_i E_e^i \left| \int \psi_{e,X^-}(\mathbf{r}) \psi_e^i(\mathbf{r})\, \mathrm{d}^3\mathbf{r} \right|^2\right] + E_g + V_{cbo} \end{aligned} \tag{3.24}$$

where the summation over 1e-states ψ_e^i accounts for a finite probability for radiative decay of the negative trion to excited single-electron states (compare Ref. 126), and $E_g = 1.7$ eV is the band gap energy of CdSe. The single-electron energy states are closely spaced in energy (typical separation 25 meV), so that separate lines are not distinguished in the emission spectra which are already broadened by phonon coupling.

The absolute values for transition energy that we calculate, are some 200 meV higher than those obtained experimentally. The discrepancy can be attributed to the uncertainty in the exact positions of CB and VB extremes, and an overestimation of the hole confinement energy (because of the approximation of infinite potential outside the CdSe core). Fortunately, however, these parameters do not affect the differences in transition energy of X^0, X^- and X^+ that we required in the main text for our assignment of the sign of the trion charge.

CHAPTER 4

Dynamics of intraband and interband Auger processes in colloidal core–shell quantum dots

Based on

Dynamics of intraband and interband Auger processes in colloidal core–shell quantum dots
Rabouw, F.T., Vaxenburg, R., Bakulin, A.A., Van Dijk-Moes, R.J.A., Bakker, H.J., Rodina, A., Lifshitz, E., Efros, Al.L., Koenderink, A.F. & Vanmaekelbergh, D.
Submitted

ABSTRACT • Conventional colloidal quantum dots (QDs) suffer from rapid energy losses by non-radiative (Auger) processes, leading to sub-ns lifetimes in all excited states but the lowest-energy single exciton. Suppression of *interband* Auger decay, such as biexciton Auger recombination, has been achieved with the design of heterostructured core–shell QDs. Auger processes are also believed to be responsible for rapid *intraband* hot-electron cooling in QDs. However, the simultaneous effect of shell growth on interband Auger recombination and intraband hot-electron cooling has not been addressed. Here we investigate how the growth of a CdS shell affects these two non-radiative processes in CdSe/CdS core–shell QDs. Using a combination of ultrafast pump-push-probe spectroscopy on the ensemble and analysis of the photon statistics from single QDs, we find that Auger losses in the biexciton state are suppressed with increasing shell thickness, while hot-electron cooling is unaffected. Calculations agree with the experiment using an eight-band k·p model for biexciton Auger decay, and provide insights into the factors determining the cooling rate of hot carriers.

4.1 • Introduction

Non-radiative Auger processes, in which one charge carrier relaxes through energy transfer to another, are undesired for many applications of luminescent colloidal quantum dots (QDs). For example, under strong optical or electrical excitation QDs can become (intermittently) charged, after which Auger recombination quenches the luminescence.[27,29,154] The result can be a lower ensemble- and time-averaged light yield in QD LEDs[198] or spectral conversion layers,[133] and dark periods in the emission from a single QD used as biolabel.[102] Auger decay of the doubly excited state of QDs (i.e. the biexciton state or X_2) results in reduced gain in QD lasers.[47,174,232] Furthermore, an Auger process has been proposed to be responsible for rapid sub-ps hot-electron intraband cooling, during which the hot-electron energy is transferred to the hole by Coulomb interaction.[21,76] Such fast hot-electron cooling complicates the use of QDs for exciting new technologies such as intraband infrared photodetection[227] and hot-electron solar cells.[141]

Although quantitative prediction of Auger recombination rates is a difficult task, the qualitative picture is that the fast Auger rates in nanocrystal QDs are due to (1) strong electron–hole wavefunction overlap, (2) enhancement of electron–hole Coulomb interactions by spatial and dielectric confinement,[85] and (3) abrupt potential barriers breaking the momentum conservation rule.[130] Progress has been made to suppress Auger processes in colloidal QDs, with the synthesis of heterostructures.[204] Auger decay rates of charged excitons and biexcitons can be reduced by more than a factor 100[155,197,245] by growing a shell into which one of the charge carriers delocalizes while the other remains confined in the QD core, or by the (intentional) formation of a compositional gradient at the core–shell interface producing a soft confining potential. The approach of interfacial alloying was also shown to suppress the Auger rate in quantum well LEDs.[222] Also QDs with a type-II structure, where the lowest-energy electron and hole states are spatially separated, show slow Auger decay of biexcitons.[175] In parallel, suppression of hot-electron cooling has been reported by spatially separating electron and hole.[31,101] In engineered type-II quantum dots, reduced electron–hole coupling was proposed to lead to an inhibition of hot-electron Auger cooling, after which coupling to vibrations of surface ligands was the next fastest cooling pathway.[101] Using this concept, slow cooling rates of 1 ns^{-1} (Ref. 101) were reported, more than three orders of magnitude slower than the >1 ps^{-1} in conventional QDs.[32,34,76,219]

Despite the experimental successes to suppress non-radiative (Auger) decay of charged excitons, biexcitons, and hot-carrier states, the underlying physics is not fully understood. For ex-

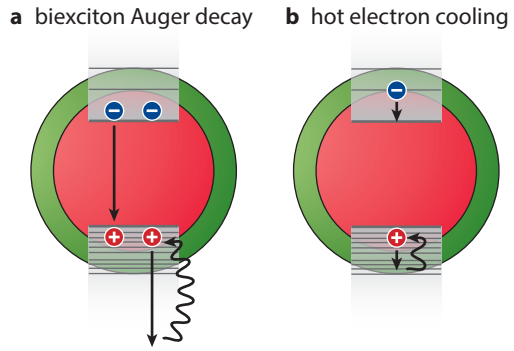

Figure 4.1 • Auger processes in colloidal quantum dots. (**a**) Biexciton Auger decay is dominated by the 'positive trion pathway',[226,235] in which the recombination energy of one electron–hole pair is transferred to the remaining hole (straight arrows). (**b**) Hot-electron Auger cooling is the relaxation of an electron to the bottom of the conduction band through energy transfer to a valence band hole (straight arrow). In both cases, the excited hole rapidly cools down to the top of the valence band by emission of phonons (wavy arrows).

ample, the ensemble averaged Auger recombination rates show clear monotonic trends with QD diameter,[40,226] but surprisingly wide variations are observed in individual QDs from batches of nominally identical ones.[161,192,180,234] Indeed, the Auger rate was theoretically predicted to be strongly dependent on the exact geometry of individual QDs.[14,247] Moreover, while fast hot-electron cooling is often explained in terms of electron–hole Auger coupling, this assignment is not unambiguous and the cooling pathways in QDs are still under investigation.[114] The intraband phonon-assisted Auger-like cooling of electrons is expected to be inhibited with decreasing QD size due to decreasing availability of energy-conserving transitions. However, an opposite trend was observed in experiments.[32,34] Moreover, intraband hole relaxation, which is the concluding step of the Auger-like electron cooling, showed striking independence on the QD size,[84] thereby suggesting additional efficient energy-conserving relaxation pathways acting alongside Auger-like cooling.

Here we compare, experimentally and theoretically, how the growth of a CdS shell on 3.8 nm CdSe QDs affects the rates of biexciton Auger recombination and $1P_e \rightarrow 1S_e$ hot-electron cooling (Fig. 4.1). Using a combination of transient absorption (TA) and single-QD photoluminescence measurements we find that Auger decay of the biexciton (X_2; Fig. 4.1a) state in QDs with a thick 18 monolayer shell is suppressed by more than an order of magnitude compared to QDs with a thin 1–2 monolayer shell. Similar suppression of X_2 Auger recombination in thick shell QDs follows from theoretical calculations using an eight-band $\mathbf{k}\cdot\mathbf{p}$ model, if we take into account the size distribution of the QD ensemble. On the same batches of QDs we perform ultrafast pump-push-probe experiments to investigate hot-electron cooling (Fig. 4.1b).[21] While X_2 Auger recombination is suppressed by the growth of a CdS shell, the cooling of hot electrons is unaffected. This finding is at odds with the standard model of hot-electron cooling by Auger coupling to the hole, because in this model the cooling rate would be reduced for increasing shell thickness as the hot $1P_e$ electron delocalizes. We suggest that the effect of delocalization could be compensated by a second counteracting effect, and discuss which effects may be involved. Furthermore, the low density of hole states in the valence band obtained from calculations suggests that rapid carrier cooling in QDs with small cores cannot be explained in terms of the simple picture of electron–hole Auger coupling alone. Such coupling must be strongly phonon-assisted or even be complemented with alternative cooling pathways.

4.2 • Slow-down of biexciton Auger decay

We examine three batches of CdSe/CdS core–shell QDs. They all have the same CdSe cores

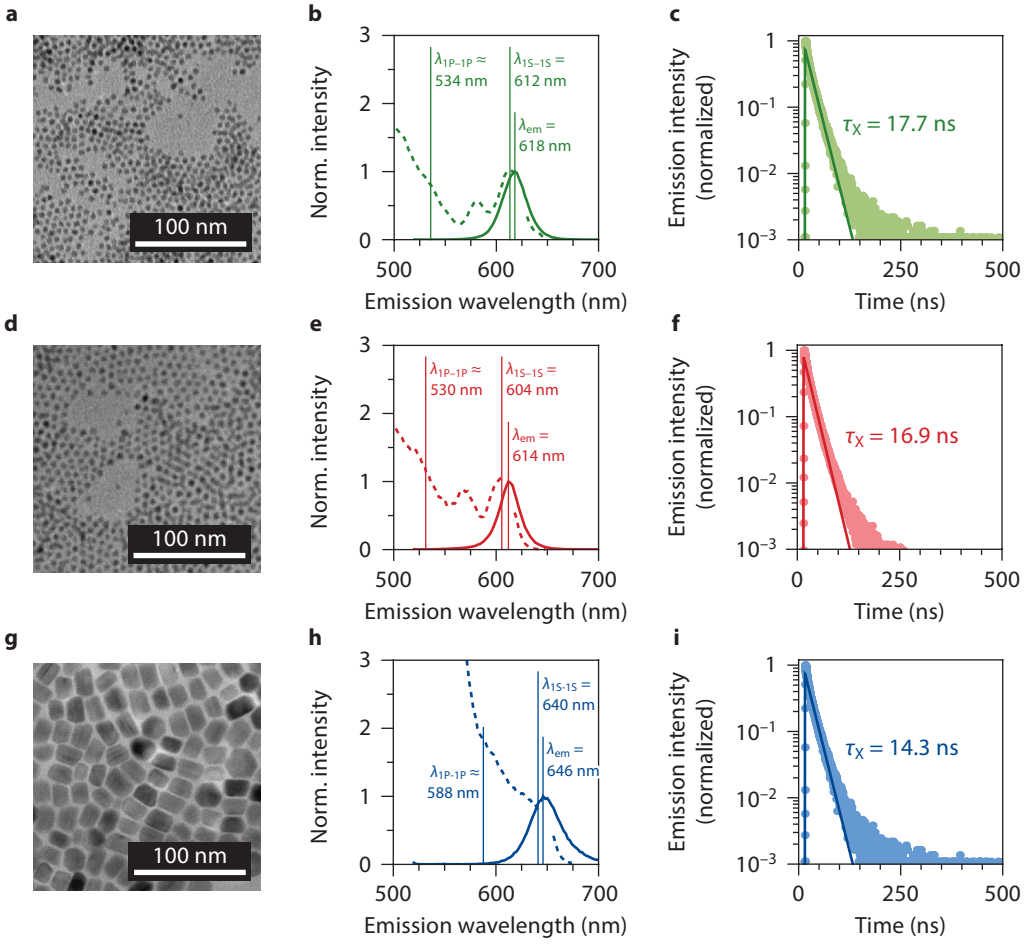

Figure 4.2 • Characteristics of the QDs investigated. (**a**,**d**,**g**) Transmission electron microscope images, (**b**,**e**,**h**) emission and absorption spectra and (**c**,**f**,**i**) photoluminescence decay curves of (**a**,**b**,**c**) the QDs with 1-monolayer shell, (**d**,**e**,**f**) the QDs with 2-monolayer shell, and (**g**,**h**,**i**) the thick-shell QDs (18 monolayers). The peak emission wavelengths λ_{max}, the positions of the $1S_{3/2}$–$1S_e$ (λ_{1S-1S}) and $1P_{3/2}$–$1P_e$ (λ_{1P-1P}) absorption transitions, and fitted exciton lifetimes τ_X are indicated in the plots. If we assume that τ_X reflects purely radiative decay, statistical scaling of radiative decay rates[235] yields estimates for biexciton radiative lifetimes τ_{r,X_2} of (**c**) 4.4 ns, (**f**) 4.2 ns and (**i**) 3.6 ns. We use these values in our analysis, to estimate the quantum efficiency of the $X_2 \rightarrow X$ transition as $\eta_{X_2} = \tau_{X_2}/\tau_{r,X_2}$ where τ_{X_2} is the experimental total lifetime of the biexciton.

with a diameter of 3.8 nm, but with a different number of CdS layers grown with the SILAR method (see Methods). There are two batches of thin-shell QDs, with 1 monolayer of CdS and a total diameter of 4.8 (± 0.5) nm, and with 2 monolayers and a total diameter of 6.0 (± 0.5) nm. A batch of thick-shell QDs has 18 monolayers of CdS, and slightly anisotropic shape of 24 (± 2) nm by 16 (± 2) nm. Representative transmission electron microscope images, ensemble emission and absorption spectra and photoluminescence decay curves are shown in Fig. 4.2.

Fig. 4.3 shows the TA signal in the infrared (IR; recorded at 1700 cm^{-1} = 0.21 eV) of the three QD batches, upon pumping at 400 nm. Pump absorption creates conduction band electrons and valence band holes, resulting in an induced intraband absorption band in the IR. The probe energy of 0.21 eV corresponds roughly to the single-particle $1S_e \rightarrow 1P_e$ transition in the conduction band[28] (see Figs. 4.2b,e,h). This transition has much larger absorption cross-section than any intraband transition in the valence band from the $1S_{3/2}$ ground state of the hole.[31] Hence, the magnitude of the TA signal reflects the concentration of excited electrons in the $1S_e$ state. At low excitation fluences (blue and green in Fig. 4.3) the TA decays slowly, with fitted time constants of longer than a nanosecond for all three QD batches. This slow component is due to radiative decay of single excitons, i.e. relaxation of conduction band electrons by radiative recombination with valence band holes.

At higher excitation fluences (yellow, orange and red in Fig. 4.3) there is a significant probability that within a single laser pulse a QD absorbs two photons, resulting in biexciton (X_2) or higher multi-exciton states. These decay much more quickly than the single-exciton state, because (1) radiative decay is faster[2,35] and (2) there is Auger recombination. The fast component in the TA signal of thin-shell QDs (Figs. 4.3a,b) at high fluences (yellow, orange, red) is due to these fast processes. We fit triple-exponential functions to the data (see figure caption for details), and obtain the X_2 lifetimes. We find a X_2 lifetime of 90 ps for the 1-monolayer batch (Fig. 4.3a) and 96 ps for the 2-monolayers batch (Fig. 4.3b). Subtracting the estimated radiative decay rates of the X_2 state (see Fig. 4.2), we obtain X_2 Auger lifetimes of 92 ps and 98 ps, respectively. These are slightly longer than typical biexciton Auger lifetimes of 30–40 ps of bare CdSe QDs with the size of our

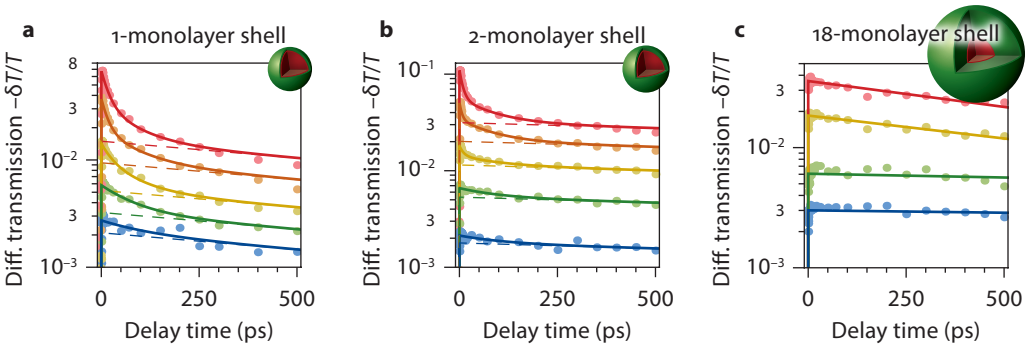

Figure 4.3 • Transient absorption in the infrared. (**a**) Induced transient mid-IR absorption at the $1S_e \rightarrow 1P_e$ transition (1700 cm^{-1}) in thin-shell QDs with 1 monolayer of CdS, at fluences of the 400 nm pump of 5 (blue), 10 (green), 20 (yellow), 50 (orange), and 100 (red) μJ cm^{-2}. (**b**) Transient absorption in thin-shell QDs with 2 monolayers of CdS, at pump fluences of 2.5 (blue), 9 (green), 25 (yellow), 50 (orange), and 100 (red) μJ cm^{-2}. (**c**) Transient absorption in thick-shell QD (18 monolayers), at pump fluences of 6 (blue), 12 (green), 40 (yellow), and 100 (red) μJ cm^{-2}. For the thin-shell QDs (panels **a** and **b**) the dashed lines are single-exponential fits to the data points between 200 and 500 ps of the lowest-fluence measurement (blue symbols), yielding (**a**) τ_1 = 1.4 ns, and (**b**) and τ_1 = 3.8 ns. The fixed value of τ_1 and two additional time constants are used in tri-exponential fits to the full curves (solid lines). We interpret the faster time constants of (**a**) $\tau_2 = 90 \pm 12$ ps (average ± standard deviation over fits to the different excitation fluences) and $\tau_3 = 20 \pm 5$ ps, and (**b**) $\tau_2 = 96 \pm 9$ ps and $\tau_3 = 7 \pm 2$ ps as due to decay of biexcitons (τ_2) and multi-excitons (τ_3). We fit the data of the thick-shell QDs (**c**) to single-exponentials, yielding time constants between 11 ns (blue) and 1 ns (red).

cores (1.9 nm radius).[50,87]

In sharp contrast to the thin-shell QDs, the measurements on the thick-shell QDs at high excitation fluences (yellow and red in Fig. 4.3c) do not show a fast component. We see nevertheless that the decay becomes faster. This indicates that the creation of biexcitons does occur, but that X_2 Auger recombination in these QDs is slower than the 500 ps timescale of our TA experiments. A single-exponential function yields a good fit to the data even at the highest excitation fluence of 100 μJ cm^{-2} (red in Fig. 4.3c), yielding a time constant of longer than 1 ns. The slow-down of X_2 Auger recombination with the growth of a CdS shell (from <100 ps to >1 ns) is consistent with previous investigations.[155] Based on the estimates of the radiative decay rate of X_2 (see Fig. 4.2) the X_2 lifetimes obtained would correspond to an average quantum efficiency of the $X_2 \rightarrow X$ transition of 2% for the thin-shell QDs, and >28% for the thick-shell QDs.

To confirm the observed suppression of Auger recombination and quantify the slow X_2 Auger decay rate in single thick-shell QDs, we performed time-correlated single photon counting (TCSPC) experiments on single QDs. Figs. 4.4a,b present the two-photon correlation function $g^{(2)}$ of the emission from a single thin-shell QD (2 monolayers; Fig. 4.4a), and a single thick-shell QD (18 monolayers; Fig. 4.4b). At low excitation fluences the zero-delay peak in such plots is proportional to the quantum yield ratio between the $X_2 \rightarrow X$ and the $X \rightarrow 0$ transitions[159] (where 0 denotes the ground state of the QD). Fast X_2 Auger recombination in the thin-shell QD leads to a X_2 quantum yield of nearly zero (see above). Indeed, there is no zero-delay peak visible over the noise in the $g^{(2)}$-plot (Fig. 4.4a). The thick-shell QD, on the other hand, shows a pronounced zero-delay peak (Fig. 4.4b). From its amplitude, and assuming that X has a near-unity quantum yield, we estimate that the X_2 quantum yield in this particular QD is 34%.

It is possible to directly quantify the X_2 lifetime from a TCSPC experiment. To this end, one must construct the two-photon correlation function $g^{(2)}$ of the emission from a single QD after first rejecting all photon counts that come within a blind period of variable length Δ after the laser pulse.[176,212] The principle is illustrated in Fig. 4.4c. Laser pulses are given at regular time intervals (green bars), while from time to time an emitted photon is detected (red bars) on either detector. Sometimes a laser pulse is followed by two photon detection events, one on both detectors (highlighted in blue). These events are due to X_2 cascade emission. Since the first step of the X_2 cascade is fast (typically within a ns), by applying a short blind period Δ after the laser pulses (gray shaded areas) one rejects coincidence counts from X_2 cascade emission more strongly than random coincidences from consecutive X emissions. Consequently, the integrated area of the zero-delay peak in the $g^{(2)}$-plot decreases more strongly with increasing blind time than those of the side peaks.

Fig. 4.4d shows the two-photon correlation functions $g^{(2)}$ (of the same single QD as examined in Fig. 4.4b) constructed after applying different blind times Δ of 0 ns (red), 5 ns (yellow), 10 ns (green), and 20 ns (blue). As expected, the area of the zero-delay peak decreases more rapidly with increasing blind time than for the side peaks. In Fig. 4.4e we plot how the peaks decay with increasing Δ. The decay of the side peaks (orange data points) contains a fast contribution from X_2 emission, while the slow component should decay with a time constant equal to half the X lifetime. The orange solid line is a fit from which we extract an X lifetime of 14.1 ns, consistent with the 16.3 ns obtained from the PL decay curve of this QD (not shown). The zero-delay peak (blue data points) is mostly due to X_2 cascades. It decays with the X_2 lifetime, for which we fit 1.7 ns (solid line). From this analysis and the X lifetime of 16.3 ns, we estimate an Auger lifetime of 2.8 ns. In other single QDs from this batch we consistently find X_2 Auger lifetimes of the order of a ns: 1.4 ± 0.6 ns over 11 QDs.

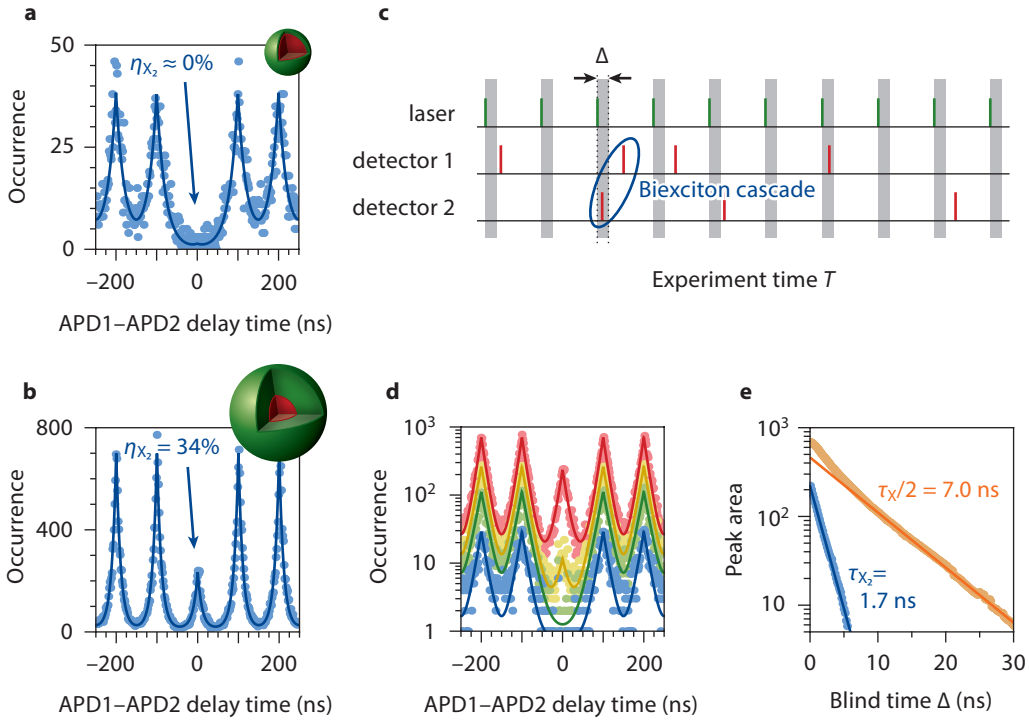

Figure 4.4 • Analysis of biexciton emission using time gating. The two-photon correlation function $g^{(2)}$ of the emission from (**a**) a single thin-shell QD (2 monolayers), and (**b**) a single thick-shell QD (18 monolayers). From the relative peak area of the zero-delay peak[159] we estimate X_2 quantum efficiencies of near 0% in **a** and 34% in **b**. (**c**) Schematic of the signals recorded during a time-correlated single photon counting experiment. Laser pulses (green bars) come at regular intervals. The two detectors, both aligned on the same single QD, sometimes detect a photon (red bars). Two consecutive photon detection events after a single laser pulse must originate from a biexciton cascade (highlighted in blue). For our analysis we discard detection events within a short variable blind time Δ (gray shaded area) after the laser pulse. (**d**) The $g^{(2)}$-plot of a single thick-shell QD constructed with blind times of Δ = 0 ns (red), 5 ns (yellow), 10 ns (green), and 20 ns (blue). Solid lines are fits to a regular array of exponentially decaying peaks. (**e**) The peak area of the zero-delay peak (blue) and the side peaks (orange) as a function of blind time Δ. The zero-delay peak area decays exponentially with a time constant equal to X_2 lifetime, for which we fit τ_{X_2} =1.7 ns.

The above results clearly reveal the trend that in CdSe/CdS core–shell QDs the X_2 Auger rate slows down with the growth of the CdS shell. The X_2 Auger rate in the thick-shell sample is slower than in the thin-shell sample by a factor 15, and slower than in core-only QDs by a factor 30–40.[50,87] In Fig. 4.5 we compare this suppression of the Auger recombination observed in experiment with calculations of the X_2 Auger rate performed using an eight-band **k·p** model (see Methods).[247] As in the experiment, we consider CdSe/CdS QDs with a fixed core diameter of 3.8 nm and variable shell thickness between 0 and 18 monolayers. We assume that after the Auger recombination event, the excited charge carrier (either an electron or a hole) resides in the continuous spectrum above the outer barrier of the QD. CdSe/CdS heteronanocrystals have a type-I½ band alignment[151] with holes strongly confined to the core region. The magnitude of the (small)

conduction band offset at the CdSe/CdS interface is however not well established.[155] Values in the range between 0 and 300 meV are typically reported,[68,104,207] and in our calculations we consider the offset energy as a variable parameter within that range. The rest of the material parameters used in the calculations are from Refs. 17 (CdSe) and 29 (CdS).

Fig. 4.5 shows the calculated X_2 Auger rates as a function of shell thickness in individual QDs (blue curves) for three conduction band offsets ΔE_{cb} = 0, 100, 200 meV. The red lines depict calculations of the ensemble-averaged Auger rate, where uncorrelated size dispersions of 10% in both core size and shell thickness were assumed. The experimental data for thin- and thick-shell QDs studied here are shown by green symbols. The yellow symbol represents a QD sample of intermediate shell thickness from Ref. 197. The calculations are in reasonable agreement with the experiment, both in terms of the absolute values of the X_2 Auger recombination rates, and on the overall trend of decreasing rate with increasing shell thickness. One can see in Fig. 4.5 that this trend is more pronounced for smaller ΔE_{cb}. This is because with decreasing conduction band offset the electron can delocalize more strongly into the shell, thereby reducing the electron–hole overlap and Coulomb interaction. The best agreement between calculation and experiment is obtained if we assume that ΔE_{cb} = 0 meV. Further, the Auger rate in individual QDs decreases with increasing shell thickness in a non-monotonic way, with oscillations of approximately an order of magnitude wide. These oscillations explain why the X_2 Auger rate measured on single QDs from one batch with slight variations in geometry varies widely (in our case, using the method of Fig. 4.4, between 0.5 ns and 2.8 ns; depicted in Fig. 4.5).[161,180,192,234] However, the oscillations average out in ensemble-based experiments (Fig. 4.3), as depicted by the red lines in Fig. 4.5.

It should be noted that the agreement between experiment and model in Fig. 4.5 can possibly be improved. Currently, the model assumes an abrupt CdSe/CdS interface between the core and the shell of the QDs. It has been demonstrated that Auger rates are affected if the interface is 'smoothened' by alloying.[155,197,245] In our samples of core–shell QDs unintentional alloying might

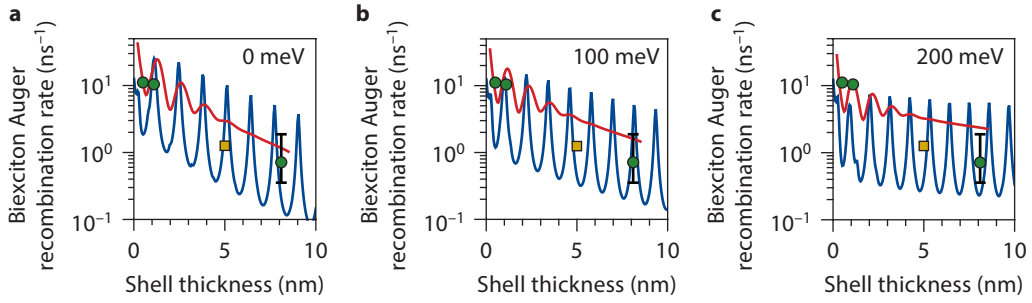

Figure 4.5 • Calculated biexciton Auger recombination rates. Calculated (lines) and experimental (symbols) X_2 Auger decay rates as a function of shell thickness in CdSe/CdS core–shell QDs with 3.8 nm core diameter, for a conduction band offset of (**a**) ΔE_{cb} = 0 meV, (**b**) ΔE_{cb} = 100 meV, or (**c**) ΔE_{cb} = 200 meV. The blue and red lines are the calculated Auger rates in individual QDs and averaged over a QD ensemble with 10% size distribution (in the size of both core and shell, uncorrelated), respectively. The green circles are the experimental data for QDs investigated in this work, having 1-, 2-, and 18-monolayer shells (with Auger lifetimes of τ_A = 92 ps, 98 ps, and 1.4 ns, respectively). The bars on the data point for the 18-monolayer QDs depict the full variation of Auger lifetimes measured on 11 different single QDs. The yellow square represents a comparable QD sample having 2.0 nm core radius, 5.0 nm shell thickness, and τ_A = 0.75 ns from Ref. 197.

occur because the shell is grown layer-by-layer over a duration of hours at high temperature.[55] The extent of smoothening of the interface could be introduced in the model as an unknown parameter. However, since there is already a reasonable consistency between the experiment and the model with an abrupt interface, we conclude that in the current experiment interfacial alloying does not have a pronounced effect. Therefore, the main mechanism responsible for the reduced Auger rates with increasing shell thickness is a reduction of the spatial overlap between ground state electron and hole wavefunctions. Another point on which our model could be fine-tuned, is the dielectric screening. We have currently used the dielectric constant of the bulk material to describe the dielectric screening of the Coulomb interaction in QDs of all sizes. In small QDs, however, dielectric screening can be reduced compared to the bulk material.[12] In the case of thick shells, the model of the Auger recombination can also be improved by taking into account the weak adiabatic Coulomb potential imposed on the electron by the strongly confined hole.[186,207]

4.3 • Hot-electron cooling in the conduction band

Next, we use ultrafast pump–push–probe experiments[31,170] to determine the rate of hot-electron cooling in QDs with different shell thickness. The experimental method is illustrated in Fig. 4.6a. A pump pulse of 400 nm (= 3.1 eV; blue arrow in Fig. 4.6a) creates excited electrons in the conduction band. A probe pulse records the induced absorption at the intra-conduction band $1S_e \rightarrow 1P_e$ transition at 1700 cm^{-1} (= 0.21 eV; dashed red arrow in Fig. 4.6a). What makes our pump-push-probe experiment different from normal pump–probe, is that a third push pulse of 1850 cm^{-1} (= 0.22 eV; red arrow in Fig. 4.6a) can excite an electron from the lowest-energy $1S_e$ level in the conduction band, to the higher lying $1P_e$ level. This push leads to a partial bleach of the $1S_e \rightarrow 1P_e$ absorption induced by the first pump pulse and measured by the probe pulse. The evolution of the transient absorption signal is schematically depicted in Fig. 4.6b, with the timing of the pump and the push pulse indicated. We are particularly interested in the recovery of the bleach signal (highlighted in green in Fig. 4.6b), as it reveals the rate at which hot $1P_e$ electrons cool down (process C in Fig. 4.6a) to the $1S_e$ level.

Figs. 4.6c–e show the recovery of the $1S_e \rightarrow 1P_e$ absorption as hot electrons cool down after the push pulse, for the three QD batches. These plots are a zoom-in of the total transient absorption trace on the region highlighted in green in the schematic graph of Fig. 4.6b. For all batches the absorption returns to the value of before the push pulse on a sub-ps timescale, evidencing fast and efficient cooling of generated $1P_e$ electrons back to the $1S_e$ level. We fit the recovery of the absorption signal to single-exponential decay convoluted with a Gaussian instrument response function of 70 fs, and obtain fitted hot-electron lifetimes of 800 fs for the thin-shell QDs with 1 monolayer shell (Fig. 4.6c), 736 fs for the thin-shell QDs with 2 monolayers shell (Fig. 4.6d), and 510 fs for the thick-shell QDs (18 monolayers; Fig. 4.6e). These values are consistent with previously reported values for core-only QDs: 220 fs determined from two-photon photoemission spectroscopy,[219] 900–1200 fs from pump-push-probe experiments,[33] or 100–600 fs from TA experiments in the visible.[34] The results of Fig. 4.6 demonstrate that the growth of a CdS shell does not suppress hot-electron cooling in CdSe QDs. Interestingly, we also see that the presence of additional charge carriers does not affect hot-electron cooling. The red data points in Fig. 4.6c depict the cooling in the biexciton regime (i.e. at high pump fluence), which is roughly equally fast as in the single-exciton regime (blue data points).

Fast sub-ps hot-electron cooling has been proposed to be an Auger process, where the hot electron transfers the relaxation energy to a valence band hole.[21,33,34] This Auger-type cooling is necessary because of the so-called phonon bottle neck in colloidal QDs: 'normal' cooling through

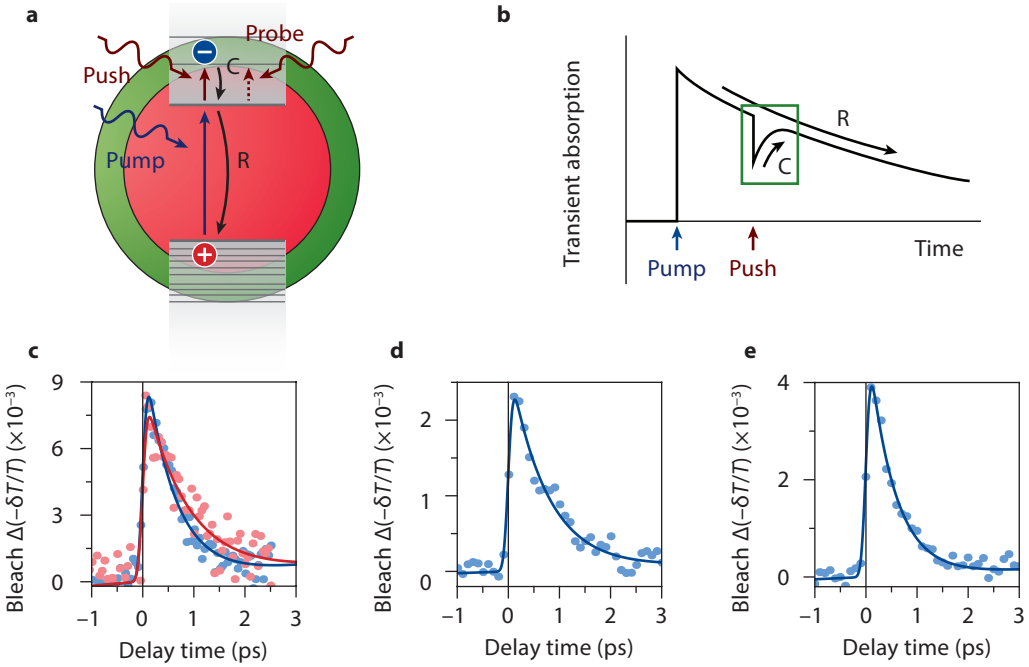

Figure 4.6 • Hot-electron cooling from pump–push–probe experiments. (**a**) In a pump–push–probe experiment an electron is excited to the conduction with a pump pulse of 400 nm (blue arrow). After relaxation to the $1S_e$ level a short push pulse of 1850 cm^{-1} (red arrow) excites it to the $1P_e$ level. The electron relaxes by first cooling down to the $1S_e$ level (labeled C), and then (radiative) recombination with the valence band hole (labeled R). A probe pulse at 1700 cm^{-1} records the absorption at the $1S_e \rightarrow 1P_e$ transition, which is induced by the pump but bleached by the probe. (**b**) Schematic of the absorption transient at the $1S_e \rightarrow 1P_e$ transition (1700 cm^{-1}) in reaction to the pump pulse (blue arrow) inducing absorption and the push pulse (red arrow) partially bleaching it. The recovery of the signals reveals the rates of cooling (C) and recombination (R). (**c**,**d**,**e**) The differential transmission transient due to $1S_e \rightarrow 1P_e$ excitation by the push pulse and subsequent electron cooling for (**c**) thin-shell QDs with 1 monolayer shell, (**d**) thin-shell QDs with 2 monolayers shell, and (**e**) thick-shell QDs. Note that the plot is inverted compared to the cartoon in **b**. In **d** and **e** the pump fluence was 20 μJ cm^{-2} and the pump–push delay 200 ps, so that at the moment of the push only single excitons exist. In panel **c** the pump–push delay is 40 ps, and the experiment was done at two pump fluences of 5 μJ cm^{-2} (blue; only single excitons) and 200 μJ cm^{-2} (red; also biexcitons). Solid lines are single-exponential fits, yielding in panel **c** 800 fs (blue; low fluence) and 859 fs (red; high fluence), in panel **d** 736 fs, and in panel **e** 510 fs.

the emission of phonons is not possible because there are no phonon modes of sufficiently high energy to bridge the separation between the conduction band levels.[21] Instead, rapid hot-electron cooling is enabled by Auger coupling with valence band holes, which is especially efficient because of spatial confinement of electrons and holes. In fact, electrons and holes are so tightly co-localized in colloidal QDs that in the smallest QDs the rate of Auger-type cooling can exceed the rate of cooling by emission of phonons in the corresponding bulk material.[34] Using time-resolved terahertz spectroscopy, Hendry *et al.*[76] have found evidence that in CdSe QDs there is indeed energy transfer from the hot electron to the hole. Pandey and Guyot-Sionnest[101] rendered Auger-type cooling impossible by spatially separating electron and hole in type-II QDs with surface hole traps.

In these specially designed QDs the electron cooling could become as slow as a ns, and in this regime was shown to be dominated by coupling to vibrations of the organic surface ligands. The equal cooling rates in the single-exciton and biexciton regimes (Fig. 4.6c) are consistent with Auger cooling if we consider statistical scaling: the biexciton state provides twice as many hole acceptors (2 rather than 1), but twice as few final states for the hot electron (1 rather than 2).

4.4 • Discussion

Table 4.1 summarizes the values found for the X_2 Auger lifetimes and the cooling rates in thin-shell and thick-shell QDs. Although hot-electron cooling is often attributed to an Auger process, in our experiments it is not affected by the growth of a CdS shell in the same way as X_2 Auger recombination. Intuitively one would expect that also hot-electron Auger cooling were suppressed by shell growth. Indeed, the hot $1P_e$ state in the conduction band strongly delocalizes in the CdS shell (Fig. 4.7a), so that the Coulomb interaction with the hole as well as the overlap with the final $1S_e$ electron state would reduce. This simple picture of hot-electron Auger coupling is not fully consistent with the experiment (Fig. 4.6). An important difference between X_2 Auger recombination and hot-electron Auger cooling is that in the former case the hole is excited to basically a continuum of states, while it is excited to one of the discrete quantum confined states in the latter case.

Fig. 4.7b presents calculated energy level structure of the quantum confined hole states as a function of shell thickness in CdSe/CdS core–shell QDs with a 3.8 nm diameter core, and conduction band offset of 200 meV. Since holes in this type-I½ structure are tightly confined to the CdSe core, the hole energy levels can be calculated assuming strong confinement for all shell thicknesses. The energy levels involved in $1P_e \rightarrow 1S_e$ hot-electron cooling are depicted as solid lines, the rest as dotted lines. Of the valence band transitions, only those from the $1S_{3/2}$ hole ground state to excited states with P symmetry can couple to the $1P_e \rightarrow 1S_e$ transition in the conduction band. We see that the energy levels of the hole are nearly independent of the shell, because the hole remains tightly confined in the CdSe core. Importantly, we see that there are large gaps of >80 meV (≈3 longitudinal optical phonons of CdSe or CdS) not only in the conduction band but also in the valence band. For instance, we see that the valence band contains a surprisingly large gap of almost 100 meV between the first ($1P_{3/2}$) and second ($1P_{5/2}$) excited hole states, and more gaps at higher energy.

In Fig. 4.7c we plot the theoretical energies for the intraband transitions involved in hot-elec-

CdS shell thickness (# monolayers)	X_2 Auger lifetime	Inverse cooling rate
1	92 ps	800 fs
2	98 ps	736 fs
18	1.4 ± 0.6 ns	510 fs

Table 4.1 • Summary of the values found for X_2 Auger and cooling rates in CdSe/CdS core–shell QDs. The X_2 Auger lifetimes of the thin-shell samples (1 and 2 monolayers) are fitted from transient absorption curves (Fig. 4.3), of the thick-shell sample (18 monolayers) from single-QD spectroscopy (Fig. 4.4). The cooling rates are fitted from the recovery of IR absorption in pump–push–probe experiments (Fig. 4.6)

tron Auger cooling as a function of shell thickness. The energies of the electron transition $1P_e \rightarrow 1S_e$ are shown in blue, while these of the simultaneous hole transitions $1S_{3/2} \rightarrow nP_j$ (j = ½, 3/2, 5/2) are shown in red. For the electron transition in CdSe/CdSe core–shell QDs the strong-confinement approximation holds only for thin-shell QDs, whereas for thick shells the adiabatic Coulomb potential produced by the strongly confined hole becomes important.[186] We therefore calculate the $1P_e \rightarrow 1S_e$ transition energy within the strong-confinement approximation for thin shells up to 3 nm (blue solid line), and including the adiabatic Coulomb potential generated by the hole for thick shells (>5 nm). The intersections of the electron and hole curves in Fig. 4.7c indicate energy-conserving Auger cooling transitions. One can see that the electron $1P_e \rightarrow 1S_e$ transition is exactly resonant with one of the hole transitions in the valence band only for a few very specific shell sizes. Clearly, since sub-ps cooling times have been measured for many different QD geometries (see Fig. 4.6 and Refs. 32,34,76,219), there must be a mechanism to compensate for the energy mismatch in the energy transfer from the excited $1P_e$ electron to the ground state $1S_{3/2}$ hole. Furthermore, the presence of large energy gaps in the valence band implies that while the model of Auger cooling can explain the absence of a phonon bottleneck for the electron, it would still be there for the hole.

Even if we assume strong homogeneous broadening of the excited hole states in the valence band of $\hbar$/50 fs = 13 meV, the large energy gaps in the valence band and large mismatches between

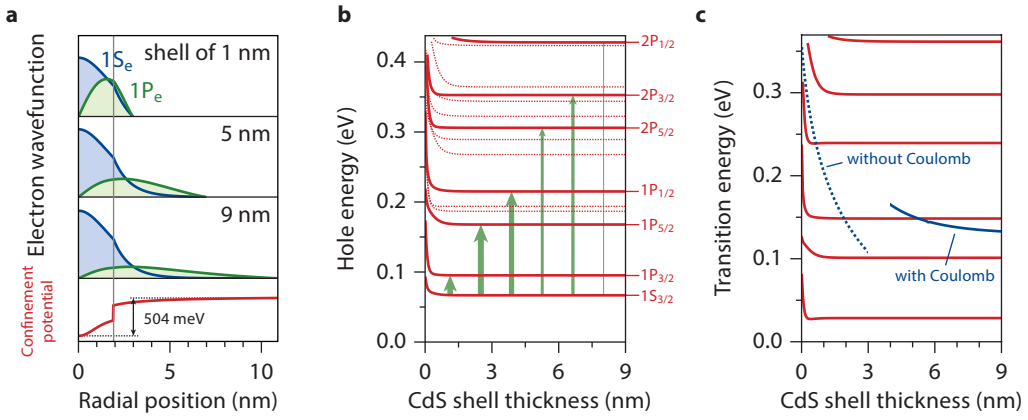

Figure 4.7 • Electron–hole Auger coupling. (**a**) The radial components of $1S_e$ (blue) and $1P_e$ (green) wavefunctions in CdSe/CdS core–shell QDs, for shell thicknesses of 1 nm, 5 nm and 9 nm. The confinement potential is due to the conduction band offset of 200 meV and Coulomb attraction by the core-confined hole (red line in the bottom panel). (**b**) The energy level structure in CdSe/CdS core–shell QDs of hole states in the valence band, for a core diameter of 3.8 nm and as a function of shell thickness. Levels involved in $1P_e \rightarrow 1S_e$ hot-electron cooling are indicated with solid lines, those not involved (because of selection rules) with dotted lines. The conduction band offset is set at ΔE_{cb} = 200 meV. The thickness of the upward arrows scales logarithmically with the Auger acceptor strength of the hole transition indicated (i.e. the Coulomb matrix element squared for the $1P_e1S_{3/2} \rightarrow 1S_enP_j$ transition), calculated for a 3 nm thick shell. An increase of 0.5 point in thickness corresponds to a 10× stronger Auger coupling. (**c**) The energies of the transitions involved in hot-electron cooling, for a core diameter of 3.8 nm and as a function of shell thickness. Red lines are the hole transitions. The blue solid line is the $1P_e$–$1S_e$ energy for ΔE_{cb} = 200 meV and with the adiabatic Coulomb potential generated by a ground-state hole, while the blue dotted line represents the $1P_e$–$1S_e$ energy calculated for the independent-particle electron states.

the electron and hole intraband transitions remain. Since the maximum phonon energy in CdSe is 26 meV, multi-phonon processes must be involved to compensate the energy mismatches.[21,76] Hence, if hot-electron Auger cooling is indeed operative in CdSe and CdSe/CdS core–shell QDs, both steps in the process (i.e. energy transfer to the hole, and cooling of the hole) are strongly dependent on phonon assistance. Indeed, atomistic calculations by Kilina *et al.*[114] have indicated that multi-phonon processes are important in hot-carrier cooling. Since the cooling pathways must be strongly phonon-assisted, one might wonder if electron–hole Auger coupling is a dominant step in the relaxation process. Unfortunately, since in addition to the conduction band offset (which sets the $1P_e \rightarrow 1S_e$ transition energy) the strength of phonon coupling is not precisely known, a quantitative theoretical prediction of the cooling pathways and rates is difficult.

If we follow the predominant assumption that hot-electron cooling is due to (phonon-assisted) Auger coupling with the hole, the independence of the CdS shell thickness (Fig. 4.6) can be qualitatively explained by realising that there are competitive effects at play. On the one hand, with increasing shell thickness the $1P_e$-electron delocalizes in the CdS shell because core-confinement (due to the conduction band offset and Coulomb attraction by the hole) is weak in CdSe/CdS (Fig. 4.7a). This effect would tend to reduce the electron–hole Auger coupling with the growth of a CdS shell. We propose two effects that could counteract this reduction. Firstly, the $1P_e$–$1S_e$ energy gap becomes smaller with increasing CdS shell thickness (Fig. 4.7c). Since energy matching is needed of the $1P_e \rightarrow 1S_e$ hot-electron transition in the conduction band to a transition in the valence band, a reduction of $1P_e$–$1S_e$ energy gap shifts the final hole state required to lower energy. We calculated the first-order Auger cooling matrix elements for the $1P_e1S_{3/2} \rightarrow 1S_e nP_j$ transitions, and found that the lower-energy hole transitions are stronger Auger acceptors than those at higher energy (see arrows in Fig. 4.7b). Consequently, the shift of the resonance condition with thicker shells in favor of the strong low-energy hole transitions could counteract the effect of electron delocalization. A second potentially compensating effect is that the exciton wavefunction for thick-shell QDs is more polarized than for thin-shell QDs because of increased spatial separation of electron and hole.[13] The coupling strength of the exciton to optical phonons should therefore increase, thus counteracting the effect of a smaller electron–hole overlap for phonon-assisted Auger coupling in thick-shell QDs. From our experimental result we can conclude that, under assumption of the Auger cooling mechanism, the effects of $1P_e$-electron delocalization roughly compensated by counteracting effects, leading to a seeming independence of the hot-electron cooling rate on shell thickness.

4.5 • Conclusion

To summarize, we have examined the dynamics of biexciton Auger recombination and hot-electron cooling in CdSe/CdS core–shell quantum dots having 3.8 nm diameter core with thin (1–2 monolayers) or thick (18 monolayers) shells. While Auger recombination of biexcitons is strongly suppressed in thick-shell quantum dots compared to thin shells, we have found that the intraband hot-electron cooling is nearly unaffected. We have described the suppression of biexciton Auger recombination theoretically, attributing it to a decrease of the electron–hole overlap due to electron delocalization with increasing shell thickness. Hot-electron cooling is generally believed to be driven by a mechanism similar to that of the Auger recombination, and would therefore be expected to show a similar slow-down upon shell growth. To explain our observation of a nearly constant cooling rate, we propose that, within the Auger cooling scheme, the slow-down due to electron delocalization can be partially compensated by the increased strength of the lower-energy hole transitions, gradually activated with increasing shell thickness. Furthermore,

our calculations have indicated large energy gaps in the hole energy spectrum, independent of shell thickness (at least for 3.8 nm core diameter and smaller). This suggests that (for all but a few specific core–shell geometries) the Auger coupling of the hot-electron with the valence band hole must be strongly phonon-assisted, or accompanied by alternative cooling pathways.

Our results contribute to the search for new methods to control non-radiative processes in colloidal quantum dots, paving the way to new exciting application. Importantly, elimination of *all* non-radiative Auger processes is not always desired. For example, for low-threshold lasing biexciton Auger decay should be inhibited while fast hot-electron cooling is a desired effect to maintain population inversion. Our work highlights the possibility of such independent control over different Auger processes.

4.6 • Methods

Synthesis of CdSe/CdS core–shell QDs following Ref. 55.

Precursor preparation. Cadmium precursor I [0.1 M $Cd(OA)_2$] was prepared by mixing oleic acid (3.68 g), octadecene (25.92 g) and $CdAc_2$ (0.64 g), and heating to 120°C under vacuum for 2 h. Cadmium precursor II [0.1 M $Cd(OA)_2$] was prepared by dissolving $CdAc_2$ (1.10 g) in oleic acid (10.83 g) and octadecene (43.20 mL), and heating to 120°C under vacuum for 2 h. Selenium precursor was prepared by dissolving elemental selenium (4.25 g) in trioctylphosphine (22.5 g) at 50°C, followed by the addition of octadecene (35.7 g). Sulfur precursor solution (0.1 M) was prepared by dissolving sulfur (0.032 g) in octadecene (10 mL) at 180°C.

Synthesis of CdSe QD seeds. CdSe QD seeds were synthesized in a 50 mL three-neck flask using a Schlenk-line. Trioctylphosphine oxide (1.11 g), ODA (3.20 g) and Cd precursor I (4.9 g) were mixed, and heated to 295°C. Se precursor (5.2 g) was then injected. The mixture was cooled down after 10 min. The particles were diluted by adding 1 equivalent of hexane. The QDs were washed by adding 2 equivalents of methanol, collecting the upper hexane layer (colored), and then precipitating the QDs with 1 equivalent of acetone. Finally, the QDs were dissolved in toluene.

Growth of a CdS shell. The CdSe seeds (10^{-7} M of QDs with 3.8 nm diameter in toluene), octadecene (5.0 g) and octadecylamine (1.5 g) were mixed and heated to 150°C for 1 h to remove all toluene. The reaction temperature was then increased to 240°C. The shell was grown layer-by-layer under N_2 by injecting a precursor solution (sufficient to form the next shell on all QDs) every 30 min, alternating cation and anion precursors. The reaction solution was kept at 240°C for 1 h, then allowed to cool down to room temperature, and diluted with 1 equivalent of hexane. The QDs were washed by adding 2 equivalents of methanol, collecting the upper hexane layer (colored), and then precipitating the QDs with 1 equivalent of acetone. Finally, the QDs were dissolved in toluene.

Pump-push-probe transient absorption. A film of QDs is deposited on an IR-transparent CaF_2 substrate from a concentrated solution in toluene, and dried.

For ultrafast experiments, the output of a regenerative 1 kHz Ti:Sapphire amplifier system (Coherent, Legend Elite Duo, 800 nm, 40 fs pulse duration, 7 mJ per pulse) was split into three parts. One part was frequency doubled in a BBO crystal to generate 400-nm 50-fs visible pump pulses. The second part was used to generate mid-IR push pulses by pumping a commercial parametric amplifier with a difference frequency generation (DFG) stage (HE TOPAS, 80 fs, 0.22 eV photons). The rest was used to pump a 3-stage home-built optical parametric amplifier followed by a DFG stage to provide independently tunable ~70 fs IR (0.21 eV) probe and reference pulses. Slight detuning of push and probe frequencies was done to minimize background of scattered push light in the detection path.

All the beams were focused on the sample using a 20 cm concave parabolic mirror. The time delays of pump and probe were controlled using mechanical delay stages. In the pump–probe measurement a 500 Hz mechanical modulator was set in the pump beam path, and for pump–push–probe measurements the modulator was moved to the push beam path. All beams had the same (p) polarization. The probe and reference IR beams passed through the sample and were spectrally dispersed and detected by a nitrogen-cooled mercury cadmium telluride detector array. The measurements were performed under N_2 flow to avoid water vapor absorption of IR light and sample degradation.

Single-QD spectroscopy. For single-QD measurements the QDs were spin-coated on a glass cover slip from a dilute dispersion in toluene, and covered with a layer of PMMA. They were excited with 10 ps, 10 MHz, 532 nm laser pulses through an 100× oil immersion objective with NA 1.4. From the absorption cross-section of the QDs ($\sigma_{abs} = 10^{-15}$ cm^2 at 532 nm)[46] we estimate that the laser power of 200 nW focused to a diffraction-limited spot corresponds to the generation of $\langle N \rangle \approx 0.1$ excitons per laser pulse.

Derivation of the effect of a blind time on the two-photon correlation function. We consider the integrated peak area of the peaks in the two-photon correlation function $g^{(2)}$ of a pulsed experiment on a single QD, as a function of the blind

time Δ applied in the analysis (see Fig. 4.4). For each coincidence count in the $g^{(2)}$-plot, a pair of two photons was detected. When the length of Δ is increased, an increasing number of coincidence counts in the $g^{(2)}$-plot are removed. Only those remain for which *both* photon detection events fall outside the blind time Δ.

The zero-delay peak originates from cascade emission events, i.e. biexciton emission ($X_2 \rightarrow X$) followed by single-exciton emission $X \rightarrow 0$. The total number of coincidence counts in the zero-delay peak N_0 is proportional to:

$$N_0(\Delta) \propto P(X_2 \notin \Delta \wedge X \notin \Delta) = P(X_2 \notin \Delta) \propto e^{-\Delta/\tau_{X_2}}. \tag{4.1}$$

Here we use that since biexciton emission *always* preceeds single-exciton emission, the probability $P(X_2 \notin \Delta \wedge X \notin \Delta)$ that both emissions are outside the blind time is the same as the probability $P(X_2 \notin \Delta)$ that the biexciton emission (i.e. the first emission) is outside.

The off-peaks originate from two single-exciton emission events following two different laser pulses (if we neglect the contribution of biexciton emission to the total emission intensity, which is justified in the limit of low excitation power). The total number of coincidence counts $N_{\neq 0}$ in these peaks is proportional to:

$$N_{\neq 0}(\Delta) \propto P(X^{(1)} \notin \Delta) \times P(X^{(2)} \notin \Delta) \propto e^{-\Delta/\tau_X} e^{-\Delta/\tau_X} = e^{-2\Delta/\tau_X} \tag{4.2}$$

where $P(X^{(j)} \notin \Delta)$ denotes the probability that emissions $j = 1,2$ fall outside the blind time.

Hence, with increasing Δ the integrated area of the zero-delay peak decays with time constant τ_{X_2} while the area of the off-peaks decays with $\tau_X/2$.

k·p calculations of the energy levels and Auger rates in core–shell QDs. The calculations of the biexciton Auger recombination rate in CdSe/CdS core–shell QDs were performed within an eight-band **k·p** model using a scheme similar to the one described in Ref. 247 where core-only CdSe QDs were addressed. The modification in the model presented here is the addition of CdS shell layer, which produces QDs having two heterointerfaces: one between the CdSe core and the CdS shell, and another between the CdS shell and the environment. The wavefunctions of the electrons and holes are written in the form $\mathbf{\Psi} = (\Psi_c, \mathbf{\Psi}_v)$, where Ψ_c is the two-component conduction band spinor envelope function, and $\mathbf{\Psi}_v = (\Psi_x, \Psi_y, \Psi_z)$ is the valence band spinor envelope vector.[56] The procedure of finding the wavefunctions is the same as in Ref. 247, except for the finite potential barriers for holes assumed here, and modified boundary conditions. In finding the electron wavefunctions of both ground and excited states, the boundary conditions imposed at each of the interfaces are those given in Eq. 3 in Ref. 247 with the matrix $\hat{T}$ set to unity and $\lambda = 0$.

For ground state (bound) hole wavefunctions, the boundary conditions at the core–shell interface are the continuity of each row of the follow vector:

$$\begin{pmatrix} \hat{\mathbf{r}} \cdot \mathbf{\Psi}_v \\ \hat{\mathbf{r}} \times \mathbf{\Psi}_v \\ \left(\frac{E_p}{E_c - E} + \beta_\ell - \beta_h\right)(\nabla \cdot \mathbf{\Psi}_v) + \beta_h \frac{\partial}{\partial r}(\hat{\mathbf{r}} \cdot \mathbf{\Psi}_v) \\ \beta_h \frac{\partial}{\partial r}(\hat{\mathbf{r}} \times \mathbf{\Psi}_v) \end{pmatrix} \tag{4.3}$$

where $\hat{\mathbf{r}}$ is the radial unit vector, $E_p = 2m_0P^2$ with m_0 the free electron mass and P the Kane parameter, E_c is the conduction band edge energy, E is the energy of the hole state, $\beta_\ell = \gamma_1 + 4\gamma$ and $\beta_h = \gamma_1 - 2\gamma$, where γ, γ_1 are modified Luttinger parameters. To describe the excited (unbound) hole states, we assume the flat-band approximation in which $\beta_h = 0$. This simplifies the excited hole boundary conditions at the core–shell interface, which reduce to the continuity of:

$$\begin{pmatrix} \hat{\mathbf{r}} \cdot \mathbf{\Psi}_v \\ \left(\frac{E_p}{E_c - E} + \beta_\ell\right)(\nabla \cdot \mathbf{\Psi}_v) \end{pmatrix} \tag{4.2}$$

Outside the QD, the hole, just like the electron, is described by a free-particle two-component spinor wavefunction. It then follows that the boundary conditions for the ground state hole at the shell–environment interface are the equality of the first and third rows in Eq. 4.3 here with the right-hand-side of Eq. 3 in Ref. 247, with an additional condition of $\hat{\mathbf{r}} \times \mathbf{\Psi}_v = 0$ at this interface. The boundary conditions for the excited holes at the shell–environment interface are the equality of Eq. 4.2 here with the right-hand-side of Eq. 3 in Ref. 247. Once the electron and hole wavefunctions and energies are found, the calculation of the Coulomb integrals is the same as in Ref. 247.

CHAPTER 5

Multi-photon quantum cutting in $Gd_2O_2S:Tm^{3+}$ to enhance the photo-response of solar cells

Based on

Multi-photon quantum cutting in $Gd_2O_2S:Tm^{3+}$ to enhance the photo-response of solar cells
Yu, D.C., Martín-Rodríguez, R., Zhang, Q.Y., Meijerink, A. & Rabouw, F.T.
Light Sci. Appl. **4**, e344 (2015)

ABSTRACT • Conventional photoluminescence yields at most one emitted photon for each absorption event. Downconversion (or quantum cutting) materials can yield more than one photon, by virtue of energy transfer processes between luminescent centers. In this work we introduce $Gd_2O_2S:Tm^{3+}$ as a multi-photon quantum cutter. It can convert near-infrared, visible, or ultraviolet photons into respectively two, three, or four infrared photons of ~1800 nm. The cross-relaxation steps between Tm^{3+} ions that lead to quantum cutting are identified from (time-resolved) photoluminescence as a function of Tm^{3+} concentration in the crystal. A model is presented reproducing how the Tm^{3+} concentration affects both the relative intensities of the various emission lines and the excited state dynamics, and providing insight in the quantum cutting efficiency. Finally, we discuss the potential application of $Gd_2O_2S:Tm^{3+}$ for spectral conversion to improve the efficiency of next-generation photovoltaics.

5.1 • Introduction

Over the last decade advanced luminescent materials have been developed exhibiting downconversion, also known as quantum cutting or quantum splitting.[35,145] In this process a high-energy photon is converted into two or more lower-energy photons, with a quantum efficiency of potentially well over 100%.[2] If the downconverted photons are in the visible range, this concept is of interest for color conversion layers in conventional lighting applications.[35,42,53,77] New exciting possibilities of downconversion to infrared (IR) photons lie in next-generation photovoltaics, aiming at minimizing the spectral mismatch losses in solar cells.[81,124,220]

Spectral mismatch is the result of the broad width of the spectrum emitted by the sun. Semiconductor absorber materials absorb only photons with an energy $\hbar\omega$ higher than the band gap E_g. To absorb many photons and produce a large electrical current, absorber materials must therefore have a small bandgap. However, since excited charge carriers rapidly thermalize to the edges of a semiconductor's conduction and valence bands, a high voltage output requires an absorber with a large band gap. Hence, materials with low transmission losses (leading to a large current) have high thermalization losses (leading to a low voltage), and vice versa.[157] These spectral mismatch losses constitute the major factor defining the relatively low Shockley-Queisser limit,[183] the maximum light-to-electricity conversion efficiency of 33% in a single-junction solar cell, obtained for a band gap of around 1.1 eV (= 1100 nm).[4]

Efficiencies higher than 33% can be reached with multi-junction solar cells, where a stack of multiple absorber materials are each optimized to efficiently convert different parts of the solar spectrum to electricity. While indeed efficiencies of over 40% have been obtained with this concept,[110] the devices are expensive and have limited tunability because of the requirement of high-quality contacts between the absorber materials with matching physical and chemical properties.

An alternative solution to beat the Shockley-Queisser limit is by optical conversion of the solar spectrum prior to entering the solar cell.[145,81,124,220] A large number of downconversion materials able to convert high-energy photons into multiple lower-energy ones have recently been developed. The downconversion process occurs by energy transfer between luminescent centers, either lanthanide ions with a wide range of energy levels[73,92,125,142,165,167,191,200] or organic molecules with low-energy triplet states.[236,237] If the IR photons generated are all absorbed by the solar cell material, the result can be a huge increase in current output.[157,169,220] Importantly, this concept does not impose requirements on the contact surface between conversion layer and solar cell, so it can

relatively easily be integrated in existing solar cell technologies.

In this work we introduce the quadruple-downconversion material $Gd_2O_2S:Tm^{3+}$. Depending on the excitation energy, it can yield two, three or even four IR photons (mainly around 1800 nm) per absorption event. The high-energy photons are cut by a series of cross-relaxation steps, where the initially excited Tm^{3+} ion transfers part of its energy to a neighboring Tm^{3+}. By examining the emission spectra and dynamics as a function of Tm^{3+} concentration in the Gd_2O_2S host crystal, we determine the operative cross-relaxation processes leading to four-photon quantum cutting, and quantify the rates and efficiencies. We find that already at a moderate Tm^{3+} concentration of 10% the excitation energy is very efficiently cut into IR quanta (in the $^3H_5$ level emitting at 1215 nm and in the $^3F_4$ level emitting at 1800 nm), with efficiencies of 199% for near-IR excitation at 800 nm, 298% for blue excitation at 470 nm, or 388% for ultraviolet (UV) excitation at 365 nm. We discuss the practical application of this multiple-downconversion material to increase the spectral response of solar cells (in particular Ge, of which the band gap is matched to the emission from the $^3F_4$ level). Efforts should be aimed at reducing losses due to concentration quenching of the $^3F_4$ level and increasing the absorption by means of a sensitizer. In addition to applications in next-generation photovoltaics, since the excitation can be in the first 'tissue-transparent spectral window' around 800 nm, and the emission of 1800 nm lies in the second window, the concept of efficient downconversion in Tm^{3+} may also be useful for bio-imaging applications.[213]

5.2 • One-to-two downconversion following excitation in the near-infrared

We start by examining downconversion from the $^3H_4$ and $^3F_{2,3}$ levels of Tm^{3+}. Fig. 5.1a shows the emission spectra of $Gd_2O_2S:Tm^{3+}(x\%)$ upon excitation in the $^3F_{2,3}$ level at 697 nm, from bottom to top for increasing Tm^{3+} concentration of x = 0.1 (black), 1 (red), 5 (yellow), and 10 (blue). The spectra are recorded on three separate detectors (boundaries indicated with vertical dashed lines), and normalized for each detector separately. Consequently, the relative intensities of emission lines can be compared between different Tm^{3+} concentrations, but not between different detectors. The emission lines are ascribed to the $^3H_4 \rightarrow {}^3H_6$ transition at 800 nm, the $^3H_5 \rightarrow {}^3H_6$ transition at 1215 nm, the $^3H_4 \rightarrow {}^3F_4$ transition at 1450 nm, and the $^3F_4 \rightarrow {}^3H_6$ transition at 1800 nm.[191,200] At low Tm^{3+} concentrations (0.1%, 1%) the emission is mainly from the $^3H_4$ level (lines indicated with a green triangle), while at higher concentrations (5%, 10%) emissions from $^3H_5$ (yellow square) and $^3F_4$ (red circle) dominate.

The observations are consistent with the relaxation pathways illustrated in Fig. 5.1b. Pathways I and II dominate at low Tm^{3+} concentrations. Pathways III and IV, which involve cross-relaxation between pairs of ions and result in downconversion, become more likely at higher Tm^{3+} concentration. Colored downward arrows represent photon emission, with symbols matching those marking the emission lines in Fig. 5.1a. Fast non-radiative $^3F_{2,3} \rightarrow {}^3H_4$ multi-phonon relaxation (dashed downward arrow) is evidenced by the absence of emission from the $^3F_{2,3}$ level. The occurrence of cross-relaxation processes (black solid arrows in pathways III and IV) is evidenced by the supralinear increase of emission intensity from the $^3H_5$ and $^3F_4$ levels with increasing Tm^{3+} concentration. Interestingly, while radiative decay from the $^3F_{2,3}$ level cannot compete with multi-phonon relaxation, cross-relaxation at high Tm^{3+} concentration (pathway IV) can, as evidenced by the observation of $^3H_5$ emission at 1215 nm at 5 and 10% Tm^{3+}. This already indicates that very fast rates are possible for cross-relaxation processes in $Gd_2O_2S:Tm^{3+}$.

To quantify the rates and efficiencies of downconversion by cross-relaxation from the $^3H_4$ state, we recorded photoluminescence (PL) decay curves excited in the $^3F_{2,3}$ level (697 nm) and record-

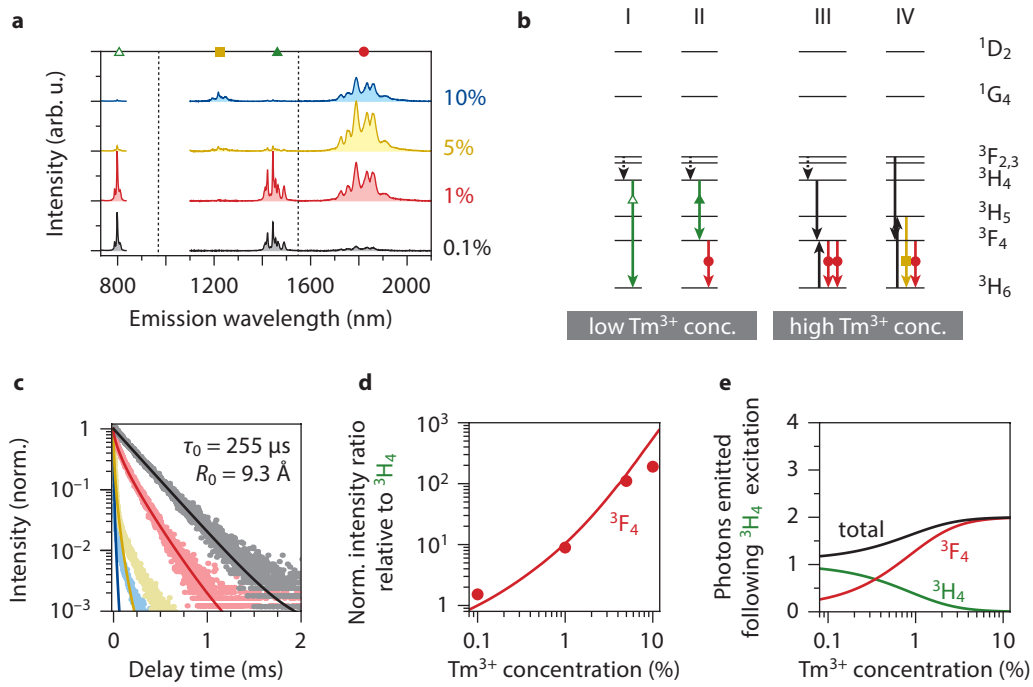

Figure 5.1 • One-to-two downconversion from the $^3F_{2,3}$ and $^3H_4$ levels. (**a**) Emission spectra of $Gd_2O_2S:Tm^{3+}(x\%)$ with x = 0.1 (black), 1 (red), 5 (yellow) and 10 (blue) excited in the $^3F_{2,3}$ level at 697 nm. They are recorded on three different detectors as indicated by vertical dashed lines, and normalized for each detector individually. (**b**) Possible decay pathways of the Tm^{3+} $^3F_{2,3}$ excited state. Pathways I and II dominate at low Tm^{3+} concentration, III and IV at high concentration. Multiphonon relaxation is depicted as dashed downward arrows, photon emission as colored arrows with symbols matching those marking emission lines in **a**, and cross-relaxation as black solid arrows. (**c**) Decay dynamics of the $^3H_4 \rightarrow {}^3H_6$ emission at 800 nm upon excitation in the $^3F_{2,3}$ level at 697 nm. Solid lines are fits to Eq. 5.2, from which we obtain an intrinsic lifetime of τ_0 = 255 µs and a critical radius for cross-relaxation of R_0 = 9.3 Å. (**d**) The ratio between the $^3F_4$ and $^3H_4$ emission intensities as obtained from the spectra shown in **a** (circles), normalized to the ratio at 0.1% Tm^{3+}. The solid line is the ratio expected based on the dynamics of **c**. (**e**) The theoretical absolute photon yield from the $^3H_4$ level (green), $^3F_4$ level (red) and the total yield (black) following excitation into the $^3H_4$ (or $^3F_{2,3}$) level.

ed at 800 nm at the $^3H_4 \rightarrow {}^3H_6$ transition. Fig. 5.1c shows that for increasing Tm^{3+} concentration the decay of the $^3H_4$ level rapidly becomes faster, consistent with cross-relaxation (pathway III in Fig. 5.1b). We fit the decay curve for 0.1% Tm^{3+} to a single exponential, assuming no cross-relaxation, and obtain an intrinsic lifetime of the $^3H_4$ level of τ_0 = 255 µs. Next we assume that at higher Tm^{3+} concentration cross-relaxation can take place via dipole–dipole coupling in pairs of Tm^{3+} ions. Cross-relaxation is a first-order ET process, i.e. involving one donor ion and one acceptor ion. In case of dipole–dipole coupling, the cross-relaxation rate Γ_{xr} for a single pair of ions is proportional to the inverse sixth power of the separation r:[73,142,241]

$$\Gamma_{xr} = C_{xr} r^{-6}. \tag{5.1}$$

The prefactor C_{xr} (which represents the strength of cross-relaxation) can alternatively be convert-

ed to a critical radius $R_0 = (\tau_0 C_{xr})^{1/6}$, defined as the pair separation at which cross-relaxation has a 50% efficiency. We fit the decay curve for 1% Tm^{3+} to an analytical model that assumes a random substitution of Tm^{3+} for Gd^{3+} in the Gd_2O_2S crystal (see the Methods section for a derivation):

$$I(t) = I(0)e^{-t/\tau_0} \prod_{i}^{\text{shells}} \left(1 - x + x\, e^{-C_{xr} t / r_i^6}\right)^{n_i} \tag{5.2}$$

where x is the Tm^{3+} acceptor concentration, and (r_i, n_i) represents the 'neighbor list' given by the crystal structure of Gd_2O_2S. The best fit is obtained for $C_{xr} = 2.5$ nm^6 ms^{-1}, corresponding to a critical radius of $R_0 = 9.3$ Å. This translates into a cross-relaxation rate in a nearest-neighbor pair (at a separation of 3.5 Å; one Tm^{3+} in the $^3H_4$ state and one in the $^3H_6$ ground state) of $1/0.75$ µs, 341× faster than radiative decay from the $^3H_4$ level. In Fig. 5.1c the solid lines through the data for 5% (yellow) and 10% (blue) Tm^{3+} are drawn following Eq. 5.2 without additional fit parameters. They show a good match with the experimental PL decay curves, despite migration processes that can occur at such high Tm^{3+} concentrations but are not accounted for in the model.

Based on the possible decay pathways of the $^3H_4$ level (Fig. 5.1b), and with the assumption that no non-radiative loss occurs, we can estimate (see Methods for details) the expected light yield following excitation at 700–800 nm in the $^3F_{2,3}$ or $^3H_4$ level. Using the fitted value for the cross-relaxation strength C_{xr} (Fig. 5.1c) we can estimate how the expected intensity ratio between $^3F_4$ and $^3H_4$ emission varies with Tm^{3+} concentration. In Fig. 5.1d we plot the result (solid red line), and compare it to the experimental data (red circles). Efficient cross-relaxation causes the relative intensity in the IR at 1800 nm from the $^3F_4$ level to increase by more than a factor 100 as the Tm^{3+} concentration increases from 0.1% to 10%. Hence, our model of $(^3H_4, {}^3H_6) \rightarrow (^3F_4, {}^3F_4)$ cross-relaxation (Fig. 5.1b) via dipole–dipole interaction is consistent with both the excited state dynamics (Fig. 5.1c) and the resulting emission intensities (Fig. 5.1d). The deviation between experiment and model that occurs in Fig. 5.1d at 10% Tm^{3+} can be understood in terms of concentration quenching of the $^3F_4$ level (see below).

In Fig. 5.1e we plot the one-to-two downconversion quantum yield η_2 (see Methods) following excitation into the $^3H_4$ level as a function of Tm^{3+} concentration. We distinguish between photons emitted from the $^3H_4$ level and those emitted from the $^3F_4$ level, based on our model and the fitted cross-relaxation strength C_{xr}. While at low Tm^{3+} concentration the emission comes primarily from the $^3H_4$ level (green line), at higher concentration $^3F_4$ emission (red line) is by far dominant. We see that $Gd_2O_2S:Tm^{3+}$ can efficiently downconvert photons of 800 nm. Because of cascade emission (pathway II in Fig. 5.1b) η_2 is already over 100% (namely, 119%) at 0.1% Tm^{3+} (Refs. 23,190,191). It increases to 199% at 10% Tm^{3+}, as cross-relaxation becomes much more efficient. Experimentally, the absolute downconversion quantum yield is difficult to determine quantitatively because emissions occur over such a large spectral range, including very close to the excitation wavelength and beyond the detector range. We can however already see in Fig. 5.1a that the absolute emission intensity from the $^3F_4$ level decreases when the Tm^{3+} goes up from 5% to 10%. This tells us that in our samples concentration quenching effects (see below) are present at high Tm^{3+} concentrations, which diminish the actual quantum yields to below those estimated in Fig. 5.1e.

5.3 • One-to-three downconversion following blue excitation

Next, we investigate the efficiency of downconversion from the $^1G_4$ level of Tm^{3+}. We perform a similar analysis as presented above in Fig. 5.1 but now for higher-energy excitation, in order to build up a complete picture of the chain of cross-relaxation processes that can take place in $Gd_2O_2S:Tm^{3+}$. The $^1G_4$ level is excited with blue photons of 470 nm, which each provide enough energy to generate three IR photons of 1800 nm ($^3F_4 \rightarrow {}^3H_6$). Fig. 5.2a shows emission spectra of $Gd_2O_2S:Tm^{3+}$ following excitation in the $^1G_4$ level at 470 nm. In addition to the emission lines observed in Fig. 5.1a, from $^3H_4$ (green triangles), $^3H_5$ (yellow square) and $^3F_4$ (red circle), we now see emission from the $^1G_4$ level (blue crosses). The line at 650 nm is from the $^1G_4 \rightarrow {}^3F_4$ transition, while the emission around 1200 nm, observed at low Tm^{3+} concentration (0.1%, 1%), originates from the $^1G_4 \rightarrow {}^3H_4$ transition. Note that at high Tm^{3+} concentration (5%, 10%) the spectrum around 1215 nm is of a different origin, namely the $^3H_5 \rightarrow {}^3H_6$ transition, as evident from a comparison to Fig. 5.1a. Overall, we see that at the lowest Tm^{3+} concentration (0.1%) the emission comes mainly from the $^1G_4$ level (blue crosses), at intermediate concentration (1%) $^3H_4$ emission is relatively strong (green triangles), while at high concentration (5%, 10%) the spectrum is dominated by $^3H_5$ (yellow square) and $^3F_4$ (red circle) emissions.

Based on these observations we propose relaxation pathways for the $^1G_4$ level as depicted in Fig. 5.2b. At low Tm^{3+} concentration pathways I, II and III result in cascade emissions from the $^1G_4$ level (while there can also be direct radiative decay to the ground state, not depicted). At high Tm^{3+} concentration ($^1G_4$, $^3H_6$) $\rightarrow$ ($^2F_{2,3}$, $^3F_4$) cross-relaxation occurs,[200] after which the $^2F_{2,3}$ and $^3H_4$ excitations are further downconverted as already discussed in Fig. 5.1. The result at high Tm^{3+} concentration (5%, 10%) can be three IR emissions for each blue excitation, consistent with the dominant contribution from $^3H_5$ (yellow square) and $^3F_4$ (red circle) emissions in the spectra of Fig. 5.2a. There may also be ($^1G_4$, $^3H_6$) $\rightarrow$ ($^3H_4$, $^3H_5$) and ($^1G_4$, $^3H_6$) $\rightarrow$ ($^3H_5$, $^3H_4$) cross-relaxation processes,[200] which would lead to similar downconversion schemes, except that the $^3H_5$ level is directly populated in the first step of the sequence of cross-relaxation steps. Since experimentally we observe $^3H_5$ emission only at the highest concentrations, the dominant first cross-relaxation process is probably ($^1G_4$, $^3H_6$) $\rightarrow$ ($^2F_{2,3}$, $^3F_4$).

We investigate the downconversion dynamics of the $^1G_4$ level, as shown in Fig. 5.2c. The solid lines are fits of the experimental data (symbols) to the model of cross-relaxation by dipole-dipole coupling (Eq. 5.2). We obtain for the $^1G_4$ level an intrinsic lifetime of $\tau_0 = 105$ µs, and a cross-relaxation strength of $C_{xr} = 11.8$ nm^6 ms^{-1}, corresponding to a critical radius of $R_0 = 10.4$ Å. This means that the cross-relaxation rate of the $^1G_4$ level in a nearest-neighbor pair is $1/0.16$ µs, 660× faster than radiative decay. Such very fast cross-relaxation rates explain why in upconversion experiments only very low Tm^{3+} concentrations of no higher than 1% yield bright blue upconversion emission.[166,224]

As we did in Fig. 5.1d for $^3H_4$ excitation, with the fit results on the decay dynamics (Fig. 5.2c) we can calculate the theoretical photon yields upon $^1G_4$ excitation (see Methods). Fig. 5.2d shows the intensity ratio of $^3F_4$ (red) or $^3H_4$ (green) emission to $^1G_4$ emission. The experimental data (data points) show a good match to the theoretical predictions (solid lines). This confirms the occurrence of the sequence of cross-relaxation processes depicted in Fig. 5.2b, which lead to the generation of three IR photons for each blue excitation. As a check, the dashed green line in Fig. 5.2d shows the expected $^3H_4$-to-$^1G_4$ intensity ratio in the hypothetical case that only the first cross-relaxation process occurred [i.e. ($^1G_4$, $^3H_6$) $\rightarrow$ ($^3F_{2,3}$, $^3F_4$)] rather than a sequence of two cross-relaxation steps. This scenario is not consistent with the experimental emission spectra.

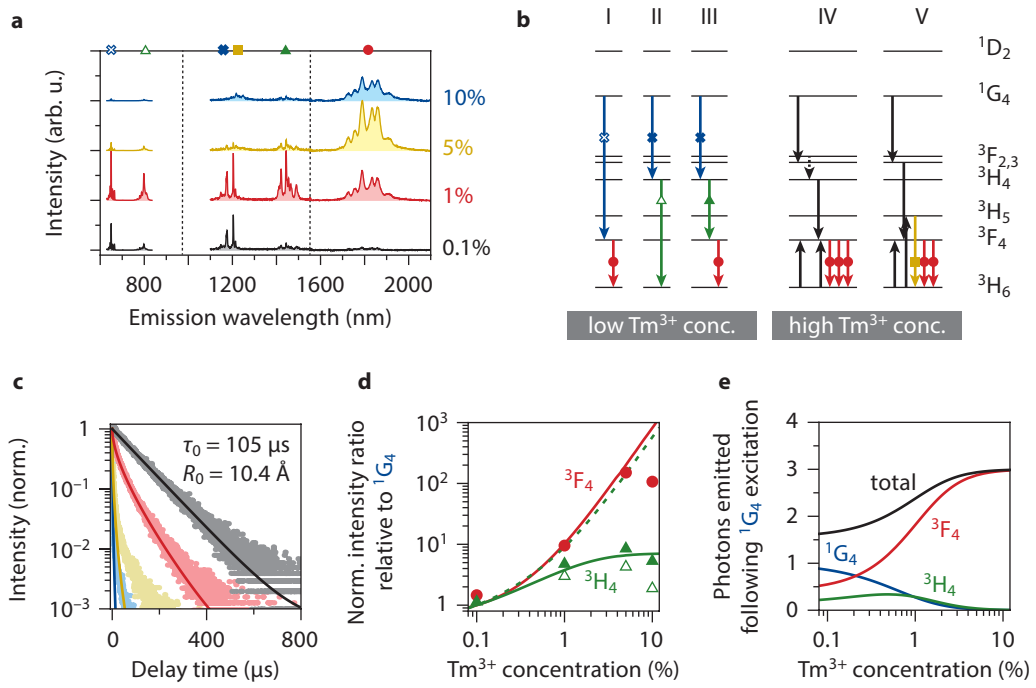

Figure 5.2 • One-to-three downconversion from the $^1G_4$ level. (**a**) Emission spectra of $Gd_2O_2S:Tm^{3+}(x\%)$ with x = 0.1 (black), 1 (red), 5 (yellow) and 10 (blue) excited in the $^1G_4$ level at 470 nm. They are recorded on three different detectors as indicated by vertical dashed lines, and normalized for each detector individually. (**b**) Possible decay pathways of the Tm^{3+} $^1G_4$ excited state include cascade processes (pathways I, II and III). At higher Tm^{3+} concentrations ($^1G_4$, $^3H_6$) → ($^3F_{2,3}$, $^3F_4$) cross-relaxation becomes the dominant decay pathway (IV and V), followed by further cross-relaxation from the $^3F_{3,2}$ and $^3H_4$ levels (see Fig. 5.1). (**c**) The decay dynamics of the $^1G_4$ level in $Gd_2O_2S:Tm^{3+}(x\%)$ with x = 0.1 (black), 1 (red), 5 (yellow) and 10 (blue), excited at 465 nm and detected for the $^1G_4$ → $^3F_4$ emission at 653 nm. Solid lines are fits to Eq. 5.2, yielding an intrinsic lifetime of τ_0 = 105 µs and a critical radius for cross-relaxation of R_0 = 10.4 Å. (**d**) The intensity of emission from the $^3F_4$ (red circles) and $^3H_4$ (filled green triangles for $^3H_4$ → $^3F_4$, open green triangles for $^3H_4$ → $^3H_6$) levels relative to the $^1G_4$ level. Solid lines are the ratios as expected from our model (see Methods). The dashed green line would be the expected ratio of $^3H_4$ emission to $^1G_4$ emission if only the first step in the sequence of cross-relaxations occurred, i.e. ($^1G_4$, $^3H_6$) → ($^3F_{2,3}$, $^3F_4$). The experimental data (green triangles) clearly deviate from this trend, proving the occurrence of multiple cross-relaxation steps. (**e**) The total downconversion efficiency from the $^1G_4$ level (black line), and separated in emission from the $^1G_4$ (blue), $^3H_4$ (green) and $^3F_4$ (red) level.

In Fig. 5.2e we plot the absolute photon yields following $^1G_4$ excitation as calculated with our model (see Methods). At low Tm^{3+} concentration the emission comes mainly from the $^1G_4$ level (blue line), although through cascade processes (pathways I, II, III in Fig. 5.2b) the other levels emit as well. Consistent with the experimental spectra (Fig. 5.2a) emission comes primarily from the $^3F_4$ level (red line) at high Tm^{3+} concentration. The total downconversion efficiency increases from 165% at 0.1% Tm^{3+} (by virtue of cascade emissions) to 298% at 10% (determined by cross-relaxation). Again, in practice the absolute photon yield is limited by concentration quenching of the $^3F_4$ emission at high Tm^{3+} concentrations.

5.4 • One-to-four downconversion following UV excitation

Finally, we increase the excitation energy even further to be resonant with the $^1D_2$ level of Tm^{3+}. Excitation photons in the UV (of 365 nm) have sufficient energy to yield as many as four IR photons from the $^3F_4$ level. Fig. 5.3a shows the emission spectra of $Gd_2O_2S:Tm^{3+}$ excited in the $^1D_2$ level at 365 nm. Interestingly, we observe emission from the $^1D_2$ level (purple diamonds), and at higher Tm^{3+} concentrations from $^3H_4$ (green triangles), $^3H_5$ (yellow square) and $^3F_4$ (red circle), but not from the $^1G_4$ level (compare Fig. 5.2a). This indicates that cross-relaxation processes occur, but not to the $^1G_4$ level.

In Fig. 5.3b we depict the decay pathways from the $^1D_2$ level dominant in $Gd_2O_2S:Tm^{3+}$. At low Tm^{3+} concentration there are possibilities for cascade emission (pathways I, II and III).[200,223,243] At high Tm^{3+} concentration, since we see in the emission spectrum that cross-relaxation to the $^1G_4$ level is not efficient, the dominant process must be ($^1D_2$, $^3H_6$) → ($^3H_4$, $^3F_{2,3}$) as depicted in pathways IV and V.[200] After reaching the $^3H_4$ and $^3F_{2,3}$ levels the Tm^{3+} ions decay further, by cross-relaxation, as discussed above in Fig. 5.1. The result can be as many as four emitted IR photons (red circles and yellow square) for each UV excitation.

Fig. 5.3c shows the decay dynamics of the $^1D_2$ level recorded for the $^1D_2 \rightarrow {}^3F_4$ emission at 465 nm. We again apply our model of cross-relaxation by dipole–dipole interaction (Eq. 5.2) to fit the dynamics. The best fit is obtained for an intrinsic lifetime of $\tau_0 = 4.0$ µs, and a cross-relaxation strength of $C_{xr} = 32.8$ nm^6 ms^{-1} (corresponding to a critical radius of $R_0 = 7.1$ Å, and a nearest-neighbor cross-relaxation rate of $1/0.06$ µs, 69× faster than the intrinsic decay). Hence, this cross-relaxation process from the $^1D_2$ level is less efficient than those from the $^3H_4$ (Fig. 5.1c) and $^1G_4$ levels (Fig. 5.2c), but still competes strongly with radiative decay.

To confirm the occurrence of one-to-four downconversion in $Gd_2O_2S:Tm^{3+}$ via the scheme of three cross-relaxation steps (Fig. 5.3b) we compare the relative emission intensities in the spectra to the predictions of our model (see Methods). Fig. 5.3d shows a good correspondence between the experiment (data points) and the model (solid lines). Downconversion already occurs at low Tm^{3+} concentration because of several possible cascade processes (pathways I, II and III in Fig. 5.3b). Nevertheless, the relative intensity of $^3F_4$ emission increases by a factor 100 as the Tm^{3+} increases from 0.1% to 10%. As a check, we can see that if we do not include the second and third steps of the sequence of cross-relaxations, the agreement between model and experiment is very poor (dashed green line, compared to the green triangles).

Fig. 5.3e presents the theoretical photon yield for excitation in the $^1D_2$ level. Already at low Tm^{3+} concentration of 0.1% the downconversion quantum yield is as high as 186% by virtue of the many possibile cascade processes (pathways I, II and II in Fig. 5.3b) through which the UV excitation can relax.[23] The downconversion quantum yield increases to 388% at 10% Tm^{3+}, as cross-relaxation becomes more efficient. By comparing the absolute emission intensities (Fig. 5.3a) from the $^3F_4$ level for 5% and 10% Tm^{3+}, however, it becomes again apparent that concentration quenching effects are at play at the highest Tm^{3+} concentration, which reduce the effective downconversion yield (see below).

5.5 • Enhancing the efficiency of a Ge solar cell

Our results highlight $Gd_2O_2S:Tm^{3+}$ as a promising material to efficiently downconvert the near-IR, visible, and UV part of the spectrum to IR photons. It is however important to realize that two challenges have to be solved if this material were to significantly enhance the photo-response of next-generation solar cells: (1) the relatively weak absorption of Tm^{3+}, and (2) concen-

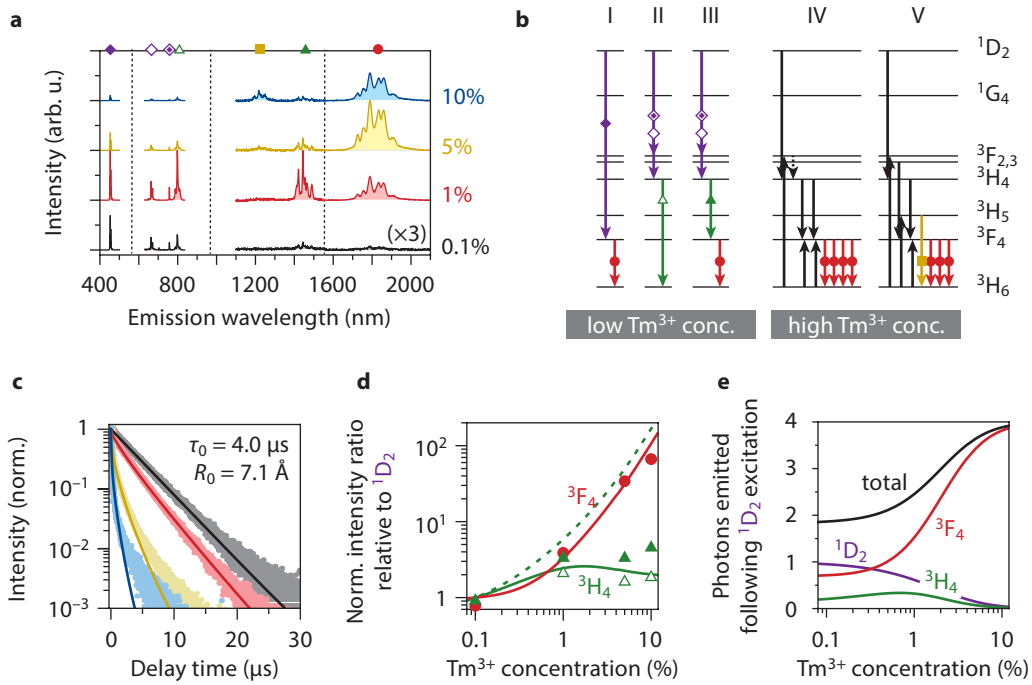

Figure 5.3 • One-to-four downconversion from the $^1D_2$ level. (**a**) Emission spectra of $Gd_2O_2S:Tm^{3+}(x\%)$ with $x = 0.1$ (black), 1 (red), 5 (yellow) and 10 (blue) excited in the $^1D_2$ level at 365 nm. (**b**) Decay pathways from the $^1D_2$ level. Pathways I, II and III involve cascade emission of photons (colored downward arrows marked with symbols corresponding to those in **a**), and are operative already at low Tm^{3+} concentration. At high Tm^{3+} concentration cross-relaxation (solid black arrows in pathways IV and V) becomes more efficient, effectively cutting the excitation energy in four and leading to emission in the IR (yellow square and red circle in **a**). (**c**) PL decay curves of the $^1D_2$ level recorded at 465 nm ($^1D_2 \rightarrow {}^3F_4$). Solid lines are fits to Eq. 5.2, yielding an intrinsic lifetime of $\tau_0 = 4.0$ µs for the $^1D_2$ level and a critical radius for cross-relaxation of $R_0 = 7.1$ Å. (**d**) The emission intensity from $^3F_4$ (red circles) and $^3H_4$ (green filled triangles: $^3H_4 \rightarrow {}^3F_4$; green open triangles: $^3H_4 \rightarrow {}^3H_6$) relative to $^1D_2$. Solid lines are the trends expected based on our model (see Methods). If we include only the first cross-relaxation step in our model [i.e. $(^1D_2, {}^3H_6) \rightarrow ({}^3H_4, {}^3F_{2,3})$] the predicted intensity ratio between $^3H_4$ and $^1D_2$ (green dashed line) deviates strongly from the experimental data points. (**e**) The total downconversion quantum yield (black line) following $^1D_2$ excitation. Emission comes mainly from the $^1D_2$ level at low Tm^{3+} concentration, and from $^3F_4$ at high Tm^{3+} concentration. Consistent with the experiment (**a**) emission from the $^3H_4$ level is brightest at intermediate concentrations around 1%.

tration quenching of the $^3F_4$ level.

The absorption spectrum of Tm^{3+}, as for most other trivalent lanthanide ions, contains a few narrow lines originating from the intraconfigurational transitions from the $^3H_6$ ground state to the many possible excited states. In the inset of Fig. 5.5a we show the excitation spectra of Tm^{3+} for the $^3H_4 \rightarrow {}^3F_4$ emission. The absorptions are relatively weak, and narrow. A more detailed investigation of the different line intensities in the full excitation spectrum, as a function of Tm^{3+} concentration, is presented in Fig. 5.4. Analysis of the excitation line intensities (Fig. 5.4c) confirms the occurrence of multi-photon quantum cutting in $Gd_2O_2S:Tm^{3+}$. To increase the effective ab-

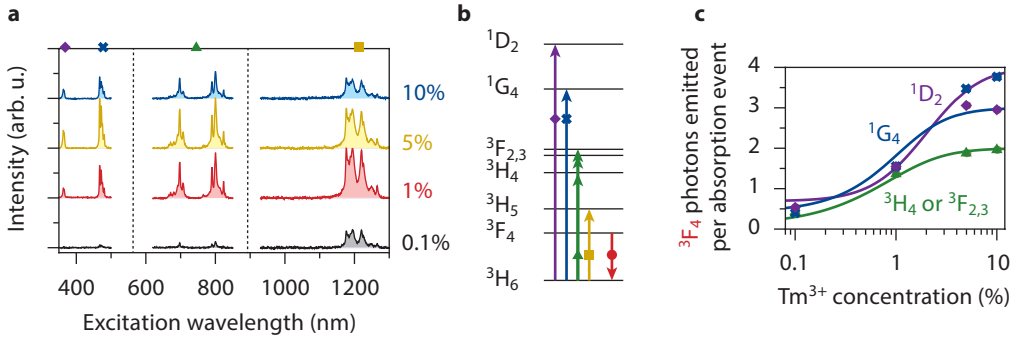

Figure 5.4 • Excitation spectra detected for the $^3F_4$ emission. (**a**) Excitation spectra of $Gd_2O_2S:Tm^{3+}(x\%)$ with $x = 0.1$ (black), 1 (red), 5 (yellow), 10 (blue) detected at the $^3F_4 \rightarrow {}^3H_6$ emission at 1800 nm. Spectra are recorded in three separate measurements (indicated with dashed vertical lines). We see that the intensity of the $^3H_6 \rightarrow {}^3H_5$ excitation line (yellow square) decreases if the Tm^{3+} is increased to above 1%, indicating concentration quenching of the $^3F_4$ emission. Excitation lines of the higher-energy transitions have the highest intensity at 5% Tm^{3+}. This indicates that upon increasing the Tm^{3+} concentration from 1% to 5%, the increased efficiency of cross-relaxation compensates concentration quenching. (**b**) Excitation transitions responsible for the lines observed in the spectra of panel **a**. The transitions are marked with symbols corresponding to those in panel **a**. The red circle marks the $^3F_4 \rightarrow {}^3H_6$ emission. (**c**) The number of $^3F_4$ photons emitted following excitation in the $^3H_4$ or $^3F_{2,3}$ levels (green solid line), $^1G_4$ level (blue), and $^1D_2$ level (purple), as predicted by our model. Data points are the relative integrated intensities of the corresponding excitation lines, normalized to the intensity of the $^3H_6 \rightarrow {}^3H_5$ excitation line around 1215 nm (yellow square in **a**). Since excitation in the $^3H_5$ level yields one $^3F_4$ photon (see the description of our model below), this procedure directly yields the number of $^3F_4$ photons resulting from excitation in the other levels. There is a reasonable agreement between the theoretical prediction and experimental data points. Note that the value of photon yield determined in this way is insensitive to concentration quenching effects of the $^3F_4$ level.

sorption strength of Tm^{3+} and make it broad-band, sensitizers would be needed.[125,223,228,243] For example, the material could be co-doped with strongly absorbing centers such as Ce^{3+} for sensitization[228] (see Ch. 7, where we investigate Ce^{3+} as a sensitizer for Tb^{3+}). The concept of sentization allows that the absorption spectrum of a material is tuned independently of the downconversion process. This opens up interesting but challenging possibilities, such as materials that convert UV and near-IR to IR photons but are transparent to visible light, for use as luminescent solar concentrators in windows.

Fig. 5.5a shows the fraction of the solar spectrum made available through downconversion, if we assume broad band effective absorption of Tm^{3+} by means of sensitization. We consider a solar cell with a bandgap of 0.65 eV (= 1900 nm; e.g. Ge) such that all $^3F_4$ emission can be absorbed. The red area in Fig. 5.5a is directly usable by this solar cell. In the ideal sensitized downconverter (based on the excitation spectrum of Tm^{3+}; inset of Fig. 5.5a) all photons with energy higher than $\hbar\omega > 3.36$ eV are funneled to the $^1D_2$ level, photons of 2.59 eV $< \hbar\omega <$ 3.36 eV to the $^1G_4$ level, and photons of 1.50 eV $< \hbar\omega <$ 2.59 eV to the $^3H_4$ level. The colored areas in Fig. 5.5a indicate the gain enabled by one-to-two (green), one-to-three (blue) and one-to-four (purple) downconversion. The spectral mismatch losses would be reduced from 59% in the bare solar cell to 37% in combination with the downconverter (compared to 50% for a Si solar cell).

The essential last step of the downconversion is the emission of photons from the $^3F_4$ level.

As apparent from the relatively low absolute emission intensities at 10% Tm^{3+} (Figs. 5.1a, 5.2a, 5.3a), the $^3F_4$ level is partially quenched at this concentration. This can be ascribed to concentration quenching, i.e. migration of the excitation energy over the Tm^{3+} sublattice until it reaches a quenching site. The effect has been studied in detail by Auzel *et al.*[51] for the lowest excited state of Yb^{3+}, Er^{3+} and Ho^{3+} in the crystalline host material Y_2O_3. They used a model where the PL quantum efficiency of the lowest excited state depends on the concentration of luminescent ions x as

$$\eta_{em}(x) = \left[1 + \frac{9}{2\pi}\left(\frac{x}{x_0}\right)^2\right]^{-1}, \qquad (5.3)$$

where x_0 is the critical concentration. Auzel *et al.* found critical concentrations of around $x_0 \approx 10\%$ for the three ions investigated.[51] The effect of concentration quenching in a crystal doped with luminescent ions depends on the material quality.[244] With our equipment we are unable to measure η_{em} for the IR emission from the lowest excited state of Tm^{3+} in our samples, but the values could be expected to be similar to those found by Auzel *et al.*[51] for Yb^{3+}, Er^{3+} and Ho^{3+} in Y_2O_3.

In Fig. 5.5b we plot how spectral losses of the situation depicted in Fig. 5.5a (solar cell of band gap 0.65 eV plus $Gd_2O_2S:Tm^{3+}$ downconverter) would depend on Tm^{3+} concentration and η_{em} of the $^3F_4$ level. Not surprisingly, the lowest spectral losses require a high Tm^{3+} concentration (for efficient cross-relaxation) and a high η_{em}. Since, as described by Eq. 5.3, high Tm^{3+} concentrations come with a lower η_{em}, there is some optimum concentration. The solid black line in Fig. 5.5b de-

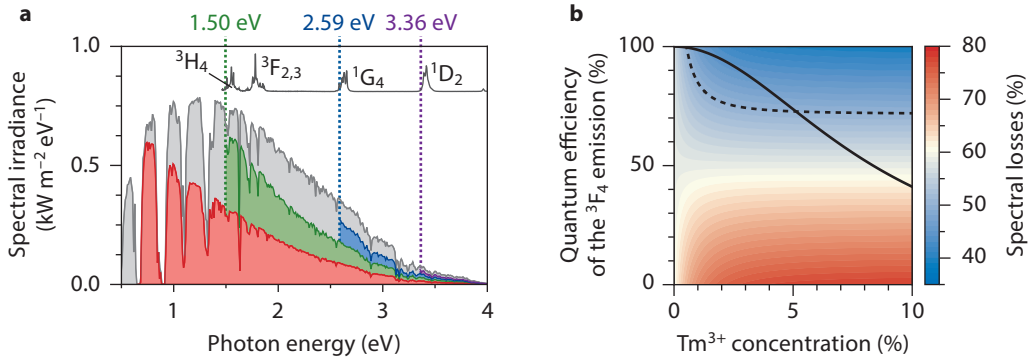

Figure 5.5 • Reducing spectral mismatch losses with $Gd_2O_2S:Tm^{3+}$. (**a**) A simple solar cell with a band gap of 0.65 eV (= 1900 nm; for example Ge) can only effectively use the part of the solar spectrum shaded red. Spectral conversion by a sensitized downconverter layer of $Gd_2O_2S:Tm^{3+}$ would make additional parts available: the green part by one-to-two downconversion from the $^3H_4$ level, the blue part by one-to-three downconversion from the $^1G_4$ level, and the purple part by one-to-four downconversion from the $^1D_2$ level. The inset shows the positions of the various absorption lines in $Gd_2O_2S:Tm^{3+}$ in the excitation spectrum of the $^3H_4 \rightarrow {}^3F_4$ emission at 1450 nm. (**b**) The calculated spectral losses as a function of the Tm^{3+} concentration in Gd_2O_2S and the PL quantum efficiency η_{em} for the IR emission from the $^3F_4$ level. The solid black line shows how η_{em} varies with Tm^{3+} concentration according to Eq. 5.3, and assuming a critical concentration of $x_0 = 10\%$. For the actual crystal where the concentration quenching is directly linked to the Tm^{3+} concentration as described by Eq. 5.3, the spectral losses as a function of Tm^{3+} concentration are the color values at the position of the solid line. They are lowest (42%) at 2–3% Tm^{3+}. The dashed line is the contour corresponding to the spectral losses of 50% for a crystalline Si solar cell (band gap = 1.1 eV). We see that a $Gd_2O_2S:Tm^{3+}$ with a Ge solar cell can beat crystalline Si.

picts how η_{em} would vary with Tm^{3+} concentration according to Eq. 5.3 with $x_0 = 10\%$. The lowest spectral losses are 42% at a Tm^{3+} concentration of 2–3%, significantly lower than the 59% for the bare solar cell with a band gap of 0.65 eV and even lower than Si (50%; dashed line).

5.6 • Conclusion

We have demonstrated that Tm^{3+} in Gd_2O_2S can effectively downconvert high-energy photons from the near-IR, visible and UV to IR photons of a wavelength of 1800 nm. By virtue of a variety of cross-relaxation processes an excitation in the $^3H_4$ level (800 nm) can be converted to two IR photons, from the $^1G_4$ level (470 nm) to three, and from the $^1D_2$ level (365 nm) to four. We have quantified the cross-relaxation rates and efficiencies for different Tm^{3+} concentrations by fitting the decay dynamics of the levels involved. For the three downconversion processes, the efficiencies are near 200%, 300% and 400% for 10% Tm^{3+}. These results are consistent with the relative intensities of emission lines as found experimentally. In the end we have discussed the potential application of $Gd_2O_2S:Tm^{3+}$ as a spectral converter for photovoltaics. In particular, this material could greatly improve the efficiency of Ge solar cells, to such extent that they could even outperform crystalline Si in terms of spectral mismatch losses.

5.7 • Methods

$Gd_2O_2S:Tm^{3+}$ powder samples. Microcrystalline samples of $Gd_2O_2S:Tm^{3+}(x\%)$ with x = 0.1, 1.0, 5.0, and 10.0 were specially prepared for this research by Tailorlux GmbH (Münster, Germany). The crystal structure was confirmed using X-ray powder diffractometry. Gd_2O_2S has a $P\bar{3}ml$ space group, where Tm^{3+} dopant ions substitute for Gd^{3+} at a site with point symmetry C_{3v} surrounded by four oxygen and three sulfur atoms.[3]

Experimental details. Emission spectra and PL decay curves were recorded using an Edinburgh Instruments FLS920 spectrofluorometer equipped with a 450 W xenon lamp. Visible emission was detected by a Hamamatsu R928 photomultiplier tube (400–850 nm). Emission spectra in the IR were recorded on a liquid-nitrogen cooled Hamamatsu R5509-72 photomultiplier tube (1100–1600 nm) and a thermoelectrically cooled G5852 InGaAs PIN photodiode (1500–2100 nm). For PL emission measurements the samples were excited with the xenon lamp. For PL decay measurements an optical parametric oscillator (OPO) system (Opotek HE 355 II) pumped by the third harmonic of a Nd:YAG laser (pulse width 10 ns; repetition rate 20 Hz) was used for excitation in the $^3F_{2,3}$ (Fig. 5.1c) or $^1G_4$ (Fig. 5.2c) levels. PL decay of the $^1D_2$ level (Fig. 5.3c) was excited with an Ekspla NR342B-10-SH/DUV OPO system (pulse width 5 ns; repetition rate 10 Hz).

Modeling the energy transfer dynamics (of cross-relaxation). Cross-relaxation is a first-order energy transfer process, i.e. a single donor ion transfers energy to a single acceptor ion. In the present case of $Gd_2O_2S:Tm^{3+}$ the donors and acceptors are both Tm^{3+}, in an excited state and in the ground state, respectively. We consider an excited donor ion in a crystalline environment, and assume that acceptors random substitute cation sites, as expected in a $Gd_2O_2S:Tm^{3+}$ crystal (or in $LaPO_4:Ce^{3+},Tb^{3+}$; Ch. 7) from the chemical similarity of ions in the lanthanide series. Each nearby cation site then has an independent probability x (the overall acceptor concentration) to contain an acceptor ion, hence add C_{xr}/r_j^6 to the decay rate or, equivalently, a factor $\exp(-C_{xr}/r_j^6)$ to the decay trace of the donor (with r_j the separation from the donor). The decay trace of the ensemble of donors contains contributions from all possible donor environments:

$$I(t) = I(0)e^{-t/\tau_0}\prod_j^{\text{sites}}\left(1 - x + x\,e^{-C_{xr}t/r_j^6}\right) \tag{5.4}$$

where the product runs over all (nearby) cation sites, and each factor accounts for a probability x that cation site j adds a decay component $\exp(-C_{xr}/r_j^6)$ and a probability $1 - x$ that it does not. Using the crystalline nature of the host we can write the above equation in terms of 'shells' (see also Fig. 7.4a),[73,142] leading to Eq. 5.2. The crystal structure determines the so-called neighbor list $\{r_i, n_i\}$, i.e. around each cation site there are shells of neighboring sites at distances $\{r_1, r_2, r_3, ...\}$ which each contain at most $\{n_1, n_2, n_3, ...\}$ acceptor ions. Since the cross-relaxation rate rapidly decreases with increasing donor–acceptor separation (as r^{-6}), we can truncate the product in Eq. 5.2 to only include shells closer than 1–2 nm. We neglect the possibility of donor-to-donor energy migration. This effect may explain deviations between the experimental decay dynamics and our model.

Calculating the light yield under excitation in $^3F_{2,3}$ or $^3H_4$. We simplify the scheme of possible decay pathways by assuming that the $^3F_{2,3}$ level and $^3H_5$ level decay via multi-phonon relaxation to the next lower-energy level ($^3H_4$ and $^3F_4$, respectively, because of the small energy gaps of ~1800 cm^{-1} between $^3F_{2,3}$ and $^3H_4$, and ~2400 cm^{-1} between $^3H_5$ and

$^3F_4$), while there is no multi-phonon relaxation from the other levels. We further neglect the possibility of upconversion processes. The $^3F_4$ level then has only a single decay pathway, namely radiative decay to the ground state $^3H_6$. The $^3H_4$ level has four decay pathways: radiative decay to (1) $^3H_5$, (2) $^3F_4$ or (3) $^3H_6$, or (4) cross-relaxation with a neighboring Tm^{3+} in the ground state. Pathways (1) and (2) are cascades yielding 1 photon from the $^3H_4$ level and 1 photon from the $^3F_4$ level, pathway (3) yields 1 single photon from $^3H_4$, while pathway (4) yields 2 photons from $^3F_4$. The relative probabilities of the pathways depend on the branching ratios of $^3H_4$, which we take from Ref. 189 determined for a crystal structure (Y_2O_3) similar to ours (Gd_2O_2S). We denote the combined branching ratio of the pathways $^3H_4 \rightarrow {}^3H_5$ (followed by $\rightarrow {}^3F_4$ multi-phonon relaxation) and $^3H_4 \rightarrow {}^3F_4$ as $\beta_2 = 8.3\% + 14.7\% = 23.0\%$. The relative decay probabilities further depend on the cross-relaxation efficiency η_{xr2} which depends on the fitted cross-relaxation strength C_{xr}. The theoretical value of η_{xr2} is calculated by integrating the area under the PL decay curve:

$$\eta_{xr2} = 1 - \tau_0^{-1} \int_0^\infty e^{-t/\tau_0} \prod_i^{\text{shells}} \left(1 - x + x\, e^{-C_{xr2} t / r_i^6}\right)^{n_i} dt\,. \tag{5.5}$$

We obtain for the expected number of photons emitted from the $^3H_4$ level

$$\langle N \rangle_{^3H_4} = 1 - \eta_{xr2}, \tag{5.6}$$

and for the number emitted from the $^3F_4$ level

$$\langle N \rangle_{^3F_4} = \beta_2 (1 - \eta_{xr2}) + 2\eta_{xr2}. \tag{5.7}$$

The total one-to-two downconversion efficiency is given by the total number of emitted photons $\eta_2 = \langle N \rangle_{^3H_4} + \langle N \rangle_{^3F_4}$.

Calculating the light yield under excitation in $^1G_4$. From the $^1G_4$ level we consider possibilities of cascade emission (pathways I–III in Fig. 5.2b) as well as the cross-relaxation ($^1G_4$, $^3H_6$) $\rightarrow$ ($^3F_{2,3}$, $^3F_4$) [or equivalently ($^1G_4$, $^3H_6$) $\rightarrow$ ($^3H_4$, $^3H_5$) and ($^1G_4$, $^3H_6$) $\rightarrow$ ($^3H_5$, $^3H_4$)] (pathways IV and V in Fig. 5.2b). For the lower lying levels ($^3F_{2,3}$, $^3H_4$, $^3H_5$, $^3F_4$) we use the same simplified treatment as explained above. The cross-relaxation efficiency η_{xr3} from the $^1G_4$ level is calculated as in Eq. 5.5 by using the relevant cross-relaxation strength C_{xr3}. We get branching ratios from Ref. 189. The combined branching ratio of $^1G_4 \rightarrow {}^3F_{2,3}$ (followed by $\rightarrow {}^3H_4$ multi-phonon relaxation) and $^1G_4 \rightarrow {}^3H_4$ is $\beta_{32} = 0.5\% + 2.0\% + 11.9\% = 14.4\%$. The combined branching ratio of $^1G_4 \rightarrow {}^3H_5$ (followed by $\rightarrow {}^3F_4$ multi-phonon relaxation) and $^1G_4 \rightarrow {}^3F_4$ is $\beta_{31} = 32.4\% + 6.4\% = 38.8\%$. We can write for the expected number of photons from the $^1G_4$ level

$$\langle N \rangle_{^1G_4} = 1 - \eta_{xr3}, \tag{5.8}$$

for the number emitted from the $^3H_4$ level

$$\langle N \rangle_{^3H_4} = \left[\eta_{xr3} + \beta_{32}(1 - \eta_{xr3})\right](1 - \eta_{xr2}), \tag{5.9}$$

and for the number emitted from the $^3F_4$ level

$$\langle N \rangle_{^3F_4} = \eta_{xr3} + \beta_{31}(1 - \eta_{xr3}) + \left[\eta_{xr3} + \beta_{32}(1 - \eta_{xr3})\right]\left[2\eta_{xr2} + \beta_2(1 - \eta_{xr2})\right]. \tag{5.10}$$

And the total one-to-three downconversion efficiency is given by the total number of emitted photons $\eta_3 = \langle N \rangle_{^1G_4} + \langle N \rangle_{^3H_4} + \langle N \rangle_{^3F_4}$.

Calculating the light yield under excitation in $^1D_2$. From the $^1D_2$ state we take into account the cascade processes of Fig. 5.3b in the main text (pathways I–III) and the cross-relaxation ($^1D_2$, $^3H_6$) $\rightarrow$ ($^3H_4$, $^3F_{2,3}$) (pathways IV and V in Fig. 5.3b in the main text). For the lower lying levels ($^3F_{2,3}$, $^3H_4$, $^3H_5$, $^3F_4$) we again use the simplified treatment as explained above. Eq. 5.5 yields the cross-relaxation efficiency η_{xr4} from the $^1D_2$ level, while we use Ref. 189 for the branching ratios. The combined branching ratio of $^1D_2 \rightarrow {}^3F_{2,3}$ (followed by $\rightarrow {}^3H_4$ multi-phonon relaxation) and $^1D_2 \rightarrow {}^3H_4$ is $\beta_{42} = 2.7\% + 4.3\% + 6.1\% = 13.2\%$. The combined branching ratio of $^1D_2 \rightarrow {}^3H_5$ (followed by $\rightarrow {}^3F_4$ multi-phonon relaxation) and $^1D_2 \rightarrow {}^3F_4$ is $\beta_{41} = 0.3\% + 67.5\% = 67.8\%$. The expected number of photons from the $^1D_2$ level is given by

$$\langle N \rangle_{^1D_2} = 1 - \eta_{xr4}, \tag{5.11}$$

for the number emitted from the $^3H_4$ level

$$\langle N \rangle_{^3H_4} = \left[2\eta_{xr4} + \beta_{42}(1 - \eta_{xr4})\right](1 - \eta_{xr2}), \tag{5.12}$$

and for the number emitted from the $^3F_4$ level

$$\langle N \rangle_{^3F_4} = \beta_{41}(1 - \eta_{xr4}) + \left[2\eta_{xr4} + \beta_{42}(1 - \eta_{xr4})\right]\left[2\eta_{xr2} + \beta_2(1 - \eta_{xr2})\right]. \tag{5.13}$$

And the total one-to-four downconversion efficiency is given by the total number of emitted photons $\eta_4 = \langle N \rangle_{^1D_2} + \langle N \rangle_{^3H_4} + \langle N \rangle_{^3F_4}$.

CHAPTER 6

Modeling the cooperative energy transfer dynamics of quantum cutting for solar cells

Based on

Modeling the cooperative energy transfer dynamics of quantum cutting for solar cells
Rabouw, F.T. & Meijerink, A.
J. Phys. Chem. C **119**, 2364–2370 (2015)

ABSTRACT • Cooperative energy transfer (ET) is a quantum cutting (or downconversion) process where a luminescent center splits its excited-state energy in two by simultaneous transfer to two nearby acceptor centers, thus yielding two low-energy photons for each high-energy photon absorbed. It has the potential to greatly enhance the efficiency of phosphors for lighting, or the UV/blue response of next generation photovoltaics. Many pairs of luminescent centers have been claimed to enable quantum cutting by cooperative ET. However, direct proof that the ET mechanism is cooperative is often lacking. Here we present a model that can be used to fit or predict the dynamics of cooperative ET in co-doped crystals, as a function of the concentration of acceptor centers. It also yields an analytical expression for the efficiency of cooperative ET. Our model can be used to provide evidence for quantum cutting materials, quantify the ET parameter(s), and optimize the doping concentration.

6.1 • Introduction

Phosphor materials convert one color of light to another. They are used in devices such fluorescent lamps and LED displays. Many phosphors are microcrystalline materials doped with luminescent ions. It can be desirable to combine different luminescent centers in the same phosphor material. This allows that one of the centers is optimized for strong absorption and transfers its energy to a different type of center, optimized for efficient emission of the desired color of light. Such a scheme also enables easier control over the phosphor properties, e.g. large 'Stokes' or 'anti-Stokes' shifts important in emerging technologies such as background-free biolabeling[168] or luminescent solar concentrators.[229] Of particular interest are couples of luminescent centers in which 'quantum cutting' (or 'downconversion') can take place.[35,124,145] In this process the excitation energy on a donor center is split in two, potentially yielding two emitted photons per absorption event. Splitting occurs either by 'cooperative' energy transfer (ET) where the energy is simultaneously transferred to two (or more) nearby acceptor centers,[73] or by cross-relaxation where the donor transfers only part of its excitation energy to an acceptor.[43,89,142,152] The maximum possible photon-to-photon conversion efficiency of downconversion phosphors is 200%. While the search for downconversion phosphors was initiated by the lighting industry, even more challenging and promising applications are in next-generation photovoltaics. If the wavelength of the emitted downconverted photons can be matched to the bandgap E_g of a solar cell material, a downconversion layer would in principle be able to boost the response of the solar cell to high-energy photons from the solar spectrum ($\hbar\omega > 2E_g$) by a factor 2.

Many materials have been reported to perform downconversion or quantum cutting.[92,94,123,128,132,193,210] Usually they are doped with lanthanide ions, where the rich energy level structure allows for many different types of ET processes. Often it is straightforward to demonstrate that ET takes place from one type of lanthanide ion to another, by recording emission and excitation spectra.[92,94,123,128,132,193,210] The challenge is to actually prove the occurrence of quantum cutting in a particular couple, and identify which ET mechanism is operative (e.g. cooperative ET, or cross-relaxation). Ideally, an integrating-sphere measurement would demonstrate a quantum efficiency of >100%, i.e. that more photons are emitted than absorbed. However, such direct proof can only be obtained if both the ET and the emission of the downconverted light in the phosphor are very efficient. Any significant loss channel would make the overall quantum efficiency drop below 100%, even if quantum cutting does take place in the material. For example, 'space separated' quantum cutting was demonstrated with an integrating-sphere measurement[165] in closely separated Si nanocrystals. Because the overall quantum efficiency does not exceed 100%,

proof of quantum cutting had to come from a step-wise increase of quantum efficiency when the excitation energy was increased to above twice the emission energy. This method is not generally applicable to other quantum cutting materials, unless they have a continuous excitation spectrum.

A more general way to prove quantum cutting, not obscured by efficiency losses due to other processes, is to examine the ET dynamics. Photoluminescence (PL) decay measurements of the donor emission reveal the rate of ET. By investigating how the ET rate changes with increasing acceptor doping concentration in the material, one can establish the type of ET process that takes place. For example, our group has demonstrated that YPO_4:Tb^{3+},Yb^{3+} is a promising downconversion material, because ET from Tb^{3+} to Yb^{3+} is cooperative.[73] $LiYF_4$:Pr^{3+},Yb^{3+} also exhibits downconversion, but here the ET process responsible was shown to be cross-relaxation from Pr^{3+} to Yb^{3+}.[142] In contrast, YAG:Ce^{3+},Yb^{3+} is no good downconversion material, because ET from Ce^{3+} to Yb^{3+} is single-step downshifting via an intermediate Ce^{4+}–Yb^{2+} charge transfer state,[123,241] where half of the original energy is lost as heat.

In these previous works a Monte Carlo method was used to model the ET dynamics as a function of acceptor concentration.[73,142,241] By comparing the modeled dynamics to the experimental PL decay curves one can distinguish between different ET mechanisms. For first-order ET processes (i.e. one donor transfers to one acceptor) we have shown that, with the same assumptions as done in the Monte Carlo model (see below), there is an exact analytical expression for the ET dynamics (see also Chs. 5,7).[142,241] In addition, the Inokuti-Hiroyama[6] and Yokota-Tanimoto[7] models provide approximate formulas by neglecting that the crystalline structure of the host material imposes a discrete distribution of donor–acceptor separations. These models are used in many publications to fit ET dynamics, and quantify ET rate constants and efficiencies. Unfortunately, a convenient analytical expression for cooperative ET — important for quantum cutting — has not been reported yet.

Here we present a quasi-continuous model for cooperative ET, which yields an analytical approximation for the cooperative ET dynamics and for the cooperative ET efficiency as a function of acceptor concentration. It explicitly takes into account the possible nearest-neighbor configurations of each donor center, but averages out the acceptor density beyond the nearest-neighbor shell. The quasi-continuous model very accurately reproduces the results of the more involved Monte Carlo model when applied to the data of Vergeer *et al.*[73] We further test that the model yields a good approximation of the ET dynamics as well as of the ET efficiency, independent of whether the host crystal geometry has a high or a low symmetry. In the end we briefly discuss that our model can easily be adjusted or extended to include the possibility of (a combination of) other ET mechanisms.

6.2 • Downconversion by cooperative energy transfer

Potential downconversion phosphors co-doped with luminescent centers must exhibit emission from the acceptor center upon excitation of the donor. However, such an observation alone does not prove downconversion. The claim of downconversion by cross-relaxation is often supported by a comparison between excitation spectra of the acceptor luminescence and of the donor luminescence.[43,89,152] While such analysis demonstrates from which energy level on the donor ion transfer to the acceptor occurs, it does not prove which ET mechanism is operative if several are possible. Our group has previously analyzed the ET dynamics in potential downconversion phosphors to investigate the contribution of cooperative ET.[73,142,241] In YPO_4 the ET from Tb^{3+} to Yb^{3+} was found to be cooperative[73] (Fig. 6.1a). Hence, there is true quantum cutting which (depending on the quantum efficiency of Yb^{3+} emission) can yield two NIR photons for each UV/blue exci-

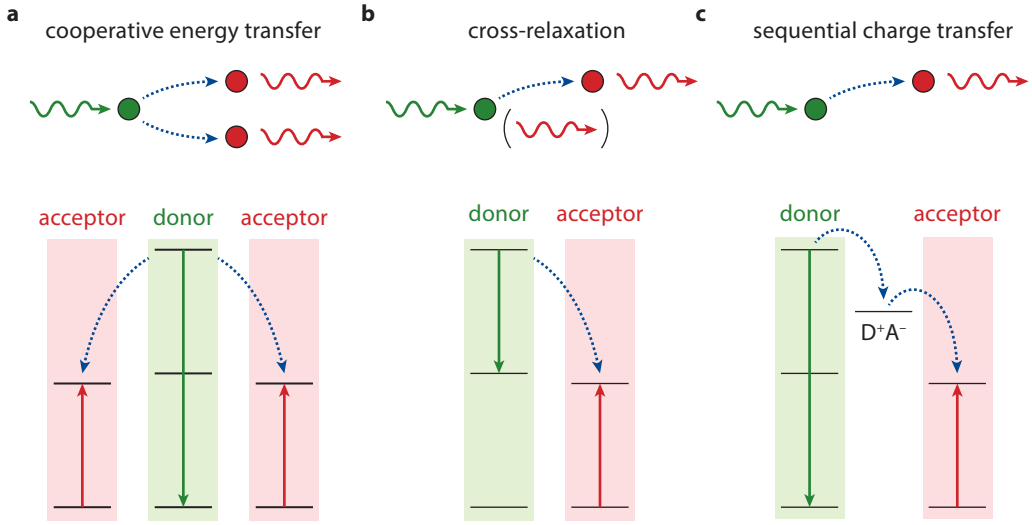

Figure 6.1 • ET mechanisms between lanthanide donor–acceptor pairs. Various ET pathways are possible, in a couple where the donor has a state at energy *E* and the acceptor a state at energy *E*/2. (**a**) Cooperative ET is simultaneous transfer to two nearby acceptors. If the acceptor emits efficiently, the result is two emitted photons for one absorbed photon. (**b**) In the case of cross-relaxation the acceptor transfers only part of its energy to a single acceptor, reaching some intermediate state. This leads to a 1-to-2 photon conversion only if both the acceptor and the intermediate state of the donor emit. (**c**) Sequential charge transfer can effectively transfer the donor energy to a single acceptor via an intermediate charge transfer state, where all excess energy is lost as heat.

tation. In $LiYF_4$ the ET from Pr^{3+} to Yb^{3+} was shown to be cross-relaxation from ($^3P_0$, $^7F_{7/2}$) to ($^1G_4$, $^7F_{5/2}$)[142] (Fig. 6.1b). Also here the final result can be two NIR photons from Yb^{3+} for each blue excitation, because after cross-relaxation the intermediate $^1G_4$ state of Pr^{3+} can transfer its energy to a second Yb^{3+} acceptor center. ET from Ce^{3+} to Yb^{3+} in YAG, on the other hand, can never lead to downconversion with a quantum efficiency of >100% because it is a one-donor-to-one-acceptor process via an intermediate charge transfer state[123,241] (Fig. 6.1c).

The dynamics and efficiency of *first-order* ET processes involving a single acceptor center (such as in Figs. 6.1b,c) can be calculated analytically, under the assumptions that (1) donor and acceptor centers randomly substitute cation sites in a crystal (justified by the chemical similarity of the lanthanide ions), (2) the ET rate is only dependent on the distance between the donor and acceptor centers (not on the orientation of the transition moments), and (3) no energy migration takes place over the donor sublattice (see also Chs. 5,7).[142,241] Alternatively, there are simpler approximate expressions that ignore the discreteness of the crystal geometry[6] but that can be extended to include the effect of donor-to-donor energy migration.[7] In contrast, the possibility of *second-order* cooperative ET has until now only been analyzed with a Monte Carlo model. Sometimes the continuous models of Inokuti-Hiroyama or Yokota-Tanimoto for *first-order* ET are used, without justification, to fit cooperative ET.[92,128]

Below we first briefly describe how the Monte Carlo model of cooperative ET works. We then show that with an approximation one can obtain an analytical 'quasi-continuous' expression for the dynamics and efficiency of cooperative ET. As for the first-order ET processes, both the Monte

Carlo and the quasi-continuous model make the basic assumptions are that (1) donors and acceptors are randomly distributed over cation sites in the crystal, (2) the ET rate depends only on the distance between donor and acceptors, and (3) there is no donor-to-donor energy migration. The difference with the first-order ET processes is that cooperative ET involves two (rather than one) simultaneous steps: ET from the donor to acceptor A, and ET from the same donor to acceptor B. The rate of cooperative ET via dipole–dipole interaction from the donor to the acceptor pair (A,B) is proportional to the inverse sixth power of both donor-acceptor separations:

$$\Gamma_{\text{coop}} = C_{\text{coop}} r_{\text{A}}^{-6} r_{\text{B}}^{-6}, \tag{6.1}$$

where C_{coop} is a constant representing the cooperative ET strength for the particular donor–acceptor couple. For a donor center with many nearby acceptors the total cooperative ET rate is a sum over all acceptor *pairs*. This difference with the first-order ET processes, where the summation is over all single acceptors, causes a different approach to be needed to obtain an analytical formula for dynamics and efficiency.

6.3 • The Monte Carlo method

In Refs. 73,142,241 the dynamics of cooperative ET were calculated with a Monte Carlo algorithm. It simulates the distribution of environments, i.e. arrangements of surrounding acceptor ions, that donor ions can have in a crystal where donors and acceptors randomly substitute cation sites. The ordered structure of the crystal allows that the cation sites around a central donor ion are grouped into 'shells', i.e. discrete distances at which cation sites can be found (the nearest-neighbor shell, the next-nearest-neighbor shell, etc.). A particular donor environment is characterized by a set of numbers (m_1, m_2, m_3, ...) denoting how many acceptor ions there are in shells 1, 2, 3, ... This set determines the number of possible acceptor pairs, and their separation from the central donor. The total cooperative ET rate of a donor ion with a particular environment is obtained by summing over all acceptor pairs:

$$\Gamma_{\text{coop}} = C_{\text{coop}} \left[\sum_{i}^{\text{shells}} \binom{m_i}{2} r_i^{-12} + \frac{1}{2} \left(\sum_{i}^{\text{shells}} m_i r_i^{-6} \right)^2 - \frac{1}{2} \sum_{i}^{\text{shells}} m_i^2 r_i^{-12} \right], \tag{6.2}$$

where $\binom{m_i}{2} = \frac{m_i!}{m_i!(m_i-2)!}$ is the binomial coefficient. The first term is for acceptor pairs within the same shell, and the other two for acceptor pairs distributed over separate shells (to be precise, the third term cancels same-shell contributions that are contained in the second). The Monte Carlo algorithm randomly generates many environments, accounting for the total numbers of cation sites (n_1, n_2, n_3, ...) in each of the shells, and for the overall acceptor concentration x. Since the ET rate rapidly drops with increasing donor–acceptor separation, it is a good approximation to only take into account a limited number of shells (e.g. only those closer than 1–2 nm). The decay dynamics of the ensemble of donor ions is obtained by adding up the dynamics of all environments simulated:

$$I(t) \propto \mathrm{e}^{-\Gamma_0 t} \sum_{k=1}^{\text{env.}} \mathrm{e}^{-\Gamma_{\text{coop}}^{(k)} t}, \tag{6.3}$$

where $I(t)$ is the emission intensity at delay time t after the excitation pulse, Γ_0 is the 'intrinsic decay rate' of the donors (in the absence of cooperative ET; often the purely radiative decay rate), the summation runs over the environments simulated, and $\Gamma_{\text{coop}}^{(k)}$ is the cooperative ET rate for environment k (Eq. 6.2). To prove that cooperative ET takes place in a certain donor–acceptor couple, the Monte Carlo model should reproduce the experimental ET dynamics for all acceptor

concentrations with a single value for the ET strength C_{coop}.

6.4 • The quasi-continuous model

Here we present a quasi-continuous model that provides an approximate analytical expression for the decay dynamics of cooperative ET in a co-doped crystalline material. It has several advantages over the Monte Carlo algorithm described above, and previously used in our group. Most importantly, it does not involve Monte Carlo simulations which can be difficult to implement. Second, the expression is shorter (2–13 exponents with fixed relative rates and amplitudes) so that data fitting is faster and easier. And third, it does not require full knowledge of the crystal structure in terms of 'shells' as described above.

In the quasi-continuous model only the first shell (i.e. the nearest neighbors) is treated in a discrete way. We explicitly take into account that it contains an integer number of acceptor ions. In contrast, the rate distribution for ET to the crystal environment beyond the first shell (i.e. next-nearest neighbors and further) is averaged out. The probability $A(m_1)$ that a central donor has m_1 nearest-neighbor acceptors in a crystal structure with in total n_1 nearest-neighbor cation sites follows a binomial distribution. It depends on the overall cation concentration x, and is given by

$$A(m_1) = \binom{n_1}{m_1} x^{m_1} (1-x)^{n_1-m_1}. \tag{6.4}$$

The rate of cooperative ET $\Gamma_{\text{coop}}(m_1)$ for a donor ion with m_1 nearest-neighbor acceptors is obtained by summing over all acceptor pairs, each adding a contribution to the total ET rate according to Eq. 6.1. Averaging out the ET to acceptors beyond the first shell, we obtain the following expression:

$$\Gamma_{\text{coop}}(m_1) = C_{\text{coop}} \left[\binom{m_1}{2} r_1^{-12} + m_1 x\, r_1^{-6} \Sigma + \frac{x^2}{2} \Sigma^2 \right]. \tag{6.5}$$

Here the first term represents ET to a pair of nearest-neighbor acceptors, the second term ET with one of the acceptors a nearest neighbor, and the last term ET to two acceptors beyond the first shell. Σ denotes the total acceptor strength of all cation sites beyond the first shell (i.e. the next-nearest neighbors and further). We can get a simple expression for it by integration:

$$\Sigma = \int_{r_0}^{\infty} \rho\, r^{-6}\, 4\pi r^2\, \mathrm{d}r = \frac{4\pi\rho}{3 r_0^3}, \tag{6.6}$$

where ρ is the (average) number density of cation sites in the crystal. r_0 is a cutoff distance that separates the first shell of nearest neighbors from the rest of the crystal, and must be chosen somewhere between the nearest-neighbor distance and the next-nearest-neighbor distance. We found that a good definition is

$$r_0^3 = \frac{9 n_1}{8\pi\rho}. \tag{6.7}$$

This definition is such that a sphere with radius r_0 contains $1.5 n_1$ cations. Conveniently, it does not require knowledge of the exact crystal structure beyond the first shell. We tested that this definition yields a close approximation to the results of the Monte Carlo method for different crystal geometries (see below). The final expression for the decay dynamics of the ensemble of donor ions in the crystal is

$$I(t) = I(0) \mathrm{e}^{-\Gamma_0 t} \sum_{m_1=0}^{n_1} A(m_1) \mathrm{e}^{-\Gamma_{\text{coop}}(m_1) t}. \tag{6.8}$$

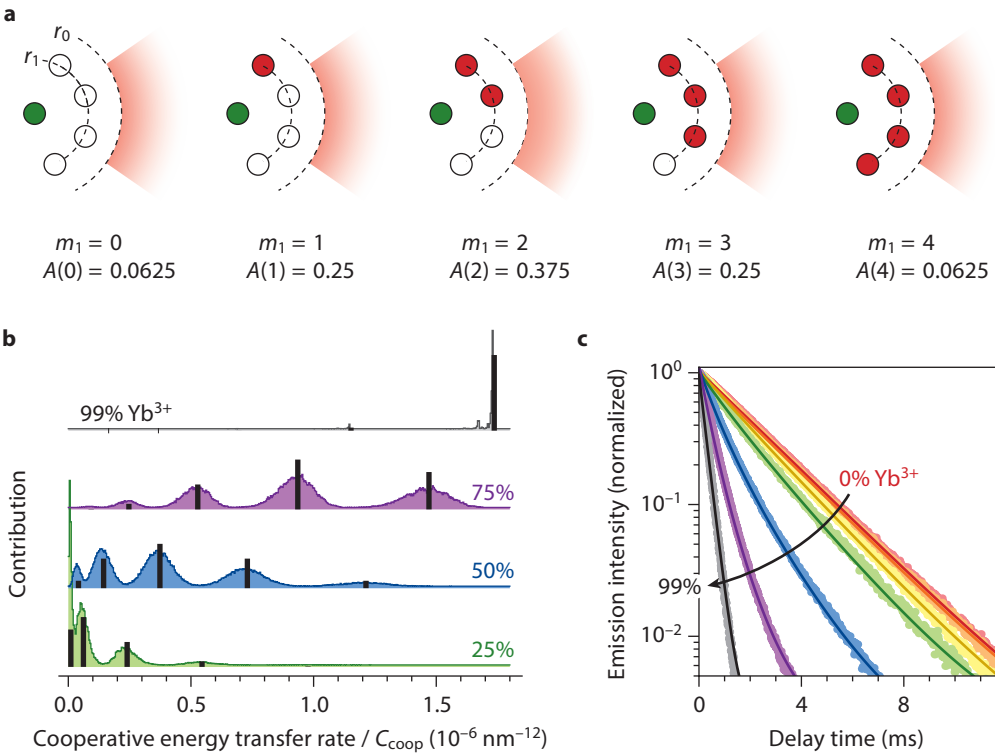

Figure 6.2 • The quasi-continuous model applied to cooperative ET in YPO_4:Tb^{3+},Yb^{3+}. (**a**) In the YPO_4 crystal with $n_1 = 4$ nearest neighbor cation sites, the quasi-continuous model explicitly considers $n_1 + 1 = 5$ different donor environments with $m_1 = 0$, 1, 2, 3, or 4 nearest-neighbor acceptors. The acceptor density beyond the first shell is averaged out to a fixed value of ρx. The numbers $A(m_1)$ indicate the probabilities for each of the five environments at an acceptor concentration of $x = 50\%$. (**b**) The distribution of ET rates at different acceptor concentrations (25%, 50%, 75%, 99%). The colored histograms represent the full distributions obtained with a Monte Carlo simulation, while the black bars are the approximation of the quasi-continuous model. (**c**) The result of fitting the experimental decay dynamics in YPO_4:Tb^{3+}(1%)Yb^{3+}(x%) with $x = 0$, 5, 15, 25, 50, 75, 99 to the quasi-continuous model (Eq. 6.8). Experimental data are reproduced from Ref. 73, with excitation in the $^7F_6 \rightarrow {}^5D_4$ transition at 489.6 nm and detection of the $^5D_4 \rightarrow {}^7F_5$ emission at 544 nm. All experimental curves are fitted accurately with a single value for the ET strength of $C_{coop} = 1.99 \times 10^{-6}$ nm^{12} ms^{-1}.

Hence, for a crystal structure where each cation site has n_1 nearest neighbors, the quasi-continuous model considers $(n_1 + 1)$ different environments (namely those with $m_1 = 0, 1, ..., n_1$) yielding a model decay function of $(n_1 + 1)$ exponentials. The relative amplitudes and the relative cooperative ET rates are fixed, so that ET is described by a single fit parameter C_{coop} defined as in Eq. 6.1.

6.5 • Cooperative energy transfer in YPO_4:Tb^{3+},Yb^{3+}

As an example, we use the quasi-continuous model to fit the dynamics of Tb^{3+}-to-Yb^{3+} ET in YPO_4, which has previously been shown to be a cooperative process.[73] YPO_4 has a cation density of $\rho = 14.0$ nm^{-3}, with $n_1 = 4$ nearest neighbors surrounding each cation site at a distance of

r_1 = 0.376 nm. Fig. 6.2a shows the five different donor environments considered by the quasi-continuous model. The first shell can be filled (from left to right) with 0, 1, 2, 3, or 4 nearest neighbors, while the rest of the crystal (beyond cut-off distance r_0) always has an acceptor density of ρx. The overall acceptor concentration x is reflected in the probabilities of the 5 possible environments (given by Eq. 6.4). For example, at x = 50% the probabilities $A(m_1)$ of the different environments are as given in Fig. 6.2a, with the most probable environment the one with $m_1 = 2$.

Fig. 6.2b shows the distribution of cooperative ET rates at different acceptor concentrations (from bottom to top: 25%, 50%, 75%, 99%) in YPO_4. The colored histograms are the distributions obtained from a full Monte Carlo simulation, taking into account all shells in a discrete way. The black bars show how the relative amplitudes (Eq. 6.4) and ET rates (Eq. 6.5) of the quasi-continuous model provide a good approximation of the full distribution.

We take the experimental results of Vergeer *et al.*[73] and do a global least-squares fit to the model dynamics of Eq. 6.8. The result is presented in Fig. 6.2c. With a single value for the ET strength C_{coop} the quasi-continuous model very accurately reproduces the decay dynamics for all acceptor concentrations from 0% to 99% Yb^{3+}. We obtain fitted values of $\Gamma_0 = 1/2.30$ ms, and $C_{coop} = 1.99 \times 10^{-6}\,nm^{12}\,ms^{-1}$. The fitted ET strength lies very close to the $C_{coop} = 2.05 \times 10^{-6}\,nm^{12}\,ms^{-1}$ obtained from a Monte Carlo fit,[73] demonstrating that the much simpler quasi-continuous model yields a good approximate method to obtain the same results.

6.6 • The effect of the crystal geometry

Since the number of exponents in the quasi-continuous model (Eq. 6.8) depends on the crystal geometry, it is important to test that the model works well also for other host crystal structures than YPO_4. In Fig. 6.3 we consider the low-symmetry structure of $LaPO_4$ (Figs. 6.3a–c; 2 nearest neighbors at r_1 = 0.410 nm; cation density of ρ = 13.0 nm^{-3}) and the high-symmetry structure of BaF_2 (Figs. 6.3d–f; 12 nearest neighbors at r_1 = 0.438 nm; cation density of ρ = 16.8 nm^{-3}). Note that BaF_2 was chosen as an example of a crystal with a large number of nearest neighbors. In practice, lanthanide ions do not substitute randomly (as is assumed here) because of the charge difference between Ba^{2+} and Ln^{3+}.[10] Figs. 6.3a,d show simulated data generated with the Monte Carlo model and with Poissonian noise, for acceptor concentrations of 10, 25, 50, 75, and 99%. As input parameters we used the rate constants of YPO_4:$Tb^{3+}$$Yb^{3+}$: $\Gamma_0 = 1/2.30$ ms, and $C_{coop} = 2.05 \times 10^{-6}\,nm^{12}\,ms^{-1}$. Fits with the quasi-continuous model (solid lines) follow the simulated data very well.

Figs. 6.3b,e compare the best fit values for C_{coop} obtained by fitting the simulated data to the quasi-continuous model (blue data points). We see that at all acceptor concentrations >5% and for both crystal structures, the fit value obtained is within 25% of the input value (solid line). At the lowest acceptor concentrations of <5% the fits are worse, because at such low concentrations ET is weak and its effect on the decay curves obscured by noise. Hence, the cooperative ET strength C_{coop} should always be obtained from a sample with acceptor concentrations >10%. The maximum 25% error introduced by the approximations of the quasi-continuous model in the fitted value of C_{coop} is acceptable in view of the many other sources of uncertainties that are hard to capture in a model. For example, defects in the crystal can act as unintentional acceptors (contributing most strongly at low acceptor concentration). Moreover, the actual distribution of donor and acceptor ions over cation sites may deviate from the random positioning assumed, or energy migration over the donor sublattice can partially average out the statistical distribution of environments. Note that the error becomes much smaller than 25% with a global fit, on measurements

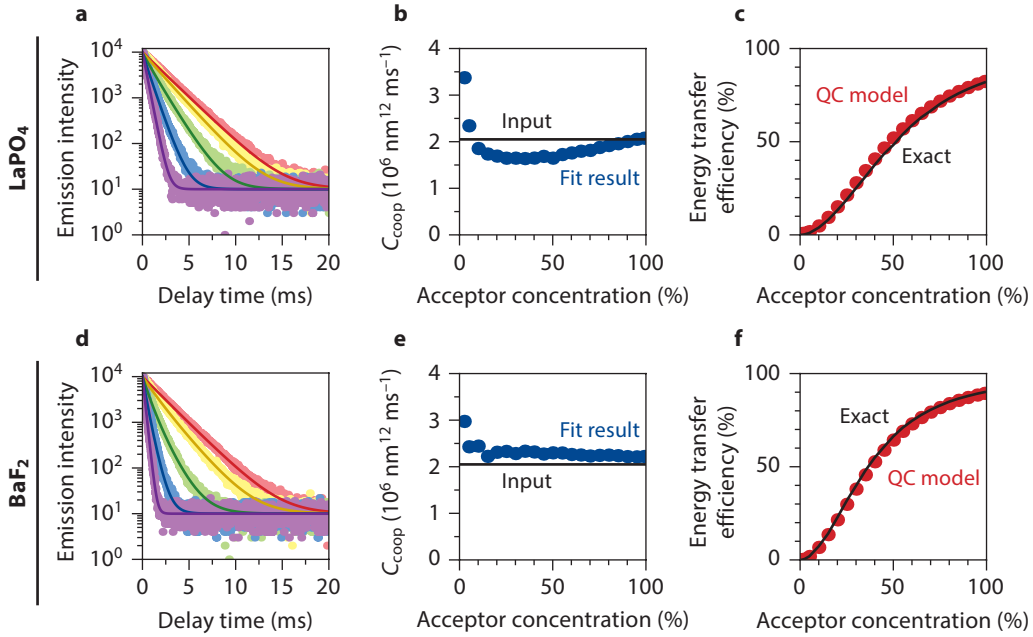

Figure 6.3 • The accuracy of the quasi-continuous (QC) model for cooperative ET, for various acceptor concentrations and different crystal structures. We test how the quasi-continuous model, which takes into account the crystallinity of the host material only for the nearest-neighbor shell, performs for (**a–c**) $LaPO_4$ (monoclinic monazite structure; 2 nearest neighbors at $r_1 = 0.410$ nm; cation density of $\rho = 13.0$ nm^{-3} and (**d–f**) BaF_2 (cubic fluorite structure; 12 nearest neighbors at $r_1 = 0.438$ nm; $\rho = 16.8$ nm^{-3}). (**a**,**d**) Simulated PL decay curves (symbols) generated by adding Poissonian noise to the Monte Carlo model for 10 (red), 25 (yellow), 50 (green), 75 (blue), and 99% (purple) acceptor concentration. The input parameters are the crystal structures, $\Gamma_0 = 1/2.30$ ms and $C_{coop} = 2.05 \times 10^{-6}$ nm^{12} ms^{-1}. Solid lines are fits with the quasi-continuous model. In the fits the intrinsic decay rate is fixed. (**b**,**e**) The best-fit values (blue circles) for C_{coop} that the quasi-continuous model extracts from the simulated data. Solid line is the input value for C_{coop}. (**c**,**f**) The cooperative ET efficiency according to the expression from the quasi-continuous model (red circles; with input $C_{coop} = 2.05 \times 10^{-6}$ nm^{12} ms^{-1}), compared to the ET efficiency from a full Monte Carlo simulation (black solid line).

of different acceptor concentrations simultaneously.

It is straightforward to calculate the efficiency of cooperative ET for each particular environment in the quasi-continuous model (Fig. 6.2a): $\eta(m_1) = \Gamma_{coop}(m_1)/[\Gamma_{coop}(m_1) + \Gamma_0]$. To obtain the ensemble averaged efficiency one simply takes the weighted average (which is equivalent to taking the area under the curve described by Eq. 6.8):

$$\eta = \sum_{m_1=0}^{n_1} A(m_1) \frac{\Gamma_{coop}(m_1)}{\Gamma_{coop}(m_1) + \Gamma_0}, \tag{6.9}$$

where $A(m_1)$ and $\Gamma_{coop}(m_1)$ are given by Eqs. 6.4 and 6.5, respectively. Figs. 6.3c,f show that this formula for the cooperative ET efficiency (red circles) accurately reproduces the efficiency calculated with a Monte Carlo simulation (solid black lines), for both crystal geometries and for all acceptor concentrations.

6.7 • Beyond cooperative energy transfer

We have now demonstrated that the quasi-continuous model can accurately reproduce and fit the dynamics of cooperative ET. Next, we discuss how the model can be further extended. For example, if one wishes to use a quasi-continuous model for the first-order ET process of cross-relaxation[132,142,193] (xr; rate of ET by dipole–dipole coupling per donor–acceptor pair $\propto r_{DA}^{-6}$), the expression for the ET rate of a donor with m_1 nearest neighbors becomes

$$\Gamma_{xr} = C_{xr}\left[m_1 r_1^{-6} + x\Sigma\right], \tag{6.10}$$

and the decay dynamics of the ensemble of donor ions are given by

$$I(t) = I(0)e^{-\Gamma_0 t}\sum_{m_1=0}^{n_1} A(m_1)e^{-\Gamma_{xr}(m_1)t}. \tag{6.11}$$

We have tested this expression, again by fitting to data generated with a Monte Carlo model [realistic input parameters as in $LiYF_4$:Pr^{3+},Yb^{3+} (Ref. 142): $\Gamma_0 = 1/35$ µs; $C_{xr} = 2\times10^{-3}$ nm^6 µs^{-1}]. Fig. 6.4 compares the cross-relaxation ET strength C_{xr} fitted with the quasi-continuous model (blue cirles) to the input (black solid line), as well as to the values obtained with the commonly used model of Inokuti and Hiroyama[6] (red triangles), in order of increasing symmetry for $LaPO_4$ (Fig. 6.4a), for YPO_4 (Fig. 6.4b), and for BaF_2 (Fig. 6.4c). There is a trend that the quasi-continuous model is better (i.e. finds a value for C_{xr} closer to the input value) at a higher number of nearest neighbors, as expected since the model treats the nearest neighbors exactly. Nevertheless, we see that our model finds the input value for C_{xr} within 10% at high acceptor concentrations >30% for all crystal structures. At low concentrations (<20%) the quasi-continuous model can be off by >50% depending on crystal structure and acceptor concentration. The biggest deviations with the input value occur in the limit of low acceptor concentrations and a small number of nearest neighbors (e.g. in $LaPO_4$; Fig. 6.4a). This can be understood by realizing that in this limit the expression provided by the quasi-continuous model (Eq. 6.11) is dominated by a single term (namely the one for zero nearest-neighbor acceptors), while the many possible acceptor distributions beyond the nearest-neighbor shell are not explicitly taken into account. We see, however, that

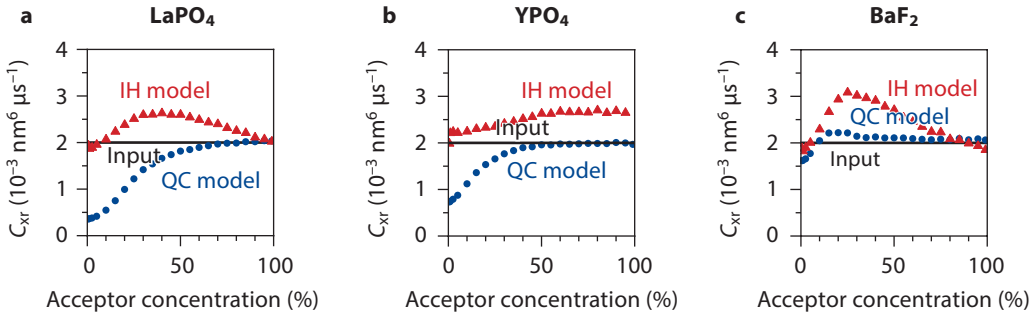

Figure 6.4 • The performance of the quasi-continuous (QC) model in the case of first-order ET. We generate simulated PL decay curves for a cross-relaxation process, and use the quasi-continuous model to extract the input parameter of $C_{xr} = 2\times10^{-3}$ nm^6 µs^{-1} (with $\Gamma_0 = 1/35$ µs). The quasi-continuous model (blue circles) is compared to the commonly used Inokuti-Hiroyama model (red triangles) for (**a**) $LaPO_4$ (monoclinic monazite structure; 2 nearest neighbors at $r_1 = 0.410$ nm; cation density of $\rho = 13.0$ nm^{-3}), (**b**) YPO_4 (tetragonal xenotime structure; 4 nearest neighbors at $r_1 = 0.376$ nm; $\rho = 14.0$ nm^{-3}) and (**c**) BaF_2 (cubic fluorite structure; 12 nearest neighbors at $r_1 = 0.438$ nm; $\rho = 16.8$ nm^{-3}).

also the commonly used Inokuti-Hiroyama model is off by more than 25% in many cases. Hence, the exact analytical expression[241] (see also Chs. 5,7) is preferrable over both the quasi-continuous and the Inokuti-Hiroyama models to accurately fit first-order ET dynamics. Only at low acceptor concentrations (<10%) the Inokuti-Hiroyama is a good approximation, while in high-symmetry crystals or at high acceptor concentrations (>30%) the quasi-continuous model performs better.

The quasi-continuous model can very conveniently be used to model a combination of different ET mechanisms. For example, a combination of cooperative ET and cross-relaxation would yield decay dynamics given by

$$I(t) = I(0)\mathrm{e}^{-\Gamma_0 t}\sum_{m_1=0}^{n_1} A(m_1)\mathrm{e}^{-\left[\Gamma_{\mathrm{coop}}(m_1)+\Gamma_{\mathrm{xr}}(m_1)\right]t}. \tag{6.12}$$

Such a model could be used to determine the relative contributions of cross-relaxation and cooperative ET to the ET for a particular donor–acceptor couple, by fitting the parameters C_{coop} and C_{xr}.

Several other extensions to the quasi-continuous model are thinkable. For example, one could adjust Eqs. 6.5 and 6.10 to describe ET mechanisms with another distance-dependence than $\propto r^{-6}$ as for dipole-dipole interaction (such as $\propto r^{-8}$ for dipole-quadrupole interaction or $\propto \exp(-r/d)$ for exchange interaction), or even use Σ as a free fit parameter to determine the range of the interaction from a fit. Moreover, it is possible to improve the accuracy of the model further (at the cost of increased complexity) by also explicitly considering the possible acceptor distributions in the next-nearest-neighbor shell, rather than only the nearest-neighbor shell. This addition can be especially useful for crystal lattices with a small number of nearest neighbors.

6.8 • Conclusion

To summarize, we have presented a simple analytical model for cooperative ET in co-doped crystals. The model explicitly takes into account the possible nearest-neighbor environments of the energy donor ion, but averages out the effect of the rest of the crystal. The result is a multi-exponential model function for the ET dynamics with relative amplitudes and decay constants fixed (depending on the concentration of acceptor ions), that can directly be used to fit experimental data. The model works well for cooperative ET in YPO_4:Tb^{3+},Yb^{3+},[73] excellently reproducing the experimental trends and yielding a very similar value for the ET strength C_{coop} as obtained from a more involved Monte Carlo algorithm. The accuracy of the model is good for various crystal host geometries, as confirmed by its power at extracting the input parameters from simulated data. We also investigate the applicability of the quasi-continuous model to first-order ET processes by dipole–dipole interaction, such as cross-relaxation. For high-symmetry crystals or at acceptor concentrations >30% it is more accurate than the commonly used Inokuti-Hiroyama model. Our simple model provides a convenient method to identify the ET processes operative in co-doped crystals, and quantify ET rates and efficiencies.

CHAPTER 7

Photonic effects on the excited state dynamics in doped nanocrystals

Based on

Photonic effects on the Förster resonance energy transfer efficiency
Rabouw, F.T., Den Hartog, S.A., Senden, T. & Meijerink, A.
Nat. Commun. **5**, 3601 (2014)

Photonic effects on the radiative decay rate and luminescence quantum yield of doped nanocrystals
Senden, T., Rabouw, F.T. & Meijerink, A.
ACS Nano **9**, 1801–1808 (2015)

ABSTRACT • Nanocrystals (NCs) doped with luminescent ions are an emerging class of materials. In contrast to the excitonic states of semiconductor NC quantum dots, the electronic states of dopant ions are not affected by quantum confinement. The transition rates in dopant ions in NCs are nevertheless different from those in the bulk analogue, because the photonic environment is different. In this chapter we use the model system of $LaPO_4$ NCs doped with Ce^{3+} and/or Tb^{3+} to investigate how the photonic environment affects the excited state dynamics, by systematically varying the solvent refractive index. We show that radiative decay is proportional to the local density of optical states (LDOS) as described by the NC-cavity model, while Förster resonance energy transfer (ET) rates are constant. As a result, solvents of a *lower* refractive index enhance the efficiency of Ce^{3+}-to-Tb^{3+} ET. Conversely, *high*-index solvents can be used to suppress the efficiency of (undesired) ET from Tb^{3+} to vibrations on the organic ligands. The quantum efficiency of the Tb^{3+} emission should therefore increase with increasing solvent refractive index. We confirm this experimentally and explain the observed effect quantitatively using the NC-cavity model.

7.1 • Introduction

Tuning of spontaneous emission by photonic crystals, plasmonic nanostructures, or dielectric cavities, has been a field of intense research.[86,131,156,160] Key is control over the local density of optical states (LDOS), which is directly proportional to the radiative emission rate. Conversely, radiative emission rates of emitters can be experimentally determined by systematically varying the LDOS.[8,181,211]

The radiative decay rate of luminescent ions doped in nanocrystals (NCs) is different than in a bulk crystal because the LDOS is different. The NC-cavity model[58,65] describes how the LDOS ρ depends on the refractive index n of the solvent in which the NCs are dispersed:

$$\rho(n) \propto n \left(\frac{3n^2}{2n^2 + n_{\mathrm{NC}}^2} \right)^2, \tag{7.1}$$

where n_{NC} is the refractive index of the NC, and the term between brackets is the so-called *local-field factor* which describes the effect of the refractive index contrast between NC and solvent.

In this chapter we investigate the excited state dynamics in dispersions of $LaPO_4$ NCs doped with Ce^{3+} and/or Tb^{3+} ions as a function of the refractive index of the solvent. We first focus on the Förster resonance energy transfer (ET) between Ce^{3+} and Tb^{3+}. In general, ET is important both in nature (e.g. for photosynthesis)[105,162] and for the operation of devices such as fluorescent tubes and solid state lasers. It also lies at the core of emerging technologies such as background-free bioimaging,[93,194] and spectral conversion for increased solar cell efficiencies.[124] The possibility to control ET with photonic structures, in analogy to spontaneous emission, would allow for precise control over energy flow and spectral output of luminescent materials. Unfortunately, previous studies disagree on the most fundamental question how ET rates scale with the LDOS. De Dood *et al.*[64] and Blum *et al.*[172] find that ET rates are independent of the LDOS, while other works claim a linear,[36,69] or even a quadratic[79] dependence.

The contradictory findings reported thus far may in part result from the complexity of the experimental systems used. The decay dynamics of the donor were measured in layered structures with (varying) distance between donor–acceptor pairs and an interface. Some studies compared separately fabricated samples,[36,172] which is not ideal because reproducible control over the thickness and refractive index of the spacer layers can be difficult. In other cases, energy migration

among donors and transfer to multiple acceptors[36,64,69,79] would lead to non-exponential decay dynamics which are hard to interpret.

Here we quantify the ET in co-doped $LaPO_4$ nanocrystals (NCs), for different LDOS and acceptor concentrations. Co-doped NCs are an ideal model system to study the influence of the LDOS on the ET rate, because the crystallinity of the host material ensures that the donor–acceptor distances and the local *electronic* environment of the luminescent ions are well-defined and fixed. At the same time, the *photonic* environment can be varied easily by dispersing the NCs in solvents with different refractive indices. A complicating factor is that random substitutional doping leads to an ensemble of donor ions with a different number of and separation from nearby acceptors. However, it is possible to accurately model the ET dynamics in a crystalline environment under the assumption that donors and acceptors are randomly distributed over cation positions (see Chs. 5,6).[73,142]

We measure the decay dynamics of the Ce^{3+} excited state as a function of the concentration of Tb^{3+} acceptor ions, and with the NCs dispersed in various solvents. By quantifying how the radiative decay rate of the Ce^{3+} excited state scales with the solvent refractive index, we provide the first convincing experimental evidence for the NC-cavity model for the LDOS in a NC (Eq. 7.1). In contrast, the Ce^{3+}-to-Tb^{3+} ET rate is shown to be independent of the LDOS. As a result, the efficiency of ET is higher if the LDOS is lower. This effect results in a higher Tb^{3+} emission intensity under excitation of Ce^{3+} if the NCs are dispersed in a solvent of lower refractive index.

Next, we focus on the emission from Tb^{3+}. The quantum efficiency (QE) of the emitting $^5D_4$ state is near but not exactly unity, because of the possibility of ET to ligand vibrations on the surface of the NC. Also for this type of ET the efficiency depends on the solvent refractive index. The QE of the Tb^{3+} $^5D_4$ emission should therefore be higher in high-index solvents. We demonstrate how the NC-cavity model can be used to determine the QE from a photoluminescence (PL) decay curve of the dopant ion, if the radiative lifetime in the doped bulk material is known. With this method we show that the QE of Tb^{3+}-doped NCs is indeed higher in a high-index solvent, or when a dopant-free shell separates the Tb^{3+} ions from ligand vibrations.

7.2 • Decay dynamics and emission spectra

We first investigate the NCs schematically depicted in Fig. 7.1a: $LaPO_4$ NCs of 4 nm diameter doped with 1% Ce^{3+} (purple; donor ions) and with Tb^{3+} at varying concentration (green; acceptor ions). Fig. 7.1b presents the energy level diagram of the Ce^{3+}–Tb^{3+} donor–acceptor pair.[117,188] After UV excitation of a Ce^{3+} ion to the $5d^1$ state (purple arrow), it can either decay radiatively (blue arrows), or resonantly transfer its energy to a nearby Tb^{3+} acceptor ion (green dashed arrow). Subsequently, Tb^{3+} emits a visible photon in the transition from the $^5D_4$ metastable state to one of the sublevels of the spin–orbit split ^7F_J ground state. This gives rise to an emission spectrum as shown in Fig. 7.1c, containing a Ce^{3+} emission band in the UV (300–360 nm) and several narrow emission lines in the visible (470–630 nm) from Tb^{3+}. As shown in Figs. 7.1d,e for methanol, the NCs form a transparent dispersion in many polar solvents, which exhibits green luminescence under UV excitation.

Fig. 7.2a shows PL decay curves of the Ce^{3+} emission for $LaPO_4$:Ce^{3+}(1%) NCs dispersed in different solvents. The decay dynamics are single-exponential and are faster in solvents with a higher refractive index, reflecting that the radiative emission rate scales with the LDOS (Eq. 7.1). The PL decay curves for $LaPO_4$:Ce^{3+}(1%)Tb^{3+}(20%) NCs are shown in Fig. 7.2b. They are non-exponential, since different Ce^{3+} centers in the ensemble have different ET rates determined by the number and proximity of neighboring Tb^{3+} acceptors. Nevertheless, the trend of faster decay for

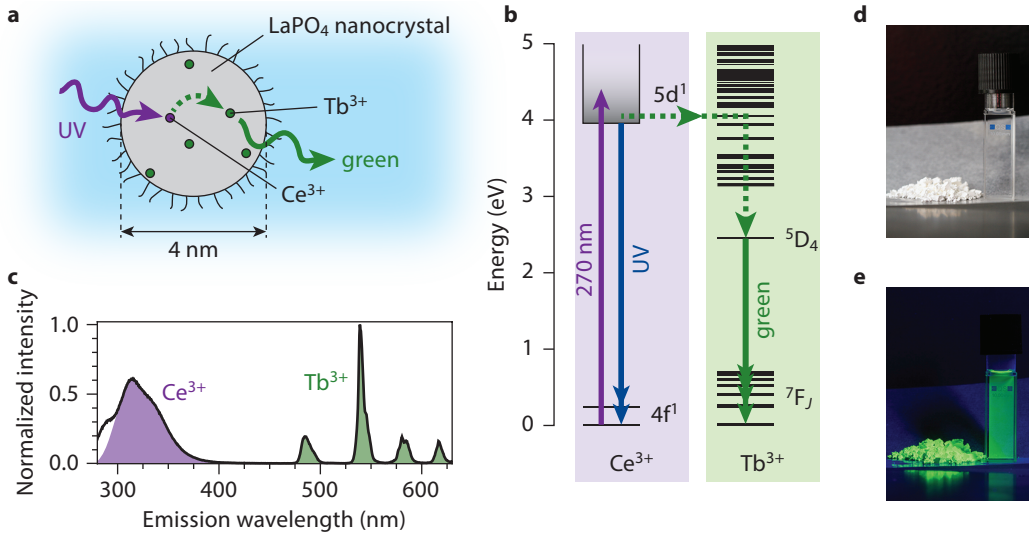

Figure 7.1 • Relaxation pathways in $LaPO_4$ nanocrystals co-doped with Ce^{3+} and Tb^{3+}. (**a**) $LaPO_4$ NCs with an average diameter of 4 nm are co-doped with Ce^{3+} (purple) and Tb^{3+} (green). A UV excited Ce^{3+} center can transfer its energy to a nearby Tb^{3+} ion, resulting in emission in the visible. (**b**) Energy level diagram: absorption of a UV photon (purple arrow) brings Ce^{3+} in the $5d^1$ configuration. Subsequently, it can either radiatively decay to the $4f^1$ ground configuration (blue arrows), or transfer its energy to a Tb^{3+} acceptor (dashed green arrow). Tb^{3+} rapidly relaxes to the $^5D_4$ metastable state, followed by radiative decay to the ^7F_J ground state under the emission of a visible photon (solid green arrows). (**c**) The emission spectrum of $LaPO_4$:Ce^{3+}(1%)Tb^{3+}(5%) NCs upon excitation in the Ce^{3+}: $4f^1 \rightarrow 5d^1$ transition at 280 nm. The relative intensity of Ce^{3+}: $5d^1 \rightarrow 4f^1$ (purple) and Tb^{3+}: $^5D_4 \rightarrow {}^7F_J$ (green) emissions is determined by the ratio between the radiative emission rate and the energy transfer rate of the Ce^{3+} $5d^1$ excited state. Around 300 nm there is background emission from organic by-products of the NC synthesis. (**d**) A photograph in ambient light of $LaPO_4$:Ce^{3+}(1%)Tb^{3+}(20%) NCs as a dried powder (left), and as a transparent NC dispersion in methanol (right). (**e**) The same NC powder (left) and dispersion (right) under UV excitation luminesce green. Photographs taken by Jasper Landman.

higher refractive index solvents is still visible.

The PL decay curves in Figs. 7.2a,b can be used as direct proof that ET rates are independent of the LDOS. The donors in the ensemble have equal radiative emission rates γ_{rad} but differ in ET rate. Hence, the decay dynamics of the ensemble can be factorized as

$$I(t) = I(0)e^{-\gamma_{rad}t}T(t) \tag{7.2}$$

where $I(t)$ is the emission intensity at delay time t after an excitation pulse. The factor $T(t)$ describes the decay due to ET, which is in general non-exponential. If we divide the non-exponential PL decay curve of Fig. 7.2b by the exponential decay dynamics as measured in the absence of Tb^{3+} acceptors (Fig. 7.2a), we directly obtain the contribution of ET $T(t)$. We plot $T(t)$ in Fig. 7.2c, for the different solvents. The trend of faster decay with increasing refractive index, which was visible in Figs. 7.2a,b, is no longer present. From this simple analysis we can already conclude that the trend observed in Fig. 7.2b is solely due to a dependence of the radiative emission rate on the LDOS, while the ET rate is independent.

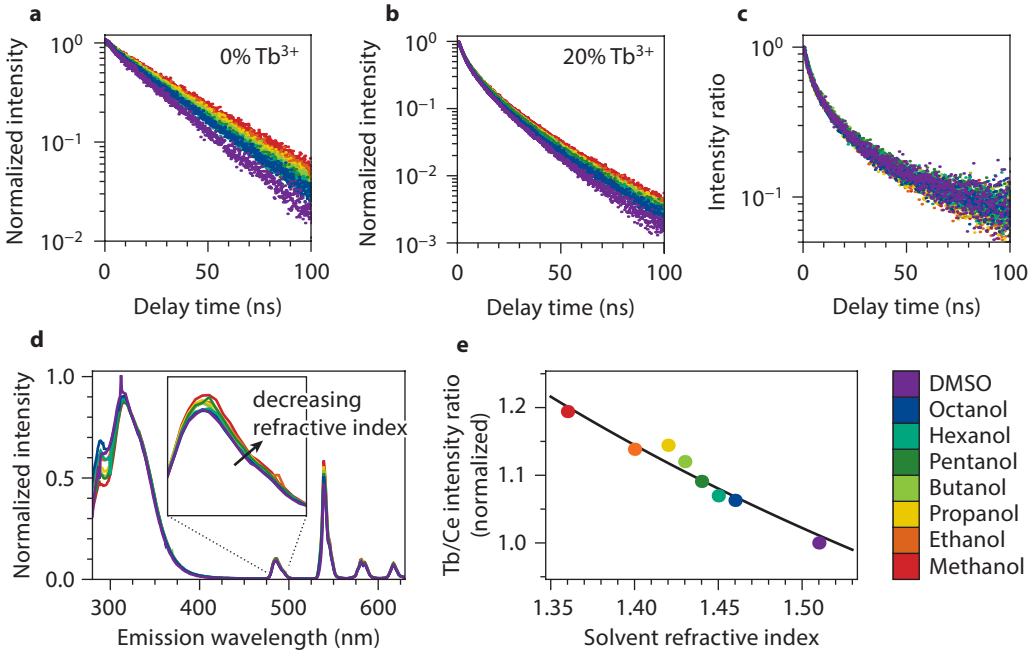

Figure 7.2 • The effects of an energy transfer rate independent of the photonic environment. (**a**) PL decay curves of the Ce^{3+} emission (at 340 nm) from $LaPO_4$:Ce^{3+}(1%) NCs dispersed in solvents of different refractive index, ranging from 1.36 for methanol (red) to 1.51 for DMSO (purple). Note that decay is purely radiative as there is no ET in the absence of Tb^{3+} acceptor ions. (**b**) PL decay curves for $LaPO_4$:Ce^{3+}(1%)Tb^{3+}(20%) NCs, in which efficient ET to Tb^{3+} is possible. (**c**) Dividing the PL decay curve of panel **b** by the radiative decay of panel **a** reveals the contribution of ET. We can see its independence of the refractive index of the solvent. (**d**) Emission spectra of $LaPO_4$:Ce^{3+}(1%)Tb^{3+}(2%) NCs normalized to the Ce^{3+} $5d^1 \rightarrow 4f^1$ emission intensity (between 310 nm and 400 nm), in different solvents. The inset is a zoom of the $^5D_4 \rightarrow {}^7F_6$ emission line. (**e**) A plot of the intensity ratio between Tb^{3+} emission (470–630 nm) and Ce^{3+} emission (310–400 nm) as a function of the solvent refractive index shows the 19% increase upon going from DMSO (n = 1.51) to methanol (n = 1.36). The solid black line depicts a good correspondence to the trend expected from Eq. 4.5.

If indeed radiative decay and ET rates scale differently with the LDOS, then the ET efficiency should be tunable by the refractive index of the solvent.[172] More precisely, Ce^{3+}-to-Tb^{3+} ET becomes more efficient when competing radiative decay of the Ce^{3+} excited state is suppressed. Hence, the Tb^{3+} intensity should increase if we reduce the solvent refractive index. This is exactly what we observe. Fig. 7.2d shows the emission spectra of $LaPO_4$:Ce^{3+}(1%)Tb^{3+}(2%) NCs dispersed in different solvents. Upon going from dimethyl sulfoxide (DMSO; refractive index n = 1.51) to methanol (n = 1.36) the relative Tb^{3+} intensity increases by 19% (Fig. 7.2e).

7.3 • Modeling energy transfer in nanocrystals

Next, we analyze the decay dynamics of the Ce^{3+} $5d^1$ state in $LaPO_4$:Ce^{3+}(1%)Tb^{3+}(x%) NCs more quantitatively. The PL decay curves of Fig. 7.2a are fitted to a single-exponential decay function. Fig. 7.3 shows how the fitted PL lifetime depends on the refractive index of the solvent, when going from methanol (n = 1.36) to DMSO (n = 1.51). The experimental data points (red dots) fol-

low the trend expected from the NC-cavity model (Eq. 7.1): the radiative decay rate scales linearly with the LDOS.

To analyze the multi-exponential PL decay curves in the presence of Tb^{3+} (Fig. 7.2b) the distribution of Ce^{3+}–Tb^{3+} distances in a $LaPO_4$ NC must be taken into account. We have an analytical model that can do this (see Ch. 5), and that reproduces how the decay dynamics of $LaPO_4$:Ce^{3+}(1%)Tb^{3+}(x%) NCs depend on x. For an isolated donor–acceptor pair at separation r having dipole–dipole interaction, the ET rate is $\gamma_{ET} = C_{ET}/r^6$ (Ref. 1) with C_{ET} the 'ET strength' parameter. The total decay rate Γ of a particular donor depends on the proximity of acceptors:

$$\Gamma = \gamma_{rad} + C_{ET} \sum_{i}^{acc.} \frac{1}{r_i^6} \tag{7.3}$$

where the summation runs over all (nearby) acceptors, and r_i is the distance to acceptor i. In a crystal only discrete donor-acceptor distances are possible, determined by the crystal lattice. For example, around the central donor ion in the schematic crystal of Fig. 7.4a there is a 'shell' with $n_1 = 2$ cation sites at distance r_1 (squares), one with $n_2 = 4$ cation sites at distance r_2 (triangles), etc. In Chs. 5,6 we have used this 'shell model' to simulate ET dynamics in doped bulk crystals.[73,142] In the Methods section of Ch. 5 we show that under the assumption of a random distribution of donor and acceptor ions, the PL decay trace of an ensemble of donors in a bulk crystal can be written as:

$$I(t) = I(0)e^{-\gamma_{rad}t} \prod_{i}^{shells} \left(1 - x + x\, e^{-C_{ET}t/r_i^6}\right)^{n_i} \tag{7.4}$$

Here, the product runs over all shells, and $x \in [0, 1]$ is the acceptor concentration.

The finite size of our NCs requires an adjustment to Eq. 7.4. As plotted in Fig. 7.4b, a donor ion close to the NC surface has fewer nearby cation sites than a donor ion in the center. To account for these finite-size effects we consider the different possible donor positions in the NCs. For each position, we introduce a geometrical factor f_i depending on the proximity of the NC surface as a correction for the different number of nearby cation sites ($n_i \rightarrow f_i n_i$ in Eq. 7.4; see Methods).

Figs. 7.5a–h shows the PL decay curves for $LaPO_4$:Ce^{3+}(1%)Tb^{3+}(x%) NCs with increasing x, in eight different solvents with refractive indices ranging from $n = 1.36$ (Fig. 7.5a; methanol) to $n = 1.51$ (Fig. 7.5h; DMSO). For each solvent we perform a global fit to our ET formula (solid lines; Eqs. 7.4 and 7.7), where we fix γ_{rad} and find the ET strength C_{ET} by simultaneously fitting the decay curves for all five acceptor concentrations. The model captures how the decay dynamics become faster and more non-exponential as the Tb^{3+} concentration increases. The dashed lines are the fits obtained if we neglect finite-size effects [i.e. use Eq. 7.4 without correction factors f_i (Eq. 7.7)]. They

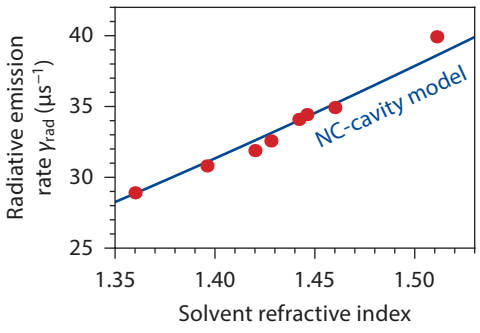

Figure 7.3 • Radiative decay of the Ce^{3+} $5d^1$ excited state. The radiative decay rate γ_{rad} of the Ce^{3+} $5d^1$ excited state, obtained from a single-exponential fit to the decay curves of Fig. 7.2a, as a function of the refractive index of the solvent. It follows the trend linear with the LDOS (blue line) as expected from the NC-cavity model[65] (Eq 7.1). Solvent refractive indices in the UV were determined from the angle of total internal reflection on an interface with quartz, as described in the Methods section.

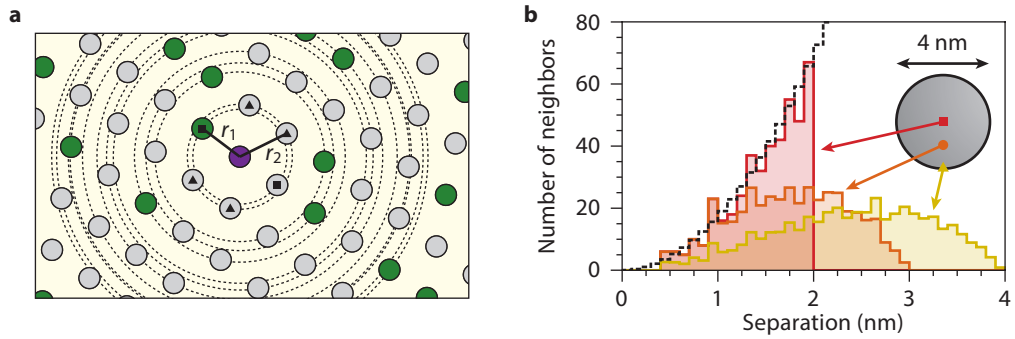

Figure 7.4 • The shell model for energy transfer in (nano)crystalline environment. (**a**) Schematic of a doped crystal with cation sites (circles) on regular positions. Donor ions (purple) and acceptor ions (green) are randomly distributed. Around a donor ion there are discrete 'shells' (dashed circles) of cation sites at distances $\{r_1, r_2, r_3, ...\}$. These shells have space for a maximum of $\{n_1, n_2, n_3, ...\}$ acceptor ions. The total ET rate of a central donor ion is set by the actual occupation of nearby shells. (**b**) The distribution of distances to nearby cation sites from a central (donor) ion, in a $LaPO_4$ NC with a diameter of 4 nm and with the central ion positioned at different depths from the NC surface (indicated by symbols in the inset). The distance distribution in a $LaPO_4$ NC is determined by the discrete nature of the crystal lattice, and by its finite size. For comparison, the black dashed line shows the distance distribution in a hypothetical glass-like continuous bulk material of the same density. The histogram bin widths are 0.1 nm.

deviate from the experiment, especially at high acceptor concentrations.

These fits to the decay dynamics allow us to extract the dependence of the ET strength C_{ET} on the LDOS. In Fig. 7.5i we plot the ET strength C_{ET} against γ_{rad} (which scales linearly the LDOS). Each data point corresponds to a different solvent, and depicts results of a global fit from Figs. 7.5a–h. Solid lines give the trends expected for the three possibilities for the power p of the LDOS dependence of ET rates.[36,64,69,79,172] The fitted values of C_{ET} are roughly constant with changing LDOS, at 0.405 ± 0.021 nm^6 s^{-1}. The linear or quadratic trends expected for $p = 1$ (blue line) or $p = 2$ (purple line) are not observed. Hence, these fit results confirm our conclusion from Fig. 7.2 that ET rates are independent of the LDOS. As an alternative visualisation, in Fig. 7.5j we plot the critical ET distance R_0 versus γ_{rad}.[172] By definition $R_0 = (C_{ET}/\gamma_{rad})^{1/6}$ is the donor–acceptor separation at which there is 50% probability of ET. We see that R_0 becomes smaller with increasing LDOS. This in agreement with the trend expected for $p = 0$ (green line). Intuitively, we can understand that when the radiative decay rate is enhanced in a high-index solvent, the donor–acceptor separation R_0 must be smaller than in a low-index solvent for the ET rate to be equally fast.

7.4 • Tuning the energy transfer efficiency

With the fitted values of the (variable) radiative rate and the constant ET strength, we can use our analytical model to calculate the Ce^{3+}-to-Tb^{3+} ET efficiency η_{ET} for NCs embedded in different photonic environments:[90]

$$\eta_{ET} = 1 - \gamma_{rad} \int_0^\infty e^{-\gamma_{rad} t} \prod_i^{\text{shells}} \left(1 - x + x\, e^{-C_{ET} t / r_i^6}\right)^{n_i} dt \qquad (7.5)$$

where again accounting for finite-size effects is needed in a nanocrystalline host. Fig. 7.2e shows that Eq. 7.5 reproduces the observed increase of the Tb^{3+} emission intensity in solvents of

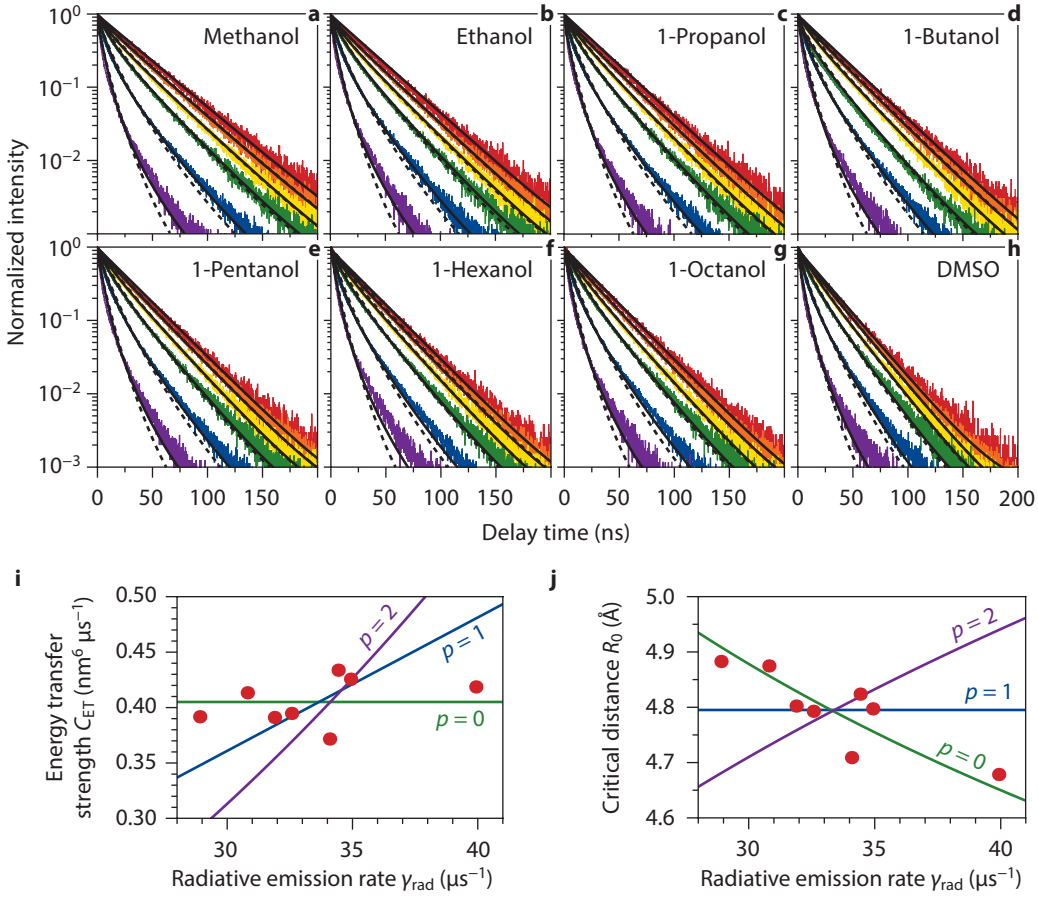

Figure 7.5 • Fitting the energy transfer dynamics as a function of acceptor concentration and solvent refractive index. (**a–h**) The decay dynamics of the Ce^{3+} $5d^1$ excited state in $LaPO_4$:Ce^{3+}(1%)Tb^{3+}(*x*%) NCs for 0% (red), 2% (orange), 5% (yellow), 10% (green), 20% (blue), and 40% (purple) Tb^{3+} in different solvents: (**a**) methanol ($n = 1.36$), (**b**) ethanol ($n = 1.40$), (**c**) 1-propanol ($n = 1.42$), (**d**) 1-butanol ($n = 1.43$), (**e**) 1-pentanol ($n = 1.44$), (**f**) 1-hexanol ($n = 1.45$), (**g**) 1-octanol ($n = 1.46$), (**h**) dimethyl sulfoxide ($n = 1.51$). At 0% Tb^{3+} (red curves) the decay is single-exponential. At higher concentrations (orange, yellow, green, blue, purple) ET makes the decay faster and multi-exponential. Solid black lines are global fits of the data for a particular solvent to our model for 4 nm NCs (Eqs. 7.4 and 7.7), which yield the ET strength C_{ET} for each solvent. Dashed lines are the fits obtained if we neglect finite-size effects (Eq. 7.7). (**i**) The ET strength C_{ET} and (**j**) the critical distance R_0 against the radiative emission rate (which is proportional to the LDOS), obtained from the fits in panels **a–h**. The fit results are consistent with the trend expected for the scenario that ET is independent of the LDOS (green; $p = 0$), not with scenarios that ET scales linearly (blue; $p = 1$) or quadratically (purple; $p = 2$) with the LDOS.

decreasing refractive index.

Finally, using our model and our finding that the ET strength is a constant, we can predict ET efficiencies in more complex photonic environments than a homogeneous dielectric. For example, a photonic crystal structure inhibiting radiative decay by a factor 10 (Ref. 115) can be used to

increase the ET efficiency in $LaPO_4$:Ce^{3+}(1%)Tb^{3+}(2%) NCs to 30% (now, 11–13% depending on the solvent). Conversely, co-doped NCs could be used as local probes for the LDOS in photonic structures, where the relative emission intensities of the dopants reveal the LDOS-dependent ET efficiency between them.

Our results demonstrate that photonic structures developed for spontaneous emission control can play an important role in increasing the efficiency of ET. The concept of ET from sensitizers such as colloidal semiconductor quantum dots,[59,78,129] dye molecules,[111,134,137,195] or silicon nanocrystals[116,187,216] is widely used. It can for example improve the spectral response of photovoltaic devices, increase the output of phosphors or optical amplifiers, or be used for color tuning in lighting. Furthermore, ET plays a crucial role in photon upconversion[143,195,224] used in bio-imaging and for next-generation photovoltaics.

7.5 • Measuring the luminescence quantum efficiency of doped nanocrystals

Alternatively, in doped NCs ET can be an undesired process which leads to a lower PL quantum efficiency (QE) for the donor emission. For example, Tb^{3+} in $LaPO_4$ NCs might lose its excitation energy through multi-phonon relaxation, i.e. ET to overtones of high energy vibrations of the organic surface ligands. The energy gap between the emitting $^5D_4$ and the next lower $^7F_0$ state is 14600 cm^{-1} (= 1.82 eV), which can be bridged by as few as five high-energy vibrational quanta on the surface ligands (e.g. C-H stretch or N-H stretch; ~3000 cm^{-1}). In bulk $LaPO_4$, with a maximum phonon energy of ~1200 cm^{-1} for the phosphate vibrations,[20] bridging the gap requires more than 10 phonons so that multi-phonon relaxation rates are negligibly slow. We will now show that, knowing that the radiative decay rate scales with solvent refractive index according to Eq. 7.1 while ET rates are constant, it is possible to determine the QE of the Tb^{3+} emission in $LaPO_4$:Tb^{3+} NCs from a PL decay measurement.

Figs. 7.6a,b present PL decay curves of the Tb^{3+} $^5D_4$ emission in $LaPO_4$:Tb^{3+} NCs (Fig. 7.6a; 1% Tb^{3+}) and in $LaPO_4$:Tb^{3+} NCs with a ~1 nm thick dopant-free shell of $LaPO_4$ (Fig. 7.6b; 1% Tb^{3+} in the core), in methanol (n = 1.33) and DMSO (n = 1.48). The data are fitted with a single-exponential decay function. We obtain decay times of 5.8 ms (methanol) and 4.4 ms (DMSO) for core-only NCs, and 6.7 ms (methanol) and 5.1 ms (DMSO) for core–shell NCs. The difference in decay time between methanol and DMSO is understood from the higher LDOS in DMSO (Eq. 7.1). We ascribe the difference in decay time between core-only and core–shell NCs to multi-phonon relaxation by coupling to high-energy vibrations of the organic surface ligands, which is weaker if a shell separates the Tb^{3+} centers from the surface. Indeed, the fit residuals (bottom panels in Figs. 7.6a,b) show that the PL decay of core–shell NCs more closely resembles a single-exponential than in core-only NCs. This is consistent with Tb^{3+} ions close to the surface of core-only NCs decaying faster because of ET to ligand vibrations.

From the NC-cavity model we can estimate the QE of the Tb^{3+} emission in NCs. We have to realize that, in terms of the photonic environment, bulk $LaPO_4$:Tb^{3+} is analogous to $LaPO_4$:Tb^{3+} NCs in an environment with refractive index $n = n_{NC}$ [= 1.79 (Ref. 49) for the present case of $LaPO_4$]. The NC-cavity model can therefore be rewritten to directly yield the radiative decay rate of luminescent dopant ions in a NC, as a function of the radiative decay rate in bulk ($\gamma_{rad}^{(0)}$) and the solvent refractive index:

$$\gamma_{rad}(n) = \gamma_{rad}^{(0)} \frac{n}{n_{NC}} \left(\frac{3n^2}{2n^2 + n_{NC}^2} \right)^2 \qquad (7.6)$$

In the Methods section we discuss to which sizes of NCs the NC-cavity model is applicable. In a sample of bulk $LaPO_4$:Tb^{3+}(1%) we measured a radiative lifetime of 3.3 ms, consistent with previ-

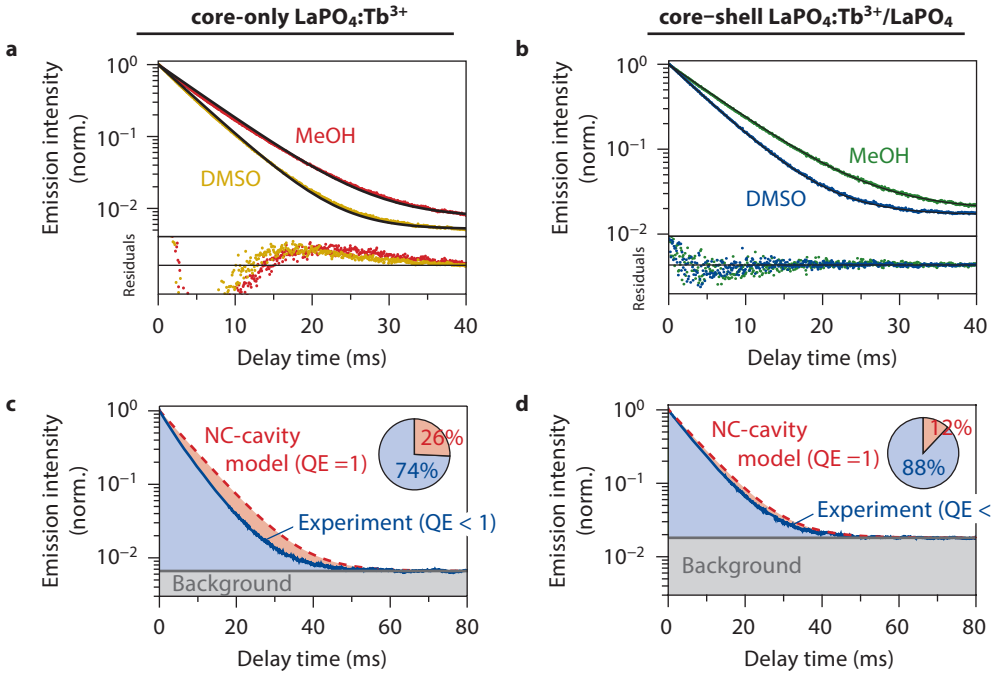

Figure 7.6 • PL decay properties of doped core-only and core–shell NCs. (**a**) PL decay curves of the Tb^{3+} $^5D_4$ excited state in core-only $LaPO_4$:Tb^{3+} NCs dispersed in methanol (red) and DMSO (yellow). Black solid lines are single-exponential fits. The bottom panel shows the fit residuals. (**b**) Same as **a**, but for and $LaPO_4$:Tb^{3+}/$LaPO_4$ core–shell NCs. Green data points are for NCs in methanol, blue in DMSO. (**c**) The experimental decay of the Tb^{3+} $^5D_4$ state in core-only NCs (blue line) is faster than expected (red dashed line) from the NC-cavity model and the bulk lifetime of 3.3 ms (Eq. 7.6). The quantum efficiency of the NCs (see pie chart) is determined by integrating the area under the experimental decay curve (blue area) and simulated PL decay curve based on the NC-cavity model (Eq. 7.6). The difference between the two curves gives the non-radiative decay (red area). (**d**) Same as **c**, but for core–shell NCs in methanol.

ous experimental results.[9,19] If the dopants in NC have a unity QE (i.e. decay is purely radiative), the experimental (total) PL decay rate should be exactly as described by Eq. 7.6. If the QE is lower than one, the PL decay rate is faster because of a non-radiative contribution.

The blue lines in Figs. 7.6c,d are the experimental PL decay curves of the Tb^{3+} emission from core-only NCs (Fig. 7.6c) and core–shell NCs (Fig. 7.6d) dispersed in methanol (n = 1.33). Red dashed line are the decay dynamics as expected from the NC-cavity model (Eq. 7.6) for a QE of unity. Clearly, the decay is faster than expected. The area under the PL decay curves (blue) is a measure for the total number of photons emitted. On the other hand, the red areas in Figs. 7.6c,d (the area between the experimental PL decay and the theoretically predicted decay for a QE of one) represent the losses due to non-radiative decay. By comparing the red and blue areas we directly obtain the average QE of the sample: 74% for the core-only NCs in methanol, and 88% for the core–shell NCs in methanol.

Fig. 7.7a gives an overview of the experimental decay rates of core-only (green data points) and core–shell NCs (red) in different solvents, obtained from single-exponential fits (as in Figs. 7.6a,c). The solid black line is the radiative decay rate of the Tb^{3+} $^5D_4$ excited state, calculated from the

decay rate in bulk $LaPO_4$:Tb^{3+} (blue square) using the NC-cavity model (Eq. 7.6). The dotted lines are the total PL decay rates expected for $LaPO_4$:Tb^{3+} NCs with a QE lower than one, obtained by adding a non-radiative contribution to the radiative decay. As a confirmation of the results of Figs. 7.6c,d we see again that the QEs of the Tb^{3+} emission from our NCs are slightly lower than unity: around 80% for core-only, or around 90% for core–shell NCs.

Fig. 7.7b summarizes the values for QE obtained using the integration method (open circles; Figs. 7.6c,d) and the single-exponential fitting procedure (filled circles; Figs. 7.6a,b and Fig. 7.7a) of core-only NCs (green) and core–shell NCs (red). We observe two clear trends. First, the core–shell NCs have a higher QE than core-only NCs. This is because in core–shell NCs the Tb^{3+} ions are further separated from high-energy vibrations on the NC surface. Second, the QE goes up with increasing refractive index. This is consistent with the results of Fig. 7.2 and Fig. 7.5: the rate of ET to ligand vibrations is fixed, while radiative decay scales with the LDOS. Indeed, we can reproduce the trends in QE with a model where the radiative decay rate follows the NC-cavity model (Eq. 7.6) while the non-radiative decay rate is fixed at 47 s^{-1} for core-only (green line in Fig. 7.7b), and 18 s^{-1} for core–shell NCs (red line).

Note that the methods of Fig. 7.6 and Fig. 7.7 can only provide an upper limit for the PL QE of doped NCs, namely of the emissive dopant ions in the ensemble. In contrast to conventional methods quantifying absorption and emission,[240] it is insensitive to ions that absorb but are otherwise completely dark, e.g., those situated next to a quenching center. Consequently, our method can yield larger ensemble QE values (by disregarding the ions with a QE of zero) than conventional methods which average over all ions. Interestingly, from the difference between values obtained with the two methods one can in principle calculate the fraction of dark ions.

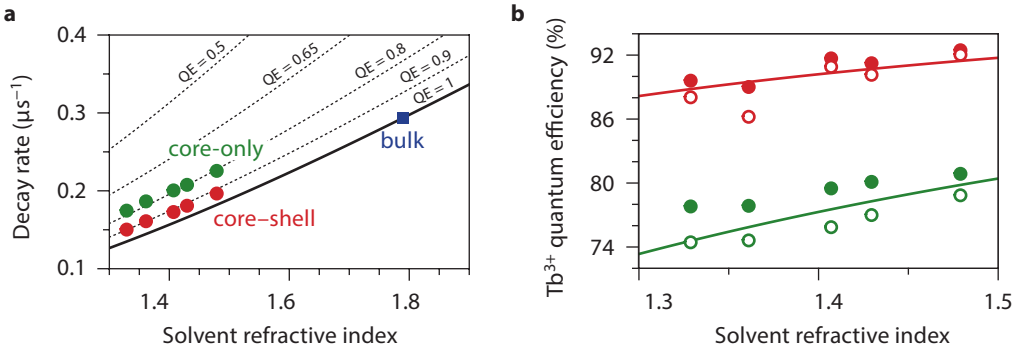

Figure 7.7 • The decay rate and quantum efficiency as a function of solvent refractive index. (**a**) The decay rate of the Tb^{3+} $^5D_4$ state as a function of the solvent refractive index. Experimental data points are the result of single-exponential fits to the PL decay (Fig. 7.6a,b) of core-only NCs (green circles), core–shell NCs (red circles) and bulk $LaPO_4$:Tb^{3+} (blue square). The solid line gives the expected total decay rates for $LaPO_4$:Tb^{3+} NCs for a unity quantum efficiency (QE), which are radiative decay rates obtained using the NC-cavity model (Eq. 7.6). The dotted lines give the expected total decay rates for $LaPO_4$:Tb^{3+} NCs with a lower QE, which are obtained by adding a non-radiative contribution. (**b**) The PL QE of core-only NCs (green) and core–shell NCs (red), determined with a single-exponential fit to the decay dynamics (filled symbols; panel **a**) or by integrating the PL decay curve (open symbols; Fig. 7.6). Solid lines are fits to a model where the radiative decay rate follows the NC-cavity model (Eq. 7.6) while the non-radiative decay rate is constant.

7.6 • Conclusion

To summarize, we have investigated the excited state dynamics in $LaPO_4$ NCs doped with Ce^{3+} and/or Tb^{3+} luminescent dopant ions, as a function of the refractive index of the solvent in which the NCs are dispersed. The radiative decay rate of the Ce^{3+} $5d^1$ excited state in $LaPO_4$:Ce^{3+} NCs accelerates with increasing solvent refractive index, as described by the NC-cavity model. We have used the model system of $LaPO_4$:Ce^{3+},Tb^{3+} NCs to prove that ET rates are not proportional to the LDOS, as claimed in previous (and later[231]) studies. As a result, the *efficiency* of ET is enhanced at lower LDOS. Indeed, we have observed a higher emission intensity from Tb^{3+} under excitation of Ce^{3+} if the solvent refractive index was lower. Conversely, the efficiency of radiative decay is higher in a high-index solvent if there is a competing ET pathway. We have shown how the NC-cavity model can be used to measure the PL QE from luminescent centers doped in a NC.

In all applications of luminescent doped NCs photonic (local-field) effects inevitably affect the decay dynamics. The method presented in this chapter to determine the QE and radiative decay rate of luminescent dopant ions is applicable to the characterization of new types of doped NCs. Furthermore, the realization that the efficiency of ET and radiative decay depend on the photonic environment is important to optimize the performance of doped NCs.

7.7 • Methods

Synthesis and characterization. The $LaPO_4$ NCs co-doped with Ce^{3+} and Tb^{3+} were synthesized using the method of Oertel *et al.*[117] Briefly, a clear solution of lanthanide chlorides (10 mmol total; La, Ce, Tb) in methanol (10 mL) was mixed with diethyl ethylphosphonate (40 mmol). Methanol was evaporated under vacuum at room temperature, after which diphenyl ether (30 mL) was added. Following the removal of water under vacuum at 105°C, we added tributylamine (40 mmol) and a 2 M solution of phosphoric acid in dihexyl ether (7 mL). Subsequently, the reaction mixture was kept overnight under nitrogen at 200°C, during which the NCs formed. They were isolated by centrifugation, washed with toluene, and dried under vacuum. For the synthesis of $LaPO_4$:Tb^{3+}(1%) core and core–shell NCs, tributyl phosphate was used instead of diethyl ethylphosphonate. The core–shell NCs were grown from the crude (unwashed) reaction mixture, by first adding another 7 mL of the 2 M phosphoric acid in dihexyl ether. Separately, a cation precursor was prepared by mixing $LaCl_3.6H_2O$ (10 mmol) in methanol (10 mL) with tributyl phosphate (40 mmol) and diphenyl ether (30 mL). After the methanol and water had been evaporated at 100°C under a vacuum, tributylamine (40 mmol) was added. The cation precursor solution was then added to the dispersion of core-only NCs at a rate of 2 mL every 5 min. Finally, the reaction mixture was kept at 200°C under nitrogen atmosphere for 18 h. The core–shell NCs produced were isolated and washed as described above. From transmission electron microscopy (Fig. 7.8a) we know that the core-only NCs have a diameter of 4 nm and a polydispersity of ~10%. Powder x-ray diffraction (Fig. 7.8b) confirms that the NCs exhibit the monazite crystal structure of $LaPO_4$ up to the highest doping concentration of 40% Tb^{3+}. The doping concentrations of $Ce^{3+}$and Tb^{3+} were confirmed using inductively coupled plasma atomic emission spectroscopy.

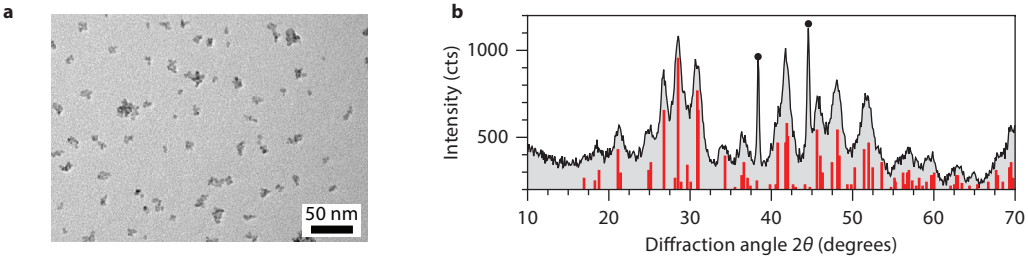

Figure 7.8 • Characterization of the $LaPO_4$:Ce^{3+},Tb^{3+} nanocrystals. (**a**) A typical transmission electron micrograph (TEM), of $LaPO_4$:Ce^{3+}(1%)Tb^{3+}(20%) NCs. All samples have NCs with an average diameter of 4 nm and a polydispersity of 10%. They form clusters when dried on the hydrophobic surface of a TEM grid. Scale bar = 50 nm. (**b**) The powder x-ray diffraction pattern of $LaPO_4$:Ce^{3+}(1%)Tb^{3+}(40%) NCs, with the red lines the reference pattern of monazite $LaPO_4$ (PDF 00-032-0493). We see that even at the highest doping concentration the NCs maintain the monazite structure. Black dots mark diffraction lines originating from the sample holder.

Experimental details. PL measurements were performed using an Edinburgh Instruments FLS920 fluorescence spectrometer. For recording emission spectra we used a 450 W Xe lamp as excitation source, and a Hamamatsu R928 PMT with a grating blazed at 300 nm for detection. For PL decay measurements in the UV (of Ce^{3+}) we used a PicoQuant PDL 800-B + PLS 8-2-409 pulsed diode emitting at 270 nm with a repetition rate of 2.5 MHz, and a Hamamatsu H74220-60 PMT with a grating blazed at 300 nm. For PL decay measurements in the visible (of Tb^{3+}) excitation was done with an optical parametric oscillator (OPO) system (Opotek HE 355 II) pumped by the third harmonic of a Nd:YAG laser, and detection with a Hamamatsu R928 PMT using the multichannel scaling (MCS) option integrated in the FLS920 fluorescence spectrometer.

To obtain the refractive index in the UV of the different solvents, we used a home-built setup to measure the critical angle of total internal reflection of a UV laser beam (Kimmon He/Cd IK3151R-E; λ_{em} = 325 nm) on the glass–solvent interface. We found refractive indices of 1.36 for methanol, 1.40 for ethanol, 1.42 for 1-propanol, 1.43 for 1-butanol, 1.44 for 1-pentanol, 1.45 for 1-hexanol, 1.46 for 1-octanol, and 1.51 for DMSO. For refractive indices in the visible we used tabulated values for 589 nm.[49] We assume that the refractive index of $LaPO_4$ in the UV is 1.82, i.e. 0.03 higher than in the visible in analogy with the solvents.

Accounting for the finite size of a nanocrystal. As depicted in Fig. 7.4b, donors close to the NC surface have a different crystalline environment than those near the center. Assuming spherical NCs, we multiply the exponents n_i in Eq. 7.4 by a geometrical factor

$$f_i(a,h) = \begin{cases} 1 & ; \quad r_i < a-h \\ \frac{(a+h-r_i)(a-h+r_i)}{4hr_i} & ; \quad a-h < r_i < a+h \\ 0 & ; \quad r_i > a+h \end{cases} \tag{7.7}$$

with h the radial coordinate of the donor ion, and a the NC radius. We take into account the possible donor positions in a spherical NC by summation of Eq. 7.4 over different values of h with h^3 evenly distributed over the interval $[0, a^3]$. We must, however, note that the actual NCs are not perfectly spherical and exhibit a 10% size distribution. We have checked that, while the precise values fitted for C_{ET} and R_0 are affected, the trends visible in Figs. 7.5i,j are robust to neglecting these geometrical details in the averaging procedure. For each solvent we determine the radiative decay rate γ_{rad} from a maximum likelihood fit[16] of a single exponential to the data for $LaPO_4$:Ce^{3+}(1%) NCs. Subsequently, we fix γ_{rad} in a global weighted least-squares fit of Eq. 7.4 (accounting for the finite NC size; Eq. 7.7) to the data for the $LaPO_4$:Ce^{3+}(1%)Tb^{3+}(x%) NCs.

Influence of nanocrystal size on radiative decay. The NC-cavity model assumes that NCs are very small with respect to the wavelength of the emitted light. More precisely, it is valid in the limit that $ka \ll 1$, where $k = 2\pi/\lambda$ is the free space wave vector of the emitted light and a is the radius of the NC. In our case of NCs with a diameter of 4 nm emitting (primarily) at 540 nm this requirement is easily met: $ka = 0.02$. Fig. 7.9 shows the theoretical LF factor for larger $LaPO_4$ NCs (n_{NC} = 1.79) in methanol (n = 1.33), for dopants in the center (blue solid line) and at the surface (blue dotted line).[45] Most importantly, we see that for small NCs of a few nm in diameter the exact size does not affect the LF factor, and the NC-cavity model (black dashed line) is very accurate. In somewhat larger NCs the biggest deviation between the exact calculations and the NC-cavity model is for dopants at the center. For these we can obtain a second-order correction to the NC-cavity model (red dot-dashed line), by expanding the expressions from Ref. 45 for small ka:

$$\gamma_{rad}(n) = \gamma_{rad}^{(0)} \frac{n}{n_{NC}} \left(\frac{3n^2}{2n^2 + n_{NC}^2} \right)^2 \left[1 + \frac{(n_{NC}^2 - n^2)(n_{NC}^2 + 10n^2)}{5(2n^2 + n_{NC}^2)} (ka)^2 \right] \tag{7.8}$$

The NC-cavity model is accurate to within 5% if the second term between square brackets in Eq. 7.8 is smaller than 0.05. For $LaPO_4$:Tb^{3+} in methanol this is for NCs smaller than 41 nm in diameter. We conclude that (depending on the refractive indices involved, the emission wavelength and the desired accuracy) the NC-cavity model is reliable for NCs with sizes of up to several tens of nm.

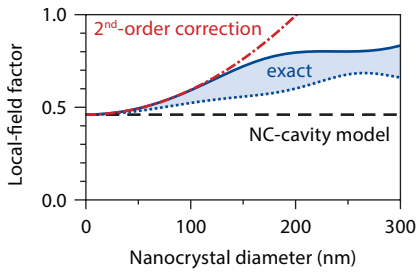

Figure 7.9 • The influence of NC size on the local-field factor appearing in the NC-cavity model for radiative decay. Theoretical local-field (LF) effect factor for doped $LaPO_4$ NCs (n_{NC} = 1.79) in methanol (n = 1.33) as a function of the NC size. Exact calculations of the LF factor following Ref. 45 are shown for dopants in the center of the NC (blue solid line) and at the surface (blue dotted line). The exact calculations are compared to the LF factor according the NC-cavity model (Eq. 7.6; black dashed line) and the NC-cavity model including a second-order correction (Eq. 7.8; red dot-dashed line).

CHAPTER 8

Delayed exciton emission and its relation to blinking in CdSe quantum dots

Based on

Delayed exciton emission and its relation to blinking in CdSe quantum dots
Rabouw, F.T., Kamp, M., Van Dijk-Moes, R.J.A., Gamelin, D.R., Koenderink, A.F., Meijerink, A. & Vanmaekelbergh, D.
Submitted

ABSTRACT • The efficiency and stability of emission from semiconductor nanocrystal quantum dots (QDs) is negatively affected by 'blinking' on the single-nanocrystal level, i.e. random alternation of bright and dark periods. The timescales of these fluctuations can be as long as many seconds, orders of magnitude longer than typical lifetimes of exciton states in QDs. In this work we investigate photoluminescence from QDs delayed over microseconds to milliseconds. Our results prove the existence of long-lived charge-separated states in QDs. We study the properties of delayed emission as a direct way to learn about charge carrier separation and recovery of the exciton state. A new microscopic model is developed to connect delayed emission to exciton recombination and blinking, from which we conclude that bright periods in blinking are in fact not characterised by uninterrupted optical cycling as often assumed.

8.1 • Introduction

Blinking, or intermittency, in the photoluminescence (PL) of individual semiconductor nanocrystal quantum dots (QDs) is a fascinating phenomenon that is still not fully understood.[96,202] Soon after the first observation of blinking in individual QDs[27] the idea was proposed that dark periods were due to temporary charging.[29] Charging would render the QD dark because subsequent excitations would decay not by the emission of a photon but by Auger recombination, i.e. transfer of the recombination energy to the excess charge carrier. This basic idea has been used to develop detailed models for blinking.[44,48,71] These models have in common that the rates of charging (by charge carrier ejection and trapping) and discharging (by recombination or release of the trapped charge) of the QD fluctuate in time, to understand the surprising power-law statistics of the durations of bright and dark periods. Recent experimental results have put into question the idea that Auger quenching alone can explain the dark periods.[139,146,150] They support alternative blinking models, where the dark states are due to charge carrier localization and non-radiative recombination on structural defects in the QD.[66,108,203] It has also been proposed that blinking can be due to a combination of Auger decay and non-radiative recombination at trap sites.[154,184] One of the reasons that there is still not one unifying physical model for blinking, is that models are based on rather indirect experimental data, namely the statistics of bright and dark durations.

In this work we examine the PL dynamics of core–shell CdSe/CdS/CdZnS/ZnS QDs over ten orders of magnitude in time. There is exciton recombination on the nanosecond timescale, and blinking on the second timescale. We focus in particular on 'delayed emission' on timescales from microseconds to milliseconds.[103,113] This component in the PL decay dynamics of QDs is often overlooked because, although its integrated intensity can be higher than 10%, the amplitude is much less than a percent of the exciton emission. We examine the properties of delayed emission, concluding that it is due to charge separation, storage, and eventual recovery of the lowest exciton state. Interestingly, the decay of delayed emission follows a power law, very similar to the statistics of bright and dark durations in blinking. A unifying microscopic model is presented to account for both delayed emission and blinking.

8.2 • Emission dynamics in core–shell quantum dots

The QDs investigated have a CdSe/CdS/CdZnS/ZnS core–shell structure with a 3.4 nm diameter CdSe core, and emit around 630 nm (Figs. 8.1a,b). Single-QD spectroscopy illustrates the many different dynamical processes that can occur in a QD. The emission intensity trace (Fig. 8.1c) of a single core–shell QD over a period of 5 min of continued excitation exhibits blinking, i.e.

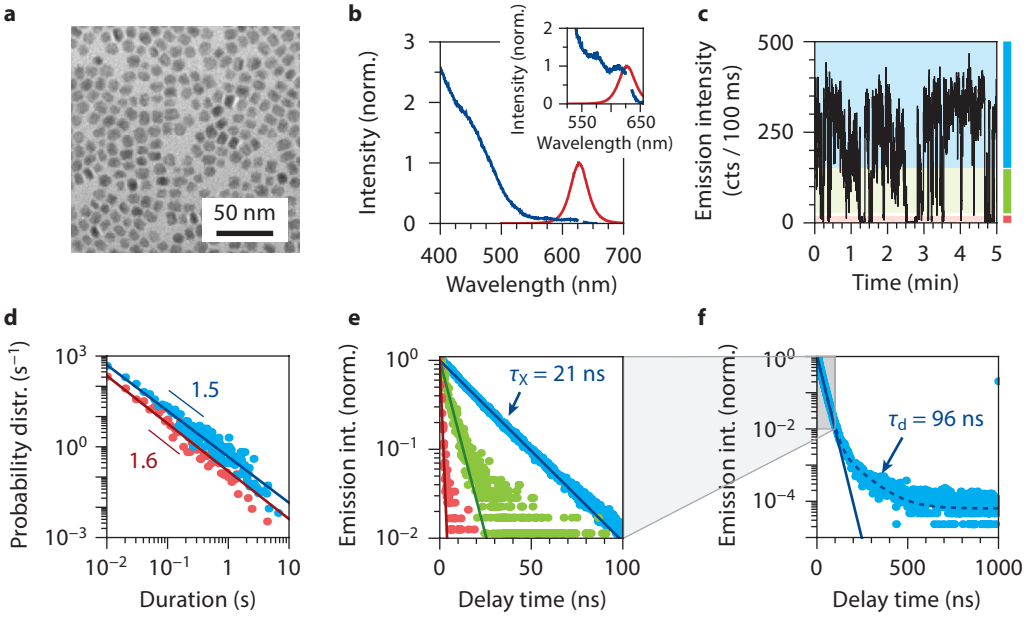

Figure 8.1 • Properties of the core–shell quantum dots investigated. (**a**) A transmission electron microscopy image of the CdSe/CdS/CdZnS/ZnS core–shell QDs. They have a slightly anisotropic shape of 11.4 ± 1.0 nm by 8.2 ± 0.7 nm (mean ± standard deviation over 100 QDs) and consist of a CdSe core with a diameter of 3.4 nm, and shells of CdS (6 monolayers), CdZnS (1 monolayer) and ZnS (1 monolayer). (**b**) PL excitation (blue) and emission (red) spectra of the ensemble of QDs. There is a single emission band centered at 630 nm originating from exciton recombination in the CdSe core. The excitation spectrum is dominated by strong absorption by the CdS shell at wavelengths shorter than 500 nm. The inset is a zoom-in, revealing the discrete electronic transitions in the CdSe core. (**c**) An emission intensity trace of a single core–shell QD under continued excitation. The bin size is 100 ms. Colored shadings indicate the ranges of intensity values which for further analysis are considered bright (blue), intermediate (green), and dark (red). (**d**) The probability distribution of the duration of bright (blue) and dark (red) periods, extracted from the emission intensity trace at a bin size of 10 ms. Solid lines are fits to a power-law trend, from which we obtain exponents of 1.5 for the bright periods, and 1.6 for the dark periods. (**e**) PL decay curves of the bright (blue), intermediate (green), and dark (red) periods, constructed after selecting time bins based on emission intensity. Solid lines are fits to single-exponential decay. We obtain the exciton lifetime of τ_X = 21.3 ns from the bright periods, and PL lifetimes of 5.5 ns and 0.9 ns during the intermediate and dark periods, respectively. With a bin width of 0.165 ns, the absolute peak counts in the PL decay curves are 21.5 (blue), 14.8 (green), and 5.3 (red) cts/100 ms. The lower peak counts during intermediate and dark periods might occur because the fastest decay component is faster than the bin size. (**f**) PL decay curve for the bright periods plotted over a time range of 1 µs. The solid line is the single-exponential fit to the first 100 ns (with τ_X = 21.3 ns; panel **e**). Adding a second exponential decay component and a background yields the dashed line. We obtain a time constant for the delayed component of τ_d = 96 ns. This PL decay curve has a bin width of 1.65 ns, 10× wider than in **e**.

on timescales of up to seconds the QD switches randomly between a state of bright emission (blue shaded area) and states of intermediate brightness (green) or near complete darkness (red). The probability distributions for the duration of bright (ON; blue) and dark (OFF; red) periods (Fig. 8.1d), obtained with a threshold analysis,[44] show that the timescales of the ON/OFF fluctuations range from 10 ms to several seconds. Solid lines are fits to a power-law distribution ($p(t) = t^{-\alpha}$

with t the duration of a period) which yield $\alpha_{ON} = 1.5$ and $\alpha_{OFF} = 1.6$, as typically found for blinking statistics.[44,147,202]

The PL decay curve of this QD during bright periods (blue data points in Fig. 8.1e) is single-exponential over two orders of magnitude in intensity with a lifetime of $\tau_X = 21$ ns, consistent with the radiative lifetime of the exciton in CdSe QDs. During periods of intermediate intensity (green) or dark periods (red) the PL decay is faster, with fitted lifetimes of 5.5 ns and 0.9 ns, respectively. Such fast decay dynamics are due to non-radiative decay pathways, which have previously been interpreted as Auger recombination of a trion state[29,109,122,180] or rapid charge carrier trapping and recombination[66,139,150] (see below for further discussion).

Clearly, a remarkably wide range of timescales is involved in the emission characteristics of QDs. On the one hand there is the timescale of nanoseconds on which excitations decay (Fig. 8.1e), while on the other hand there is the timescale of milliseconds to seconds on which the emission intensity fluctuates (Fig. 8.1d). There are a few papers[103,113] discussing 'delayed' PL from CdSe QDs on the timescale of up to 1–10 μs. Indeed, on timescales beyond 100 ns the PL decay curve of the bright state in our single QD (Fig. 8.1f) deviates from the single exponent with the exciton lifetime of $\tau_X = 21$ ns (solid line). We can add an exponential 'delayed component' plus background to the fit (dashed line) and obtain a delayed lifetime of $\tau_d = 96$ ns. The lifetime of this component is too long to originate from direct radiative recombination of an exciton. In analogy to previous papers[103,113] we ascribe the delayed emission to exciton storage in a charge-separated state for long periods, before eventual recovery of the delocalized $1S_{3/2}1S_e$ exciton state (i.e. with conduction and valence band states occupied) and emission. In this charge-separated state (at least) one charge carrier is trapped on the surface or in the environment of the QD.

8.3 • Connecting the nanosecond and millisecond time scales

To further examine the delayed emission dynamics we measure the PL decay of the QD ensemble when dispersed in toluene. On a 100 ns timescale the PL decay of the ensemble (Fig 8.2a) looks similar to that of the single QD discussed above. At delay times longer than 100 ns the decay curve (Fig. 8.2b) deviates from the double-exponential fit of Fig. 8.2a (dot-dashed line). In fact, the PL decay follows a power-law over the next four orders of magnitude in time (from ~100 ns to 1 ms) and seven orders of magnitude in emission intensity. The power exponents that we fit are similar to those of the blinking statistics (Fig. 8.1d), namely 1.7 between 200 ns and 400 μs, and 2.0 between 50 μs and 5 ms. Interestingly, the integrated intensity of delayed emission contributes as much as 10%–15% of the total number of emitted photons. This would mean that following excitation there is a 10%–15% probability of charge separation. The observation of delayed emission from several single QDs (Fig. 8.3)[103] indicates that the competition between direct and delayed emission happens on the single-QD level, rather than being an ensemble effect.

Figs. 8.2c,d compare the exciton emission and delayed emission spectra of the ensemble of QDs in toluene. In the first 200 ns (Figs. 8.2c) after excitation the emission peak shifts to the red, because smaller QDs in the ensemble emitting at shorter wavelengths have a faster radiative decay rate than the larger ones emitting at longer wavelengths.[72] The spectrum of the delayed emission (Fig. 8.2d) is similar to the exciton emission, but with the emission peak position slightly red shifted by ~10 meV (see also Fig. 8.2e). From this similarity we conclude that delayed emission is the result of recovery of and emission from the delocalized $1S_{3/2}1S_e$ exciton state, rather than direct radiative recombination of charge carriers in the charge-separated state. The red shift of ~10 meV of the delayed emission compared to the exciton emission might indicate that in the smaller QDs

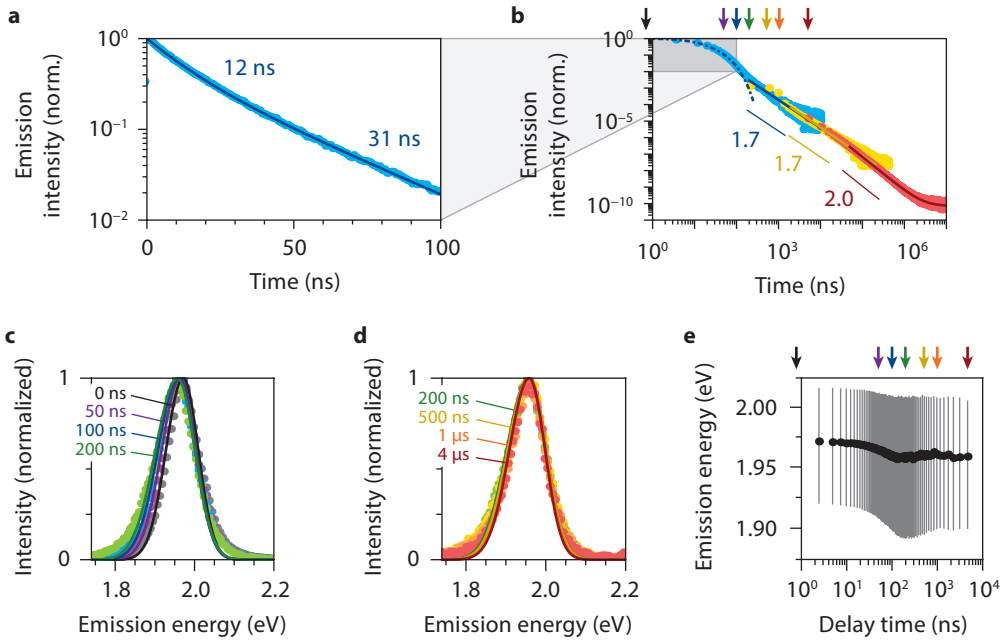

Figure 8.2 • Delayed emission after up to milliseconds. (**a**) The ensemble PL decay curve of the core–shell QDs appears near exponential on a 100 ns time scale. A biexponential fit yields lifetime components of 12 ns and 31 ns. (**b**) We can measure PL from the ensemble of QDs until up to as long as milliseconds after the laser pulse. On time scales longer than 100 nanoseconds the PL decay clearly deviates from the biexponential behavior (blue dash-dotted line) fitted to the first 100 ns. Blue, yellow, and red data points are three separate measurements, taken with a diode laser with a repetition rate of 100 kHz (blue), or an OPO laser with a repetition rate of 20 Hz (yellow and red). The red curve was taken on a concentrated QD dispersion over a measurement time of 3 days. The PL decay after a delay time of 200 ns can be fitted to power-law decay, yielding a power exponent of 1.7 between 200 ns and 400 µs, and 2.0 between 50 µs and 5 ms. (**c**) The emission spectrum of the ensemble of QDs in toluene at varying time delays after the excitation pulse of 0 (black), 50 (purple), 100 (blue), and 200 (green) ns. The emission peak redshifts over 15 meV and the spectrum becomes broader by 20 meV. The solid lines are fits to a two-sided Gaussian (see Methods). (**d**) The emission spectrum at longer delay times of 200 (green; same as in **c**), 500 (yellow), 1000 (orange), and 4000 (red) ns. The changes occurring in the first 200 ns are partially reversed: the peak blueshifts over 2 meV, and the band width decreases by 10 meV. (**e**) The emission energy (dots) and band width (lines) of the ensemble of QDs as a function of delay time after the excitation pulse, as obtained from two-sided Gaussian fits to the emission spectra (see Methods). Arrows on the top mark the spectra shown in panels **c** and **d**.

of the ensemble, i.e. those emitting at shorter wavelengths, charge carrier separation (which eventually leads to delayed emission) is somewhat less likely than in the larger QDs.

To learn more about the process of charge carrier separation, we measured the PL decay of the ensemble of QDs while dispersed in solvents of different refractive indices. Fig. 8.4a shows how the decay dynamics change when going from a low refractive index (hexane; red; $n = 1.375$) to a high refractive index solvent (carbon disulfide; blue; $n = 1.627$). Solid lines are fits (see Methods). The average PL lifetime of the exciton becomes longer at lower refractive index (Fig. 8.4b) because radiative decay is slower in a medium with lower refractive index, as described by the nanocrys-

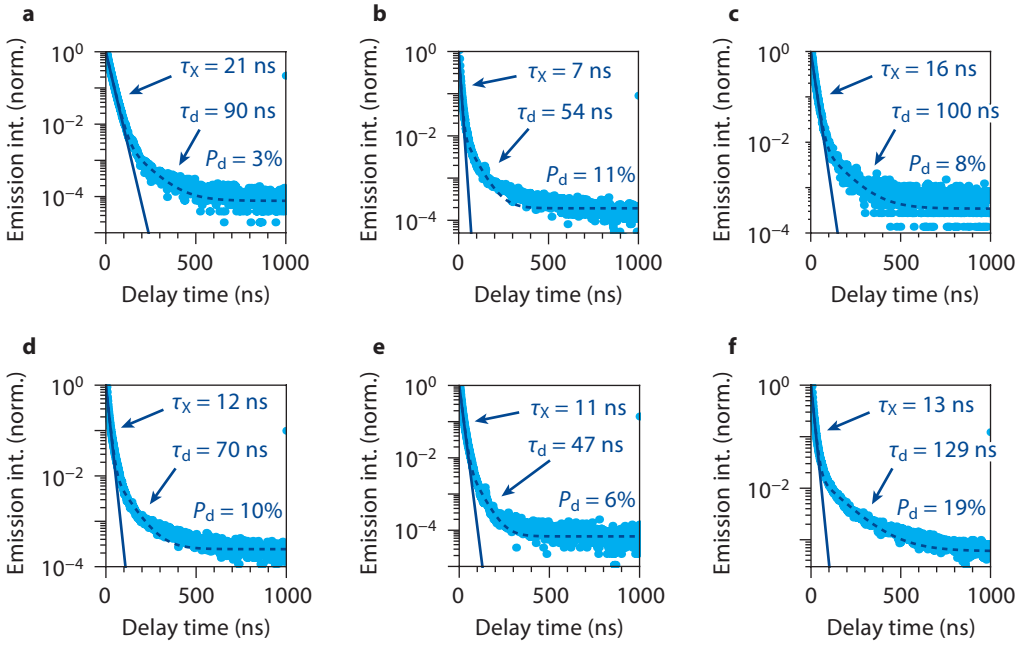

Figure 8.3 • PL decay curves of six single core–shell QDs. (**a–f**) The exciton lifetime τ_X is estimated from a single-exponential fit to the first 100 ns. At longer timescales, typically at a normalised intensity of 10^{-3}–10^{-2}, the decay deviates from this single exponential. A 'delayed component' and a background is added, from which we obtain a 'delayed lifetime' τ_d and the relative contribution of the delayed component $P_d = A_d\tau_d / (A_X\tau_X + A_d\tau_d)$ (where A_X and A_d are the amplitudes of the direct and the delayed component). The fitted values for τ_X, τ_d and P_d are given each panel. The values for P_d are underestimated because part of the delayed contribution is hidden by the background noise with a normalized intensity of 10^{-4}–10^{-3}. Indeed, the absolute count rates of the fitted 'background' [which are (**a**) 4, (**b**) 14, (**c**) 3, (**d**) 17, (**e**) 6, and (**f**) 18 counts per time bin of 1.65 ns over a 5 min measurement] show a correlation with with delayed contribution P_d, indicating that the background consists in part of delayed photons. We see that a delayed component is apparent in the PL decay of all single QDs, but the relative contribution varies from QD to QD.

tal-cavity model (see Ch. 7). From the data of Fig. 8.4b we estimate that the quantum efficiency of direct exciton emission is around 80%–90% (see Methods). This is consistent with a significant probability of charge separation.

Fig. 8.4c shows that the relative contribution of the delayed component as a percentage of the total emission intensity is lower if the refractive index of the solvent is higher. This is the result of competition between charge carrier separation and direct exciton emission from the same excited state. If in a high refractive index solvent the rate of radiative decay from the exciton state is enhanced, then the probability of separation is reduced (analogous to the competition between radiative decay and energy transfer in Ch. 7). Hence, we must conclude that charge carrier separation occurs from the lowest-energy exciton state of our QDs (i.e. the emitting one), not from hot carrier states as previously proposed to explain so-called B-type blinking.[154] In fact, our model presented below provides an alternative but natural explanation for B-type blinking[154] (Fig. 8.6).

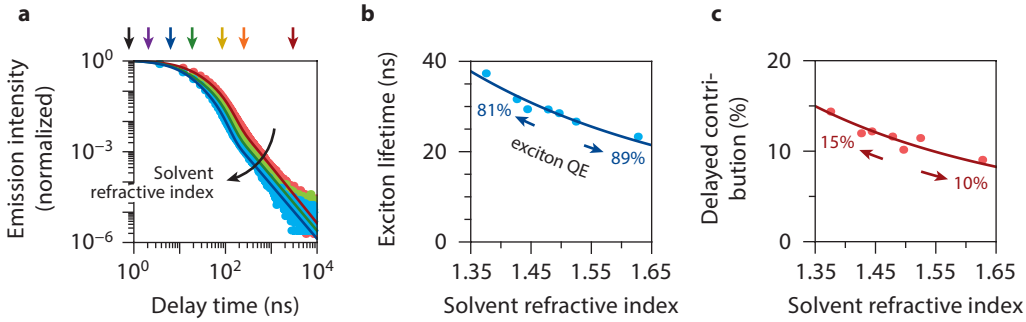

Figure 8.4 • Photonic effects on charge carrier trapping. (**a**) PL decay curves of the ensemble of QDs over a time scale of 10 μs for different solvents in which they are dispersed: hexane (red; refractive index $n = 1.375$), trichloroethylene (green; $n = 1.478$), and carbon disulfide (blue; $n = 1.627$). Solid lines are fits to decay with a biexponential contribution from direct exciton recombination and a power-law contribution from delayed emission. Arrows on the top mark the delay times for which the spectra are shown in Figs. 8.2c,d. (**b**) The exciton lifetime [average lifetime from a biexponential fit to the first 100 ns of decay (see Figs. 8.2a), weighted by integrated intensity] is shorter in solvents with higher refractive index, because the the local density of optical states is higher (see Ch. 7). From the data we fit that the quantum efficiency of the exciton, i.e. the probability of direct radiative decay, is roughly 80%–90% depending on the refractive index. (**c**) The contribution of power-law delayed emission as a percentage of the total number of photons emitted, as obtained from a fit to Eq. 8.2. The presence of a trend with solvent refractive index indicates that charge carrier separation happens from the lowest exciton state and competes with direct radiative recombination of the exciton. The solid line is a fit assuming that the rate of charge separation is fixed, while the rate of radiative decay of the exciton changes with the local density of optical states (analogous to the competition between radiative decay and energy transfer in Figs. 7.2d,e).

8.4 • Monte Carlo simulation of blinking and delayed emission

The similarity in power-law statistics for blinking (Fig. 8.1f) and delayed emission (Fig. 8.2b) suggests that the same physical process underlies the two phenomena. Can delayed emission be explained in terms of existing models for blinking?[202] A model for blinking must at least contain (1) an explanation for the power-law statistics of ON and OFF durations, and (2) a microscopic picture for the dark state. Based on the early paper of Efros & Rosen,[29] most models are 'charging models' (Fig. 8.5a). They ascribe the dark periods to temporary charging of the QD. The excess charge carrier quenches emission by enabling Auger recombination (step A in Fig. 8.5a). Alternative 'recombination center models'[66,108] propose that the QD becomes dark when fluctuations in the QD structure open non-radiative recombination pathways via recombination centers.

Only models based on charging are consistent with the observation of delayed emission on time scales from 100 ns to 1 ms (Fig. 8.2b), because delayed emission requires a long-lived metastable electronically excited state only present in charging models[44,48,71] (highlighted in Fig. 8.5a). In existing charging models for blinking this is a long-lived charge-separated state with one delocalized and one trapped charge. The release rates for the trapped charge fluctuate widely in time, to explain the power-law distribution in OFF durations (Fig. 8.1d). These wide fluctuations would also lead to power-law decay of the delayed emission (Fig. 8.2b). We therefore conclude that our observation of delayed emission over long timescales supports a charging model for blinking, involving long-lived charge-separated states.

Recently, in specially designed core–shell structures a 'gray state' with 10%–40% intensity has

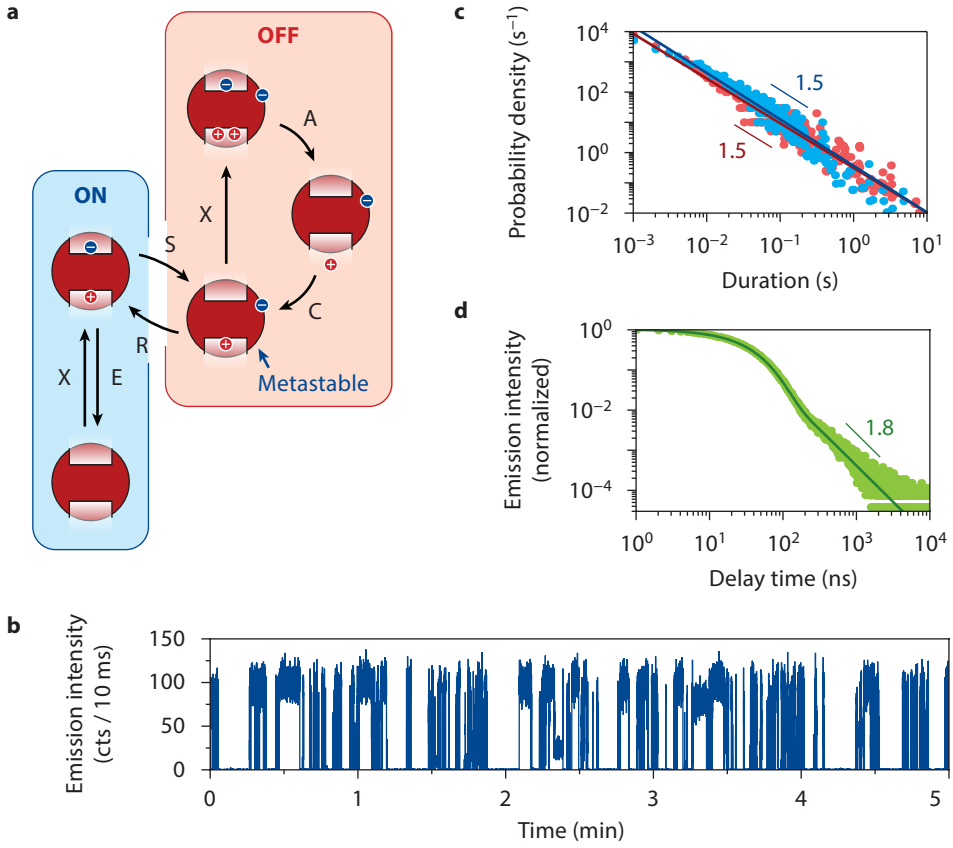

Figure 8.5 • Simulation of power-law delayed emission and power-law blinking. (**a**) In the charging model for blinking, optical cycling (X: excitation, E: emission) in the ON-state (blue panel) is sometimes interrupted by charge carrier separation (S): ejection of a carrier from the QD core and trapping in the environment, e.g. on the surface or in the shell. This leaves the QD with a single delocalized carrier. The QD is then OFF (red panel) because subsequent excitations (X) decay non-radiatively via Auger recombination (A) and charge carrier cooling (C). The QD returns to the ON-state if the delocalized exciton state recovers (R) by release of the trapped carrier. In our model the probability for charge separation P_S is fixed, while the recovery rate γ_R fluctuates strongly over time (see Methods). (**b**) An emission intensity trace simulated with our model for a laser repetition period of 1 µs, an exciton decay rate of γ_X = 1/30 ns, a probability of charge carrier separation of P_S = 15%, and diffusion and release exponents of α_D = 1.7 and α_R = 1.55 (see Methods). (**c**) The durations of bright and dark periods are power-law distributed, although there is a deviation in the bright statistics for durations shorter than 10 ms (blue data points deviate from the blue line). (**d**) The histogram of delay times shows an exponential component originating from direct exciton recombination and a power-law delayed component. From a fit to Eq. 8.2 we obtain a power exponent of α = 1.8, and recover the input values of P_S = 15.4% and γ_X = 1/29.7 ns.

been often observed in the blinking traces. It could be identified as a *negatively* charged state,[184,207] with exponential blinking statistics[154] rather than power-law (see also Fig. 3.5). The dynamics of this gray state are consistent with those of the negative trion state created electrochemically[112,154] or photochemically.[226] However, in most QDs a dark state (rather than a gray state) is dominant

in the blinking trace. This darkest state (which comes with power-law statistics; see Fig. 3.5) has recently been proposed by Park *et al.*[235] to involve ejection and trapping of an electron, leaving the QD with an excess *positive* charge in the valence band. We therefore tentatively identify the trapped charge in the charge-separated state involved in power-law blinking and delayed emission as the electron (see Fig. 8.4a). Indeed, positive trions (consisting of an exciton plus the excess hole) created in the charge-separated dark state exhibit much faster Auger decay than negative trions involved in the gray state,[226,235] explaining that the charge-separated state is dark. Alternatively, to explain apparent discrepancies at the single-QD level between the decay rate of the dark state in blinking and the biexciton decay rate,[146] one might assume that the excess hole localizes at a defect or surface site. Indeed, also localized charge carriers can enable rapid Auger quenching.[201]

At first sight delayed emission seems to fit in existing charging models for blinking, which propose long-lived charge-separated states.[44,48,71] There is however one important feature of delayed emission that is not properly accounted for in existing models, namely that the integrated intensity amounts to as much as 10%–15% of the total emission. The models explain the long ON times that occur (see Fig. 8.1d) in terms of unperturbed optical cycling (processes X,E in Fig. 8.5a). In these models charge carrier separation is sometimes prevented for long periods, for example by fluctuating tunnelling barriers and heights,[44] Coulomb blockade,[48] or diffusion of the relative energies of the exciton state and the charge-separated state.[71] If optical cycling went indeed un-

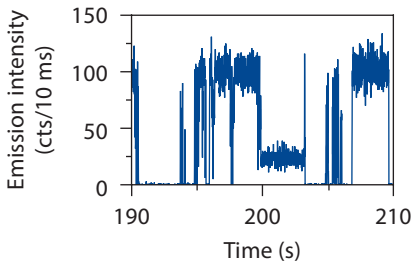

Figure 8.6 • A discussion of B-type blinking in terms of our new blinking model. Recently, Galland *et al.*[154] observed what they called 'B-type blinking': the QD blinks between a bright state and a state with lower intensity but the same PL decay rate. B-type blinking was ascribed to hot-electron capture, which explains that while traps are active fewer excitations cool down to a ground state exciton (hence the lower intensity) but that the lowest exciton state itself is not affected (hence the unaffected PL decay rate). An alternative explanation of B-type blinking, not involving the scenario of hot-electron capture, would be that in their experiment a type of charge carrier trap is introduced (perhaps in the electrode used) that can make a charge-separated state with a recovery rate γ_R on the order of the excitation rate of the QD. If such trap were active, the QD would exhibit ON durations of on average $T_{ON} = 1/P_S\gamma_{exc}$ (with γ_{exc} the excitation rate of the QD) and OFF durations of on average $T_{OFF} = 1/\gamma_R$. Averaged over a time bin in the intensity trace, the apparent quantum efficiency during the active period of the trap would be $\eta = T_{ON}/(T_{ON} + T_{OFF}) = \gamma_R/(P_S\gamma_{exc} + \gamma_R)$. Conversely, an apparent quantum efficiency η would correspond to an exciton recovery rate of $\gamma_R = P_S\gamma_{exc}\eta/(1 - \eta)$. The plot is a zoom-in of the simulated intensity trace of Fig. 8.5b. It shows a period between 199 s to 203 s where the intensity is at some intermediate level between the brightest state and the darkest state. Note that in our model the OFF state is completely dark, so that intermediate intensities must be due to rapid switching between ON and OFF on timescales faster than the binning time of the intensity trace. The rate of switching is determined by the recovery rate γ_R, which can be fixed for a long period T. The intermediate intensity state occurring around $t = 200$ s, with an apparent quantum efficiency of $\eta \approx 25\%$ occurs because during these 4 s the trap has a release rate of $\gamma_R \approx 0.05\ \mu s^{-1}$.

perturbed for milliseconds or even seconds as existing models suggest, the relative contribution of the delayed emission could never become 10%–15% of the total emission.

We have developed a simple model (Fig. 8.5a) for blinking that simultaneously explains the (power-law distributed) ON and OFF durations of seconds in the intensity trace of a single QD (Fig. 8.1c), and the significant contribution of delayed emission to the total emission (Fig. 8.2b). In its simplest form the model assumes a single trap that can cause charge separation by trapping an excited charge carrier, rendering the QD dark because of Auger quenching by the remaining carrier. The key ingredients of the model are that (1) the probability of charge carrier separation is fixed at a few percent (determined by competition with radiative decay; Fig. 8.4), that (2) the exciton recovery rate is constant only during a power-law distributed time T, and that (3) after time T the recovery rate changes to a random new value such that the time-averaged distribution of recovery rates follows a power-law.[44,48,71] Power-law distributed times T would naturally follow from a microscopic picture that charge separation involves charge carrier trapping on a structural defect or a particular arrangement of the organic ligand shell, and that energetic barriers for structural changes are exponentially distributed. For details of the model see the Methods section.

The most radical difference with existing blinking models is the proposal here that at all times there is a finite probability of charge separation (which we assume fixed, but it can also be allowed to fluctuate around some mean value). This assumption ensures that the delayed emission has a sufficiently high integrated intensity, and is supported by our finding that the contribution of delayed emission increases with decreasing refractive index (Fig. 8.4). However, the assumption implies that long ON periods are in fact not characterised by unperturbed optical cycling, as currently assumed. Instead, they occur when for a long period T the exciton recovery rate is much faster than the excitation rate (~0.3 μs^{-1} in Figs. 8.1c–f, 8.3). The QD is then 'effectively ON', i.e. optical cycling is interrupted by OFF periods so short (i.e. ns–μs) that they do not affect the emission intensity during period T. Note that these short OFF periods are however responsible for the delayed emission that we observe in the PL decay traces of single QDs (Fig. 8.1f and Fig. 8.3). Figs. 8.5b–d present the results of a Monte Carlo simulation of the emission dynamics in a QD using our model. The intensity trace (Fig. 8.5b) and distributions of ON and OFF durations (Fig. 8.5c) are as typically encountered for single QDs. At the same time, the PL decay curve (Fig. 8.5d) contains a power-law delayed component with a relative contribution of 15%. Hence, our new model successfully reproduces the most important aspects of the emission dynamics of QDs.

8.5 • Conclusion

To summarize, we have observed delayed emission from semiconductor QDs as direct evidence for the existence of a charge-separated state which recovers on timescales of nanoseconds to milliseconds. Charge separation takes place from the lowest exciton state, and the charge-separated state recovers to the lowest exciton state before emitting a delayed photon. The delayed emission exhibits power-law statistics very similar to those of the durations of bright and dark periods in blinking, suggesting a common origin. Indeed, we have successfully reproduced the delayed emission and the blinking statistics with a new blinking model, realizing that there is in fact no uninterrupted optical cycling during bright periods. The power-law distribution of exciton recovery rates implies that charge-separated states have lifetimes ranging from μs to s. Short-living charge-separated states (μs) hardly affect the brightness of the QD, as long as the excitation rate is slower than the exciton recovery rate. Efforts should mainly be aimed at reducing the effect of long-living charge-separated states (ms–s), because these lead to blinking and a resulting reduction in overall time-averaged brightness of the QD.

8.6 • Methods

Synthesis of CdSe/CdS/CdZnS/ZnS core–multi-shell QDs following Ref. 74.

Precursor preparation. Cadmium precursor I [0.1 M $Cd(OA)_2$] was prepared by mixing oleic acid (3.68 g), octadecene (25.92 g) and $CdAc_2$ (0.64 g), and heating to 150°C under vacuum for 2 h. Cadmium precursor II [0.1 M $Cd(OA)_2$] was prepared by dissolving $CdAc_2$ (1.10 g) in oleic acid (10.83 g) and octadecene (43.20 mL), and heating to 150°C under vacuum for 2 h. Selenium precursor was prepared by dissolving elemental selenium (4.25 g) in trioctylphosphine (22.5 g) at 50°C, followed by the addition of octadecene (35.7 g). Zinc precursor [0.1 M $Zn(OA)_2$] was prepared by dissolving diethyl zinc (0.494 g) in oleic acid (5.05 mL) and octadecene (19.8 mL) at 310°C. Sulfur precursor solution (0.1 M) was prepared by dissolving sulfur (0.032 g) in octadecene (10 mL) at 180°C.

Synthesis of CdSe QD seeds. CdSe QD seeds were synthesized in a 50 mL three-neck flask using a Schlenk-line. Trioctylphosphine oxide (1.11 g), octadecylamine (3.20 g) and Se precursor (4.9 g) were mixed, and heated to 295°C. When this temperature was reached, the $Cd(OA)_2$-precursor I (5.2 g) was added rapidly. The mixture was cooled down after 5 min. The particles were diluted by adding 1 equivalent of hexane. The QDs were washed by adding 2 equivalents of methanol, collecting the upper hexane layer (colored), and then precipitating the QDs with 1 equivalent of acetone. Finally, the QD seeds were dissolved in toluene.

Growth of a CdS/CdZnS/ZnS shell. The Cd-, Zn-, and Cd/Zn-precursor solutions were kept at about 80°C, the sulfur precursor solution at room temperature. The CdSe seeds (10^{-7} M of QDs with 3.4 nm diameter in toluene), octadecene (5.0 g) and octadecylamine (1.5 g) were mixed and heated to 150°C for 1 h to remove all toluene. The reaction temperature was then increased to 240°C. The shell was grown layer-by-layer under N_2 by injecting a precursor solution every 30 min, alternating cation and anion precursors. 6 layers of CdS, 1 layer of CdZnS, and 1 layer of ZnS were grown. After the final injection of sulfur precursor the reaction was kept at 240°C for 1 h. It was then allowed to cool down to room temperature and diluted with 1 equivalent of toluene. The particles were washed by precipitation using 2 equivalents of a butanol:methanol (1:2) mixture, and centrifugation. The final product was dissolved in toluene.

Single quantum dot spectroscopy. For single-QD measurements the QDs were spin-coated on a HMDS (hexamethyl disilazane) coated borosilicate glass coverslip from a dilute dispersion in toluene, and protected with a layer of spin-coated PMMA (polymethyl methacrylate). Single QDs were excited with supercontinuum light source (Fianium SC450) at a repetition rate of 1 MHz and a fluence of ~10^{-4} J/cm^2. The excitation wavelength of 532 nm was selected by spectral filtering using an acousto-optical tunable filter (Crystal Technologies) and an additional short pass filter. Fluorescence light was collected through the same objective used for excitation, and separated from laser reflections using a long-pass filter with a cut-off at 590 nm. We used a Hanbury Brown-Twiss setup with two ID Quantique id100-20 ULN avalanche photodiodes (APDs; dark counts <10 Hz) connected to a timing card (DPC 230, Becker & Hickl GmbH) with 165 ps time resolution.

Monte Carlo simulation of the emission dynamics in a QD. The Monte Carlo simulation yielding the results of Fig. 8.5 is done as follows. First the initial state of the trap is set, i.e. the recovery rate γ_R and the 'stationary time' T until diffusion to a new state. A recovery rate is generated from a power-law distribution with exponent $\alpha_R = 1.55$, a low-end cut-off of 1/10 s and a high-end cut-off of 1/60 ns (see Fig. 8.7). The stationary time is generated by first generating a trap diffusion rate γ_D from a power-law distribution with exponent $\alpha_D = 1.7$, a low-end cut-off of 1/10 s and a high-end cut-off of 1/60 ns, and then T from an exponential distribution with decay constant γ_D. The QD is excited every 1 μs for a period of 5 min. Following each excitation, there is a probability of $P_S = 15\%$ for charge carrier separation by trapping. If there is no separation (i.e. there is direct exciton recombination), a delay time t is simulated from an exponential distribution with decay constant $\gamma_X = 1/30$ ns. If there is separation, the actual recovery rate γ_R is used to generate from an exponential distribution the time t until recovery of the delocalized exciton state and delayed emission. Optical cycling does not proceed until after the trapped carrier is released. When the stationary time T is exceeded, the trap state is reset by generating a new recovery rate γ_R and a new stationary time T as described above.

Fitting delayed emission dynamics. The normalised decay function due to a distribution of decay rates $\rho(\gamma) = \gamma^{\alpha-2}$ with an upper limit of γ_{max} is

$$I_d(t) = \int_0^{\gamma_{max}} \gamma\rho(\gamma)\,d\gamma = \frac{\alpha-1}{\gamma_{max}^{\alpha-1}}\,t^{-\alpha}\,\left[\Gamma(\alpha) - \Gamma(\alpha, \gamma_{max}t)\right], \tag{8.1}$$

where $\Gamma(s)$ is the Gamma function, and $\Gamma(s,x)$ the incomplete Gamma function. Eq. 8.1 describes power-law decay $I_d = t^{-\alpha}$ at long delay times $t \gg 1/\gamma_{max}$, while the factor between square brackets is a correction to keep the function well-behaved at short times $t \approx 0$. In Fig. 8.7 we show that Eq. 8.1 with $\gamma_{max} = \gamma_X/2$ (where γ_X is the exciton decay rate) can be used as a good approximation for the delayed emission in case of back and forth charge separation and recovery of the exciton state. To fit the complete PL decay dynamics we use a model function with one (Fig. 8.5d) or two (Fig. 8.4a) components of the form:

$$I(t) = (1-P_S)\gamma_X e^{-\gamma_X t} + P_S\,\frac{\alpha-1}{(\gamma_X/2)^{\alpha-1}}\,t^{-\alpha}\,\left[\Gamma(\alpha) - \Gamma(\alpha, \gamma_X t/2)\right]. \tag{8.2}$$

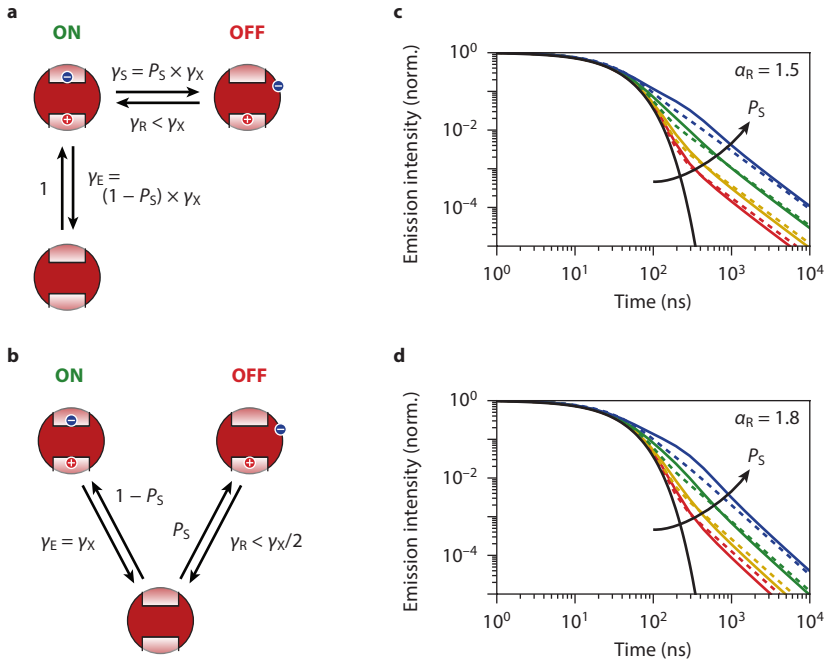

Figure 8.7 • Photoluminescence decay following charge carrier trapping, storage and release. (**a**) The kinetic scheme of charge carrier trapping, storage and release. The corresponding three-level rate equation model is solved to yield the decay of the population in the exciton state $N_X(t)$. In our model the values of γ_X and γ_S are fixed, while γ_R varies over time and samples a power-law distribution. We integrate the exciton decay $N_X(t)$ over the distribution of γ_R with an upper limit $\gamma_{max} = \gamma_X$. (**b**) A much simpler model where a fraction $P_S = \gamma_S/\gamma_X$ of the photons are contained in the delayed emission component, with a power-law distributed rate having $\gamma_{max} = \gamma_X/2$. The factor 1/2 here accounts for the fact that a pathway leading to delayed emission goes through the exciton state with decay rate γ_X (at least) twice. The power-law decay of the trapped state is as described by Eq. 8.1. The rest (fraction $1 - P_S$) of the photons are emitted from the exciton state and contribute an exponential component with decay constant γ_X. The total PL decay is therefore as described by Eq. 8.2. (**c**,**d**) The normalized PL decay trace in case of power exponents of (**c**) $\alpha_R = 1.5$ or (**d**) $\alpha_R = 1.8$ for the recovery rates, at different trapping probabilities of $P_S = 0\%$ (black), 5% (red), 10% (yellow), 25% (green), and 50% (blue), and simulated with the three-level rate equation model (depicted in **a**; solid lines) or with the simpler model (depicted in **b**; dashed lines; Eq. 8.2). We took $\gamma_X = 1/30$ ns.

The first term is the exponential contribution due to direct exciton recombination. The second term is the delayed contribution. In Fig. 8.7 we explain that P_S must be interpreted as the probability of charge carrier separation for times longer than the intrinsic exciton lifetime $\tau_X = 1/\gamma_X$.

The interplay between charge carrier trapping and release. As mentioned above, we model delayed emission with an upper limit to the distribution of decay rates of $\gamma_{max} = \gamma_X/2$. In principle, however, there is no reason to assume that the recovery rates are widely (power-law) distributed from s^{-1} to ns^{-1}, but that there is some finite upper limit. The choice of $\gamma_{max} = \gamma_X/2$ is inspired by the fact that if at a certain point in time a trap is active with a recovery rate of order ns^{-1} or faster, it will hardly affect the dynamics of photon emission. More precisely, in that case the rate limiting step is the emission process itself, not detrapping and recovery of the delocalized exciton state. The charge-separated state is formed on a timescale of $1/\gamma_X$ (where $\gamma_X = \gamma_E + \gamma_S$ is the total decay rate of the exciton), recovers to the delocalized exciton on a timescale of $1/\gamma_R$, which then emits on a timescale of $1/\gamma_X$. Hence, the shortest possible time scale of delayed emission $2/\gamma_X$.

In Fig. 8.7 we compare a full rate-equation model with back-and-forth charge carrier trapping and release, with the analytical model of Eq. 8.2. We see a good correspondence, concluding that the analytical model (where the competition between trapping and release is captured in a single parameter P_S) is a good approximation to describe the dynamics. The parameter P_S must be interpreted as the probability of charge separation due to charge carrier trapping in a trap with a release rate slower than the intrinsic exciton decay rate ($\gamma_R < \gamma_X$), since only such traps are considered in the rate-equation

model (Fig. 8.7a).

Estimating the PL quantum efficiency with the nanocrystal-cavity model. The rate of radiative decay γ_{rad} scales linearly with the local density of optical states experienced by an emitter. In a nanocrystal the local density of optical states depends on the refractive index of the surrounding solvent n, as described by the nanocrystal-cavity model (see Ch. 7):

$$\gamma_{\mathrm{rad}} \propto n \left(\frac{3n^2}{2n^2 + n_{\mathrm{NC}}^2} \right)^2 . \tag{8.3}$$

Here n_{NC} is the refractive index of the nanocrystal. We take $n_{\mathrm{NC}} = 2.5$, which is the refractive index for CdS around 600 nm.[11] The experimental exciton lifetimes τ_{X} as a function of refractive index (Fig. 8.4b) are determined by a refractive-index dependent radiative component and a (presumably) fixed non-radiative component. We fit the data to

$$\tau_{\mathrm{X}} = \left[A\, n \left(\frac{3n^2}{2n^2 + n_{\mathrm{NC}}^2} \right)^2 + B \right]^{-1} , \tag{8.4}$$

where the first term describes radiative decay, and the second nonradiative decay. Using the fitted values of A and B the PL quantum efficiency $\eta(n)$ is calculated as

$$\eta(n) = 1 - B \left[A\, n \left(\frac{3n^2}{2n^2 + n_{\mathrm{NC}}^2} \right)^2 + B \right]^{-1} \tag{8.5}$$

The solvents used are hexane ($n = 1.375$), cyclohexane ($n = 1.426$), chloroform ($n = 1.444$), trichloroethylene ($n = 1.478$), toluene ($n = 1.496$), chlorobenzene ($n = 1.524$), and carbon disulphide ($n = 1.627$).

Fitting emission spectra to a two-sided Gaussian. The emission spectra of Figs. 8.2c,d have an asymmetric shape, determined by the distribution of sizes and shapes in the ensemble. To fit the peak positions and band widths, we use two-sided Gaussian functions on energy (rather than wavelength) scale:

$$I(E) = A \begin{cases} \mathrm{e}^{-(E-E_0)^2/2\sigma_1^2} & ; \quad E < E_0 \\ \mathrm{e}^{-(E-E_0)^2/2\sigma_2^2} & ; \quad E > E_0 \end{cases} , \tag{8.6}$$

where A is the amplitude, E_0 the peak energy, σ_1 the width on the red side, and σ_2 the width on the blue side of the spectrum. In Fig. 8.2e we plot the peak positions E_0 and the full-widths-at-half-maximum $\sqrt{2\ln 2}(\sigma_1 + \sigma_2)$ of the emission spectra.

CHAPTER 9

Summary & outlook

ABSTRACT • The experiments and modeling described in this thesis have provided new insights into the excited state dynamics of luminescent (nano)crystals. We have investigated Auger processes and charge carrier trapping in colloidal semiconductor nanocrystals, and we have demonstrated how energy transfer processes can be controlled in crystals doped with luminescent ions. Here, we summarize the main results, and briefly discuss potential directions for future research.

9.1 • Auger processes and charge carrier trapping in quantum dots

Colloidal quantum dots (QDs) are interesting owing to the strong absorption and the size- and shape-tunable emission. When used in bio-imaging applications or as phosphor materials, the QDs must have efficient photoluminescence (PL). Other applications, where the QDs convert electricity to light (i.e. in light-emitting diodes; LEDs) or vice versa (i.e. in solar cells), further require that a film of QDs is conductive to electricity. The challenge is to limit non-radiative recombination pathways for charge carriers, and capture of charge carriers on trap sites. In Chs. 3,4,8 we report fundamental studies of non-radiative Auger recombination and charge carrier trapping in CdSe/CdS QDs.

Our experiments in Chs. 3,4, as well as several other recent studies,[130,155,161,175,192,197,207,226,235,245] have focused on the suppression of Auger recombination processes in QDs of various geometries. The basic idea is that Auger rates are reduced in core–shell structures compared to core-only structures, especially if there is a compositional gradient over the core–shell interface. Indeed, the core–shell structures that we investigated in Chs. 3,4 have significantly suppressed Auger rates compared to conventional core-only QDs. We have concluded that both spherical core–shell and dot-in-rod structures are promising nanocrystal (NC) geometries with reduced Auger losses. Measurements on the single-QD level, however, have revealed a wide variations in Auger rates for a batch of nominally identical QDs (see Chs. 3,4, and Refs. 155,161,175,192,197,207,235,245). The link between (subtle) differences in geometry and variations in Auger rates is not understood. For full control over Auger processes in QDs, such understanding is crucial. The ideal future experiment would correlate spectroscopic measurements on single QDs to electron microscopy with atomic resolution on the same QDs. Such experiments are however very challenging, because the high illumination powers involved in both single-QD spectroscopy and electron microscopy tend to induce structural changes (such as melting).

In Ch. 8 we have discovered that charge carrier separation is a process that occurs surprisingly often in QDs: in the core–multi-shell QDs we studied, it occurs for 10%–15% of the excitations. A photon is eventually emitted after release of the trapped charge, resulting in delayed emission. Analyzing delayed emission can therefore be a convenient and fast way to study charge carrier traps. One can however imagine that QDs contain multiple kinds of traps, so that some types could be invisible in studies of delayed emission. Based on the statistics of delayed emission we have proposed in Ch. 8 that the traps causing delayed emission, are the same as those responsible for blinking. Further studies should reveal if delayed emission can provide insights into other processes that can experience competition from charge carrier trapping, such as charge transport through QD films.[242]

Charge carrier traps are usually associated with the surface of QDs, where the coordination of ions is incomplete. As a result, one might expect that charge carrier trapping in CdSe QDs would be reduced by the growth of a thicker protective CdS shell. Our preliminary results on

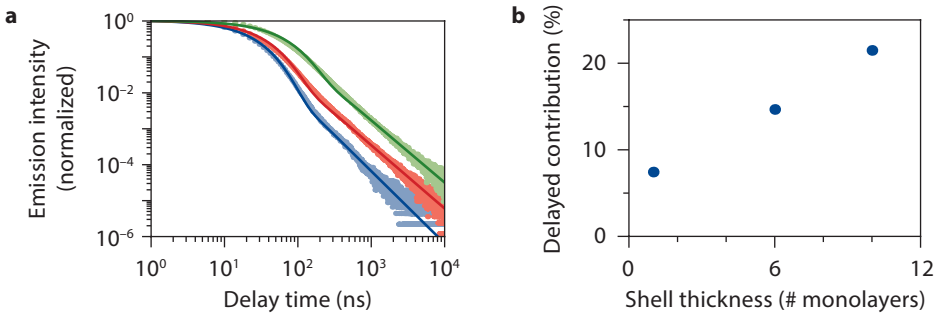

Figure 9.1 • Delayed emission from quantum dots with different shell thicknesses. (**a**) PL decay curves from CdSe/CdS core–shell QDs with shell thicknesses of 1 monolayer (blue), 6 monolayers (red), and 10 monolayers (green), dispersed in toluene. The solid lines are fits to our model of direct exciton emission with exponential dynamics followed by a power-law delayed component (Eq. 8.2). (**b**) The contribution of delayed emission to the total emission of QDs (parameter P_S in Eq. 8.2) as a function of shell thickness.

CdSe/CdS QDs with different shell thicknesses reveal that the trend is exactly opposite to this expectation. Fig. 9.1a shows the PL decay dynamics of CdSe/CdS core–shell QDs with shell thicknesses of 1 monolayer (blue), 6 monolayers (red) and 10 monolayers (green), on a time scale up to 10 μs after excitation. Solid lines are fits to Eq. 8.2, which yield the contribution P_S of delayed emission to the total emission. The fit results, presented in Fig. 9.1b, reveal the trend that the delayed contribution (and hence the probability of charge carrier trapping) is larger for QDs with a thicker shell.

Fig 9.1 implies that the charge carrier traps responsible for delayed emission are not located on the QD surface. Indeed, the influence of surface traps should decrease upon growing a thicker shell, because the charge carrier wavefunctions are mostly localized in the QD core. Instead, the data presented in Fig. 9.1 suggest that the charge carrier traps are in fact situated *in* the CdS shell or on the core–shell interface. The charge carrier trapping can be more probable for thicker shells for several reasons: because there is a larger average number of traps per QD, because the electron wavefunction delocalizes more into the shell, or because strain at the core–shell interface is higher. The notion that the effect of charge carrier traps becomes more important with increasing CdS shell thickness is consistent with the finding of Bae *et al.*[197] that the quantum yield of an ensemble of CdSe/CdS core–shell QDs is in fact lower for thicker shells. Furthermore, Nasilowski *et al.*[245] have recently measured that the PL dynamics in giant-shell QDs (>40 nm diameter) are completely dominated by very slow (μs) decay, which would be consistent with a major influence of temporary charge carrier trapping. The growth of a CdS shell, although a successful method to suppress Auger losses, seems to introduce additional (undesired) charge carrier traps in QDs. A challenge is to design new synthesis routes leading to superior CdS shells,[199] yielding QDs with low Auger losses as well as few charge carrier traps.

9.2 • Energy transfer in doped (nano)crystals

Crystals doped with luminescent (lanthanide) ions find numerous applications in lighting, lasers and medical imaging. The composition of such crystals, i.e. the types and concentrations of dopant ions, determines the absorption, the color output, and the conversion efficiency. Although

luminescent doped crystals have been investigated and widely used for decennia, the understanding of the energy transfer processes was until now mostly qualitative. Only quantitative modeling can however yield useful predictions of the properties of new material compositions, and identify the efficiency limiting processes. In this thesis we present methods to analyze simple energy transfer from donors to acceptors (Chs. 6,7), cooperative energy transfer (Ch. 6), and cross-relaxation (Chs. 5,6). Further work should be directed at building a full theoretical model for all processes that can take place in an excited doped crystal, including energy migration, back-transfer from acceptor to donor, and upconversion, in bulk crystals as well as in NCs.

A potential future application, as mentioned in Ch. 5, of luminescent doped crystals is spectral conversion for next-generation solar cells. The spectral mismatch losses (i.e. thermalization and transmission) of solar cells could be reduced substantially, if the incoming spectrum from the sun were converted by up- and downconversion. Fig. 9.2 illustrates that for a crystalline silicon solar cell, the spectral mismatch losses can be almost halved. To realize this, however, existing up- and downconversion phosphors must be improved. The main challenges are to improve the absorption strength and to increase the conversion and emission efficiency, as discussed in Ch. 5 for the downconversion phosphor $Gd_2O_2S:Tm^{3+}$.

To improve the absorption strength of luminescent doped crystals, a sensitizer ion is usually incorporated. For example for cooperative ET in the Tb^{3+}–Yb^{3+} couple (Ch. 6), sensitization by Ce^{3+} (as in Ch. 7) could greatly enhance the effective absorption in the ultraviolet. For the strongest possible absorption by Ce^{3+}, efficient ET to Tb^{3+}, and efficient cooperative ET to Yb^{3+}, all three types of dopant ions should be present in the crystal at high concentrations. Similarly, in

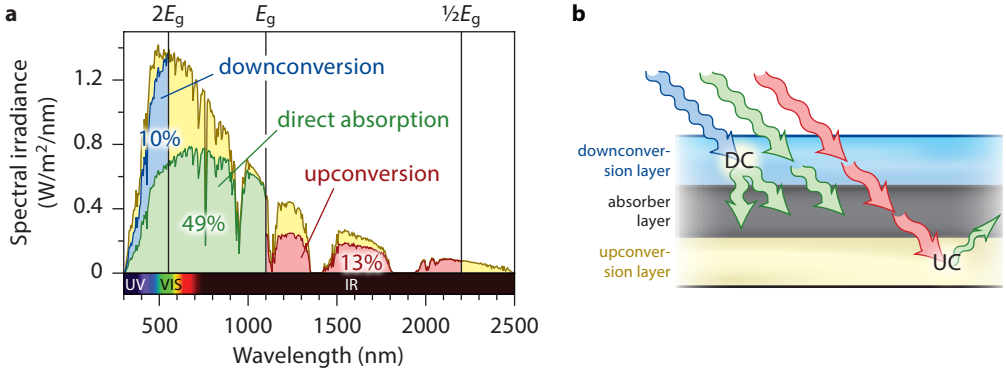

Figure 9.2 • Spectral conversion for next-generation photovoltaics. (**a**) Of the AM1.5D solar spectrum as it reaches the earth's surface (yellow), in a solar cell of crystalline silicon all except 49% (green) of the energy is lost because of spectral mismatch alone. Any photon energy in excess of the bandgap of E_g = 1.1 eV is lost to thermalization, while photons of energy below the bandgap are not absorbed at all. Up- and downconversion (see Chs. 2,5,6) have the potential to reduce transmission and thermalization losses, respectively. (**b**) The thermalization losses could be reduced from 30% to 20% with an ideal downconverter material (blue layer). This material should convert each photon from the sun with an energy higher than $2E_g$ = 2.2 eV (blue arrow) to two photons with an energy of at least E_g = 1.1 eV, *before* they enter the solar cell. The transmission losses could be reduced from 20% to 7% with an ideal upconverter material (yellow layer). It should convert any two low-energy photons of equal wavelength to one high-energy photon with an energy above the bandgap. This conversion step can take place either before or after the light has passed through the solar cell.

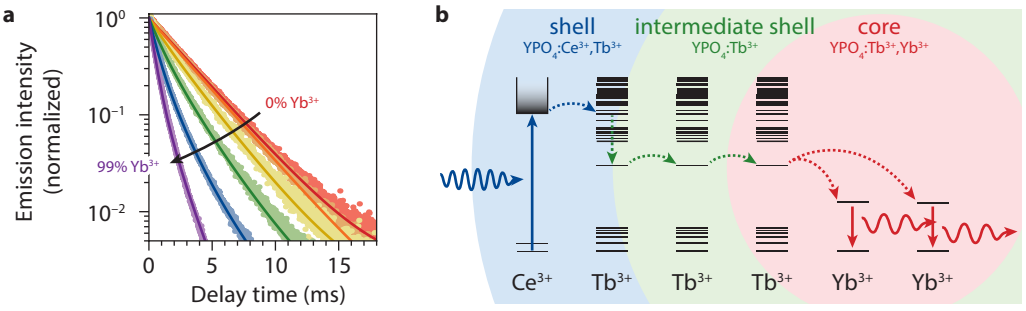

Figure 9.3 • Downconversion in YPO_4:Tb^{3+},Yb^{3+} nanocrystals. (**a**) The dynamics of the excited $^5D_4$ state of Tb^{3+} in YPO_4:Tb^{3+},Yb^{3+} NCs can be modeled with a model for cooperative ET (as described in Ch. 6) adjusted to account for the finite size of the NCs (as is done for first-order ET in Ch. 7). If we model the NCs as spheres of 5 nm diameter, the fitted value for the ET strength is $C_{coop} = 1.34 \times 10^{-6}$ nm^{12} ms^{-1}. (**b**) The downconversion couple Tb^{3+}–Yb^{3+} would benefit from sensitization by the strong UV absorption of Ce^{3+}. However, an excited Ce^{3+} ion tends to directly transfer its energy to an Yb^{3+} neighbor in a first-order process via a Ce^{4+}–Yb^{2+} charge transfer state.[241] This is an undesired decay pathway, because only cooperative ET between Tb^{3+} and Yb^{3+} is a downconversion process that can yield two emitted photons for each absorption event. The possibility to create core–shell geometries is an important advantage of NCs. It allows Ce^{3+}, Tb^{3+} and Yb^{3+} to be incorporated in the same NC, but with Ce^{3+} and Yb^{3+} spatially separated to avoid first-order ET.

upconversion phosphors such as Gd_2O_2S:Er^{3+} high dopant concentrations are needed for strong absorption and efficient ET. However, at the same time high dopant concentrations lead to concentration quenching (see Fig. 2.17).[244] To model and understand excited state dynamics at high dopant concentrations, including the beneficial effect of efficient ET[166] and the negative effect of concentration quenching,[239] energy migration must be explicitly taken into account.

Of particular interest are luminescent doped *nanocrystals*. In contrast to the bulk analogues, doped NCs can be used as biolabels and can form a transparent luminescent material when dispersed in a plastic or liquid. Transparency is essential for a downconverter for solar cells, because the downconverter should act on the high-energy region of the solar spectrum before it enters the solar cell (Fig. 9.2b), while transmitting the rest (i.e. it should not scatter incoming light). Fig. 9.3a shows preliminary data of the decay dynamics of the excited $^5D_4$ state of Tb^{3+} in NCs of YPO_4:Tb^{3+},Yb^{3+}. A Monte Carlo model for cooperative ET (see Ch. 6), corrected for the finite size of the NCs (see Ch. 7) reproduces the data for all Yb^{3+} concentrations. These YPO_4:Tb^{3+},Yb^{3+} NCs are the first downconverter NCs, and may be applied in transparent downconversion layers.

NCs offer possibilities for compositional tuning not present in bulk crystals. Core–shell NCs can be grown with different compositions (i.e. different concentrations of dopant ions or different host materials) of core and shell, coupled through ET processes.[166] Using this concept, one can for example independently optimize the absorption strength and PL efficiency of the NCs. Fig. 9.3b proposes core–shell–shell NCs of YPO_4 for sensitized downconversion, where the outer shell, the intermediate shell, and the core have different roles. Ce^{3+} in the outer shell strongly absorbs ultraviolet light, Tb^{3+} in the intermediate shell transfers the absorbed energy to the core while spatially separating Ce^{3+} and Yb^{3+},[241] and the Tb^{3+}–Yb^{3+} couple in the core achieves downconversion by cooperative ET. Further research should aim at realizing doped NC structures like these, and at understanding and optimizing the spectral conversion efficiency.

REFERENCES

1. Förster, T.; "Zwischenmolekulare Energiewanderung und Fluoreszenz"; *Ann. Phys.* **437**, 55–75 (1948)
2. Dexter, D.L.; "Possibility of luminescent quantum yield greater than unity"; *Phys. Rev.* **108**, 630–633 (1957)
3. Eick, H. A.; "The preparation, lattice parameters and some chemical properties of the rare earth mono-thio oxides"; *J. Am. Chem. Soc.* **80**, 43–44 (1958)
4. Shockley, W. & Queisser, H.J.; "Detailed balance limit of efficiency of p-n junction solar cells"; *J. Appl. Phys.* **32**, 510–519 (1961)
5. Geusic, J.E., Marcos, H.M. & Van Uitert, L.G.; "Laser oscillations in Nd-doped yttrium aluminum, yttrium gallium and gadolinium garnets". *Appl. Phys. Lett.* **4**, 182–184 (1964)
6. Inokuti, M. & Hirayama, F.; "Influence of energy transfer by the exchange mechanism on donor luminescence"; *J. Chem. Phys.* **43**, 1978–1989 (1965)
7. Yokota, M. & Tanimoto, O.; "Effects of diffusion on energy transfer by resonance"; *J. Phys. Soc. Jap.* **22**, 779–784 (1967)
8. Drexhage, K.H.; "Influence of a dielectric interface on fluorescence decay time"; *J. Lumin.* **1&2**, 693–701 (1970)
9. Bourcett, J.-C. & Fong, F. K.; "Quantum efficiency of diffusion limited energy transfer $La_{1-x-y}Ce_xTb_yPO_4$"; *J. Chem. Phys.* **60**, 34–39 (1974)
10. Miller, M.P. & Wright, J.C.; "Single site multiphonon and energy transfer relaxation phenomena in $BaF_2:Er^{3+}$"; *J. Chem. Phys.* **68**, 1548–1562 (1978)
11. Jensen, B. & Torabit, A.; "Refractive index of hexagonal II-VI compounds CdSe, CdS, and $CdSe_xS_{1-x}$"; *J. Opt. Soc. Am. B* **3**, 857–863 (1986)
12. Roussignol, P., Kull, M., Ricard, D., De Rougemont, F., Frey, R. & Flytzanis, C.; "Time-resolved direct observation of Auger recombination in semiconductor-doped glasses"; *Appl. Phys. Lett.* **51**, 1882–1884 (1987)
13. Schmitt-Rink, S., Miller, D.A.B. & Chemla, D.S.; "Theory of the linear and nonlinear optical properties of semiconductor microcrystallites"; *Phys. Rev. B* **35**, 8113–8125 (1987)
14. Chepic, D.I., Efros, Al.L., Ekimov, A.I., Ivanov, M.G., Kharchenko, V.A., Kudriavtsev, I.A. & Yazeva, T.V.; "Auger ionization of semiconductor quantum drops in a glass matrix"; *J. Lumin.* **47**, 113–127 (1990)
15. Pillar, F.L.; "Elementary quantum chemistry"; McGraw-Hill Pub., New York (1990)
16. Bajzer, Z., Therneau, T.M., Sharp, J. C. & Prendergast, F. G.; "Maximum likelihood method for the analysis of time-resolved fluorescence decay curves"; *Eur. Biophys. J.* **20**, 247–262 (1991)
17. Ekimov, A.I., Hache, F., Schanne-Klein, M.C., Ricard, D., Flytzanis, C., Kudryavtsev, I.A., Yazeva, T.V., Rodina, A.V. & Efros, Al.L.; "Absorption and intensity-dependent photoluminescence measurements on CdSe quantum dots: assignment of the first electronic transitions"; *J. Opt. Soc. Am. B* **10**, 100–107 (1993)
18. Murray, C.B., Norris, D.J. & Bawendi, M.G.; "Synthesis and characterization of nearly monodisperse CdE (E = S, Se, Te) semiconductor nanocrystallites"; *J. Am. Chem. Soc.* **115**, 8706–8715 (1993)
19. Van Schaik, W., Lizzo, S., Smit, W. & Blasse, G.; "Influence of impurities on the luminescence quantum efficiency of $(La,Ce,Tb)PO_4$"; *J. Electrochem. Soc.* **140**, 216–222 (1993)
20. Blasse, G. & Grabmaier, B. C.; "Luminescent Materials"; Springer-Verlag, Heidelberg (1994)
21. Efros, Al.L., Kharchenko, V.A. & Rosen, M.; "Breaking the phonon bottleneck in nanometer quantum dots: role of Auger-like processes"; *Solid State Commun.* **93**, 281–284 (1995)
22. Egorov. S.A. & Skinner, J.L.; "On the theory of multiphonon relaxation rates in solids"; *J. Chem. Phys.* **103**, 1533–1543 (1995)
23. O'Connor, R., Mahiou, R., Martinant, D. & Fournier, M.T.; "Luminescence and dynamics in $Tm^{3+}:NaYF_4$"; *J. Alloys Compd.* **225**, 107–110 (1995)
24. Efros, Al.L., Rosen. M., Kuno, M., Nirmal, M., Norris, D.J. & Bawendi, M.; "Band-edge exciton in quantum dots of semiconductors with a degenerate valence band: dark and bright exciton states"; *Phys. Rev. B* **54**, 7, 4843–4853 (1996)
25. Empedocles, S.A., Norris, D.J. & Bawendi, M.G.; "Photoluminescence spectroscopy of single CdSe nanocrystallite quantum dots"; *Phys. Rev. Lett.* **77**, 3873–3876 (1996)
26. Kharchenko, V.A. & Rosen, M.; "Auger relaxation processes in semiconductor nanocrystals and quantum wells"; *J. Lumin.* **70**, 158–169 (1996)
27. Nirmal, M. Dabbousi, B.O., Bawendi, M.G., Macklin, J.J., Trautman, J.K., Harris, T.D. & Brus, L.E.; "Fluorescence intermittency in single cadmium selenide nanocrystals"; *Nature* **383**, 802–804 (1996)
28. Norris, D.J. & Bawendi, M.G.; "Measurement and assignment of the size-dependent optical spectrum in CdSe quantum dots"; *Phys. Rev. B* **53**, 24, 16338–16346 (1996)
29. Efros, Al.L. & Rosen, M.; "Random telegraph signal in the photoluminescence intensity of a single quantum dot"; *Phys. Rev. Lett.* **78**, 1110–1113 (1997)

30. Efros, Al.L. & Rosen, M.; "Quantum size level structure of narrow-gap semiconductor nanocrystals: effect of band coupling"; *Phys. Rev. B* **58**, 7120–7135 (1998)
31. Guyot-Sionnest, P. & Hines, M.A.; "Intraband transitions in semiconductor nanocrystals"; *Appl. Phys. Lett.* **72**, 686–688 (1998)
32. Klimov, V.I. & McBranch, D.W.; "Femtosecond 1P-to-1S electron relaxation in strongly confined semiconductor nanocrystals"; *Phys. Rev. Lett.* **80**, 4028–4031 (1998)
33. Guyot-Sionnest, P., Shim, M., Matranga, C. & Hines, M.; "Intraband relaxation in CdSe quantum dots"; *Phys. Rev. B* **60**, R2181–R2184 (1999)
34. Klimov, V.I., McBranch, D.W., Leatherdale, C.A. & Bawendi, M.G.; "Electron and hole relaxation pathways in semiconductor quantum dots"; *Phys. Rev. B* **60**, 13740–13749 (1999)
35. Wegh, R.T., Donker, H., Oskam, K.D. & Meijerink, A.; "Visible quantum cutting in $LiGdF_4:Eu^{3+}$ through down-conversion"; *Science* **283**, 663–666 (1999)
36. Andrew, P. & Barnes, W.L.; "Förster energy transfer in an optical microcavity"; *Science* **290**, 785–788 (2000)
37. Dorenbos, P.; "The 5d level positions of the trivalent lanthanides in inorganic compounds"; *J. Lumin.* **91**, 155–176 (2000)
38. Efros, Al.L. & Rosen, M.; "The electronic structure of semiconductor nanocrystals"; *Annu. Rev. Mater. Sci.* **30**, 475–521 (2000)
39. Franceschetti, A., Williamson, A. & Zunger, A.; "Addition spectra of quantum dots: the role of dielectric mismatch"; *J. Phys. Chem. B* **104**, 3398–3401 (2000)
40. Klimov, V.I., Mikhailovsky, A.A., McBranch, D.W., Leatherdale, C.A. & Bawendi, M.G.; "Quantization of multiparticle Auger rates in semiconductor quantum dots"; *Science* **287**, 1011–1013 (2000)
41. Neuhauser, R.G., Shimizu, K.T., Woo, W.K., Empedocles, S.A. & Bawendi, M.G.; "Correlation between fluorescence intermittency and spectral diffusion in single semiconductor quantum dots"; *Phys. Rev. Lett.* **85**, 3301–3304 (2000)
42. Nikol, H. & Jüstel, T.; "Optimization of luminescent materials for plasma display panels"; *Adv. Mater.* **12**, 527–530 (2000)
43. Feldmann, C., Jüstel, T., Ronda, C.R. & Wiechert, D.U.; "Quantum efficiency of downconversion phosphor $LiGdF_4$:Eu"; *J. Lumin.* **91**, 245–254 (2001)
44. Kuno, M., Fromm, D.P., Hamann, H.F., Gallagher, A. & Nesbitt, D.J.; ""On"/"off" fluorescence intermittency of single semiconductor quantum dots"; *J. Chem. Phys.* **115**, 1028–1040 (2001)
45. Dung, H., Knöll, L. & Welsch, D.-G.; "Spontaneous decay in the presence of dispersing and absorbing bodies: general theory and application to a spherical cavity"; *Phys. Rev. A* **62**, 053804 (2002)
46. Leatherdale, C.A., Woo, W.-K., Mikulec, F.V. & Bawendi, M.G.; "On the absorption cross section of CdSe nanocrystal quantum dots"; *J. Phys. Chem. B* **106**, 7619–7622 (2002)
47. Mikhailovsky, A.A., Malko, A.V., Hollingsworth, J.A., Bawendi, M.G. & Klimov, V.I.; "Multiparticle interactions and stimulated emission in chemically synthesized quantum dots"; *Appl. Phys. Lett.* **80**, 2380–2382 (2002)
48. Verberk, R., Van Oijen, A.M. & Orrit, M.; "Simple model for the power-law blinking of single semiconductor nanocrystals"; *Phys. Rev. B* **66**, 233202 (2002)
49. Weber, M. J.; "Handbook of Optical Materials"; CRC Press, Boca Raton (2002)
50. Achermann, M., Hollingsworth, J.A. & Klimov, V.I.; "Multiexcitons confined within a subexcitonic volume: spectroscopic and dynamical signatures of neutral and charged biexcitons in ultrasmall semiconductor nanocrystals"; *Phys. Rev. B* **68**, 245302 (2003)
51. Auzel, F., Baldacchini, G., Laversenne, L. & Boulon, G.; "Radiation trapping and self-quenching analysis in Yb^{3+}, Er^{3+}, and Ho^{3+} doped Y_2O_3"; *Opt. Mater.* **24**, 103–109 (2003)
52. Barandiarán, Z. & Seijo, L.; "Quantum chemical analysis of the bond lengths in f^n and $f^{n-1}d^1$ states of Ce^{3+}, Pr^{3+}, Pa^{4+}, and U^{4+} defects in chloride hosts"; *J. Chem. Phys.* **119**, 3785–3790 (2003)
53. Feldmann, C., Jüstel, T., Ronda, C.R. & Schmidt, P.J.; "Inorganic luminescent materials: 100 years of research and application"; *Adv. Funct. Mater.* **13**, 511–516 (2003)
54. Kömpe, K., Borchert, H., Storz, J., Lobo, A., Adam, S., Möller, T. & Haase, M.; "Green-emitting $CePO_4$:Tb/$LaPO_4$ core–shell nanoparticles with 70% photoluminescence quantum yield"; *Angew. Chem. Int. Ed.* **42**, 5513–5516 (2003)
55. Li, J.J., Wang, A., Guo, W., Keay, J.C., Mishima, T.D., Johnson, M.B. & Peng, X.; "Large-scale synthesis of nearly monodisperse CdSe/CdS core/shell nanocrystals using air-stable reagents via successive ion layer adsorption and reaction"; *J. Am. Chem. Soc.* **125**, 12567–12575 (2003)

56. Rodina, A.V., Efros, Al.L. & Alekseev, A.Yu.; "Effect of the surface on the electron quantum size levels and electron *g*-factor in spherical semiconductor nanocrystals"; *Phys. Rev. B* **67**, 155312 (2003)
57. Talapin, D.V., Koeppe, R., Go, S., Kornowski, A., Lupton, J.M., Rogach, A.L., Benson, O., Feldmann, J. & Weller, H.; "Highly emissive colloidal CdSe/CdS heterostructures of mixed dimensionality"; *Nano Lett.* **3**, 1677–1681 (2003)
58. Toptygin, D.; "Effects of the solvent refractive index and its dispersion on the radiative decay rate and extinction coefficient of a fluorescent solute"; *J. Fluoresc.* **13**, 201–219 (2003)
59. Bakalova, R., Ohba, H., Zhelev, Z., Ishikawa, Z. & Baba, Y.; "Quantum dots as photosensitizers?"; *Nat. Biotechnol.* **22**, 1360–1361 (2004)
60. Brokmann, X., Coolen, L., Dahan, M. & Hermier, J.; "Measurement of the radiative and nonradiative decay rates of single CdSe nanocrystals through a controlled modification of their spontaneous emission"; *Phys. Rev. Lett.* **92**, 107403 (2004)
61. Delerue, C. & Lannoo, M.; "Nanostructures – Theory and Modelling"; Springer-Verlag, Berlin (2004)
62. Kobayashi, Y., Misawa, K., Kobayashi, M., Takeda, M., Konno, M., Satake, M., Kawazoe, Y., Ohuchi, N. & Kasuya, A.; "Silica-coating of fluorescent polystyrene microspheres by a seeded polymerization technique and their photo-bleaching property"; *Colloids Surf. A* 242, 47–52 (2004)
63. Shavel, A., Gaponik, N. & Eychmüller, A.; "Efficient UV-blue photoluminescing thiol-stabilized water-soluble alloyed ZnSe(S) nanocrystals"; *J. Phys. Chem. B* **108**, 5905–5908 (2004)
64. De Dood, M.J.A., Knoester, J., Tip., A. & Polman, A.; "Förster transfer and the local optical density of states in erbium-doped silica"; *Phys. Rev. B* **71**, 115102 (2005)
65. Duan, C.-K., Reid, M.F. & Wang, Z.; "Local field effects on the radiative lifetime of emitters in surrounding media: virtual- or real-cavity model?"; *Phys. Lett. A* **343**, 474–480 (2005)
66. Frantsuzov, P.A. & Marcus, R.A.; "Explanation of quantum dot blinking without the long-lived trap hypothesis"; *Phys. Rev. B* **72**, 155321 (2005)
67. Li, Y.Q., Delsing, A.C.A., De With, G. & Hintzen, H.T.; "Luminescence properties of Eu^{2+}-activated alkaline-earth silicon-oxynitride $MSi_2O_{2-\delta}N_{2+2/3\delta}$ (M = Ca, Sr, Ba): a promising class of novel LED conversion phosphors"; *Chem. Mater.* **17**, 3242–3248 (2005)
68. Müller, J., Lupton, J.M., Lagoudakis, P.G., Schindler, F., Koeppe, R., Rogach, A.L., Feldmann, J., Talapin, D.V. & Weller, H.; "Wave function engineering in elongated semiconductor nanocrystals with heterogeneous carrier confinement"; *Nano Lett.* **5**, 2044–2049 (2005)
69. Nakamura, T., Fujii, M., Imakita, K. & Hayashi, S.; "Modification of energy transfer from Si nanocrystals to Er^{3+} near a Au thin film"; *Phys. Rev. B* **72**, 235412 (2005)
70. Peijzel, P.S., Meijerink, A., Wegh, R.T., Reid, M.F. & Burdick, G.W.; "A complete $4f^n$ energy level diagram for all trivalent lanthanide ions"; *J. Solid State Chem.* **178**, 448–453 (2005)
71. Tang, J. & Marcus, R.A.; "Mechanisms of fluorescence blinking in semiconductor nanocrystal quantum dots"; *J. Chem. Phys.* **123**, 054704 (2005)
72. Van Driel, A.F., Allan, G., Delerue, C., Lodahl, P., Vos, W.L. & Vanmaekelbergh, D.; "Frequency-dependent spontaneous emission rate from CdSe and CdTe nanocrystals: influence of dark states"; *Phys. Rev. Lett.* **95**, 236804 (2005)
73. Vergeer, P., Vlugt, T.J.H., Kox, M.H.F., Den Hertog, M.I., Van der Eerden, J.P.J.M. & Meijerink, A.; "Quantum cutting by cooperative energy transfer in $Yb_xY_{1-x}PO_4:Tb^{3+}$"; *Phys. Rev. B* **71**, 014119 (2005)
74. Xie, R., Kolb, U., Li, J., Basch, T. & Mews, A.; "Synthesis and characterization of highly luminescent CdSe–core $CdS/Zn_{0.5}Cd_{0.5}S/ZnS$ multishell nanocrystals"; *J. Am. Chem. Soc.* **127**, 7480–7488 (2005)
75. Barandiarán, Z. & Seijo, L.; "On the bond length change upon $4f^1 \rightarrow 5d^1$ excitations in eightfold coordination: $CaF_2:Ce^{3+}$ cubic defects"; *Theor. Chem. Acc.* **116**, 505–508 (2006)
76. Hendry, E., Koeberg, M., Wang, F., Zhang, H., De Mello Donegá, C., Vanmaekelbergh, D. & Bonn, M.; "Direct observation of electron-to-hole energy transfer in CdSe quantum dots"; *Phys. Rev. Lett.* **96**, 057408 (2006)
77. Lee, T.J., Luo, L.Y., Diau, E.W.G., Chen, T.M., Cheng, B.M. & Tung, C.Y.; "Visible quantum cutting through down-conversion in green emitting $K_2GdF_5:Tb^{3+}$ phosphors"; *Appl. Phys. Lett.* **89**, 131121 (2006)
78. Li, Y., Rizzo, A., Cingolani, R. & Gigli, G.; "Bright white-light-emitting device from ternary nanocrystal composities"; *Adv. Mater.* **18**, 2545–2548 (2006)
79. Nakamura, T., Fujii, M., Miura, S., Inui, M. & Hayashi, S.; "Enhancement and suppression of energy transfer from Si nanocrystals to Er ions through a control of the photonic mode density"; *Phys. Rev. B* **74**, 045302 (2006)
80. Oron, D., Kazes, M., Shweky, I. & Banin, U.; "Multiexciton spectroscopy of semiconductor nanocrystals under quasi-continuous-wave optical pumping"; *Phys. Rev. B* **74**, 115333 (2006)
81. Richards, B.S.; "Luminescent layers for enhanced silicon solar cell performance: down-conversion"; *Sol. Energy Mater. Sol. Cells* **90**, 1189–1270 (2006)

82. Zhang, K, Chang, H., Fu, A., Alivisatos, A.P. & Yang, H.; "Continuous distribution of emission states from single CdSe/ZnS quantum dots"; *Nano Lett.* **6**, 843–847 (2006)
83. Carbone, L., Nobile, C., De Giorgi, M., Della Sala, F., Morello, G., Pompa, P., Hytch, M., Snoeck, E., Fiore, A., Franchini, I.R., Nadasan, M., Silvestre, A.F., Chiodo, L., Kudera, S., Cingolani, R., Krahne, R. & Manna, L.; "Synthesis and micrometer-scale assembly of colloidal CdSe/CdS nanorods prepared by a seeded growth approach"; *Nano Lett.* **7**, 2942–2950 (2007)
84. Cooney, R.R., Sewall, S.L., Anderson, K.E.H., Dias, E.A. & Kambhampati, P.; "Breaking the phonon bottleneck for holes in semiconductor quantum dots"; *Phys. Rev. Lett.* **98**, 177403 (2007)
85. Klimov, V.I.; "Spectral and dynamical properties of multiexcitons in semiconductor nanocrystals"; *Annu. Rev. Phys. Chem.* **58**, 635–673 (2007)
86. Noda, S., Fujita, M. & Asano, T.; "Spontaneous-emission control by photonic crystals and nanocavities"; *Nature Photon.* **1**, 449–458 (2007)
87. Pandey, A. & Guyot-Sionnest, P.; "Multicarrier recombination in colloidal quantum dots"; *J. Chem. Phys.* **127**, 111104 (2007)
88. Talapin, D.V., Nelson, J.H., Shevchenko, E.V., Aloni, S., Sadtler, B. & Alivisatos, A.P.; "Seeded growth of highly luminescent CdSe/CdS nanoheterostructures with rod and tetrapod morphologies"; *Nano Lett.* **7**, 2952–2959 (2007)
89. Tzeng, H.-Y., Cheng, B.-M. & Chen, T.-M.; "Visible quantum cutting in green-emitting $BaGdF_5:Tb^{3+}$ phosphors via downconversion"; *J. Lumin.* **122–123**, 917–920 (2007)
90. Van Driel, A.F., Nikolaev, I.S., Vergeer, P., Lodahl, P., Vanmaekelbergh, D. & Vos, W.L.; "Statistical analysis of time-resolved emission from ensembles of semiconductor quantum dots: interpretation of exponential decay models"; *Phys. Rev. B* **75**, 035329 (2007)
91. Xie, R., Battaglia, D. & Peng, X.; "Colloidal InP nanocrystals as efficient emitters covering blue to near-infrared"; *J. Am. Chem. Soc.* **129**, 15432–15433 (2007)
92. Zhang, Q.Y., Yang, C.H. & Pan, Y.X.; "Cooperative quantum cutting in one-dimensional $(Yb_xGd_{1-x})Al_3(BO_3)_4:Tb^{3+}$ nanorods"; *Appl. Phys. Lett.* **90**, 021107 (2007)
93. Chatterjee, D.K., Rufaihah, A.J. & Zhang, Y.; "Upconversion fluorescence imaging of cells and small animals using lanthanide doped nanocrystals"; *Biomaterials* **29**, 937–943 (2008)
94. Chen, D.Q., Wang, Y.S., Yu, Y.L., Huang, P. & Weng, F.Y.; "Near-infrared quantum cutting in transparent nanostructured glass ceramics"; *Opt. Lett.* **33**, 1884–1886 (2008)
95. Chen, Y., Vela, J., Htoon, H., Casson, J.L., Werder, D.J., Bussian, D.A., Klimov, V.I. & Hollingsworth, J.A.; ""Giant" Multishell CdSe nanocrystal quantum dots with suppressed blinking"; *J. Am. Chem. Soc.* **130**, 5026–5027 (2008)
96. Frantsuzov, P., Kuno, M., Jankó, B. & Marcus, R.A.; "Universal emission intermittency in quantum dots, nanorods and nanowires"; *Nature Phys.* **4**, 519–522 (2008)
97. Koole, R., Van Schooneveld, M.M., Hilhorst, J., De Mello Donegá, C., Hart, D.C., Van Blaaderen, A., Vanmaekelbergh, D. & Meijerink, A.; "On the incorporation mechanism of hydrophobic quantum dots in silica spheres by a reverse microemulsion method"; *Chem. Mater.* **20**, 2503–2512 (2008)
98. Lupo, M.G., Della Sala, F., Carbone, L., Zavelani-Rossi, M., Fiore, A., Lüer, L., Polli, D., Cingolani, R., Manna, L. & Lanzani, G.; "Ultrafast electron-hole dynamics in core/Shell CdSe/CdS dot/rod nanocrystals"; *Nano Lett.* **8**, 4582–4587 (2008)
99. Mahler, B., Spinicelli, P., Buil, S., Quelin, X., Hermier, J.-P. & Dubertret, B.; "Towards non-blinking colloidal quantum dots"; *Nature Mater.* **7**, 659–664 (2008)
100. Morello, G., Della Sala, F., Carbone, L., Manna, L., Maruccio, G., Cingolani, R. & De Giorgi, M.; "Intrinsic optical nonlinearity in colloidal seeded grown CdSe/CdS nanostructures: Photoinduced screening of the internal electric field"; *Phys. Rev. B* **78**, 195313 (2008)
101. Pandey, A. & Guyot-Sionnest, P.; "Slow electron cooling in colloidal quantum dots"; *Science* **322**, 929–932 (2008)
102. Resch-Genger, U., Grabolle, M., Cavaliere-Jaricot, S., Nitschke, R. & Nann, T.; "Quantum dots versus organic dyes as fluorescent labels"; *Nat. Methods* **5**, 763–775 (2008)
103. Sher, P.H., Smith, J.M., Dalgarno, P.A., Warburton, R.J., Chen, X., Dobson, P.J., Daniels, S.M., Pickett, N.L. & O'Brien, P.; "Power law carrier dynamics in semiconductor nanocrystals at nanosecond timescales"; *Appl. Phys. Lett.* **92**, 101111 (2008)
104. Steiner, D., Dorfs, D., Banin, U., Della Sala, F., Manna, L. & Millo, O.; "Determination of band offsets in heterostructured colloidal nanorods using scanning tunneling spectroscopy"; *Nano Lett.* **8**, 2954–2958 (2008)
105. Cheng, Y.-C. & Fleming, G.R.; "Dynamics of light harvesting in photosynthesis"; *Ann. Rev. Phys. Chem.* **60**, 241–262 (2009)

106. De Mello Donegá, C. & Koole, R.; "Size dependence of the spontaneous emission rate and absorption cross section of CdSe and CdTe quantum dots"; *J. Phys. Chem. C* **113**, 6511–6520 (2009)
107. Fernée, M.J., Littleton, B.N. & Rubinsztein-Dunlop, H.; "Detection of bright trion states using the fine structure emission of single CdSe/ZnS colloidal quantum dots"; *ACS Nano* **3**, 3762–2768 (2009)
108. Frantsuzov, P.A., Volkán-Kacsó, S. & Jankó, B; "Model of fluorescence intermittency of single colloidal semiconductor quantum dots using multiple recombination centers"; *Phys. Rev. Lett.* **103**, 207402 (2009)
109. Gómez, D.E., Van Embden, J., Mulvaney, P., Fernée, M.J. & Rubinsztein-Dunlop, H.; "Exciton-trion transitions in single CdSe-CdS core-shell nanocrystals"; *ACS Nano* **3**, 2281–2287 (2009)
110. Green, M.A., Emery, K., Hishikawa, Y. & Warta, W.; "Solar cell efficiency tables (version 33)"; *Prog. Photovolt.: Res. Appl.* **17**, 85–94 (2009)
111. Hardin, B.E., Hoke, E.T., Armstrong, P.B., Yum, J.-H., Comte, P., Torres, T., Fréchet, J.M.J., Nazeeruddin, M.K., Grätzel, M. & McGehee, M.D.; "Increased light harvesting in dye-sensitized solar cells with energy relay dyes"; *Nature Photon.* **3**, 406–411 (2009)
112. Jha, P.P. & Guyot-Sionnest, P.; "Trion decay in colloidal quantum dots"; *ACS Nano* **3**, 1011–1015 (2009)
113. Jones, M., Lo, S.S. & Scholes, G.D.; "Quantitative modeling of the role of surface traps in CdSe/CdS/ZnS nanocrystal photoluminescence decay dynamics"; *Proc. Natl. Acad. Sci. U. S. A.* **106**, 3011–3016 (2009)
114. Kilina, S.V., Kilin, D.S. & Prezhdo, O.V.; "Breaking the phonon bottleneck in PbSe and CdSe quantum dots: time-domain density functional theory of charge carrier relaxation"; *ACS Nano* **3**, 93–99 (2009)
115. Leistikow, M.D., Johansen, J., Kettelarij, A.J., Lodahl, P. & Vos, W.L.; "Size-dependent oscillator strength and quantum efficiency of CdSe quantum dots controlled via the local density of states"; *Phys. Rev. B* **79**, 045301 (2009)
116. Navarro-Urrios, D., Pitanti, A., Daldosso, N., Gourbilleau, F., Rizk, R., Garrido, B. & Pavesi, L.; "Energy transfer between amorphous Si nanoclusters and Er^{3+} ions in a SiO_2 matrix"; *Phys. Rev. B* **79**, 193312 (2009)
117. Oertel, A., Lengler, C., Walther, T. & Haase, M.; "Photonic properties of inverse opals fabricated from lanthanide-doped $LaPO_4$ nanocrystals"; *Chem. Mater.* **21**, 3883–3888 (2009)
118. Peterson, J.J. & Nesbitt, D.J.; "Modified power law behavior in quantum dot blinking: a novel role for biexcitons and Auger ionization"; *Nano Lett.* **9**, 338–345 (2009)
119. Saba, M., Minniberger, S., Quochi, F., Roither, J., Marceddu, M., Gocalinska, A., Kovalenko, M.V., Talapin, D.V., Heiss, W., Mura, A. & Bongiovanni, G.; "Exciton-exciton interaction and optical gain in colloidal CdSe/CdS dot/rod nanocrystals"; *Adv. Mater.* **21**, 4942–4946 (2009)
120. Sitt, A., Della Sala, F., Menagen, G. & Banin, U.; "Multiexciton engineering in seeded core/shell nanorods: transfer from type-I to quasi-type-II regimes"; *Nano Lett.* **9**, 3470–3476 (2009)
121. Smith, A.M., Mohs, A.M. & Nie, S.; "Tuning the optical and electronic properties of colloidal nanocrystals by lattice strain"; *Nature Nanotech.* **4**, 56–63 (2009)
122. Spinicelli, P., Buil, S., Quélin, X., Mahler, B., Dubertret, B. & Hermier, J.-P.; "Bright and grey states in CdSe-CdS nanocrystals exhibiting strongly reduced blinking"; *Phys. Rev. Lett.* **102**, 136801 (2009)
123. Ueda, J. & Tanabe, S.; "Visible to near infrared conversion in Ce^{3+}–Yb^{3+} co-doped YAG ceramics"; *J. Appl. Phys.* **106**, 043101 (2009)
124. Van der Ende, B.M., Aarts, L. & Meijerink, A.; "Lanthanide ions as spectral converters for solar cells"; *Phys. Chem. Chem. Phys.* **11**, 11081–11095 (2009)
125. Van der Ende, B.M., Aarts, L. & Meijerink A.; "Near-infrared quantum cutting for photovoltaics"; *Adv. Mater.* **21**, 3073–3077 (2009)
126. Wang, X., Ren, X., Kahen, K., Hahn, M.A., Rajeswaran, M., Maccagnano-Zacher, S., Silcox, J., Cragg, G.E., Efros, A.L. & Krauss, T.D.; "Non-blinking semiconductor nanocrystals"; *Nature* **459**, 686–689 (2009)
127. Wood, V., Panzer, M.J., Chen, J., Bradley, M.S., Halpert, J.E., Bawendi, M.G. & Bulović, V.; "Inkjet-printed quantum dot–polymer composites for full-color AC-driven displays"; *Adv. Mater.* **21**, 2151–2155 (2009)
128. Xie, L., Wang, Y. & Zhang, H.; "Near-infrared quantum cutting in YPO_4:Yb^{3+},Tm^{3+} via cooperative energy transfer"; *Appl. Phys. Lett.* **94**, 061905 (2009)
129. Buhbut, S., Itzhakov, S., Tauber, E., Shalom, M., Hod, I., Geiger, T., Garini, Y., Oron, D. & Zaban, A.; "Built-in quantum dot antennas in dye-sensitized solar cells"; *ACS Nano* **4**, 1293–1298 (2010)
130. Cragg, G.E. & Efros, Al.L.; "Suppression of Auger processes in confined structures"; *Nano Lett.* **10**, 313–317 (2010)
131. Curto, A.G., Volpe, G., Taminiau, T.H., Kreuzer, M.P., Quidant, R. & Van Hulst, N.F.; "Unidirectional emission of a quantum dot coupled to a nanoantenna"; *Science* **329**, 930–933 (2010)
132. Eilers, J.J., Biner, D., Van Wijngaarden, J.T., Krämer, K., Güdel, H.-U. & Meijerink, A.; "Efficient visible to infrared quantum cutting through downconversion with the Er^{3+}–Yb^{3+} couple in $Cs_3Y_2Br_9$"; *Appl. Phys. Lett.* **96**, 151106 (2010)

133. Jang, E., Jun, S., Jang, H., Lim, J., Kim, B. & Kim, Y.; "White-light-emitting diodes with quantum dot color converters for display backlights"; *Adv. Mater.* **22**, 3076–3080 (2010)
134. Kang, B.-H., Seo, J.-S., Jeong, S., Lee, J., Han, C.-S., Kim, D.-E., Kim, K.-J., Yeom, S.-H., Kwon, D.-H., Kim, H.-R., Kang, S.-W.; "Highly efficient hybrid light-emitting device using complex of CdSe/ZnS quantum dots embedded in co-polymer as an active layer"; *Opt. Expr.* **18**, 18303–18311 (2010)
135. Louyer, Y., Biadala, L., Tamarat, P. & Lounis, B.; "Spectroscopy of neutral and charged exciton states in single CdSe/ZnS nanocrystals"; *Appl. Phys. Lett.* **96**, 203111 (2010)
136. Luo, Y. & Wang, L.-W.; "Electronic structures of the CdSe/CdS core-shell nanorods"; *ACS Nano* **4**, 91–98 (2010)
137. Mor, G.K., Basham, J., Paulose, M., Kim, S., Varghese, O.K., Vaish, A., Yoriya, S. & Grimes, C.A.; "High-efficiency Förster resonance energy transfer in solid-state dye sensitized solar cells"; *Nano Lett.* **10**, 2387–2394 (2010)
138. Pukhov, K. K. & Basiev, T. T.; "Radiative transitions in nanocrystals"; *Opt. Mater.* **32**, 1664–1667 (2010)
139. Rosen, S., Schwartz, O. & Oron, D.; "Transient fluorescence of the off state in blinking CdSe/CdS/ZnS semiconductor nanocrystals is not governed by Auger recombination"; *Phys. Rev. Lett.* **104**, 157404 (2010)
140. Semonin, O.E., Johnson, J.C., Luther, J.M., Midgett, A.G., Nozik, A.J. & Beard, M.C.; "Absolute photoluminescence quantum yields of IR-26 dye, PbS, and PbSe quantum dots"; *J. Phys. Chem. Lett.* **1**, 2445–2450 (2010)
141. Tisdale, W.A., Williams, K.J., Timp, B.A., Norris, D.J., Aydil, E.S., Zhu, X.-Y.; "Hot-electron transfer from semiconductor nanocrystals"; *Science* **328**, 1543–1547 (2010)
142. Van Wijngaarden, T., Scheidelaar, S., Vlugt, T.J.H., Reid, M.F. & Meijerink, A.; "Energy transfer mechanism for downconversion in the (Pr^{3+},Yb^{3+}) couple"; *Phys. Rev. B* **81**, 155112 (2010)
143. Wang, F., Deng, R., Wang, J., Wang, Q., Han, Y., Zhu, H., Chen, X., Liu, X.; "Tuning upconversion through energy migration in core-shell nanoparticles"; *Nat. Mater.* **10**, 968–973 (2010)
144. Zavelani-Rossi, M., Lupo, M.G., Tassone, F., Manna, L. & Lanzani, G.; "Suppression of biexciton Auger recombination in CdSe/CdS dot/rods: role of the electronic structure in the carrier dynamics"; *Nano Lett.* **10**, 3142–3150 (2010)
145. Zhang, Q.Y. & Huang, X.Y.; "Recent progress in quantum cutting phosphors"; *Prog. Mater. Sci.* **55**, 353–427 (2010)
146. Zhao, J., Nair, G., Fisher, B.R. & Bawendi M.G.; "Challenge to the charging model of semiconductor-nanocrystal fluorescence intermittency from off-state quantum yields and multiexciton blinking"; *Phys. Rev. Lett.* **104**, 157403 (2010)
147. Bharadwaj, P. & Novotny, L.; "Robustness of quantum dot power-law blinking"; *Nano Lett.* **11**, 2137–2141 (2011)
148. Brovelli, S., Schaller, R.D., Crooker, S.A., García-Santamaría, F., Chen, Y., Viswanatha, R., Hollingsworth, J.A., Htoon, H. & Klimov, V.I.; "Nano-engineered electron–hole exchange interaction controls exciton dynamics in core–shell semiconductor nanocrystals"; *Nat. Commun.* **2**, 280 (2011)
149. Cordones, A.A., Bixby, T.J. & Leone, S.R.; "Evidence for multiple trapping mechanisms in single CdSe/ZnS quantum dots from fluorescence intermittency measurements over a wide range of excitation intensities"; *J. Phys. Chem. C* **115**, 6341–6349 (2011)
150. Cordones, A.A., Bixby, T.J. & Leone, S.R.; "Direct measurement of off-state trapping rate fluctuations in single quantum dot fluorescence"; *Nano Lett.* **11**, 3366–3369 (2011)
151. De Mello Donegá, C.; "Synthesis and properties of colloidal heteronanocrystals"; *Chem. Soc. Rev.* **40**, 1512–1546 (2011)
152. Deng, K., Gong, T., Hu, L., Wei, X., Chen, Y. & Yin, M.; "Efficient near-infrared quantum cutting in $NaYF_4$:Ho^{3+},Yb^{3+} for solar photovoltaics"; *Opt. Express* **19**, 1749–1754 (2011)
153. Frimmer, M., Chen, Y. & Koenderink, A.F.; "Scanning emitter lifetime imaging microscopy for spontaneous emission control"; *Phys. Rev. Lett.* **107**, 123602 (2011)
154. Galland, C., Ghosh, Y., Steinbrück, A., Sykora, M., Hollingsworth, J.A., Klimov, V.I. & Htoon, H.; "Two types of luminescence blinking revealed by spectroelectrochemistry of single quantum dots"; *Nature* **479**, 203–207 (2011)
155. García-Santamaría, F., Brovelli, S., Viswanatha, R., Hollingsworth, J.A., Htoon, H., Crooker, S.A. & Klimov, V.I.; "Breakdown of volume scaling in Auger recombination in CdSe/CdS heteronanocrystals: the role of the core-shell interface"; *Nano Lett.* **11**, 687–693 (2011)
156. Leistikow, M.D., Mosk, A.P., Yeganegi, E., Huisman, S.R., Lagendijk, A. & Vos, W.L.; "Inhibited spontaneous emission of quantum dots observed in a 3D photonic band gap"; *Phys. Rev. Lett.* **107**, 193903 (2011)
157. Luque, A.; "Will we exceed 50% efficiency in photovoltaics?"; *J. Appl. Phys.* **110**, 031301 (2011)
158. Malko, A.V., Park, Y.-S., Sampat, S., Galland, C., Vela, J., Chen, Y., Hollingsworth, J.A., Klimov, V.I. & Htoon, H.; "Pump-intensity- and shell-thickness-dependent evolution of photoluminescence blinking in individual core/shell CdSe/CdS nanocrystals"; *Nano Lett.* **11**, 5213–5218 (2011)

159. Nair, G., Zhao, J. & Bawendi, M.G.; "Biexciton quantum yield of single semiconductor nanocrystals from photon statistics"; *Nano Lett.* **11**, 1136–1140 (2011)
160. Novotny, L. & Van Hulst, N.; "Antennas for light"; *Nature Photon.* **5**, 83–90 (2011)
161. Park, Y.-S., Malko, A.V., Vela, J., Chen, Y., Ghosh, Y., García-Santamaría, F., Hollingsworth, J.A., Klimov, V.I. & Htoon, H.; "Near-unity quantum yields of biexciton emission from CdSe–CdS nanocrystals measured using single-particle spectroscopy"; *Phys. Rev. Lett.* **106**, 187401 (2011)
162. Scholes, G.D., Fleming, G.R., Olaya-Castro, A. & Van Grondelle, R.; "Lessons from nature about solar light harvesting"; *Nat. Chem.* **3**, 763–774 (2011)
163. She, C., Demortière, A., Shevchenko, E.V. & Pelton, M.; "Using shape to control photoluminescence from CdSe/CdS core/shell nanorods"; *J. Phys. Chem. Lett.* **2**, 1469–1475 (2011)
164. Smith, E.R, Luther, J.M. & Johnson, J.C.; "Ultrafast electronic delocalization in CdSe/CdS quantum rod heterostructures"; *Nano Lett.* **11**, 4923–4931 (2011)
165. Timmerman, D., Valenta, J., Dohnalová, K., De Boer, W.D.A.M. & Gregorkiewicz, T.; "Steplike enhancement of luminescence quantum yield of silicon nanocrystals"; *Nat. Nanotech.* **6**, 710–713 (2011)
166. Wang, F., Deng, R., Wang, J., Wang, Q., Han, Y., Zhu, H., Chen, X. & Liu X.; "Tuning upconversion through energy migration in core-shell nanoparticles"; *Nat. Mater.* **10**, 968–973 (2011)
167. Yu, D.C., Huang, X.Y., Ye, S., Peng, M.Y., Zhang, Q.Y. & Wondraczek, L.; "Three-photon near-infrared quantum splitting in β-$NaYF_4$:Ho^{3+}"; *Appl. Phys. Lett.* **99**, 161904 (2011)
168. Zhou, J., Liu, Z. & Li, F.; "Upconversion nanophosphors for small-animal imaging"; *Chem. Soc. Rev.* **41**, 1323–1349 (2011)
169. Abrams, Z.R., Charghi, M., Niv, A., Gladden, C. & Zhang X.; "Theoretical efficiency of 3rd generation solar cells: comparison between carrier multiplication and down-conversion"; *Sol. Energy Mater. Sol. Cells.* **99**, 308–315 (2012)
170. Bakulin, A.A., Rao, A., Pavelyev, V.G., Van Loosdrecht, P.H.M., Pshenichnikov, M.S., Niedzialek, D., Cornil, J., Beljonne, D. & Friend, R.H.; "The role of driving energy and delocalized states for charge separation in organic semiconductors"; *Science* **335**, 1340–1344 (2012)
171. Bertoni, G., Grillo, V., Brescia, R., Ke, X., Bals, S., Catelanni, A., Li, H. & Manna, L.; "Direct determination of polarity, faceting, and core location in colloidal core/shell wurtzite semiconductor nanocrystals"; *ACS Nano* **6**, 6453–6461 (2012)
172. Blum, C., Zijlstra, N., Lagendijk, A., Wubs, M., Mosk, A.P., Subramaniam, V. & Vos, W.L.; "Nanophotonic control of the Förster resonance energy transfer efficiency"; *Phys. Rev. Lett.* **109**, 203601 (2012)
173. Climente, J.I., Movilla, J.L. & Planelles, J.; "Auger recombination suppression in nanocrystals with asymmetric electron–hole confinement"; *Small* **8**, 754–759 (2012)
174. Dang, C., Lee, J., Breen, C., Steckel, J.S., Coe-Sullivan, S. & Nurmikko, A.; "Red, green and blue lasing enabled by single-exciton gain in colloidal quantum dot films"; *Nat. Nanotechnol.* **7**, 335–339 (2012)
175. Dennis, A.M., Mangum, B.D., Piryatinski, A., Park, Y.-S., Hannah, D. C., Casson, J. L., Williams, D.J., Schaller, R.D., Htoon,H. & Hollingsworth, J.A.; "Suppressed blinking and Auger recombination in near-infrared type-II InP/CdS nanocrystal quantum dots"; *Nano Lett.* **12**, 5545–5551 (2012)
176. Deutsch, Z., Schwartz, O., Tenne, R., Popovitz-Biro, R. & Oron, D.; "Two-color antibunching from band-gap engineered colloidal semiconductor nanocrystals"; *Nano Lett.* **12**, 2948–2952 (2012)
177. Eilers, J.J., Groeneveld, E., De Mello Donegá, C. & Meijerink, A.; "Optical properties of Mn-doped ZnTe magic size nanocrystals"; *J. Phys. Chem. Lett.* **3**, 1663–1667 (2012)
178. Fernée, M. J., Sinito, C., Louyer, Y., Potzner, C., Nguyen, T.-L., Mulvaney, P., Tamarat, P. & Lounis, B.; "Magneto-optical properties of trions in non-blinking charged nanocrystals reveal an acoustic phonon bottleneck"; *Nat. Commun.* **3**, 1287 (2012)
179. Fu, H. & Tsang, S.-W.; "Infrared colloidal lead chalcogenide nanocrystals: Synthesis, properties, and photovoltaic applications"; *Nanoscale* **4**, 2187–2201 (2012)
180. Galland, C., Ghosh, Y., Steinbrück, A., Hollingsworth, J.A., Htoon, H. & Klimov, V.I.; "Lifetime blinking in non-blinking nanocrystal quantum dots"; *Nat. Commun.* **3**, 908 (2012)
181. Kwadrin, A. & Koenderink, A.F.; "Gray-tone lithography implementation of Drexhage's method for calibrating radiative and nonradiative decay constants of fluorophores"; *J. Phys. Chem. C* **116**, 16666–16673 (2012)
182. Pietra, F., Rabouw, F.T., Evers, W.H., Byelov, D.V., Petukhov, A.V., De Mello Donegá, C. & Vanmaekelbergh, D.; "Semiconductor nanorod self-assembly at the liquid/air interface studied by in situ GISAXS and ex situ TEM"; *Nano Lett.* **12**, 5515–5523 (2012)

183. Polman, A. & Atwater, H.A.; "Photonic design principles for ultrahigh-efficiency photovoltaics"; *Nat. Mater.* **11**, 174–177 (2012)
184. Qin, W., Shah, R.A. & Guyot-Sionnest, P.; "CdSeS/ZnS alloyed nanocrystal lifetime and blinking studies under electrochemical control"; *ACS Nano* **6**, 912–918 (2012)
185. Sargent, E.H.; "Colloidal quantum dot solar cells"; *Nature Photon.* **6**, 133–135 (2012)
186. Shabaev, A., Rodina, A.V. & Efros, Al.L.; "Fine structure of the band-edge excitons and trions in CdSe/CdS core/shell nanocrystals"; *Phys. Rev. B* **86**, 205311 (2012)
187. Timmerman, D., Saeed, S., Gregorkiewicz, T., Roldán Gutiérrez, M.A. & Molina, S.I.; "Investigation of saturation and excitation behavior of 1.5 μm emission from Er^{3+} ions in SiO_2 sensitized with Si nanocrystals"; *Phys. Status Solidi C* **9**, 2312–2317 (2012)
188. Wilson, P.R.J., Khatami, Z., Dabkowski, R., Dunn, K., Chelomentsev, E., Wojcik, J. & Mascher, P.; "XANES and XEOL investigation of cerium and terbium co-doped silicon oxide films"; *ECS Trans.* **45**, 43–38 (2012)
189. Yi, Q., Tsuboi, T., Zhou, S., Nakai, Y., Lin, H. & Teng, H.; "Investigation of emission properties of Tm^{3+}:Y_2O_3 transparent ceramic"; *Chin. Opt. Lett.* **10**, 091602 (2012)
190. Yu, D.C., Ye, S., Peng, M.Y., Zhang, Q.Y. & Wondraczek, L.; "Sequential three-step three-photon near-infrared quantum splitting in β-$NaYF_4$:Tm^{3+}"; *Appl. Phys. Lett.* **100**, 191911 (2012)
191. Yu, D.C., Zhang, J.P., Chen, Q.J., Zhang, W.J., Yang, Z.M. & Zhang, Q.Y.; "Three-photon near-infrared quantum cutting in Tm^{3+}-doped transparent oxyfluoride glass ceramics"; *Appl. Phys. Lett.* **101**, 171108 (2012)
192. Zhao, J., Chen, O., Strasfeld, D.B. & Bawendi, M.G.; "Biexciton quantum yield heterogeneities in single CdSe (CdS) core (shell) nanocrystals and its correlation to exciton blinking"; *Nano Lett.* **12**, 4477–4483 (2012)
193. Zheng, W., Zhu, H., Li, R., Tu, D., Liu, Y., Luo, W. & Chen, X.; "Visible-to-infrared quantum cutting by phonon-assisted energy transfer in YPO_4:Tm^{3+},Yb^{3+} phosphors"; *Phys. Chem. Chem. Phys.* **14**, 6974–6980 (2012)
194. Zhou, J., Zhuang, L. & Li, F.; "Upconversion nanophosphors for small-animal imaging"; *Chem. Soc. Rev.* **41**, 1323–1349 (2012)
195. Zou, W., Visser, C., Maduro, J.A., Pshenichnikov, M.S. & Hummelen, J.C.; "Broadband dye-sensitized upconversion of near-infrared light"; *Nature Photon.* **6**, 560–563 (2012)
196. Aldakov, D., Lefrançois, A. & Reiss, P.; "Ternary and quaternary metal chalcogenide nanocrystals: synthesis, properties and applications"; *J. Mater. Chem. C* **1**, 3756–3776 (2013)
197. Bae, W.K., Padilha, L.A., Park, Y.-S., McDaniel, H., Robel, I., Pietryga, J.M., Klimov, V.I.; "Controlled alloying of the core/shell interface in CdSe/CdS quantum dots for suppression of Auger recombination"; *ACS Nano* **7**, 3411–3419 (2013)
198. Bae, W.K., Park, Y.-S., Lim, J., Lee, D., Padilha, L.A., McDaniel, H., Robel, I., Lee, C., Pietryga, J.M. & Klimov, V.I.; "Controlling the influence of Auger recombination on the performance of quantum-dot light-emitting diodes"; *Nat. Commun.* **4**, 2661 (2013)
199. Chen, O., Zhao, J., Chauhan, V.P., Cui, J., Wong, C., Harris, D.K., Wei, H., Han, H.-S., Fukumura, D., Jain, R.K. & Bawendi, M.G.; "Compact high-quality CdSe–CdS core–shell nanocrystals with narrow emission linewidths and suppressed blinking"; *Nat Mater.* **12**, 445–451 (2013)
200. Chen, X.B., Salamo, G.J., Yang, G.J., Li, Y.L., Ding, X.L., Gao, Y., Liu, Q.L. & Guo, J.H.; "Multiphonon near-infared quantum cutting luminescence phenomena of Tm^{3+} ion in $(Y_{1-x}Tm_x)_3Al_5O_{12}$ powder phosphor"; *Opt. Express* **21**, A829–A840 (2013)
201. Cohn, A.W., Schimpf, A.M., Gunthardt, C.E. & Gamelin, D.R.; "Size-dependent trap-assisted Auger recombination in semiconductor nanocrystals"; *Nano Lett.* **13**, 1810–1815 (2013)
202. Cordones, A.A. & Leone, S.R.; "Mechanisms for charge trapping in single semiconductor nanocrystals probed by fluorescence blinking"; *Chem. Soc. Rev.* **42**, 3209–3221 (2013)
203. Frantsuzov, P.A., Volkán-Kacsó, S. & Jankó, B.; "Universality of the fluorescence intermittency in nanoscale systems: experiment and theory"; *Nano Lett.* **13**, 402–408 (2013)
204. Hollingsworth, J.A.; "Heterostructuring nanocrystal quantum dots toward intentional suppression of blinking and Auger recombination"; *Chem. Mater.* **25**, 1318–1331 (2013)
205. Huang, X., Han, S., Huang, W. & Liu, X.; "Enhancing solar cell efficiency: the search for luminescent materials as spectral converters"; *Chem. Soc. Rev.* **42**, 173–201 (2013)
206. Hughes, S.M. & Alivisatos A.P.; "Anisotropic formation and distribution of stacking faults in II–VI semiconductor nanorods"; *Nano Lett.* **13**, 106–110 (2013)
207. Javaux, C., Mahler, B., Dubertret, B., Shabaev, A., Rodina, A.V., Efros, Al.L., Yakovlev, D.R., Liu, F., Bayer, M., Camps, G., Biadala, L., Buil, S., Quelin, X. & Hermier, J.-P.; "Thermal activation of non-radiative Auger recombination in charged colloidal nanocrystals"; *Nature Nanotech.* **8**, 206–212 (2013)

208. Kunneman, L.T., Zanella, M., Manna, L., Siebbeles, L.D.A. & Schins, J.M.; "Mobility and spatial distribution of photoexcited electrons in CdSe/CdS nanorods"; *J. Phys. Chem. C* **117**, 3146–3151 (2013)

209. Lhuillier, E., Keuleyan, S., Liu, H. & P. Guyot-Sionnest, P.; "Mid-IR colloidal nanocrystals"; *Chem. Mater.* **25**, 1272–1282 (2013)

210. Liu, T.-C., Zhang, G., Qiao, X., Wang, J., Seo, H.J., Tsai, D.-P. & Liu, R.-S.; "Near-infrared quantum cutting platform in thermally stable phosphate phosphors for solar cells"; *Inorg. Chem.* **52**, 7352–7357 (2013)

211. Lunnemann, P., Rabouw, F.T., Van Dijk-Moes, R.J.A., Pietra, F., Vanmaekelbergh, D. & Koenderink, A.F.; "Calibrating and controlling the quantum efficiency distribution of inhomogeneously broadened quantum rods by using a mirror ball"; *ACS Nano* **7**, 5984–5992 (2013)

212. Mangum, B.D., Ghosh, Y., Hollingsworth, J.A. & Htoon, H.; "Disentangling the effects of clustering and multiexciton emission in second-order photon correlation experiments"; *Opt. Express* **21**, 7419–7426 (2013)

213. Naczynski, D.J., Tan, M.C., Zevon, M., Wall, B., Kohl, J., Kulesa, A., Chen, S., Roth, C.M., Riman, R.E. & Moghe, P.V.; "Rare-earth-doped biological composites as in vivo shortwave infrared reporters"; *Nat. Commun.* **4**, 2199 (2013)

214. Park, Y.-S., Ghosh, Y., Chen, Y., Piryatinski, A., Xu, P., Mack, N.H., Wang, H.-L., Klimov, V.I., Hollingsworth, J.A. & Htoon, H.; "Super-Poissonian statistics of photon emission from single CdSe–CdS core–shell nanocrystals coupled to metal nanostructures"; *Phys Rev. Lett.* **110**, 117401 (2013)

215. Pisanello, F., Leménager, G., Martiradonna, L., Carbone, L., Vezzoli, S., Desfonds, P., Cozzoli, P.D., Hermier, J.-P., Giacobino, E., Cingolani, R., De Vittorio, M. & Bramati, A.; "Non-Blinking single-photon generation with anisotropic colloidal nanocrystals: towards room-temperature, efficient, colloidal quantum sources"; *Adv. Mater.* **25**, 1974–1980 (2013)

216. Podhorodecki, A., Zatryb, G., Golacki, L.W., Misiewicz, J., Wojcik, J. & Mascher, P.; "On the origin of emission and thermal quenching of SRSO:Er^{3+} films grown by ECR-PECVD"; *Nanoscale Res. Lett.* **8**, 98 (2013)

217. Saba, M., Aresti, M., Quochi, F., Marceddu, M., Loi, M.A., Huang, J., Talapin, D.V., Mura, A. & Bongiovanni, G.; "Light-induced charged and trap states in colloidal nanocrystals detected by variable pulse rate photoluminescence spectroscopy"; *ACS Nano* **7**, 229–238 (2013)

218. Shirasaki, Y., Supran, G.J., Bawendi, M.G. & Bulović, V.; "Emergence of colloidal quantum-dot light-emitting technologies"; *Nature Photon.* **7**, 13–23 (2013)

219. Sippel, P., Albrecht, W., Mitoraj, D., Eichberger, R., Hannappel, T. & Vanmaekelbergh, D.; "Two-photon photoemission study of competing Auger and surface-mediated relaxation of hot electrons in CdSe quantum dot solids"; *Nano Lett.* **13**, 1655–1661 (2013)

220. Ten Kate, O.M., De Jong, M., Hintzen, H.T. & Van der Kolk, E.; "Efficiency enhancement calculations of state-of-the-art solar cells by luminescent layers with spectral shifting, quantum cutting, and quantum tripling function"; *J. Appl. Phys.* **114**, 0844502 (2013)

221. Tenne, R., Teitelboim, A., Rukenstein, P., Dyshel, M., Mokari, T., Oron, D.; "Studying quantum dot blinking through the addition of an engineered inorganic hole trap"; *ACS Nano* **7**, 5084–5090 (2013)

222. Vaxenburg, R., Lifshitz, E. & Efros, Al.L.; "Suppression of Auger-stimulated efficiency droop in nitride-based light emitting diodes"; *Appl. Phys. Lett.* **102**, 031120 (2013)

223. Wang, Y.Z., Yu, D.C., Lin, H.H., Ye, S., Peng, M.Y. & Zhang, Q.Y.; "Broadband three-photon near-infrared quantum cutting in Tm^{3+} singly doped YVO_4"; *J. Appl. Phys.* **114**, 203510 (2013)

224. Zhao, J., Jin, D., Schartner, E.P., Lu, Y., Liu, Y., Zvyagin, A.V., Zhang, L., Dawes, J.M., Xi, P., Piper, J.A., Goldys, E.M. & Monro, T.M.; "Single-nanocrystal sensitivity achieved by enhanced upconversion luminescence"; *Nat. Nanotechnol.* **8**, 729–934 (2013)

225. Boneschanscher, M.P., Evers, W.H., Geuchies, J.J., Altantzis, T., Goris, B., Rabouw, F.T., Van Rossum, S.A.P., Van der Zant, H.S.J., Siebbeles, L.D.A., Van Tendeloo, G., Swart, I., Hilhorst, J., Petukhov, A.V., Bals, S. & Vanmaekelbergh, D.; "Long-range orientation and atomic attachment of nanocrystals in 2D honeycomb superlattices"; *Science* **344**, 1377–1380 (2014)

226. Cohn, A.W., Rinehart, J.D., Schimpf, A.M., Weaver, A.L. & Gamelin, D.R.; "Size dependence of negative trion Auger recombination in photodoped CdSe nanocrystals"; *Nano Lett.* **14**, 353–358 (2014)

227. Deng, Z., Jeong, K.S. & Guyot-Sionnest, P.; "Colloidal quantum dots intraband photodetectors"; *ACS Nano* **8**, 11707–11714 (2014)

228. Dong, S.L., Lin, H.H., Yu, T. & Zhang, Q.Y.; "Near-infrared quantum-cutting luminescence and energy transfer properties of $Ca_3(PO_4)_2$:Tm^{3+},Ce^{3+} phosphors"; *J. Appl. Phys.* **116**, 023517 (2014)

229. Erickson, C.S., Bradshaw, L.R., McDowall, S., Gilbertson, J.D., Gamelin, D.R. & Patrick, D.L.; "Zero-reabsorption doped-nanocrystal luminescent solar concentrators"; *ACS Nano* **8**, 3461–3467 (2014)

230. Foucher, C., Guilhabert, B., Laurand, N. & Dawson, M.D.; "Wavelength-tunable colloidal quantum dot laser on ultra-thin flexible glass"; *Appl. Phys. Lett.* **104**, 141108 (2014)
231. Ghenuche, P., De Torres, J., Moparthi, S. B., Grigoriev, V. & Wenger, J.; "Nanophotonic enhancement of the Förster resonance energy-transfer rate with single nanoapertures"; *Nano Lett.* **14**, 4707–4714 (2014)
232. Grim, J.Q., Christodoulou, S., Di Stasio, F., Krahne, R., Cingolani, R., Manna, L. & Moreels, I.; "Continuous-wave biexciton lasing at room temperature using solution-processed quantum wells"; *Nat. Nanotechnol.* **9**, 891–895 (2014)
233. Meinardi, F., Colombo, A., Velizhanin, K.A., Simonutti, R., Lorenzon, M., Beverina, L., Viswanatha, R., Klimov, V.I. & Brovelli, S.; "Large-area luminescent solar concentrators based on 'Stokes-shift-engineered' nanocrystals in a mass-polymerized PMMA matrix"; *Nature Photon.* **8**, 392–399 (2014)
234. Park, Y.-S., Bae, W.K., Padilha, L.A., Pietryga, J.M. & Klimov, V.I.; "Effect of the core/shell interface on Auger recombination evaluated by single-quantum-dot spectroscopy"; *Nano Lett.* **14**, 396–402 (2014)
235. Park, Y.-S., Bae, W.K., Pietryga, J.M. & Klimov, V.I.; "Auger recombination of biexcitons and negative and positive trions in individual quantum dots"; *ACS Nano* **8**, 7288–7296 (2014)
236. Tabachnyk, M., Ehrler, B., Gélineas, S., Böhm, M.L., Walker, B.J., Musselman, K.P., Greenham, N.C., Friend, R.H. & Rao, A.; "Resonant energy transfer of triplet excitons from pentacene to PbSe nanocrystals"; *Nat. Mater.* **13**, 1033–1038 (2014)
237. Thompson, N.J., Wilson, M.W.B., Congreve, D.N., Brown, P.R., Scherer, J.M., Bischof, T.S., Wu, M., Geva, N., Welborn, M., Van Voorhis, T., Bulović, V., Bawendi, M.G. & Baldo, M.A.; "Energy harvesting of non-emissive triplet excitons in tetracene by emissive PbS nanocrystals"; *Nat. Mater.* **13**, 1039–1043 (2014)
238. Van der Stam, W., Gantapara, A.P., Akkerman, Q.A., Soligno, G., Meeldijk, J.D., Van Roij, R., Dijkstra, M. & De Mello Donegá, C.; "Self-assembly of colloidal hexagonal bipyramid- and bifrustum-shaped ZnS nanocrystals into two-dimensional superstructures"; *Nano Lett.* **14**, 1032–1037 (2014)
239. Wang, J., Deng, R., MacDonald, M.A., Chen, B., Yuan, J., Wang, F., Chi, D., Hor, T.S.A., Zhang, P., Liu, G., Han, Y., Liu, X.; "Enhancing multiphoton upconversion through energy clustering at sublattice level"; *Nat. Mater.* **13**, 157–162 (2014)
240. Würth, C., Geißler, D., Behnke, T., Kaiser, M. & Resch-Genger, U.; "Critical review of the determination of photoluminescence quantum yields of luminescent reporters"; *Anal. Bioanal. Chem.* **407**, 59–78 (2014)
241. Yu, D.C., Rabouw, F.T., Boon, W.Q., Kieboom, T., Ye, S., Zhang, Q.Y. & Meijerink, A.; "Insights into the energy transfer mechanism in Ce^{3+}–Yb^{3+} codoped YAG phosphors"; *Phys. Rev. B* **90**, 165126 (2014)
242. Bozyigit, D., Lin, W.M.M., Yazdani, N., Yarema, O. & Wood, V.; "A quantitative model for charge carrier transport, trapping and recombination in nanocrystal-based solar cells"; *Nat. Commun.* **6**, 6180 (2015)
243. Chen, X.B., Li, S., Salamo, G.J., Li, Y.L., He, L.Z., Yang, G.J., Gao, Y. & Liu, Q.L.; "Sensitized intense near-infrared downconversion quantum cutting three-photon luminescence phenomena of the Tm^{3+} ion activator in $Tm^{3+}Bi^{3+}$:$YNbO_4$ powder phosphor"; *Opt. Express* **23**, A51–A61 (2015)
244. Martín-Rodríguez, R., Rabouw, F.T., Trevisani, M., Bettinelli, M. & Meijerink, A.; "Upconversion dynamics in Er^{3+}-doped Gd_2O_2S: influence of excitation power, Er^{3+} concentration, and defects"; *Adv. Optical Mater.* **3**, 558–567 (2015)
245. Nasilowski, M., Spinicelli, P., Patriarche, G. & Dubertret, B.; "Gradient CdSe/CdS quantum dots with room temperature biexciton unity quantum yield"; *Nano Lett.* **15**, 3953–3958 (2015)
246. Van der Stam, W., Berends, A.C., Rabouw, F.T., Willhammar, T., Xiaoxing Ke, X., Meeldijk, J.D., Bals, S. & De Mello Donegá, C.; "Luminescent $CuInS_2$ quantum dots by partial cation exchange in $Cu_{2-x}S$ nanocrystals"; *Chem. Mater.* **27**, 621–628 (2015)
247. Vaxenburg, R., Rodina, A., Shabaev, A., Lifshitz, E. & Efros, Al.L.; "Nonradiative Auger recombination in semiconductor quantum dots"; *Nano Lett.* **15**, 2092–2098 (2015)

SAMENVATTING IN HET NEDERLANDS

ABSTRACT • In dit proefschrift proberen we de eigenschappen van luminescente kristallen te begrijpen. We beschouwen naast kristallen ter grootte van een zandkorrel, bestaande uit typisch 1000000000000000000 atomen, ook *nanokristallen* opgebouwd uit 1000 tot 10000 atomen. Luminescente nanokristallen zijn zo klein dat ze in (bio)medisch onderzoek kunnen worden gebruikt als labels die zich binden aan bepaalde typen cellen of biomoleculen. Daarnaast kunnen ze 'onzichtbaar' in een transparant materiaal zoals een vloeistof of plastic worden ingebracht, omdat ze geen licht verstrooien. Dit zijn belangrijke voordelen van luminescente nanokristallen t.o.v. macroscopische luminescente materialen. Bovendien veranderen van sommige typen materialen de optische eigenschappen (d.w.z. de absorptie en uitzending van licht) als ze zo klein worden als een nanokristal. In dit proefschrift onderzoeken we hoe het uitzenden van licht door luminescente (nano)kristallen werkt: welke processen leiden uiteindelijk tot het uitzenden van de gewenste kleur licht, en welke alternatieve ongewenste processen zijn er voor het nanokristal om zijn energie kwijt te raken? De verkregen kennis kan bijdragen aan de verhoging van de efficiëntie van bekende typen luminescente (nano)kristallen, en aan de ontwikkeling van nieuwe typen.

De luminescente materialen onderzocht in dit proefschrift, kunnen worden onderverdeeld in twee soorten. Hst. 3,4,8 gaan over luminescente nanokristallen van halfgeleiders. In Hst. 5–7 onderzoeken we (nano)kristallen van isolatoren waarin een kleine hoeveelheid luminescente dotering is ingebracht: een deel van de ionen van het kristal is vervangen door een luminescente ionen van een ander element. We bestuderen steeds de aangeslagen toestand van de kristallen, d.w.z. de situatie waarin het kristal een overschot aan energie heeft door absorptie van licht. We onderzoeken hoe snel na absorptie van licht het kristal zijn energie kwijtraakt. Hieruit leiden we af welke processen plaatsvinden, en met welke efficiëntie.

I • Luminescente nanokristallen van halfgeleiders

Halfgeleiders (Hst. 3,4,8) zijn essentieel voor de hedendaagse technologie. Ze kunnen zichtbaar of infrarood licht absorberen en uitzenden. De elektrische geleiding door halfgeleiders kan gemakkelijk worden gemanipuleerd, bijvoorbeeld aan de hand van de chemische samenstelling of een elektrische spanning. Dit fenomeen wordt gebruikt in transistoren, die de basis vormen van de moderne elektronica. De meest alomtegenwoordige halfgeleider is silicium (Si; Fig. Ia), gebruikt in chips in vrijwel alle elektronica en als licht-absorberend materiaal in de meeste zonnecellen. De halfgeleider indiumgalliumnitride [(In,Ga)N; Fig. Ib] is het materiaal dat in moderne LED-lampen (light-emitting diodes) verantwoordelijk is voor de efficiënte omzetting van elektriciteit in licht. In dit proefschrift bestuderen we halfgeleiderkristallen kleiner dan ongeveer 10 nm (≈10000 atomen). Van zulke kleine kristallen zijn de optische eigenschappen afhankelijk van de exacte grootte. Het meest opvallende is dat de kleuren licht die worden geabsorbeerd en uitgezonden, sterk veranderen met de grootte. Fig. Ic toont bijvoorbeeld de kleuren licht uitgezonden door nanokristallen van cadmiumselenide (CdSe), variërend tussen rood voor relatief grote CdSe nanokristallen van 6 nm diameter (rechts) en blauw voor kleine CdSe nanokristallen van 2 nm diameter.

In Hst. 3,4 onderzoeken we Augerverval in halfgeleidernanokristallen. Dit is een proces waarbij energie verloren gaat zonder dat er licht uit een nanokristal komt. Het vindt plaats wanneer het nanokristal geladen is (Hst. 3) of wanneer het snel na elkaar twee fotonen heeft geabsorbeerd (Hst. 4). Beide situaties komen voor wanneer een nanokristal intens belicht wordt, bijvoorbeeld in een microscoop voor biomedisch onderzoek of in een kleur-conversielaag voor LED-schermen.

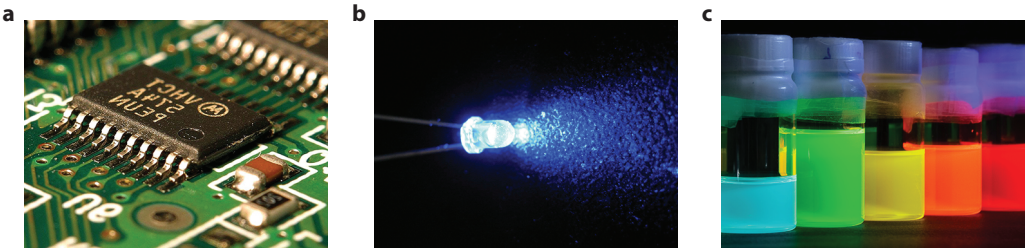

I • Verschijningsvormen van halfgeleiders. (**a**) De halfgeleider silicium wordt alom gebruikt in elektronica voor computerchips. Het is ook het meest voorkomende licht-absorberende materiaal in zonnecellen. (**b**) De halfgeleider indiumgalliumnitride zet efficiënt elektriciteit om in licht in LED-lampen. De uitgezonden kleur is aanvankelijk blauw, maar kan vervolgens met een ander luminescent materiaal worden omgezet naar wit. (**c**) De halfgeleider cadmiumselenide wordt veel gebruikt in het onderzoek naar halfgeleidernanokristallen, omdat de syntheseprocedures goed ontwikkeld zijn. De kleur uitgezonden door nanokristallen onder UV-belichting is afhankelijk is van de grootte van de nanokristallen: van blauw (links) naar rood (rechts) neemt de diameter van de nanokristallen toe van 2 nm tot 6 nm. Bron voor **a** en **b**: Wikimedia Commons. Foto **c** is gemaakt door Mark Vis.

Het onderdrukken van Augerverval is dus belangrijk voor de efficiëntie van luminescente nanokristallen onder condities relevant voor toepassingen. In Hst. 3 vinden we dat het Augerverval in staafvormige nanokristallen van CdSe en cadmiumsulfide (CdS) een minder groot probleem vormt dan in conventionele bolvormige nanokristallen. In Hst. 4 meten, berekenen en bediscussiëren we waarom sommige, maar niet alle, typen Augerverval minder efficiënt worden als CdSe nanokristallen worden beschermd met een schil van CdS van toenemende dikte.

Hst. 3,8 gaan over *blinking*, het fenomeen dat luminescente nanokristallen zichzelf op tijdschalen van milliseconden tot seconden voortdurend en schijnbaar willekeurig aan- en uitschakelen. Blinking is voor veel toepassingen een ongewenst fenomeen, omdat het de tijdsgemiddelde lichtintensiteit lager maakt. Helaas wordt het nog slecht begrepen, en is er meer onderzoek nodig naar de oorzaak en de factoren die blinking kunnen onderdrukken. De conclusie van Hst. 3 is dat staafvormige nanokristallen van CdSe en CdS, in tegenstelling tot veel bolvormige nanokristallen nooit volledig uit staan, maar altijd ten minste 25% van hun maximale lichtintensiteit blijven tonen. Dit is een direct gevolg van het minder efficiënt zijn van Augerverval, zoals hierboven besproken. In Hst. 8 stellen we een nieuw model voor om het verschijnsel van blinking te verklaren. Terwijl tot nu toe de lichtemissie uit nanokristallen vooral werd gemeten op tijdschalen van nanoseconden, hebben wij doorgemeten tot milliseconden na excitatie met een laserpuls. De statistiek van de emissie op zulke lange tijdschalen bleek identiek aan de statistiek van blinking. Ons nieuwe model verklaart hoe het vasthouden van elektronen door defecten in een nanokristal zowel kan leiden tot emissie op lange tijdschalen als tot blinking.

II • Nanokristallen van isolatoren met luminescente dotering

In tegenstelling tot halfgeleiders, zijn kristallen van pure isolatoren in het algemeen kleurloos, omdat ze geen zichtbaar licht absorberen. Met dotering, d.w.z. het inbrengen van luminescente ionen, kunnen echter interessante optische eigenschappen worden geïntroduceerd (Hst. 5–7). Gedoteerde kristallen van isolatoren zijn wellicht het meest bekend in het dagelijks leven als sieraden. Bijvoorbeeld kristallen van puur alpha-aluminiumoxide (α-Al_2O_3) zijn kleurloos en lijken op diamant (Fig. IIa), terwijl een kleine hoeveelheid vervuiling (<1%) van titanium (Ti^{4+}) en ijzer

II • Het doteren van isolatoren. (**a**) Puur alpha-aluminiumoxide, oftewel corundum, is een isolator die kleurloze kristallen vormt. Interessante optische eigenschappen krijgt het materiaal pas als het wordt gedoteerd, d.w.z. als er een kleine hoeveelheid (<1%) van een vreemd element wordt ingebracht. (**b**) Gedoteerd met titanium en ijzer staat het materiaal bekend als blauw saffier. (**c**) Gedoteerd met chroom heet het materiaal robijn. Bron: jiyunjung.blogspot.com.

(Fe^{2+}) een blauwe saffier oplevert (Fig. IIb), of een kleine hoeveelheid chroom (Cr^{3+}) een rode robijn (Fig. IIc). Behalve decoratieve waarde hebben gedoteerde isolatorkristallen ook technologische waarde. De eerste werkende laser was bijvoorbeeld gebaseerd op robijn (Fig. IIc). Nog steeds is het actieve materiaal in veel lasers een gedoteerde isolator. Ook in vrijwel alle moderne lampen worden de kleuren gemaakt door gedoteerde isolatoren, bijvoorbeeld het gele licht in LED-lampen door granaatkristallen met cerium (Ce^{3+}).

In dit proefschrift (Hst. 5–7) houden we ons in het bijzonder bezig met (nano)kristallen gedoteerd met *twee* verschillende luminescente elementen, in plaats van slechts één. Dotering met twee verschillende elementen brengt interessante mogelijkheden met zich mee. Het ene element kan licht absorberen, om de opgenomen energie over te dragen aan het andere, dat vervolgens licht uitzendt van een andere kleur. Door de juiste combinatie van elementen te kiezen, kunnen we de absorptie en emissie van licht onafhankelijk van elkaar optimaliseren. Lanthaanfosfaat ($LaPO_4$) gedoteerd met een combinatie van cerium (Ce^{3+}) en terbium (Tb^{3+}) wordt bijvoorbeeld in spaarlampen en tl-buizen gebruikt voor om de groene kleur te maken: cerium absorbeert het UV-licht gegenereerd door een gasontlading, draagt energie over aan terbium, dat vervolgens efficiënt groen licht maakt.

In Hst. 7 bestuderen we $LaPO_4$ gedoteerd met Ce^{3+} en Tb^{3+} in nanokristallijne vorm. Een model wordt beschreven en getest om de snelheid en efficiëntie van energieoverdracht in nanokristallen te berekenen als functie van de concentratie van dotering. Ons model kan dienen om de processen in gedoteerde nanokristallen beter te begrijpen. Het doel is uiteindelijk om de compositie van de luminescente nanokristallen te kunnen optimaliseren, bijvoorbeeld voor maximaal signaal en weinig achtergrond in biomedisch onderzoek. Daarnaast beschrijven en verklaren we in Hst. 7 onze vinding dat de efficiëntie van energieoverdracht in nanokristallen hoger is, als de brekingsindex hoger is van de vloeistof waarin ze zich bevinden.

In Hst. 5,6 beschouwen we een bijzondere vorm van energieoverdracht. Hier wordt de energie niet simpelweg overgedragen van het ene element (de donor) naar het andere (de acceptor), maar *opgesplitst*. Dit kan op twee manieren gebeuren: (1) de donor draagt slechts een deel van de energie over, en houdt de rest zelf; of (2) de donor verdeelt de energie over twee acceptoren. Dergelijke splitsing van energie heeft als netto resultaat dat er voor elk foton dat wordt geabsorbeerd, uiteindelijk twee fotonen kunnen worden uitgezonden: kleuromzetting met een efficiëntie van 200%. In Hst. 5 meten we dat energieopsplitsing via methode (1) in gadoliniumoxysulfide (Gd_2O_2S) ge-

doteerd met thulium (Tm^{3+}) meerdere keren achter elkaar kan gebeuren, waardoor uiteindelijk vier fotonen kunnen worden uitgezonden voor elk geabsorbeerd foton. In Hst. 6 beschrijven we een relatief simpel model om de snelheid van verscheidene manieren van energieoverdracht in gedoteerde kristallen te analyseren en voorspellen.

In Hst. 9 vatten we de belangrijkste resultaten samen, en bespreken we mogelijk vervolgonderzoek voor naar aanleiding van het werk beschreven in dit proefschrift. Daarnaast wordt genoemd op welke manier onze resultaten op de lange duur relevant kunnen zijn voor toepassingen.

ACKNOWLEDGEMENTS

ABSTRACT • Many people have contributed to the completion of my PhD thesis. With some I have done some sort of collaboration, or they have taught me important things. Other people just made my PhD time pleasant, during working hours or outside working hours. I want to thank all these people. Below you can read a more detailed and more or less chronological account (mostly in Dutch) of my first encounters with the people who were most directly involved in my studies and work.

Het begon allemaal op 5 augustus 1988, op een half bewolkte vrijdagmiddag. Mijn moeder Dinie Bakker is wiskundelerares, mijn vader Fred Rabouw was ooit natuurkundeleraar. Vanaf het eerste begin hebben zij de dingen gestimuleerd die uiteindelijk belangrijk zouden zijn tijdens mijn PhD-project. Een grappig voorbeeld: zoals veel jongetjes mocht ik niet de hele dag spelletjes spelen op de computer. Als ik mijn computertijd echter gebruikte om mijn vaardigheid te trainen met programma's als PowerPoint en Excel, dan was de maximale tijd wat langer. Van die regeling maakte ik, al op de basisschool, uiteraard graag gebruik. Later toen ik ging studeren en promoveren, was het fijn dat mijn ouders altijd hebben kunnen begrijpen wat ik leerde of waar ik mee bezig was. Ook mijn broertje Huib Rabouw is erg geïnteresseerd in de dingen die in het departement scheikunde onderzocht worden. Hij vraagt vooral vaak naar meer informatie over dingen als *colloidal nanosurfaces* of *solid quantum wires*.

Twee dagen voor mij was Robin Geitenbeek geboren in hetzelfde ziekenhuis in Gouda. We kunnen niet helemaal uitsluiten dat we verwisseld zijn. Robin is al sinds onze geboorte, ruim 27 jaar lang, een groot goeroe voor mij op het gebied van klaverjassen. Pas recentelijk zijn we echter begonnen met serieuze veelbelovende samenwerkingsprojecten op het gebied van wetenschap. Inmiddels hebben we al een gezamenlijke sample box.

Op de middelbare school, het *Coornhert Gymnasium* in Gouda, koos ik aan het eind van het derde jaar vol overtuiging voor een bètaprofiel. Omdat ik niet kon beslissen welk bètavak het leukste was, koos ik in de zesde als studie het 'breedste': scheikunde.

Van mijn practicumgroep waarmee ik in het eerste jaar begon, heeft alleen Tamara Stegmann de scheikundestudie afgemaakt. De eerste indruk die ik op haar maakte was erg slecht, toen ik probeerde te kopiëren door als een idioot op de aan/uit-knop van een kopieerapparaat te drukken. Desondanks hebben we, met Remco Rodenburg, Kristel Boere en

Christine Tjong,

nog veel samengewerkt bij bachelorvakken. Als hoogtepunten zou ik noemen het bijna winnen van een posterprijs, en het refereren naar de Chemiekaarten. Helaas kozen Tamara, Remco, Kristel en Christine stuk voor stuk voor de biochemische kant van de scheikunde. Daardoor zijn ze voor mij nu echter een interessante bron van unieke roddels en informatie.

Tijdens mijn bachelorstudie ben ik student-assistent geweest. Bij de begeleiding van middelbare scholieren op de practicumzaal leerde ik Elleke van Harten kennen. We gaven beiden introductielessen over – jawel – spectroscopie. Nu zijn we collega's, en durft ze zelfs aan mij toe te geven dat ze spectroscopie en data-analyse met Mathematica "stiekem toch best wel leuk" begint te vinden. Met Mark Vis heb ik een jaar lang middelbare scholieren bijgestaan die hun profielwerkstuk scheikunde kwamen uitvoeren op de UU. Ik heb gedurende dit jaar niet alleen veel geleerd op het gebied van scheikunde, maar Mark heeft mij ook geleerd snel nieuwe taken en e-mails af te handelen, in plaats van uit te stellen en te vergeten. Mijn eerste contact met Andries Meijerink stamt uit dezelfde tijd. Hij stelde zijn apparatuur beschikbaar voor het profielwerkstuk van een

middelbare scholier, en heeft een hele dag lang enthousiast geholpen. Later, ten tijde van mijn masterproject, heeft hij de basis gelegd voor alles wat ik nu weet over spectroscopie. Hij heeft bij besprekingen de basale theorie (herhaaldelijk) uitgelegd, en is vele malen komen helpen bij experimenten op de Eddy. Dit soort directe hulp werd gelukkig minder nodig tijdens mijn promotie, maar de begeleiding en ideeën van Andries zijn altijd belangrijk gebleven. Hij is dan is ook een van mijn favoriete promotoren.

In mijn tweede jaar heb ik bijgedragen aan de organisatie van de scheikundeolympiade op de UU. Daarbij was Mathijs de Jong lid van de commissie *sociale activiteiten*. Ik had nadien de eer toe te mogen treden tot zijn lijst met goede vrienden die op de hoogte werden gesteld van zijn nieuwe e-mailadres toen hij in het buitenland ging studeren. De verrassing was groot toen hij enkele jaren later terug was, en mijn collega werd. Ik heb vaak met plezier geleerd van zijn pretentieuze opmerkingen, onder andere over typografie. Mathijs heeft daarmee belangrijke bijdragen geleverd aan de vormgeving van de tekst en vergelijkingen in deze thesis.

Het researchproject aan het einde van het tweede jaar, in 2007, voerde ik al uit in de CMI-groep. Op hetzelfde moment deed Ward van der Stam zijn eerstejaarsonderzoeksstage bij CMI. We zijn dus beiden echte fossielen, die al 8 jaar in hetzelfde gebouw rondhangen. Tijdens onze master zaten Ward en ik op verschillende (vijandige) masterkamers, en negeerden we elkaar voornamelijk. Deze situatie werd pas anders toen Ward op stage in het buitenland was, en ik hem womanizede met nieuws over beschikbare PhD-posities bij CMI. Bij terugkomst als brave collega besloot hij zich dan ook in kamer OL158 te vestigen. Deze beslissing mondde uit in een lang succesverhaal, dat nog niet ten einde is. Ik ben benieuwd naar het altaar dat hij heeft beloofd in te richten als ik vertrek. Terug naar het researchproject uit mijn tweede jaar: ik werkte samen met Marie Anne van de Haar aan een zeer succesvol project over de synthese van zinkoxide nanodraden voor zonnecellen. Bij onze presentatie voorspelden we al dat het is nog slechts een kwestie van tijd zal zijn tot onze resultaten zullen worden erkend als grote doorbraak. Sinds het tweede jaar hebben we onze onderzoeksprojecten samen (maar elk individueel) gedaan. We hebben snoepjes gesorteerd en gegeten, europiumvlammen gemaakt, en gewed om een ananas. Ondanks ons succes in het tweede jaar, heeft Marie Anne altijd 'hard to get' gespeeld als ik een officieel samenwerkingsproject voorstelde (tot ze vier maanden voor het einde van onze promotie ineens omsloeg). Het succes van mijn researchproject was overigens mede te danken aan Mark Boneschanscher. Het was een grote eer dat hij (als masterstudent!) voor ons op internet wilde opzoeken welke molariteit geconcentreerd zoutzuur heeft. Ook toen we collega-promovendi waren bleef Mark een bron van nuttige informatie, onder andere over de reglementen van FOM en over platanen.

Mijn vroegste herinnering aan Daniël Vanmaekelbergh zijn de colleges over hout nanodeeltjes bij het vak *Nanomaterialen*. Voor inzage van het tentamen heb ik zijn (oude, kleinere) kamer mogen betreden. Dit zou de eerste van vele honderden keren zijn dat ik hem op zijn kamer kwam storen, om iets te vragen, iets te laten zien of iets te laten ondertekenen. Hij heeft bijna altijd tijd, en is bijna altijd snel met het doorlezen en corrigeren van mijn werk. In de loop van mijn tijd als PhD-student is Daniël met veel wilde ideeën gekomen, die in sommige gevallen resulteerden in mooie resultaten. Ik ben met name blij dat hij me heeft aangedreven om 'moeilijke' dingen te ondernemen en tot een goed einde te brengen, zoals de experimenten in Grenoble en op AMOLF.

Mijn eerste dappere pogingen om wetenschappelijk onderzoek te doen waren voor mijn bachelorproject bij 'Fysische en Colloïdchemie'. Onder begeleiding van Daniela Kraft en Willem Kegel werkte ik aan depletie-interactie tussen colloïdale deeltjes. Ik heb het erg naar mijn zin gehad bij FCC, maar ben de FCC'ers ook dankbaar dat ze me hebben aangeraden voor mijn masterproject

naar CMI te gaan. Met de (nogal onconventionele) presentatie van Stefan Scheidelaar over zijn bachelorproject maakte ik kennis met energieoverdracht in gedoteerde kristallen (Hst. 5–7). Later deed Stefan zijn masterproject op hetzelfde onderwerp in de CMI-groep, en heeft hij mij er enthousiast voor gemaakt. Helaas hebben we geen gezamenlijk publicatie overgehouden aan onze samenwerking. Overigens hebben de minder wetenschappelijke bezigheden die we uitvoerden op onze masterkamer mij bijna mijn baan gekost, omdat Daniël er soms zijn deur door dicht moest doen.

I did my master thesis work in the CMI group under the supervision of Yiming Zhao, on the synthesis of alkaline earth sulfide nanocrystals doped with luminescent ions. Yiming has taught me how to work in a glovebox (wearing three pairs of gloves while handling a reaction mixture at over 200°C) and on the Eddy spectrometers. He also made my master project a success with his suggestion for single-source precursors. Uiteindelijk was het Celso de Mello Donegá die met het idee kwam om de ontleding van de precursor in puur amine te doen. Uiteraard was ik te lui om zijn idee precies te volgen en (vast) *octadecylamine* te gebruiken, maar gelukkig lukte het ook om CaS nanodeeltjes te maken in puur *oleylamine*. In de loop van mijn PhD-tijd hebben Celso en ik samen meegedaan aan verschillende synchrotronprojecten, eerst met Francesca en later met Ward. Onbetwist het meest gedenkwaardige waar we samen aan hebben gewerkt, is echter de poging spectroscopie te doen aan individuele $CuInS_2$-nanodeeltjes van Anne.

In de eerste maanden van mijn masterthesis was ik officieel kamergenoten met Joren Eilers, maar hij was voornamelijk druk thuis aan het werk. Als collega had hij gelukkig wel af en toe tijd voor leuke activiteiten op CMI, zoals mijn lunch verstoppen. De tweede collega die ik uit de masterkamer OL159 ken, is Jaco Geuchies. Toen ik uit de masterkamer vertrok, nam hij zelfs mijn computer over (in plaats van een altaar in te richten). Het is mooi geweest te zien hoe Jaco in vijf jaar is gegroeid van hbo-bachelorstudent tot één van de meest promising en best wiskundig onderlegde PhD-studenten, en de ambassadeur van CMI in Frankrijk. During my time as a master student, Francesca Pietra arrived in the group as an Erasmus exchange student. In the first month of my PhD contract we had a joint beam trip to the synchrotron in Grenoble, during which we became BFFs. This was the beginning of a long and fruitful collaboration, both on X-ray scattering and on spectroscopy. Having Francesca as a colleague was bonding not only for scientific, but also for non-scientific reasons. Most importantly, she was present and (somewhat) supportive on the second and the third worst days of my life.

De cursus in mijn studie die mij het meest is bijgebleven is *Nanophotonics* van Albert Polman. Ik leerde over het tot dat moment voor mij onbekende veld van plasmonics. De inleveropgaven waren zo uitdagend dat het ons studenten, waaronder Gydo van Zundert, Niek den Hartog, Hinke Schokker en Benjamin Brenny nader tot elkaar bracht. Door het netwerken met Niek en Gydo heb ik meermaals de eer gehad kasteel Rijnhuizen te mogen betreden. Ze hebben bovendien bewonderenswaardige maar mislukte pogingen gedaan mij zowel slim als sterk te maken. Hinke en Benjamin hebben sinds *Nanophotonics* een grote liefde voor koediekoedies, die ze uiteraard krijgen wanneer ik maar in Amsterdam ben. In feite is mijn keuze om voor mijn masterstage naar AMOLF (Amsterdam) te gaan ingegeven door de cursus *Nanophotonics*. Ik werkte op AMOLF voor Martin Frimmer en Femius Koenderink, en probeerde individuele colloïdale quantum dots te hechten aan een oppervlak. Van hen heb ik geleerd kritisch te zijn op mijn eigen werk en dat van anderen, en altijd vragen te blijven stellen. Ook later, tijdens mijn PhD-periode, zijn hun commentaren zeer nuttig geweest. De gemoedstoestand van Martin toen hij zijn PhD-thesis schreef (o.a. de neiging om in de gaatjes van de optische tafel te poepen), beangstigden mij enigszins. Gelukkig was mijn periode van schrijven minder mentaal belastend. Marko Kamp begon op AMOLF

als technicus op dezelfde dag dat ik mijn stage begon. Tijdens mijn PhD-onderzoek heeft hij belangrijke ondersteuning gegeven bij de experimenten op AMOLF.

When I returned to CMI after my internship, two people new had arrived: Rosa Martín-Rodriguez and Relinde Moes (now: van Dijk-Moes). Rosa has ever since continued to challenge me for being a better friend to Francesca than I am. Despite this eternal struggle, we worked together on two projects about the interesting topics of up- and downconversion (Ch. 5). Relinde heeft vier jaar lang mooie quantum dots voor mij gemaakt, die (onder andere) zijn gebruikt voor Hst. 3,4,8. Ik had ook de grote eer af en toe haar glovebox te mogen gebruiken.

In de eerste maand van mijn PhD-contract kreeg ik Tim Senden als masterstudent. Tim is een van de braafste studenten die ooit op CMI hebben rondgelopen, een echte braveling. Hij had een success rate op syntheses van boven de 75%. Belangrijker nog, zijn werk vormt de basis van Hst. 7 uit deze thesis. Kleine jongetjes worden groot, en Tim is nu mijn collega geworden. Ik wens hem net zulke brave studenten toe als hij zelf ooit was. Er kwamen nog vele andere studenten: Stephan den Hartog (zie Hst. 7), Thomas Gardenier (zie Fig. 9.3), Marieke Castelijns, Bas Salzmann en Maaike van der Sluijs voor hun bachelorthesis, en Jasper Landman, Jantina Fokkema, Jarich Haitjema, Ali al Samarai, en Marieke Castelijns (wederom; Marieke heeft goede intuïtie voor het kiezen van de meest veelbelovende projecten) voor hun masterthesis. De ene was nog braver dan de andere, en uiteindelijk hebben ze (tot nu toe) hun projecten allemaal afgerond zonder een vervangende opdracht te hoeven doen.

Na een half jaar op kamer OL158 kreeg ik gezelschap van Joost van der Lit. Hij is de meeste dagen druk bezig bij 'het apparaat' in de kelder, maar is desondanks een belangrijke aanwinst voor de kamer geweest. Niet alleen zorgt hij heel liefdevol voor de plant Herman, hij zorgt er ook voor dat de kamer leefbaar blijft door ongenode gasten de deur te wijzen. De hoge positie van OL158 in de ranglijst van leuke kamers op CMI is in grote mate aan Joost te danken. Besides Ward, Herman and me there is only one other individual that Joost could tolerate in our room for longer than a day: Daniel Gamelin, who stayed for a total of about four months during two 'sabbaticals'. I valued his lectures and the casual discussions in our room very much. They have inspired the work presented in Ch. 8 of this thesis.

Joep Peters verscheen op ons lab aan het einde van mijn eerste jaar. Hij begon tegelijk met een groep tweedejaarsstudenten te werken aan een project bij Daniël. Toen tegen de zomervakantie de tweedejaarsstudenten weggingen maar Joep niet, werd het duidelijk dat hij masterstudent was. Inmiddels is hij zelfs social boy en PhD-student geworden. During my second year, Dechao Yu came to our lab for a year on exchange from China. I loved his stories about Chinese culture, and his interest in the Dutch culture. We supervised first-year students together, and had two good collaborations on downconversion materials (see Ch. 5). Aan het begin van mijn derde jaar kwam Carlo van Overbeek. Op het vlak van werelddominantie zijn we gezworen vijanden. Dat heeft ons er echter niet van weerhouden wat gezamenlijke reisjes naar het synchrotron in Grenoble te ondernemen, die uiteraard erg bonding waren. Ook Anne Berends begon in het begin van mijn derde jaar op onze groep, aanvankelijk als masterstudente. Ze had een uitdagend masterproject onder mijn begeleiding kunnen doen, maar helaas wees ze me af wegens strengheid. In de loop van de tijd leerde ze gelukkig door de strengheid heen te kijken, en begonnen we zelfs samen te werken aan de spectroscopie van haar nanodeeltjes. Inmiddels is Anne een collega, maar wel een bijzondere, want ze leest niet alleen *JACS* en *Nano Letters*, maar ook de *Cosmo* en de *Linda*. In de loop van mijn derde jaar promoveerde ook Jacobine van Hest van masterstudent naar collega. We delen een liefde voor Eu^{3+} en voor conferenties in Oost-Europa.

Andrei Petukhov en Hans Ligthart hebben gedurende de hele periode van mijn PhD-project hun bijdragen geleverd. Andrei was betrokken bij alle synchrotronexperimenten. We hebben vele middagen op zijn kantoor resultaten en plannen zitten bespreken, onder het genot van kilo's snoep. Hans heeft goede en snelle ondersteuning gegeven bij technische problemen of bij het bestellen van spullen. Daarnaast heb ik altijd zijn koelkast mogen gebruiken voor mijn boter en melk. Ik wil bij deze ook de Stichting FOM noemen, en in het bijzonder het onderzoeksprogramma 'Light management in new photovoltaic materials' van Albert Polman, dat mijn onderzoek heeft gefinancierd. Hans Meeldijk en Chris Schneijdenberg hebben de elektronenmicroscopen onderhouden die ik ongeveer maandelijks heb gebruikt, en ondersteuning geboden wanneer nodig. Thea Pozzi is een fijne secretaresse geweest, in deeltijd voor onze groep, die mij ergernissen heeft bespaard met formulieren en dingen regelen.

There are several people who were not my direct colleagues, but who have worked with me at some point during my PhD time. Per Lunnemann helped me at AMOLF to set up the experiments on single-nanorod spectroscopy (Ch. 3). Jan Hilhorst was vaak van de partij bij experimenten in Grenoble, en was zelfs eens onze zeer ijverige local contact. Peter van Rhee heeft experimenten en analyse gedaan op de magnetische uitlijning van Francesca's nanorods. Jenya Tilchin did beautiful low-temperature experiments on large quantum dots. And Roman Vaxenburg has done advanced theoretical work on the decay processes in quantum dots, of which the results are included in Ch. 4.

Ik heb niet alleen nut en plezier gehad van mijn collega's en mijn eigen studenten, maar ook van veel van de andere studenten op de groep. Een aantal van hen wil ik in het bijzonder noemen. Tim van Puffelen heeft met succes verder gewerkt aan mijn oude masterproject. We hebben daarnaast beiden geprobeerd wat sportiever te worden dan we eigenlijk zijn. Christian van Engers was een toonbeeld van ijver en ambitie. Hij heeft me op de hoogte gehouden van zijn avonturen tijdens zijn stage op ETH Zürich, en me zo geënthousiasmeerd dat ik daar mijn postdoc ga doen. Annelies van der Bok was eveneens een erg ijverige student. Ze heeft het voor elkaar gekregen op ons lab prachtige nanoplatelets te maken, die interessante en niet eerder onderzochte optische eigenschappen bleken te hebben. Stijn Hinterding en Sander Vonk zijn ducklings van Ward, en zijn als zodanig meegegaan op beamtrip naar het synchrotron. Stijn is daarnaast een geduchte concurrent voor Tim (Senden) om de titel 'grootste braveling van Nederland' (Sander net niet). Ze hebben zich beiden nuttig gemaakt zowel tijdens de experimenten als bij de analyse erna.

Finally I would like to mention a few people who have joined our lab earlier this year. I have actually known Sergiu Anghel from the time before he came to the Netherlands. We enjoyed lectures together by Frau Hett on Tenerife. Just before he left the group, we started examining different types of emission from Eu^{2+}. Annalisa Brodu will continue my work on single quantum dot spectroscopy after I leave. Federico Montanarella impressed me with his familiarity with the streets of Paris. I hope to examine more of the spectroscopic properties of his quantum dot supraballs. Maryam Alimoradi Jazi thinks I hate her, but I don't. We are building a fancy setup for transmission and photoluminescence measurements. Let's hope that before I leave Utrecht, all of these projects can lead to some supperpromising results.

Besides the people mentioned specifically above, there are many more who have played a role during my PhD time in some way. They have shared their knowledge, asked good questions, helped me with problems, or simply played a game of cards during lunch. I thank everyone.

ABOUT THE AUTHOR

Freddy Rabouw was born in Gouda, the Netherlands, on August 5, 1988. In 2006 he graduated from the Coornhert Gymnasium in Gouda, after which he studied chemistry at Utrecht University. He obtained his bachelor's degree *cum laude* in 2009 with a project on colloidal self-assembly by depletion attraction, in the group of Willem Kegel. He did his master's thesis research under the supervision of Andries Meijerink, developing a new synthesis method for lanthanide doped II^{A}-VI semiconductor nanocrystals. For his 5-month internship at the FOM institute AMOLF in Amsterdam in the group of Femius Koenderink, he worked on the lithographic positioning of colloidal quantum dots on flat substrates. He received his master's degree *cum laude* in 2011.

In September 2011, Freddy started as a PhD researcher under the supervision of Daniël Vanmaekelbergh and Andries Meijerink at Utrecht University. The main results of his work are described in this thesis, have been published in scientific journals, and presented at (inter)national conferences. For his contributions at conferences he has received an award for best oral presentation (Nanogé conference on Single Quantum Dots, Mallorca, Spain, 2013), and two poster prizes (PAC Symposium, Utrecht, The Netherlands, 2011 and 30 Years of Quantum Dots conference, Paris, France, 2014). During his PhD project Freddy supervised six master students and five bachelor students. He was a teaching assistent for several chemistry courses. Furthermore, from 2012 to 2014 he was the secretary of the Debye PhD committee, representing PhD students of the Debye Institute for Nanomaterials Science of Utrecht University.